Lehrstuhl für Hochfrequenztechnik
Technische Universität München

Investigations on Compact Antenna Arrays for Multiple Input Multiple Output Communication Systems

Kun Wang

Vollständiger Abdruck der von der Fakultät für Elektrotechnik und Informationstechnik der Technischen Universität München
zur Erlangung
des akademischen Grades eines

- Doktor-Ingenieurs -

genehmigten Dissertation.

Vorsitzender: Univ.-Prof. Dr. techn., Dr. h.c. Josef A. Nossek

Prüfer der Dissertation: 1. Univ.-Prof. Dr.-Ing. Thomas Eibert

2. Univ.-Prof. Dr.-Ing Wolfgang Menzel, Universität Ulm

Die Dissertation wurde am 08.09.2015 bei der Technischen Universität München eingereicht und durch die Fakultät für Elektrotechnik und Informationstechnik am 17.12.2015 angenommen.

Acknowledgment

I would like to show my sincere gratitude to Prof. Dr.-Ing. Thomas Eibert for providing me the opportunity to perform my doctoral research at the Chair of High-Frequency Engineering, Technische Universität München. His guidance and encouragement inspired me a lot in both daily life and research work. I was always motivated under his supervision. I am also grateful to my second examiner Prof. Dr.-Ing Wolfgang Menzel from Universität Ulm. His comments are quite helpful to enhance the quality of this thesis. Also, I would like to thank all my colleagues for the nice working environment and the instructive suggestions. I appreciate the colleagues from our workshop for their support during manufacturing the antenna components. Many thanks to Prof. Dr. Sheng Sun for giving me the chance to visit the University of Hong Kong, where I had a very nice experience. I would specially thank my wife and my parents. Without the support and encouragement from them, my doctoral work would not be so successful. Last but not least, I would like to thank all my family members and friends.

Abstract

Multiple input multiple output wireless communication systems are advantageous for pursuing high data rates within limited frequency bands. For low profile devices such as smart phones, compact antenna arrays are of high demand. However, the compactness of antenna arrays is restricted due to the mutual coupling effects between the radiation elements, which degrade the system performance in terms of impedance matching, radiation efficiency and antenna diversity. For solving this problem, matching and decoupling strategies are required. In this thesis, investigations of matching and decoupling approaches for compact antenna arrays are performed and a series of issues, which have not been solved in the past, are addressed.

Matching and decoupling networks implemented between the input ports and the antenna array based on eigenmode excitation or multiport conjugate matching are introduced to overcome the mutual coupling effects. Three designs of compact monopole arrays with feeding networks based on one-layer microstrip line structures are presented. Two two-element monopole antenna arrays with separations of 10% of the wavelength in free space and a four-element monopole array with separations of 7% of the wavelength in free space operating around 2.45 GHz have been designed, manufactured and measured. Comparisons and relationships between the two design theories are demonstrated. Based on the multiport conjugate matching method, beamforming applications for linearly aligned compact monopole arrays are studied. Moreover, particular decoupling approaches for printed compact arrays are developed. Simple and efficient solutions are utilized for realizing three novel compact printed arrays, consisting of two-element printed monopole arrays with partially extended ground plane, a three-element printed antenna array with combined antenna types and a dual-band two-element array with low profile elements. Promising performances of the arrays are demonstrated.

The received signal correlation between the ports of an array can be estimated from the radiation pattern correlation. According to the power conservation law, it is possible to relate the pattern correlation coefficient to the scattering parameters for lossless antenna arrays. For lossy antenna arrays with decoupling approaches such as decoupling networks, the previously published methods are not able to calculate the exact pattern correlation through the scattering parameters. Therefore, a new semi analytical method is introduced to characterize the coupling loss in a compact array with decoupling network. Hence, the pattern correlation can be approximated through the scattering parameters together with the coupling loss.

The channel capacities for compact antenna arrays with different decoupling approaches are evaluated for both statistical and deterministic models, where the radiation properties are included as well. Through comparisons between the obtained results, general methods for predicting the capacity performance according to the radiation patterns are addressed. New parameters such as a pattern on-off ratio for evaluating systems based on statistical indoor channel models are derived in this thesis.

Contents

List of Abbreviations

AWGN	additive white Gaussian noise
CCM	compact array with conjugate matching
CEM	compact array with eigenmode excitation
CLG	compact array with large ground
CNDN	compact array with no decoupling network
CPU	central processing unit
EBG	electromagnetic band gap
GO	geometrical optics
GTD	geometrical theory of diffraction
GPU	graphics processing unit
i.i.d.	independent and identically distributed
IEEE	institute of electrical and electronics engineers
LOS	line of sight
LTE	long term evolution
MIMO	multiple input multiple output
PCB	printed circuit board
PEC	perfect electric conductor
PEG	partially extended ground
PIFA	planar inverted F antenna
PMC	perfect magnetic conductor

RMS	root mean square
RX	receiving
SISO	single input single output
SNDN	sparse array with no decoupling network
SNR	signal to noise ratio
SV	Saleh-Valenzuela
SVD	singular value decomposition
TL	transmission line
TX	transmitting
UTD	uniform geometrical theory of diffraction
UWB	ultra wide band
VNA	vector network analyzer
VSWR	voltage standing wave ratio

List of Symbols

a	input wave amplitude
$\vec{A}$	magnetic vector potential
b	output wave amplitude
B	bandwidth
C	channel capacity
C'	average channel capacity
D	directivity
$\vec{e}$	unit vector
$\vec{E}$	electric field
f	frequency
G	gain
$\vec{H}$	magnetic field
$\mathbf{H}$	channel matrix
$\mathbf{I}$	unit matrix
I	current
$\vec{J}$	electric current density
j	imaginary unit
P	power
Q	quality factor
$\vec{S}$	Poynting vector

$\mathbf{S}$	scattering matrix
S	scattering parameter
V	voltage
$\mathbf{Y}$	admittance matrix
Y	admittance
$\mathbf{Z}$	impedance matrix
Z	impedance
ε	permittivity
μ	permeability
η	power efficiency
Γ	reflection coefficient
λ	wavelength in free space
ρ	correlation coefficient
ω	angular frequency

1 Introduction

Antenna arrays have been extensively investigated since several decades due to the advantages in achieving high directivity and for their beamforming capabilities [Collin and Zucker, 1969]. However, with the development of modern wireless communication techniques, antenna arrays become more and more popular for other applications, such as for multiple input multiple output (MIMO) systems in the current and upcoming generations of wireless communication systems. For example, the IEEE standard 802.11n and the Long-Term Evolution (LTE) technique already include MIMO configurations [Li et al., 2010b]. Utilizing MIMO techniques in wireless communication systems brings many benefits, e.g., high channel capacity can be achieved within limited frequency bands, so that the band usage efficiency is enhanced, and the multipath interference problem can be avoided as well [Paulraj et al., 2004]. Nowadays, wireless communication systems are even more exploited in daily life, e.g., the research for car to car communications has been established in recent years [Dikaiakos et al., 2007]. As a result, research on antenna arrays in MIMO systems is important and rewarding. In consequence, the relevant topics of compact antenna arrays are investigated in this thesis.

It is well known that when two or more antenna elements are placed close to each other, there are mutual coupling effects between them. For general types of antennas such as dipoles, a reasonable distance between the antennas should be maintained in order to get rid of the mutual coupling effect between neighboring radiation elements. It is commonly accepted that the minimum distance should be half of a wavelength, e.g., 60 mm at 2.4 GHz. However, this space requirement does not correspond to the dimension considerations of small mobile terminals, where the antenna elements should be positioned compactly. Under such a condition, the mutual coupling problem seems unavoidable. Consequently, the performance of the antenna arrays with respect to antenna diversity, efficiency of power transmission and so on, is highly degraded [Jensen and Wallace, 2004]. As a result, additional approaches and novel structures must be developed in order to design a multiport radiation system with good port isolation and a minimized overall dimension.

It is true that with respect to signal processing, the problems caused by mutual coupling might be solved by appropriate algorithms. E.g., in [Lui and Hui, 2010, Yu et al., 2011], methods based on the receiving mutual impedance have been investigated for compensating the mutual coupling effects. However, these methods do not take into account the decreased power matching of compact arrays, which is critical in practical MIMO systems. For improving power matching, several recent researches concerning this topic have been put forward. The core idea behind all these studies and designs is to isolate and match the input ports of compact antenna arrays in the analog domain. For example, the following approaches, which are suitable for compact monopole arrays, have been published. In [Chaloupka and Wang, 2004, Chaloupka et al., 2004, Volmer et al., 2008a,b, Yu and Hui, 2011], matching and decoupling networks are deployed; either networks with realistic lumped elements or directional couplers based on microstrip technology are utilized. Eigenmode excitation theory [Volmer et al., 2008b] and multiport conjugate matching methods [Wallace and Jensen, 2004] are the two basic theories for designing the matching and decoupling networks. However, the networks with lumped components bring extra Ohmic losses

into the system, which lowers the radiation efficiency. Alternatively, methods of applying parasitic scattering components have been studied in [Lau and Andersen, 2012, Salama and Solbach, 2014], which means one or more parasitic elements with specialized loads are implemented between the radiation elements to isolate the array input ports. However, there are two major drawbacks of this method. Firstly, extra array elements are required for the system and the total cost for mass fabrication is also increased. Moreover, the design appears as an $(M+m)$-element antenna array which works actually as an M-element array, where m is the number of the additional parasitic elements. Consequently, and as reported in [Pelosi et al., 2012], it is not easy to derive an analytical formulation for designing the parasitic elements. In consequent continuation of the above discussions, a method of using matching and decoupling networks with low loss technology is the most suitable candidate for designing compact monopole arrays. In this thesis, three novel prototypes of compact monopole antenna arrays with separations of only 10% of the free space wavelength operating at 2.45 GHz are presented, where microstrip line based matching and decoupling networks are investigated and implemented based on the two above mentioned theories. Good MIMO performance is obtained through both simulations and measurements. Compared to the previous designs, the networks introduced in this thesis show a number of advantages with respect to power efficiency, simplicity, compactness and so on. Besides the antenna designs, some physical insights are investigated in this thesis as well, which have not been addressed in previous publications. For example, the connection between the two theories is derived, the relationship between the radiation pattern correlation and scattering parameters is investigated, and beamforming applications of compact monopole arrays are also studied.

However, the proposed matching and decoupling networks are difficult to realize in small mobile devices such as smart phones, in which the antennas are mostly based on printed circuit technology. For printed antenna arrays, there are also several decoupling concepts published recently, e.g., the defect ground plane in [Georgakopoulos et al., 2001, Saleem et al., 2015, Younkyu et al., 2004, Zhu et al., 2009], electromagnetic band gap (EBG) structures shown in [Kim et al., 2013, Yang and Rahmat-Samii, 2003a,b], and neutralization techniques in [Su et al., 2012, Wang and Du, 2014b]. In this thesis, to expand the variety of choices for antenna designs, novel decoupling strategies for compact printed arrays are investigated as well. Due to the particular features of printed antennas such as printed monopoles, the obtained operation bandwidth is much wider as compared to other techniques and the dimension of the array is much more compact. The partially extended ground plane and modified ground planes are utilized in the designs to achieve improved MIMO performance. Additionally, a very innovative antenna design concept named contour integrated antenna for future ultra thin mobile terminals is presented, which occupies even less space. The proposed antennas and arrays can be integrated at the contour of mobile devices and require quite little space extended from the contour. Promising antenna performance is obtained by combining many novel approaches with some known techniques. Based on this concept, a two-element compact MIMO array is designed as well and a new decoupling technique especially for arrays with radiation elements with two radiation apertures, named self-neutralization, is introduced.

In this thesis, the channel capacity is chosen as an evaluation standard for the MIMO

system performance. Different wireless communication models integrated with practical antenna array properties are utilized for the investigations, consisting of statistical models for outdoor and indoor wireless communication channels and deterministic models for room and corridor scenarios. For this study, the Kronecker model [Maharaj et al., 2007, Yu et al., 2004] and the Saleh-Valenzuela model [Saleh and Valenzuela, 1987] are utilized for the statistical analysis. The ray tracing method is exploited for the deterministic studies. Afterwards, the capacity performance of the antenna arrays is evaluated and interesting results are obtained and shown. Some new parameters for predicting the performance based on antenna patterns are also derived.

The content of this thesis is organized as follows. The antenna basics and the important parameters used in this thesis are defined and derived in Chapter 2. Chapter 3 derives the basic mathematics for calculating the channel capacity for MIMO systems based on information theory and defines the design objectives for compact antenna arrays. The matching and decoupling networks for compact arrays and the relevant investigations are proposed in Chapter 4. Novel compact printed antennas and arrays are introduced in Chapter 5. In Chapter 6, the channel capacity performance of MIMO systems is evaluated based on different models. The summary of the thesis and the outlook of this research topic are given in Chapter 7.

2 Antenna Basics

In this chapter, the basic concepts and definitions of antennas are introduced. Most of the parameters used for defining and evaluating the properties and performances of antennas or antenna arrays are presented.

2.1 Introduction to Antennas

There are a number of definitions for antennas given in literature, such as in the IEEE standards of antennas [IEEE, 1983]. Instead of writing down all these definitions, the functionality of antennas is summarized from available documents. In general, an antenna is a transducer between a guided electromagnetic wave in a waveguide structure and an unguided wave such as the wave propagating in free space, as shown in Figure 2.1. The physical radiation mechanisms of antennas can be deduced from the Maxwell equations, which make it possible to calculate the antenna properties numerically and to predict the performance of an antenna. Nowadays, commercial electromagnetic simulation software packages like CST MWS [CST MWS, 2014], HFSS [HFSS, 2014] and FEKO [FEKO, 2014] are quite efficient in solving electromagnetic problems. In this thesis, the antenna simulations are carried out with CST MWS.

Antennas are widely used in daily life for a wide variety of applications, e.g., antennas are applied for receiving radio broadcasting signals, antennas are implemented in cell phones or laptops, antenna arrays are utilized in radar systems, and so on. In general, different applications require different types of antennas. In the following, the antenna types and the development history are introduced briefly.

The history of antennas can be traced back to the 1830s when Faraday made the experiment with a magnetic coil which was used to track an electromagnetic pulse. This magnetic coil was operated as an antenna. Around 1890, the first group of antennas, such as induction coils used for wireless communication experiments, were developed [Ramsay, 1981]. The most important progresses in antennas were made in the 20th century. In the beginning of the 20th century, several popular antenna concepts were developed for radio telegraphy applications, for instance the linear dipoles were widely deployed and improved. Based on the dipoles, in the 1920s the Yagi-Uda antenna was firstly proposed, which has been deployed for a long period [Yagi, 1928]. Nowadays, on the roofs of buildings, there are still such antennas which are installed to receive broadcasting signals for television. The design concept from the Yagi-Uda antenna is also applied quite often in designing planar antennas such as the wide band quasi Yagi antenna [Kaneda et al., 2002]. Horn antennas or hollow waveguide antennas were developed around 1939. They are directional antennas and functional from lower frequency ranges such as hundreds of MHz to millimeter wave frequencies. Nowadays, hollow waveguide antennas are still widely used, e.g., they are implemented as probes for antenna measurements and radiation elements for millimeter wave antenna arrays. In the early 1940s, reflector antennas were firstly investigated to meet the demands of early radar systems. Commonly, reflector antennas own a directivity of more than 20 dB and can be found very often at airports, ground to satellite communication stations as well as on the balconies of buildings. At the same period, dielectric lens antennas

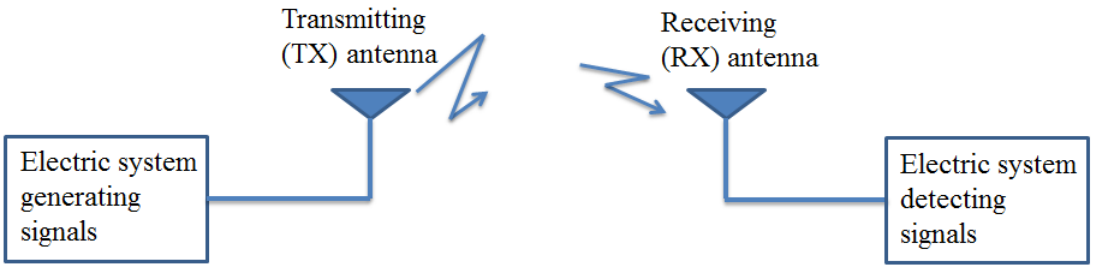

Figure 2.1: Functionality of transmitting and receiving antennas.

and antenna phased arrays also got developed. With the progress of printed circuit board (PCB) technology in the 1970s, printed antennas such as patch antennas were invented and they were extensively employed in electronic devices. In the 1990s, the planar inverted F antenna (PIFA) was developed to satisfy the size requirement of portable mobile terminals. Since the 21st century, metamaterial antennas, dielectric resonator antennas, compact antenna arrays and so on have become more and more popular. Some classic antenna types are shown in Figure 2.2 [AntennaWeb, 2015, Balanis, 1992].

2.2 Antenna Parameters and Basic Equations

In this section, general parameters and definitions for antenna design and analysis are introduced. Some derivations are carried out for further discussions.

2.2.1 Isotropic Antenna and the Coordinate System

An isotropic antenna is a specialized electromagnetic radiator, radiating equal power in all directions. It does not exist in reality, but it is utilized as a standard reference antenna for defining parameters of practical antennas.

As done in most literature, the spherical coordinate system is adopted in this thesis to indicate the antenna far field radiation properties, as shown in Figure 2.3. For example, the position of point P in the figure can be described as (r, θ, ϕ) and the radiated field and power are then depicted as a function of r, θ and ϕ. It is well known that in the far field approximation, the radiated electromagnetic waves are assumed to be locally plane waves ($r \to \infty, E_r \approx 0$), and the polarization of the fields can also be described by the θ and ϕ components, which are orthogonal in space. For example, the electric field $\vec{E}$ and the magnetic field $\vec{H}$ at a point P in the far field can be written as

$$\begin{cases} \vec{E} = E_\theta \vec{e}_\theta + E_\phi \vec{e}_\phi, \\ \vec{H} = H_\theta \vec{e}_\theta + H_\phi \vec{e}_\phi, \end{cases} \tag{2.1}$$

where $\vec{e}_\theta$ and $\vec{e}_\phi$ are unit vectors towards the θ and ϕ directions, respectively. Also, it should be noted that time harmonic fields with a suppressed time factor $e^{j\omega t}$ are considered. The

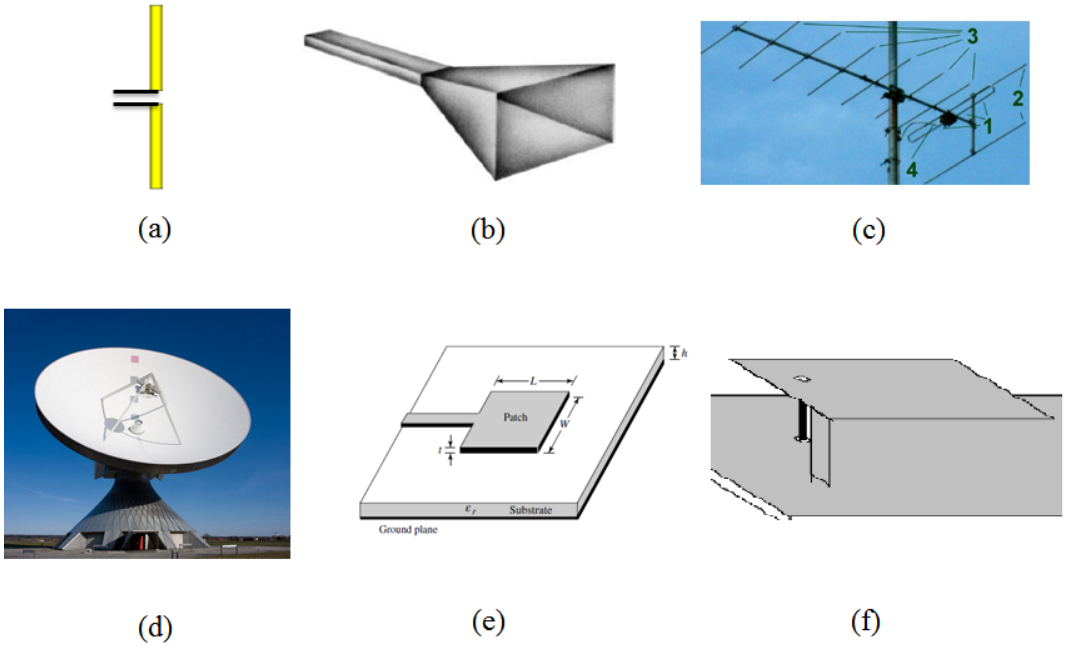

(a) (b) (c)

(d) (e) (f)

Figure 2.2: Some popular antenna types: (a) dipole antenna; (b) horn antenna [Balanis, 2005]; (c) Yagi-Uda antenna [Wikipedia, 2015c];(d) parabolic reflector antenna [Wikipedia, 2015a]; (e) rectangular patch antenna [Balanis, 2005]; (f) PIFA [Wikipedia, 2015b].

root mean square (RMS) radiated power density can be expressed as $\mathrm{Re}[\vec{S}]$ with

$$\vec{S}(\theta,\phi,r) = \frac{1}{2}\vec{E}(\theta,\phi,r) \times \vec{H}^*(\theta,\phi,r), \tag{2.2}$$

where $\vec{S}(\theta,\phi,r)$ is the complex Poynting vector. Only the real part of the complex Poynting vector is related to the radiated power, while the imaginary part corresponds to the stored energy around the antenna in the near field. Consequently, the total radiated power over a closed sphere surface equals

$$P_{\mathrm{rad}} = \int_0^{2\pi}\int_0^{\pi} \frac{1}{2} Re[\vec{E}(\theta,\phi,r) \times \vec{H}^*(\theta,\phi,r)] r^2 \sin\theta d\theta d\phi. \tag{2.3}$$

For isotropic radiators, the radiation power density depends only on r, based on equation (2.3),

$$|\vec{S}_i(r)| = \frac{P_{\mathrm{rad}}}{4\pi r^2}. \tag{2.4}$$

2.2.2 Input Impedance and Operation Frequency Bandwidth

The input impedance of an antenna is defined as the ratio between the voltage at the antenna feeding point representing the electric field and the current flowing into the antenna

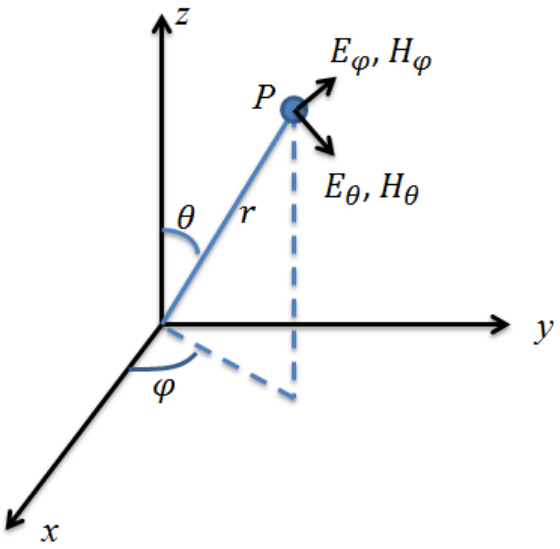

Figure 2.3: The spherical coordinate system.

representing the magnetic field. Mathematically, it is written as

$$Z_a = \frac{V_a}{I_a} = R_a + X_a j, \tag{2.5}$$

where V_a and I_a are the corresponding voltage and current at the antenna feed, R_a and X_a are the real and imaginary part of the antenna input impedance. If there is a mismatch between the port impedance and the antenna impedance, the undesired reflection at the interface occurs and the reflection coefficient is calculated through

$$\Gamma = \frac{Z_a - Z_0}{Z_a + Z_0}, \tag{2.6}$$

where Z_0 is the port or reference impedance. Generally the reflection coefficient is shown in logarithmic scale, the value is

$$|\Gamma| \text{ [dB]} = 20 \log_{10} |\Gamma|. \tag{2.7}$$

Sometimes, the impedance matching property of antennas is also characterized by the voltage standing wave ratio (VSWR). The VSWR is defined as the ratio of the maximum standing wave amplitude to the minimum standing wave amplitude and is, thus, calculated as

$$\text{VSWR} = \frac{1 + |\Gamma|}{1 - |\Gamma|}. \tag{2.8}$$

The operation bandwidth of an antenna generally indicates in which frequency band the desired antenna performance in terms of radiation pattern or return loss is achieved. In

most cases, the operation bandwidth is referred to the matching bandwidth. In this thesis, -10 dB return loss is chosen to define the matching bandwidth. The relative bandwidth BW is expressed in percentage as

$$BW = \frac{\Delta f}{f_c} 100\%, \tag{2.9}$$

where Δf is the operation frequency band and f_c is the center frequency. For ultra wide band (UWB) antennas, the bandwidth can also be expressed as the ratio between the highest operation frequency to the lowest one.

The maximum achievable matching bandwidth normally depends on the structure of radiation elements, e.g., electrically small antennas always encounter bandwidth problems. In [Yaghjian and Best, 2005], an analytical derivation is performed with respect to the relationship between the achievable bandwidth and the antenna quality factor Q, which is

$$Q(\omega_0) = \frac{(2\sqrt{\beta})}{BW(\omega_0)}, \quad \sqrt{\beta} = \frac{(s-1)}{2\sqrt{s}}, \tag{2.10}$$

where BW is the matching bandwidth corresponding to the desired VSWR and s is the limiting value of the VSWR. It is shown that the quality factor is inversely proportional to the bandwidth.

2.2.3 Directivity, Gain and Efficiency

The maximum value of directivity defines how directional an antenna is. The directivity of an antenna is the ratio between the radiated power density of this antenna in a particular direction at a certain distance and the radiated power density of an isotropic antenna at the same distance with the same total radiated power. The directivity D is mathematically defined as

$$D(\theta, \phi) = \lim_{r \to \infty} \frac{|\vec{S}(\theta, \phi, r)|}{\frac{P_{\text{rad}}}{4\pi r^2}} = \lim_{r \to \infty} \frac{|\vec{S}(\theta, \phi, r)|}{|\vec{S}_i(r)|}, \tag{2.11}$$

where $\vec{S}_i(r)$ is the radiation power density of the isotropic antenna with the total radiated power P_{rad}. It is clear that the directivity of an isotropic antenna is 1, which is normally marked as 0 dB. In some literature and antenna manuscripts, the directivity of an antenna is just given as a particular number, in this case, it means the maximum directivity. The directivity is an important parameter for characterizing the radiation properties. E.g., in cell phone applications the directivity should be low because an isotropic radiation pattern is desired, due to the electromagnetic waves impinging from arbitrary directions in a rich scattering environment. For radar applications the directivity needs to be high, i.e., more than 20 dB in general.

The gain of an antenna is defined in a similar way as the directivity. It is the ratio between the radiated power intensity of an antenna in a particular direction and the radiated

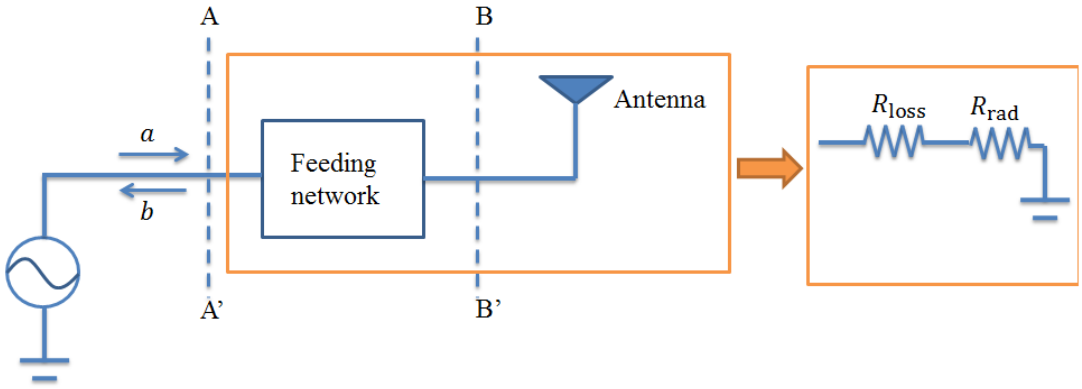

Figure 2.4: Definition of the antenna input interface and the equivalent circuit model.

power intensity of a lossless isotropic antenna with the same accepted power. The gain can be expressed as

$$G(\theta,\phi) = \lim_{r\to\infty} \frac{|\vec{S}(\theta,\phi,r)|}{\frac{P_{\text{ac}}}{4\pi r^2}}, \tag{2.12}$$

where P_{ac} means the accepted power of the antenna. Here, the accepted power is defined as

$$P_{\text{ac}} = P_{\text{in}} - P_{\text{re}} = \frac{1}{2}|a|^2 - \frac{1}{2}|b|^2 = (1-|\Gamma|^2)P_{\text{in}}, \tag{2.13}$$

where P_{in} and P_{re} are the input and reflected power, a and b are the input and reflected power wave amplitudes, Γ is the reflection coefficient. In this thesis, the interface for the input and reflected waves of an antenna is chosen at the AA' plane as shown in Figure 2.4, because feeding networks are quite often adopted in designing compact antenna arrays, and they are an integrated part of the array. Due to their losses, their consideration is important for a realistic characterization of the antenna array performance.

The antenna radiation efficiency is utilized for evaluating the losses. It is defined as the ratio between the radiated power P_{rad} and the accepted power P_{ac},

$$\eta_r = \frac{P_{\text{rad}}}{P_{\text{ac}}} = \frac{R_{\text{rad}}}{R_{\text{rad}} + R_{\text{loss}}}, \tag{2.14}$$

where R_{rad} is the equivalent radiation resistance and R_{loss} is the equivalent loss resistance in the series equivalent circuit model as shown in Figure 2.4 (the reactive elements are neglected in the circuit model). Consequently, the total efficiency is defined as the ratio between the total radiated power and the input power. From equations (2.14) and (2.15), the total efficiency is written as

$$\eta_t = \frac{P_{\text{rad}}}{P_{\text{in}}} = (1-|\Gamma|^2)\eta_r. \tag{2.15}$$

It is also noticed that the relationship between directivity and gain is

$$G(\theta, \phi) = \eta_r D(\theta, \phi). \tag{2.16}$$

This relationship can be applied for radiation efficiency measurements, where the gain can be measured with a reference antenna and the directivity can be calculated from 3D pattern measurements.

The reflection coefficient Γ can be reduced by inserting appropriate matching networks. However, the matching network can bring additional losses and reduce the overall efficiency. Therefore, the total efficiency should be evaluated after adding the matching network to ensure maximum radiated power. In this thesis, the gain and efficiency of MIMO antenna arrays are defined in the same way, as shown in Appendix A.

2.2.4 Effective Receiving Area and Friis Transmission Equation

When an antenna works in RX mode, the effective receiving area is utilized to characterize the maximum received power, which equals the effective area multiplied with the power density W of the incident plane wave according to

$$P_{\mathrm{RX}} = A_{\mathrm{eff}} |\vec{S}|. \tag{2.17}$$

The effective receiving area of an isotropic radiator is given as [Balanis, 2005],

$$A_{\mathrm{effi}} = \frac{\lambda^2}{4\pi}, \tag{2.18}$$

where λ is the wavelength in free space. The effective receiving area of realistic antennas is given as

$$A_{\mathrm{eff}}(\theta, \phi) = G(\theta, \phi) \frac{\lambda^2}{4\pi}. \tag{2.19}$$

It shows that the effective area for the incoming wave from a particular direction depends on its gain towards this direction, which agrees well with reciprocity. Antennas always receive more power from the direction towards which they transmit more power.

Once the antenna receiving power is calculated, the power transmission from one antenna to another antenna can be characterized. Figure 2.5 plots a transmission system between two antennas. P_{TX} is the accepted power by the transmitting antenna. P_{RX} is the output power at the receiving antenna assuming conjugate matching. The transmitted power density towards the specific direction $(\theta_{\mathrm{TX}}, \phi_{\mathrm{TX}})$ in the far field is

$$|\vec{S}(\theta_{\mathrm{TX}}, \phi_{\mathrm{TX}})| = \frac{G_T(\theta_{\mathrm{TX}}, \phi_{\mathrm{TX}}) P_{\mathrm{TX}}}{4\pi r^2}, \tag{2.20}$$

where r is the distance between the antennas. The received power of the RX antenna is

$$\begin{aligned} P_{\mathrm{RX}} =& |\vec{S}(\theta_{\mathrm{TX}}, \phi_{\mathrm{TX}})| A_{\mathrm{reff}}(\theta_{\mathrm{RX}}, \phi_{\mathrm{RX}}) \\ =& \frac{G_T(\theta_{\mathrm{TX}}, \phi_{\mathrm{TX}}) P_{\mathrm{TX}}}{4\pi r^2} \frac{G_R(\theta_{\mathrm{RX}}, \phi_{\mathrm{RX}}) \lambda^2}{4\pi}, \end{aligned} \tag{2.21}$$

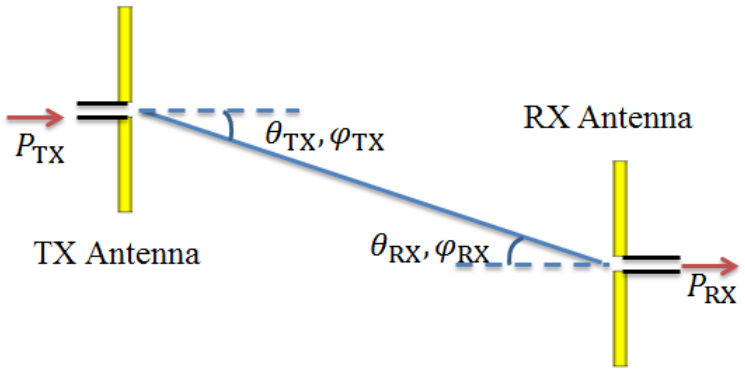

Figure 2.5: Transmission between two dipole antennas.

where A_{reff} is the effective area of the RX antenna. Equation (2.22) is known as the Friis transmission equation, the maximum transmission coefficient can be achieved when the two antennas are aligned to obtain the maximum gain of both the TX and RX antennas, respectively. Then, the transmission coefficient becomes

$$\frac{P_{\text{RX}}}{P_{\text{TX}}} = \left(\frac{\lambda}{4\pi r}\right)^2 G_{Tm} G_{Rm}, \tag{2.22}$$

where G_{Tm} and G_{Rm} are the maximum gains of the TX and RX antennas. The factor $(\frac{\lambda}{4\pi r})^2$ is the free space loss factor, and its dependency on wavelength is with respect to the size of the effective receiving area. It is noticed that this factor is inversely proportional to the square of the distance between the two antennas and the frequency. This explains why for long distance communication systems, lower frequencies are mostly adopted, while for indoor communications, the frequencies are normally higher in order to achieve larger available bandwidth. The Friis equation is applied in the following chapters to characterize the channel properties of wireless communication systems.

2.2.5 Array Factor of Linear Antenna Arrays

When more than one radiation elements appear at the TX or RX stage in a communication system, an antenna array is obtained. Antenna arrays have extensively been implemented for radar applications since several decades due to their beamforming capabilities. In this subsection, beamforming with linear antenna arrays is introduced. In Figure 2.6, an N-element linear antenna array with a uniform distance d between the elements is plotted, all the radiation elements are the same and it is assumed that the existence of one antenna does not affect the radiation of other elements. In the far field, the radiation pattern of the array is expressed as the linear superposition of the contributions from all the elements.

The total radiated electric field is

$$\vec{E}_t(\alpha, P) = \sum_{i=1}^{N} \vec{E}_i(\alpha, P). \tag{2.23}$$

$\vec{E}_i(\alpha, P)$ is the radiated electric field due to the ith antenna, the plane P is parallel to the antenna alignment and the angle α is indicated in Figure 2.6. If the ith element is excited with a constant amplitude a_i and a constant phase β_i, the radiated electric fields of two neighboring elements own the relationship

$$\frac{\vec{E}_i(\alpha, P)}{\vec{E}_{i-1}(\alpha, P)} = \frac{a_i e^{j(-\frac{2\pi}{\lambda} d\cos\alpha + \beta_i)}}{a_{i-1} e^{j\beta_{i-1}}} \tag{2.24}$$

under the far field condition. The phase term $e^{-\frac{2\pi}{\lambda} d\cos\alpha}$ is due to the additional travel distance $d\cos\alpha$. Then, equation (2.24) can be written as

$$\vec{E}_t(\alpha, P) = \vec{E}_1(\alpha, P) F_A, \tag{2.25}$$

where

$$F_A = 1 + \frac{a_2 e^{j(-\frac{2\pi}{\lambda} d\cos\alpha + \beta_2)}}{a_1 e^{j\beta_1}} + \frac{a_3 e^{j(-2\frac{2\pi}{\lambda} d\cos\alpha + \beta_3)}}{a_1 e^{j\beta_1}} + \cdots + \frac{a_N e^{j(-(N-1)\frac{2\pi}{\lambda} d\cos\alpha + \beta_N)}}{a_1 e^{j\beta_1}} \tag{2.26}$$

is called the array factor. For uniform linear arrays, the excitation amplitude of each element is identical and the phase difference between the neighboring elements is equal to $\Delta\beta = \beta_i - \beta_{i-1}$. In this case, the array factor becomes

$$F_A = \sum_{i=1}^{N} e^{j(N-1)(-\frac{2\pi}{\lambda} d\cos\alpha + \Delta\beta)}. \tag{2.27}$$

In order to obtain the maximum array factor, the term $(-\frac{2\pi}{\lambda} d\cos\alpha + \Delta\beta)$ must equal integer multiples of 2π, including 0. In the broadside direction of the array ($\alpha = 90°$), the condition $\Delta\beta = 0$ leads to the maximum array factor. In the end fire direction ($\alpha = 0°$), the condition $\Delta\beta = \frac{2\pi}{\lambda} d$ leads to the maximum array factor. If d is larger than half a wavelength for a certain $\Delta\beta$, there are more than one peak values of F_A, which are called grating lobes. 2D and 3D arrays can be analyzed by applying the same approach.

2.2.6 Scattering, Impedance and Admittance Matrices of Antenna Arrays

For N-port networks, scattering, impedance and admittance matrices are convenient mathematical tools for describing the properties such as the voltage-current relationship, reflections, couplings between the ports, and so on. It is important and beneficial to apply these tools during the investigation of compact antenna arrays. In this subsection, a two-port network is analyzed as an example as shown in Figure 2.7. V_i and I_i are defined as the

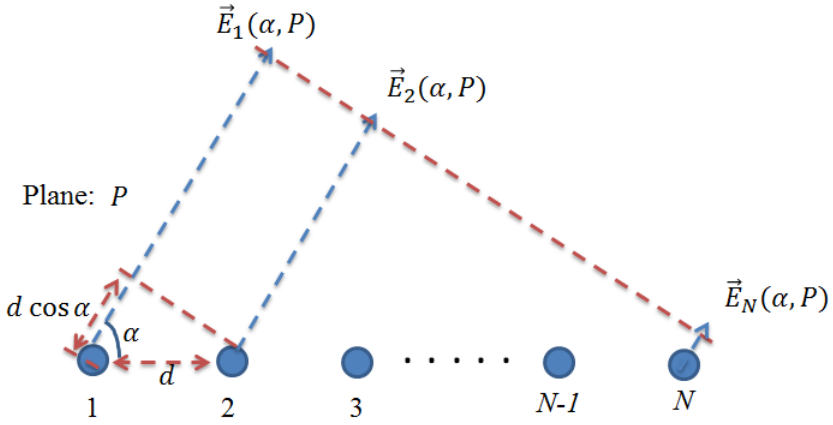

Figure 2.6: Linear uniform array with N radiation elements.

voltage and current at the ith port. a_i and b_i are the input and output wave amplitudes at the ith port. The relationships between a_i, b_i, V_i and I_i are

$$\begin{cases} a_i = \frac{V_i^+}{\sqrt{Z_0}}, \\ b_i = \frac{V_i^-}{\sqrt{Z_0}}, \\ V_i = V_i^+ + V_i^-, \\ I_i = I_i^+ - I_i^- = \frac{1}{\sqrt{Z_0}}(V_i^+ - V_i^-). \end{cases} \tag{2.28}$$

Z_0 is the port impedance and the standard value of it is 50 Ω in most microwave systems, V_i^+ is the input voltage wave and V_i^- is the reflected or output voltage wave. The same definition is also applied to the current waves. The definition of the elements in the scattering matrix is

$$S_{ij} = \frac{b_i}{a_j} \mid_{a_k=0 \text{ for } k\neq j}, \tag{2.29}$$

where S_{ij} is the ratio of the output wave amplitude at the ith port and the input wave amplitude at the jth port when the remaining ports are not excited but loaded with the reference impedance Z_0. Similarly, the definition of the elements in the impedance and admittance matrices are

$$\begin{cases} Z_{ij} = \frac{V_i}{I_j} \mid_{I_k=0 \text{ for } k\neq j}, \\ Y_{ij} = \frac{I_i}{V_j} \mid_{V_k=0 \text{ for } k\neq j}. \end{cases} \tag{2.30}$$

The two-port network can be characterized by the scattering matrix in the form of

$$\vec{b} = \begin{bmatrix} b_1 \\ b_2 \end{bmatrix} = \begin{bmatrix} S_{11} & S_{12} \\ S_{21} & S_{22} \end{bmatrix} \begin{bmatrix} a_1 \\ a_2 \end{bmatrix} = \mathbf{S}\vec{a}, \tag{2.31}$$

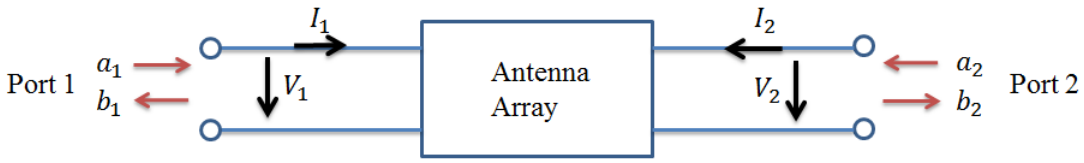

Figure 2.7: Two-port antenna array network.

where $\vec{a}$ and $\vec{b}$ are the input and output wave vectors and $\mathbf{S}$ stands for the scattering matrix. The impedance matrix $\mathbf{Z}$ and the admittance matrix $\mathbf{Y}$ are expressed in a similar way. If one of the three matrices is known, the other ones can be found from

$$\begin{cases} \mathbf{Z} = Z_0(\mathbf{I}+\mathbf{S})(\mathbf{I}-\mathbf{S})^{-1}, \\ \mathbf{Y} = \mathbf{Z}^{-1}, \end{cases} \tag{2.32}$$

where $\mathbf{I}$ is the unit matrix.

2.2.7 Multipath Interference and Antenna Array Diversity

When an antenna array is utilized in a communication system instead of a single antenna, the diversity improvement is an important factor indicating how the communication system benefits from the antenna array. Considering communication systems in reality, multipath interference problems commonly exist. For example, in Figure 2.8 there are two possible paths between the TX and RX antennas. If the signals from the two paths are in phase and constructive interference occurs, very good transmission is achieved. On the other hand, if the signals are out of phase, then destructive interference occurs and the received signal power is very low. For illustrating this phenomenon, the following situation is analyzed. The TX and RX antennas are assumed to be isotropic and they are 20 m above the ground, the reflection coefficient at the ground plane is -1 and the polarization is not considered. According to equation (2.23), the received power of path 1 is

$$P_{\mathrm{RX1}} = (\frac{\lambda}{4\pi D})^2 P_{\mathrm{TX}} \tag{2.33}$$

and the received power of path 2 is

$$P_{\mathrm{RX2}} = \left(\frac{\lambda}{4\pi(2\sqrt{(\frac{D}{2})^2+h^2})}\right)^2 P_{\mathrm{TX}}. \tag{2.34}$$

The phase of the transmission coefficient between the two isotropic radiators is calculated as $e^{j(-\frac{2\pi}{\lambda}L)}$, where L is the travel distance of the wave. Considering the interference effect, the received power at the RX antenna is

$$P_{\mathrm{RX}} = \left|\sqrt{P_{\mathrm{RX1}}}e^{j(-\frac{2\pi}{\lambda}D)} - \sqrt{P_{\mathrm{RX2}}}e^{j\left(-\frac{2\pi}{\lambda}(2\sqrt{(\frac{D}{2})^2+h^2})\right)}\right|^2. \tag{2.35}$$

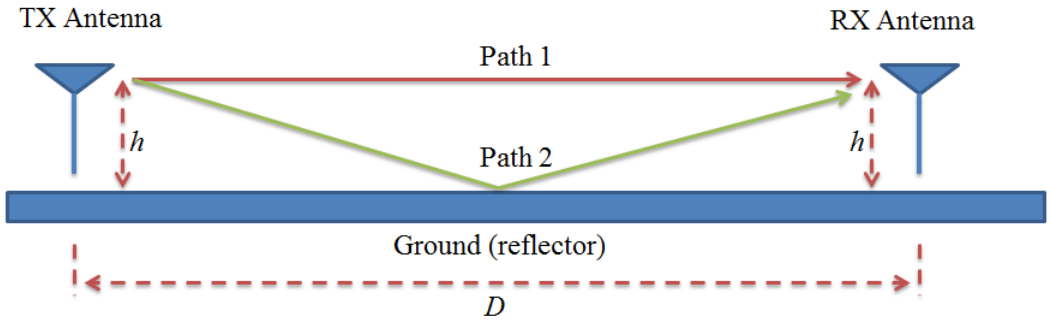

Figure 2.8: Multipath interference between two antennas.

The transmitted power is assumed to be 1 W and the frequency is selected as 1 GHz. Figure 2.9 plots the received powers versus the distance between the antennas. There are several positions where the received signal power is as low as -60 dBm and the link is bad. When two antennas are properly implemented in the receiver, the multipath problem is solved due to the diversity of the two antennas. For example, one antenna can be set at the position of 100 m while the other is located at 95 m. This ensures that at least one of the antennas receives the transmitted signal well. The benefit of this arrangement is called space diversity of antenna arrays. However, in practical communication devices such as mobile terminals, the antennas can not be arranged with such a large separation, so that space diversity is not feasible. Then, an arrangement named radiation pattern diversity is adopted in antenna arrays, where the radiation patterns of the antennas in an array should be angularly diverse. The antenna array shown in Figure 2.10 can be adopted for the situation shown in Figure 2.8,, where the two RX antennas have different main beam directions. Then, by proper combination techniques of the received signals, the multipath problem is solved. In some literature, a quantity named diversity gain is applied to assess the diversity performance of antenna arrays. A detailed definition is found in [Kildal and Rosengren, 2004].

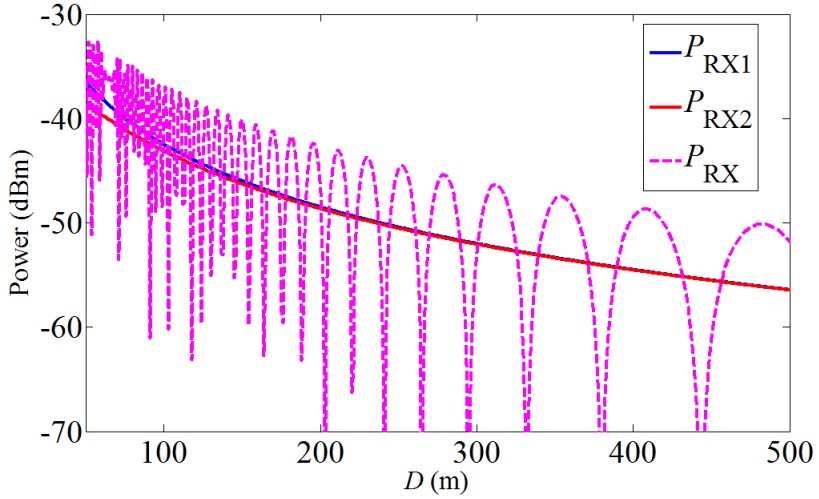

Figure 2.9: Received signal power versus the distance between two antennas.

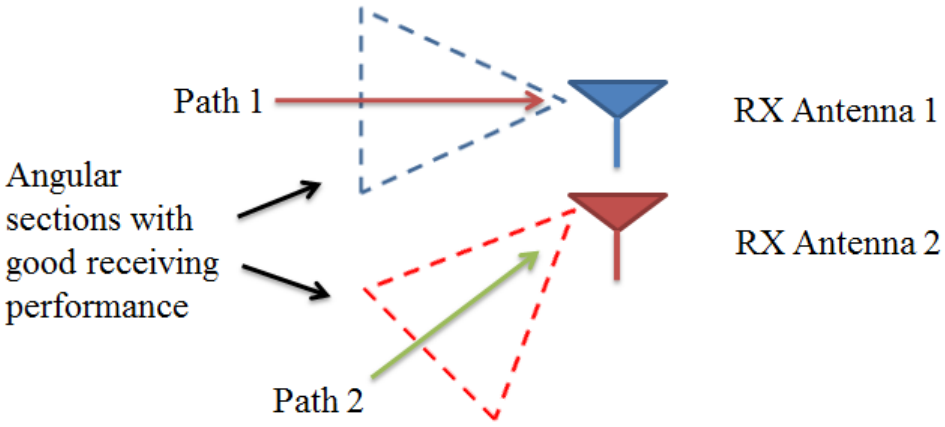

Figure 2.10: An example of an RX antenna array with pattern diversity.

3 Fundamentals of Multiple Input Multiple Output Communication Systems

In this chapter, the theoretical fundamentals of multiple input multiple output (MIMO) communication systems are introduced and derived. The basic configuration of MIMO systems and the corresponding mathematical descriptions are presented. The advantages of MIMO systems are verified through channel capacity evaluations. Discussions with respect to the challenges of applying MIMO antenna arrays in practical communication devices are carried out. Consequently, possible solutions and the design objectives of MIMO antenna arrays are addressed.

3.1 Introduction to MIMO Communication Systems

In the previous chapter, it has already been shown that multiple RX antennas are beneficial in solving multipath problems. However, MIMO communication systems are also advantageous in pursuing high data rates within limited frequency bandwidth and with power constraints, and this can be proved by evaluating the wireless channel capacity. Intuitively, when more parallel channels are utilized in a transmission link, more information can be transferred from the transmitter to the receiver through all these channels.

Figure 3.1 shows the general configuration of a MIMO system, where M TX antennas and N RX antennas are utilized. x_n is the complex transmitted signal of the nth antenna among the TX antennas and $\vec{x} = [x_1, x_2, ...x_M]^T$ is the complex transmitted signal vector. Similarly, $\vec{y} = [y_1, y_2, ...y_M]^T$ is the complex received signal vector, which is obtained through

$$\vec{y} = \begin{bmatrix} y_1 \\ y_2 \\ \vdots \\ y_N \end{bmatrix} = \begin{bmatrix} h_{11} & \cdots & h_{1M} \\ \vdots & \ddots & \vdots \\ h_{N1} & \cdots & h_{NM} \end{bmatrix} \begin{bmatrix} x_1 \\ x_2 \\ \vdots \\ x_M \end{bmatrix} + \begin{bmatrix} n_1 \\ n_2 \\ \vdots \\ n_N \end{bmatrix} = \mathbf{H}\vec{x} + \vec{n}. \tag{3.1}$$

$\mathbf{H}$ is the channel matrix with the dimension of $N \times M$. $\vec{n}$ is a zero mean complex Gaussian noise vector at the receiver. Element h_{ij} represents the transmission coefficient between the ith RX antenna and the jth TX antenna. In order to evaluate the performance of a MIMO system, the channel matrix should be firstly characterized. The channel matrix can be obtained either by simulations or by measurements. Popular simulation methods consist of statistical modeling methods [Spencer et al., 2000], full wave electromagnetic field simulations [Zhang and Sarris, 2014], ray tracing methods [Gesbert et al., 2002], and so on. Measurements of course return the most practical results, but the measurement setups are problematic for different scenarios.

3.2 Advantages of MIMO Systems

As mentioned above, MIMO systems are advantageous for pursuing high data rates. The data rate performance can be represented by the channel capacity [Cover and Gamal, 1979]. Channel capacity means the upper bound of the rate for information transfer in the

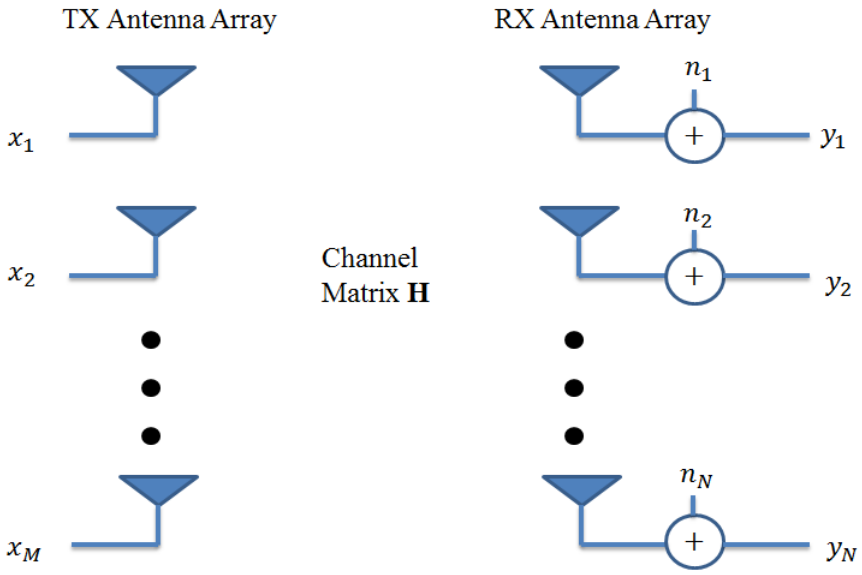

Figure 3.1: Configuration of a MIMO communication system.

channel. When the desired system data rates are smaller than the channel capacity, it is said that reliable communication can be achieved by applying proper coding techniques. Mathematically, channel capacity is defined as the maximum mutual information $I(X,Y)$ per unit time duration between the TX and RX ports [Gray, 2011],

$$I(X,Y) = H(X) - H(X|Y) = H(Y) - H(Y|X), \tag{3.2}$$

where $H(X)$ is the entropy of a discrete random process $\{X\}$ and X_i is the ith element in $\{X\}$ with the probability $p(X_i)$. $H(X)$ is also called the self information and for discrete distributions, it is calculated through

$$H(X) = -\sum_{i=1}^{N} p(X_i) \log_2 p(X_i). \tag{3.3}$$

In this case, the unit of $H(X)$ is bit. For example, if $\{X\}$ contains two elements and the probability of each is 0.5, the corresponding self information is 1 bit. For continuous distributions $\{X\}$ with the probability density function $p(x)$, the self information is

$$H(X) = -\int p(x) \log_2 p(x) dx. \tag{3.4}$$

$H(X|Y)$ is the conditional entropy, which means the uncertainty of $\{X\}$ when elements in $\{Y\}$ appear. For discrete distributions, it is

$$H(X|Y) = -\sum_{k=1}^{M} p(Y_k) \sum_{i=1}^{N} p(X_i|Y_k) \log_2 p(X_i|Y_k), \tag{3.5}$$

and for continuous distributions, it is

$$H(X|Y) = -\int\int p(y)p(x|y)\log_2 p(x|y)dxdy. \tag{3.6}$$

If there is no uncertainty between the TX and RX ports such as $p(X_i|Y_k) = 1$, thus $H(X|Y) = 0$, the mutual information equals the self information at the TX port. However, uncertainties always exist in reality due to the existence of noise, and the mutual information is always less than the self information at the TX port. In this chapter, the investigation focuses on continuous channels.

3.2.1 Channel Capacity of Single Input Single Output (SISO) Systems

The channel capacity of a zero mean additive white Gaussian noise (AWGN) channel is given by the Shannon information theorem as [Shannon, 1948]

$$C = B\log_2\left(1 + \frac{S}{N}\right), \tag{3.7}$$

where B is the bandwidth of the channel, S is the received signal power, N is the noise power at the receiver, and $\frac{S}{N}$ is the receiver signal to noise ratio (SNR). The unit of C is bit/s. Equation (3.7) can be proved as follows. It is assumed that the TX signal x satisfies the Gaussian distribution and the received signal is

$$y = hx + n. \tag{3.8}$$

Based on equation (3.4), the entropy of $\{X\}$ with Gaussian distribution and standard deviation δ is [Telatar, 1999]

$$H(X) = -\int p(x)\log_2 p(x)dx = \log_2(\sqrt{2\pi e}\delta). \tag{3.9}$$

where e is the Euler number.

Since the distributions of x and n are both zero mean Gaussian, y is also zero mean Gaussian. In this case, the time average signal power equals the variance. Based on the power conservation low,

$$P_y = \delta_y^2 = |h|^2\delta_x^2 + \delta_n^2 = S + N. \tag{3.10}$$

Then,

$$H(Y) = \log_2\sqrt{2\pi e(S+N)}. \tag{3.11}$$

$H(Y|X)$ is the conditional entropy and it equals the entropy of the noise $H(n)$ [Telatar, 1999]. Based on equation (3.2), the mutual information is written in the form of

$$\begin{aligned} I(X,Y) =& \log_2\sqrt{2\pi e(S+N)} - \log_2\sqrt{2\pi eN} \\ =& \frac{1}{2}\log_2(1+\frac{S}{N}). \end{aligned} \tag{3.12}$$

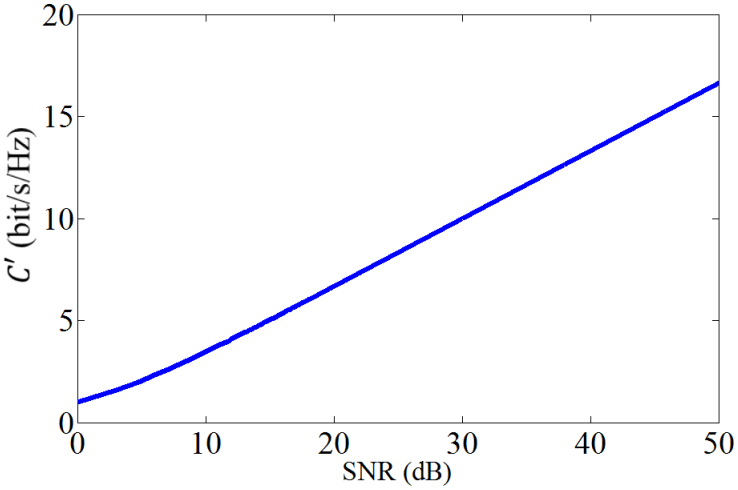

Figure 3.2: The average channel capacity versus receiver SNR.

For the realization of data transfer, discrete transmissions of signals are assumed, where the ideal sampling rate based on the Nyquist theorem is $t_s = \frac{1}{2B}$. As a result, the maximum data rate of the channel becomes

$$C = I(X,Y)\frac{1}{t_s} = B\log_2\left(1+\frac{S}{N}\right). \tag{3.13}$$

It is noticed that the maximum data rate of a channel is related to the bandwidth and the SNR at the receiver. When infinite signal power or zero noise power exists, the channel capacity can be infinite in theory. As a result, it is important to ensure a good SNR at the RX stage in communication systems, since the bandwidth is always limited by the standards or regulations. The average channel capacity (spectrum channel capacity density) is defined as

$$C' = \log_2\left(1+\frac{S}{N}\right), \tag{3.14}$$

where the unit is bit/s/Hz. Figure 3.2 plots the average channel capacity versus the SNR. For example, if 1 Gbit/s data rate is desired and the receiver SNR is 50 dB, 75 MHz bandwidth are required according to equation (3.13).

3.2.2 Channel Capacity of MIMO Systems

The considerations concerning MIMO channel theory follow [Goldsmith et al., 2003, Telatar, 1999, Wang et al., 2005]. When multiple antennas are used in a communication system, the entropy of the input signals should be redefined. The TX signals are presented as the elements in the vector $\vec{x}$ in equation (3.1). When the real and imaginary parts of the elements of $\vec{x}$ are both Gaussian, $\vec{x}$ is called a complex Gaussian vector. Each element

in $\vec{x}$ is assumed to have zero mean and all signals are assumed to be independent from the others. Then, the covariance matrix of the TX signals is

$$\mathbf{Q}_x = E[\vec{x}\vec{x}^H] = \begin{bmatrix} T_1 & \cdots & 0 \\ 0 & \ddots & 0 \\ 0 & \cdots & T_M \end{bmatrix}, \tag{3.15}$$

where $[]^H$ is the conjugate transpose operator and $E[]$ denotes expectation. T_i is the average transmitted power of the ith TX port. The total transmitted power is the sum of them, given by

$$P_{\mathrm{TX}} = \sum_{i=1}^{M} T_i. \tag{3.16}$$

The probability density of the multivariate Gaussian distribution is defined as [UIUC, 2015]

$$p(\vec{x}) = \frac{1}{\sqrt{|2\pi\mathbf{Q}_x|}} e^{(-\frac{1}{2}(\vec{x}-\vec{\mu})^T \mathbf{Q}_x^{-1}(\vec{x}-\vec{\mu}))}, \tag{3.17}$$

where $\vec{\mu}$ is the mean vector which is assumed zero in the following analysis and $||$ denotes the determinant of a matrix. The entropy of a complex vector $\vec{x}$ is derived as

$$\begin{aligned} H(\vec{x}) =& -\int p(\vec{x}) \log_2 p(\vec{x}) d\vec{x} \\ =& \frac{1}{2} \log_2 |2\pi e \mathbf{Q}_x|. \end{aligned} \tag{3.18}$$

According to equation (3.1), the covariance matrix of the RX signal vector $\vec{y}$ is

$$\begin{aligned} \mathbf{Q}_y =& E[\vec{y}\vec{y}^H] \\ =& E[(\mathbf{H}\vec{x} + \vec{n})(\mathbf{H}\vec{x} + \vec{n})^H] \\ =& \mathbf{H}E[\vec{x}\vec{x}^H]\mathbf{H}^H + \mathbf{H}E[\vec{x}\vec{n}^H] + \mathbf{H}^H E[\vec{n}\vec{x}^H] + E[\vec{n}\vec{n}^H]. \end{aligned} \tag{3.19}$$

Since the noise at the RX ports is not correlated with the TX signals and the noise from different RX ports is also independent, then $E[\vec{n}\vec{x}^H] = E[\vec{x}\vec{n}^H] = 0$ and $E[\vec{n}\vec{n}^H] = P_n\mathbf{I}_N$, where P_n is the average noise power at the RX ports and $\mathbf{I}_N$ is the $N \times N$ unit matrix. Equation (3.19) can be simplified as

$$\mathbf{Q}_y = \mathbf{H}\mathbf{Q}_x\mathbf{H}^H + P_n\mathbf{I}_N. \tag{3.20}$$

Since the TX signals and the noise at the RX ports are all Gaussian, the RX signals are also Gaussian, so based on equation (3.18), the entropy of the RX signals is

$$\begin{aligned} H(\vec{y}) =& \frac{1}{2} \log_2 |2\pi e \mathbf{Q}_y| \\ =& \frac{1}{2} \log_2 \left|2\pi e(\mathbf{H}\mathbf{Q}_x\mathbf{H}^H + P_n\mathbf{I}_N)\right|. \end{aligned} \tag{3.21}$$

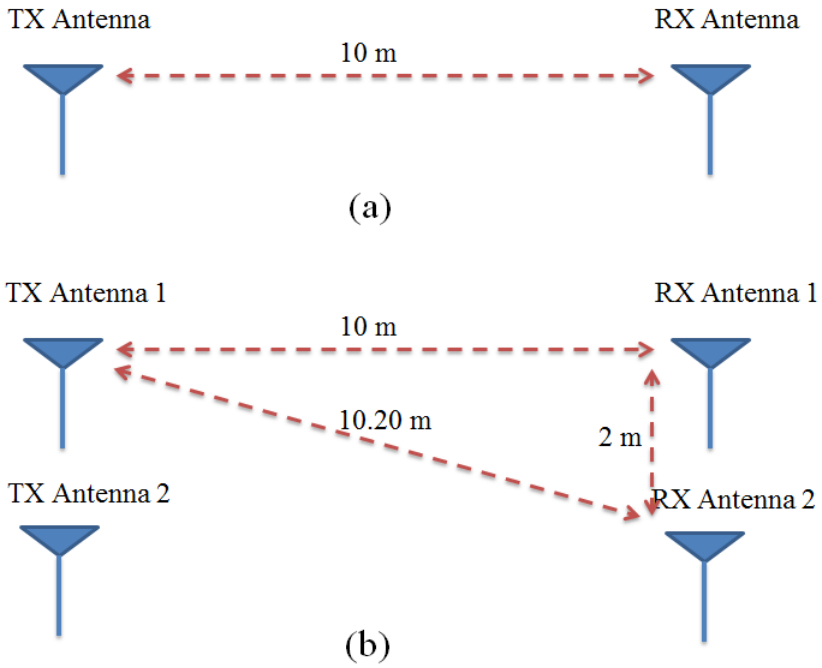

Figure 3.3: Communication between TX and RX antennas: (a) SISO; (b) 2×2 MIMO.

The conditional entropy $H(\vec{y}|\vec{x})$ equals the entropy of the noise, where

$$H(\vec{n}) = \frac{1}{2}\log_2|2\pi e\mathbf{Q}_n| = \frac{1}{2}\log_2|2\pi eP_n\mathbf{I}_N|. \tag{3.22}$$

The mutual information between the TX ports and the RX ports is

$$\begin{aligned} I(\vec{x},\vec{y}) =& H(\vec{y}) - H(\vec{n}) \\ =& \frac{1}{2}\log_2\left|\mathbf{I}_N + \frac{\mathbf{H}\mathbf{Q}_x\mathbf{H}^H}{P_n}\right|. \end{aligned} \tag{3.23}$$

The channel capacity equals the maximum mutual information times the sampling rate as shown in equation (3.13),

$$C = I(\vec{x},\vec{y})\frac{1}{t_s} = B\log_2\left|\mathbf{I}_N + \frac{\mathbf{H}\mathbf{Q}_x\mathbf{H}^H}{P_n}\right|. \tag{3.24}$$

The average channel capacity (spectrum channel capacity density) for MIMO systems is defined as

$$C' = \log_2\left|\mathbf{I}_N + \frac{\mathbf{H}\mathbf{Q}_x\mathbf{H}^H}{P_n}\right|. \tag{3.25}$$

Once the channel matrix $\mathbf{H}$ has been obtained, the capacity performance of the system can be evaluated. Since the average noise power is constant at each RX port, the channel

capacity only depends on the channel coefficients and the power allocation strategy of the TX signals. A simple example is investigated to show how much a MIMO system benefits in channel capacity. Assuming the situation shown in Figure 3.3(a), a SISO communication system is built up with two isotropic antennas at 1 GHz, the distance between the TX and RX antennas is 10 m. In Figure 3.3(b), a 2×2 MIMO communication system is shown, the element spacing of the TX and RX antenna arrays is 2 m and the distance between the TX array and the RX array is 10 m. Within the MIMO arrays, it is assumed that there is no mutual coupling between the antennas. For comparison, it is assumed that the SISO and MIMO systems transmit equal power and the two antennas within the MIMO TX array carry the same amount of power, where $P_{\mathrm{TX1}} = P_{\mathrm{TX2}} = \frac{1}{2}P_{\mathrm{SISO}}$. The average noise power of all RX antennas is assumed identical. The amplitude of the transmission coefficient is calculated through equation (2.23) and the phase constant is approximated by $e^{j(-\frac{2\pi}{\lambda}L)}$, where L is the distance between the isotropic antennas. The transmission coefficient of the SISO system is

$$h_{\mathrm{SISO}} = 0.0024e^{-120^\circ j}. \tag{3.26}$$

The channel matrix of the 2×2 MIMO system is

$$\mathbf{H} = \begin{bmatrix} 0.0024e^{-120^\circ j} & 0.0023 \\ 0.0023 & 0.0024e^{-120^\circ j} \end{bmatrix}. \tag{3.27}$$

Then, the average channel capacities are calculated through equations (3.14) and (3.25), respectively. The results are plotted in Figure 3.4. Different from Figure 3.2, the average channel capacity is plotted versus the ratio of the total TX power and the average noise power at each RX antenna. It is clearly noticed that with the same P_{TX}/P_n, the 2×2 MIMO system owns much higher channel capacity and with increasing P_{TX}, the channel capacity of the 2×2 MIMO system increases faster.

In a MIMO communication system, the channel matrix plays an important role during the analysis of the channel performance, which is performed by a singular value decomposition (SVD) in the following. SVD is a mathematical tool commonly adopted in linear algebra. It decomposes a complicated matrix and extracts the features of the matrix. In practical communication systems, the channel matrix is commonly complex, especially when a number of scatterers exist in the propagation paths. As a result, the SVD is adopted to investigate the MIMO channel matrix. An $N \times M$ channel matrix $\mathbf{H}$ can be decomposed as

$$\mathbf{H} = \mathbf{U}\mathbf{D}\mathbf{V}^H. \tag{3.28}$$

where $\mathbf{U}$ is an $N \times N$ unitary matrix, $\mathbf{V}$ is an $M \times M$ unitary matrix, and $\mathbf{D}$ is an $N \times M$ diagonal matrix. The columns of $\mathbf{U}$ are the normalized eigenvectors of $\mathbf{H}\mathbf{H}^H$, the columns of $\mathbf{V}$ are the normalized eigenvectors of $\mathbf{H}^H\mathbf{H}$, and the entries of $\mathbf{D}$ are the square roots of the eigenvalues of $\mathbf{H}\mathbf{H}^H$. The eigenvectors $\vec{v}$ and eigenvalues λ of a matrix $\mathbf{M}$ are defined as

$$\mathbf{M}\vec{v} = \lambda\vec{v}. \tag{3.29}$$

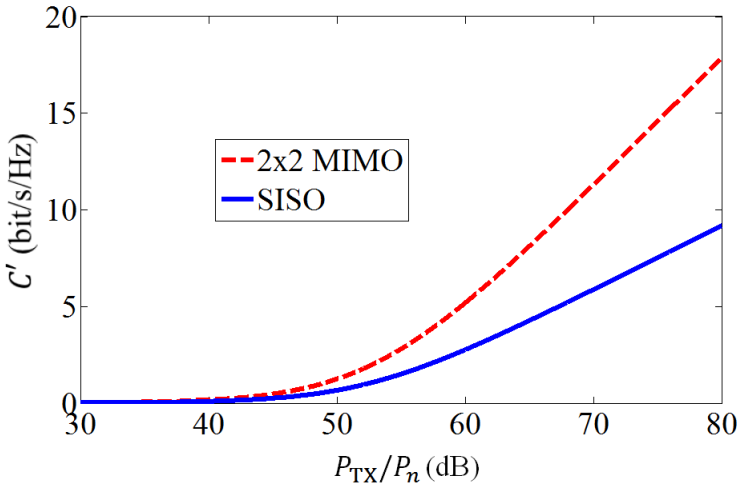

Figure 3.4: The average channel capacity versus the ratio of the total TX power and the average noise power at each RX antenna.

The elements of the SVD components are placed in descending order. For example, the first column of $\mathbf{U}$ is the normalized eigenvector corresponding to the largest eigenvalue and the same holds for $\mathbf{V}$. The first entry of $\mathbf{D}$ is the square root of the largest eigenvalue of $\mathbf{H}\mathbf{H}^H$.

The RX signal vector can be described as

$$\vec{y} = \mathbf{U}\mathbf{D}\mathbf{V}^H\vec{x} + \vec{n}. \tag{3.30}$$

Set $\vec{y}\,' = \mathbf{U}^H\vec{y}$, $\vec{x}\,' = \mathbf{V}^H\vec{x}$ and $\vec{n}\,' = \mathbf{U}^H\vec{n}$. Because $\mathbf{U}^H\mathbf{U} = \mathbf{I}_M$, equation (3.29) becomes

$$\vec{y}\,' = \mathbf{D}\vec{x}\,' + \vec{n}\,'. \tag{3.31}$$

The covariance matrix of $\vec{n}'$ is

$$\mathbf{Q}_{n'} = E[\vec{n}'\vec{n}'^H] = E[\mathbf{U}^H\vec{n}\vec{n}^H\mathbf{U}] = P_n\mathbf{U}^H\mathbf{I}_N\mathbf{U} = P_n\mathbf{I}_N = \mathbf{Q}_n. \tag{3.32}$$

It is concluded that $\vec{n}\,'$ owns the same probability distribution as $\vec{n}$, which is zero mean and Gaussian. The diagonal entries of $\mathbf{D}$ should have $\min(M,N)$ non-zero elements. The elements in $\vec{y}\,'$ can then be written as

$$\begin{cases} y_i' = \sqrt{\lambda_i}x_i' + n_i, & (i = 1, ..., \min(M,N)) \\ y_i' = n_i, & (i = \min(M,N)+1, ..., \max(M,N)). \end{cases} \tag{3.33}$$

For the elements $i \leq \min(M,N)$, the channel is functional between the TX and RX antennas. For $i > \min(M,N)$, the RX signals only contain noise components. According to this, the communication system can be equivalent to the one shown in Figure 3.5, where the sizes of $\vec{x}''$, $\vec{n}''$ and $\vec{y}''$ are the same and equal to $\min(M,N)$. The equivalent channel matrix $\mathbf{H}'$ is diagonal and has a dimension of $\min(M,N) \times \min(M,N)$. If all the TX ports transmit

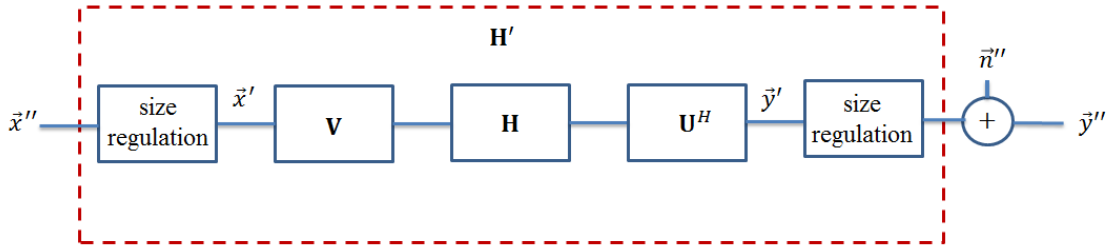

Figure 3.5: Representation of the channel matrix by SVD.

the same power, similar to equation (3.32), the covariance matrix of $\vec{x}'$ can be written as

$$\mathbf{Q}_{x'} = E[\vec{x}'\vec{x}'^H] = E[\mathbf{V}^H\vec{x}\vec{x}^H\mathbf{V}] = \frac{P_{\mathrm{TX}}}{M}\mathbf{V} = \frac{P_{\mathrm{TX}}}{M}\mathbf{I}_N = \mathbf{Q}_x. \tag{3.34}$$

The covariance matrix $\mathbf{Q}_{x''}$ of $\vec{x}''$ contains the first $\min(M,N)$ columns and rows of $\mathbf{Q}_{x'}$. Then, the equivalent average channel capacity of such a system is

$$\begin{aligned} C' &= \log_2\left|\mathbf{I}_N + \frac{\mathbf{H}'\mathbf{Q}_{x''}\mathbf{H}'^H}{P_n}\right| \\ &= \sum_{i=1}^{\min(M,N)} \log_2\left(1 + \frac{\lambda_i P_{\mathrm{TX}}}{MP_n}\right). \end{aligned} \tag{3.35}$$

The channel capacity of MIMO systems here is written in the form of the summation of the capacity of several individual transmission channels with the channel gain λ_i of the ith channel. Evenly distributing the power among the ports of the TX array might not be the ideal strategy. In order to maximize the channel capacity, optimized power allocation methods should be utilized. Assume the power transmitted from the ith equivalent TX port is $P'_{\mathrm{TX}i}$, then the total transmitted power is

$$P'_{\mathrm{TX}} = \sum_{i=1}^{\min(M,N)} P'_{\mathrm{TX}i}. \tag{3.36}$$

Since $\mathbf{V}^H\mathbf{V} = \mathbf{I}_M$, $P'_{\mathrm{TX}} = P_{\mathrm{TX}}$ is true. The average channel capacity becomes

$$C' = \sum_{i=1}^{\min(M,N)} \log_2\left(1 + \frac{\lambda_i P'_{\mathrm{TX}i}}{P_n}\right). \tag{3.37}$$

By the so called 'water-filling' method, an ideal distribution of the power is obtained to maximize the channel capacity for a certain total transmitted power. According to equation (3.36), the power of the ith TX port should be [Telatar, 1999]

$$P'_{\mathrm{TX}i} = \max\left(\mu\frac{P'_{\mathrm{TX}}}{\min(M,N)} - \frac{P_n}{\lambda_i}, 0\right), \tag{3.38}$$

where μ is a constant and its value can be calculated from equation (3.36). Then, equation (3.37) becomes

$$C' = \sum_{i=1}^{\min(M,N)} \log_2 \left(\max(\frac{\lambda_i \mu P'_{\mathrm{TX}}}{P_n \min(M,N)}, 1) \right). \tag{3.39}$$

To sum up, in a MIMO communication system, the optimal power allocation strategy depends on the channel condition. If the transmitter is able to get the channel information feedback from the receiver, it can adjust the transmitted power at each antenna by following the results based on the above equations. To ensure high data rates, the channels with good conditions should be assigned more information while the poor quality channels should be assigned less. However, if the transmitter can not obtain the channel information feedback, the power at the transmitter should be evenly assigned. In reality, it is also difficult to realize the hardware for random power assignment, so for later investigations in Chapter 6, the strategy of evenly distributing the power is always deployed.

In order to illustrate the benefits of applying the 'water-filling' method, a simple example is analyzed. The example is shown in Figure 3.6, which is modified from the one in Figure 3.3(b). In this case, an absorber is placed in the middle which blocks the transmissions from TX Antenna 1 to RX Antenna 2 and from TX Antenna 2 to RX Antenna 1. The elements h_{12} and h_{21} in the channel matrix become 0 and now $\mathbf{H}$ is diagonal. It is assumed that there is an absorption environment between TX Antenna 2 and RX Antenna 2 and only 10% of the power is received as compared to before, which means $h_{22} = 0.33h_{11}$. Since $h_{11} > h_{22}$ and $\mathbf{H}$ is diagonal, the equivalent matrix $\mathbf{H'}$ in Figure 3.5 equals $\mathbf{H}$. The channel capacity is calculated according to two strategies, one is that the power is evenly distributed to the two TX antennas and the second is that the power is allocated under the 'water-filling' approach. The calculated results are plotted in Figure 3.7. It is noticed that if P_{TX}/P_n is less than 65 dB, the 'water-filling' method shows better channel capacity. When P_{TX}/P_n is larger, the two methods show the same channel capacity. Figure 3.8 plots the power allocation ratio. It shows that when P_{TX}/P_n is small, the power is more allocated to the channel with better condition. When the P_{TX}/P_n becomes larger, the power is evenly allocated.

In this section, it was shown that MIMO communication systems are advantageous in pursuing high data rates. The channels were modeled in a deterministic manner for arrays with isotropic radiators. For more complex channel situations such as channels in multipath fading environments with practical antenna elements, the channel capacity will be investigated in more detail in Chapter 6.

3.3 Challenges of MIMO Antenna Arrays in Modern Communication Devices

The implementation of MIMO antenna arrays in practical communication devices encounters several challenges. For instance, nowadays, the mobile terminals are becoming more and more compact. As a result, the room left for the antennas is quite limited. If the antenna elements of an array are placed close to each other, mutual coupling occurs, which

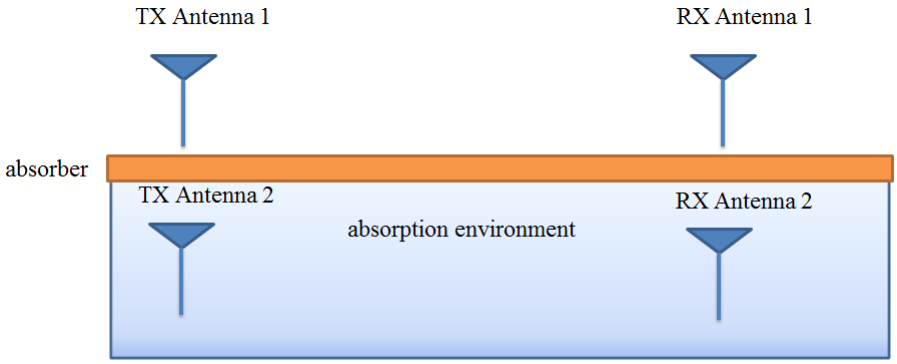

Figure 3.6: 2×2 MIMO system with absorber and absorption environment.

means that parts of the TX signal from one antenna can be directly received by another TX antenna in its near field. Consequently, the transmission efficiency of the antenna array is lower. For indicating this effect, three two-element antenna arrays are investigated here as shown in Figure 3.9. In Figure 3.9(a), a monopole array is modeled in CST MWS operating around 2.4 GHz with an edge to edge distance of around $0.15\lambda_0$, where λ_0 is the free space wavelength. The monopole and ground plane material are chosen as copper, the simulated S-parameters are shown in Figure 3.10(a). In Figure 3.9(b), the elements of the array are printed monopoles. The printed monopoles are built on the substrate RO 4350 [Rogers, 2015] with a thickness of 0.762 mm, the metallization is 0.018 mm, the dielectric constant is 3.66, and $\tan\delta$=0.004. The printed monopole array also works around 2.4 GHz with an edge to edge distance of $0.15\lambda_0$. The simulated S-parameters of this array are plotted in Figure 3.10(b). A patch antenna array operating at 2.45 GHz is shown in Figure 3.9(c) and the radiation elements are aligned in parallel with the H-plane. The same substrate is used for the printed monopole array and the edge to edge distance is still $0.15\lambda_0$. The simulated S-parameters are shown in Figure 3.10(c). To characterize the influence on the radiated power from the mutual coupling effect, the following calculations are carried out. The radiated power from one port can be written in the form of

$$P_{\text{rad}} = (1 - |S_{11}|^2 - |S_{21}|^2)P_{\text{in}} - P_{\text{loss}}. \tag{3.40}$$

If the ports are both individually matched, e.g. $|S_{11}| = 0$, the radiated power becomes

$$P_{\text{rad}} = (1 - |S_{21}|^2)P_{\text{in}} - P_{\text{loss}} = P_{\text{in}} - P_{\text{loss}} - P_{\text{couple}}, \tag{3.41}$$

where P_{couple} is the coupled power from one antenna to the other. The radiated power of a single indicated element in the matched case is

$$P_{\text{s,rad}} = P_{\text{in}} - P_{\text{s,loss}}. \tag{3.42}$$

$P_{\text{s,loss}}$ is the power loss of the single element. Then, the radiated power reduction ratio can be defined as

$$\xi = \frac{P_{\text{s,rad}} - P_{\text{rad}}}{P_{\text{in}}}. \tag{3.43}$$

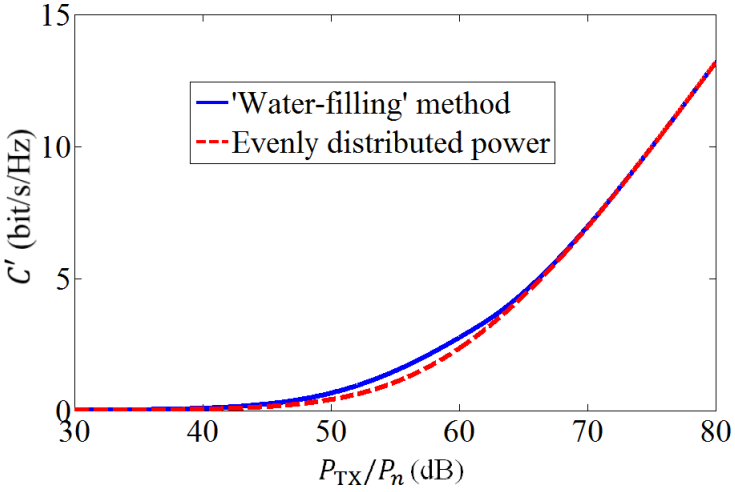

Figure 3.7: The average channel capacity for the configuration in Figure 3.6 versus the ratio of the TX power and noise power at each RX antenna according to different power allocation strategies.

If $P_{\text{s,loss}} = P_{\text{loss}}$, it can be shown that $\xi = |S_{21}|^2$. For example, for the two-element monopole array, 30% power cannot be radiated due to the mutual coupling. The coupling between radiation elements depends on the distance between the antennas and also the type of the antennas. For example, for antennas based on printed circuit board (PCB) technology, the coupling of the printed monopole array is much higher than the one for the patch antenna array, of which the coupling coefficient is as low as -18 dB. This is due to their different radiation mechanisms. For patch antennas, the radiation is due to the fringe electric fields at the open ends of the resonator in the E-plane. Since the antennas are aligned in the H-plane, even with a small separation, the mutual coupling is still low.

The second effect of mutual coupling is the change of radiation patterns. When one antenna of the array is working, the neighboring antennas perform as loaded parasitic elements. As a result, the radiation pattern of an antenna in a compact array can be different from the pattern of an individual element. Consequently, parameters such as gain and pattern correlation are affected. Therefore, these considerations should be treated carefully during the design of MIMO antenna arrays for modern communication devices.

3.4 Design Objectives for Compact MIMO Antenna Arrays

In this section, the design objectives for compact antenna arrays are presented. In order to enhance the radiated power, matching and decoupling between the array input ports should be achieved. Generally, decoupling is always firstly performed, because when the ports are decoupled and able to radiate, each port can be matched individually by proper matching circuits. Mathematically, matching and decoupling means the scattering matrix of an antenna array is a null matrix. There are a number of solutions to achieve this objective. For example, matching and decoupling networks can be implemented between the

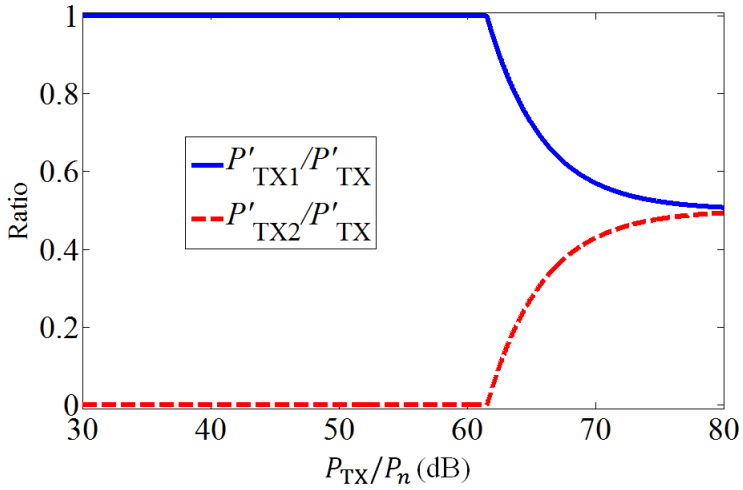

Figure 3.8: Power allocation ratio of the TX signals according to the water-filling method for the system in Figure 3.6.

input ports and the radiation elements [Volmer et al., 2008a,b]; electromagnetic bandgap (EBG) structures can be used to block the surface wave prorogation in the substrate of planar antennas [Yang and Rahmat-Samii, 2003a]; particularly loaded parasitic elements can be placed between the radiation elements for decoupling purposes [Lau and Andersen, 2012]; the characteristic modes excitation can be adopted in the design of communication devices mostly with conducting body [Li et al., 2014, Martens et al., 2011]. All these solutions can match and decouple the input ports, but of course there are some drawbacks as well, such as the decrease of operation bandwidth, reduction of efficiency, more cost and so on.

The second consideration in MIMO antenna array design is the radiation property. The radiation patterns of the elements in an array should correspond to the requirements of different applications. Generally, for MIMO antenna arrays, the received signal correlation can be applied to estimate the performance of MIMO systems. The signal correlation between the received signals (zero mean) of the ith and jth port ρ_{ij} is defined as

$$\rho_{ij} = \frac{E[y_i y_j^*]}{\sqrt{E[y_i y_i^*]E[y_j y_j^*]}}, \tag{3.44}$$

where $[]^*$ denotes the conjugate operator. Take a 2×2 MIMO system as an example, the numerator of the signal correlation between two RX ports is

$$\begin{aligned} E[y_1 y_2^*] =& E[(h_{11}x_1 + h_{12}x_2 + n_1)(h_{21}x_1 + h_{22}x_2 + n_2)^*] \\ =& E[(h_{11}x_1)(h_{21}x_1)^*] + E[(h_{12}x_2)(h_{21}x_1)^*] + E[n_1(h_{21}x_1)^*] + \\ & E[(h_{11}x_1)(h_{22}x_2)^*] + E[(h_{12}x_2)(h_{22}x_2)^*] + E[n_1(h_{22}x_2)^*] + \\ & E[(h_{11}x_1)n_2^*] + E[(h_{12}x_2)n_2^*] + E[n_1 n_2^*] \\ =& E[(h_{11}x_1)(h_{21}x_1)^*] + E[(h_{12}x_2)(h_{22}x_2)^*]. \end{aligned} \tag{3.45}$$

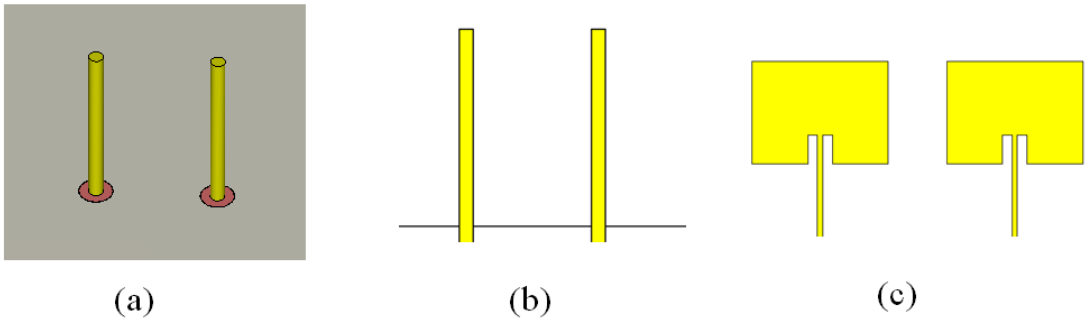

Figure 3.9: Two-element compact antenna arrays: (a) monopole array; (b) printed monopole array; (c) patch antenna array.

In this equation, it is assumed that the TX signals are uncorrelated and the noise at the RX ports is independent from the TX signals. According to equation (3.21), the entropy of the RX signals is maximized if the RX signals are uncorrelated. Consequently, the channel capacity is also maximized. As a result, if the transmitted power is evenly distributed to the TX ports, to obtain the optimal channel performance, the channel matrix should fulfill the condition

$$h_{11}h_{21}^* + h_{12}h_{22}^* = 0. \tag{3.46}$$

However, it is still difficult to extract the desired radiation property from equation (3.46). In [Vaughan and Anderson, 1987] and [Dietrich et al., 2001], approximation methods are utilized to evaluate the radiation performance of antenna arrays based on the signal correlation. In outdoor communication systems, there are a great number of scatterers such as buildings, plants and so on. As a result, it is reasonable to assume that the RX antennas receive signals from all directions. For example, Figure 3.11 depicts a two-element MIMO antenna array in the RX mode. The coordinate origin is defined at the middle point between the two antennas. Electromagnetic waves from direction (θ, ϕ) are time dependent and expressed as $\vec{E}(\theta, \phi, t) = E_\theta(\theta, \phi, t)\vec{e_\theta} + E_\phi(\theta, \phi, t)\vec{e_\phi}$, containing two polarization components. The gain of an antenna for a certain direction can be expressed in the form of $G(\theta, \phi) = G_\theta(\theta, \phi) + G_\phi(\theta, \phi)$, so the received power from a certain direction is

$$\begin{cases} P_{\mathrm{RX},\theta}(\theta, \phi) = \frac{|E_\theta(\theta,\phi)|^2}{2Z_s}(\frac{\lambda^2}{4\pi})G_\theta(\theta, \phi) \\ P_{\mathrm{RX},\phi}(\theta, \phi) = \frac{|E_\phi(\theta,\phi)|^2}{2Z_s}(\frac{\lambda^2}{4\pi})G_\phi(\theta, \phi), \end{cases} \tag{3.47}$$

where Z_s is the impedance of free space, $\frac{|E(\theta,\phi)|^2}{2Z_s}$ is the power density of the plane wave in free space and E is the electric field magnitude. The power of the received signal from a certain direction is defined as $\frac{|u(\theta,\phi)|^2}{Z_0}$, where $u(\theta, \phi)$ is the RX port voltage and Z_0 is the

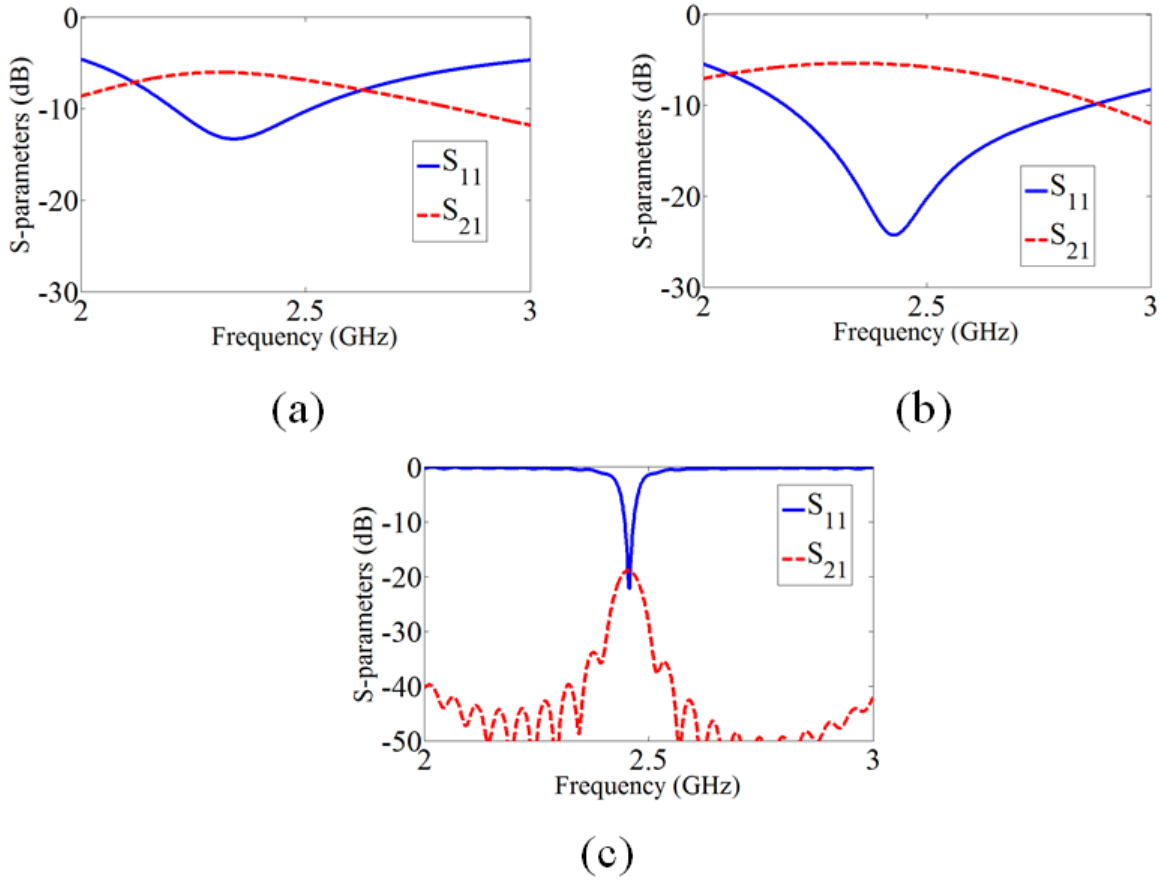

Figure 3.10: Simulated S-parameters in CST MWS: (a) monopole array; (b) printed monopole array; (c) patch antenna array.

port impedance. Then the following relationship can be found:

$$\begin{cases} |u_\theta(\theta,\phi)| = |E_\theta(\theta,\phi)|\sqrt{\frac{Z_0}{Z_s}(\frac{\lambda^2}{4\pi})G_\theta(\theta,\phi)} = \chi\sqrt{G_\theta(\theta,\phi)}|E_\theta(\theta,\phi)| \\ |u_\phi(\theta,\phi)| = |E_\phi(\theta,\phi)|\sqrt{\frac{Z_0}{Z_s}(\frac{\lambda^2}{4\pi})G_\phi(\theta,\phi)} = \chi\sqrt{G_\phi(\theta,\phi)}|E_\phi(\theta,\phi)|, \end{cases} \tag{3.48}$$

with

$$\chi = \sqrt{\frac{Z_0}{Z_s}(\frac{\lambda^2}{4\pi})}. \tag{3.49}$$

For convenience, the magnitude of the normalized radiation pattern is defined as

$$|F(\theta,\phi)|^2 = \frac{G(\theta,\phi)}{G_m} = \frac{G_\theta(\theta,\phi)}{G_m} + \frac{G_\phi(\theta,\phi)}{G_m} = |F_\theta(\theta,\phi)|^2 + |F_\phi(\theta,\phi)|^2, \tag{3.50}$$

where G_m is the maximum gain of the antenna. The complex normalized radiation pattern on a sphere with radius R is

$$\vec{F}(\theta,\phi) = F_\theta(\theta,\phi)e^{j\psi_\theta(\theta,\phi)}\vec{\mathbf{e}_\theta} + F_\phi(\theta,\phi)e^{j\psi_\phi(\theta,\phi)}\vec{\mathbf{e}_\phi}, \tag{3.51}$$

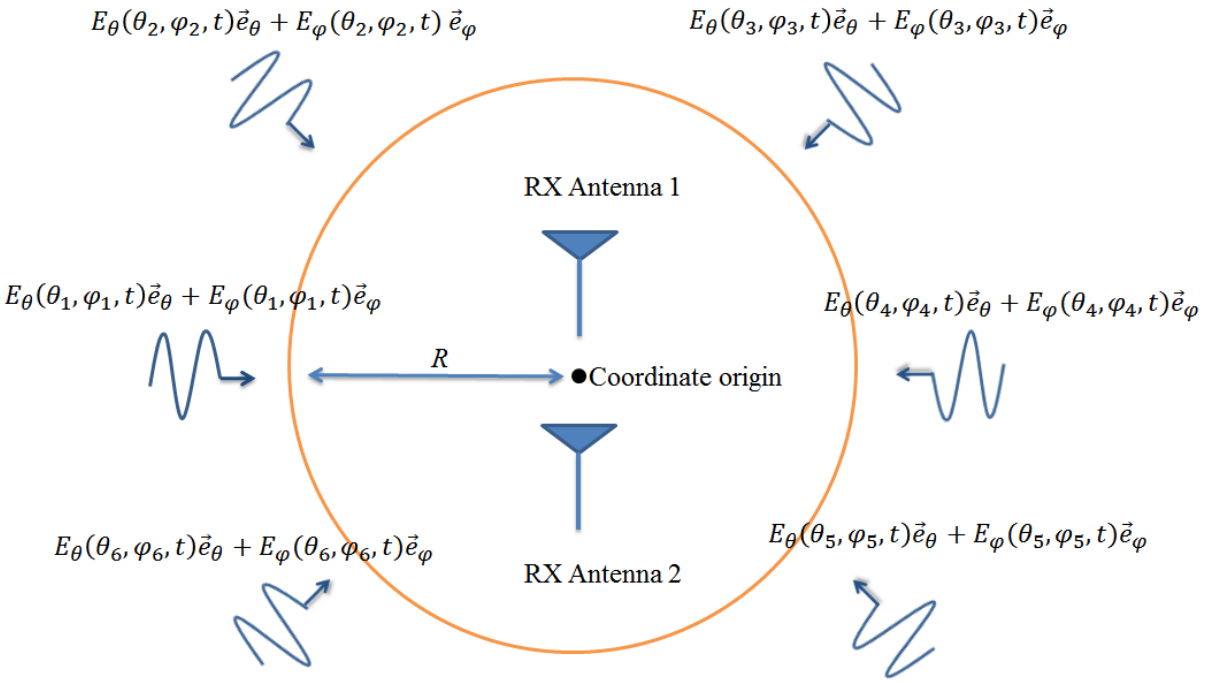

Figure 3.11: A two-element RX MIMO array receives signals from different directions.

where ψ_θ and ψ_ϕ are the phase constant of the two polarizations on the sphere. Then, based on the above equations and the reciprocity theory, the received signal from a certain direction is

$$u(\theta,\phi,t) = \chi\vec{F}(\theta,\phi)\cdot\vec{E}(\theta,\phi,t). \tag{3.52}$$

For a MIMO array, the received signal of the ith antenna is

$$u_i(t) = \sum_{k=1}^{N} u_i(\theta_k,\phi_k,t) = \sum_{k=1}^{N} \chi\vec{F}_i(\theta_k,\phi_k)\cdot\vec{E}(\theta_k,\phi_k,t). \tag{3.53}$$

The correlation coefficient between the voltages of the RX ports is

$$\rho_{ij} = \frac{E[u_i u_j^*]}{\sqrt{E[u_i u_i^*]E[u_j u_j^*]}}, \tag{3.54}$$

with

$$\begin{cases} E[u_i u_j^*] = E[\sum_{k=1}^{N}\chi\vec{F}_i(\theta_k,\phi_k)\cdot\vec{E}(\theta_k,\phi_k,t)\sum_{k=1}^{N}\chi\vec{E}^*(\theta_k,\phi_k,t)\cdot\vec{F}_j^*(\theta_k,\phi_k)] \\ E[u_i u_i^*] = E[\sum_{k=1}^{N}\chi\vec{F}_i(\theta_k,\phi_k)\cdot\vec{E}(\theta_k,\phi_k,t)\sum_{k=1}^{N}\chi\vec{E}^*(\theta_k,\phi_k,t)\cdot\vec{F}_i^*(\theta_k,\phi_k)] \\ E[u_j u_j^*] = E[\sum_{k=1}^{N}\chi\vec{F}_j(\theta_k,\phi_k)\cdot\vec{E}(\theta_k,\phi_k,t)\sum_{k=1}^{N}\chi\vec{E}^*(\theta_k,\phi_k,t)\cdot\vec{F}_j^*(\theta_k,\phi_k)]. \end{cases} \tag{3.55}$$

As mentioned before, in an outdoor rich scattering environment, signals from different directions and with different polarizations can be assumed to be uncorrelated, which means

$$\begin{cases} E[E_\theta(\theta_k,\phi_k,t)E_\theta^*(\theta_l,\phi_l,t)]=0, & \text{for } k\neq l \\ E[E_\theta(\theta_k,\phi_k,t)E_\phi^*(\theta_l,\phi_l,t)]=0, & \text{for all } k,l\ . \end{cases} \tag{3.56}$$

Often it is reasonable to assume that the signal power is uniform for the signals from all directions and polarizations, which means

$$\begin{cases} E[E_\theta(\theta_k,\phi_k,t)E_\theta^*(\theta_k,\phi_k,t)]=E[E_\theta(\theta_j,\phi_j,t)E_\theta^*(\theta_l,\phi_l,t)]=C & \text{for all } k,l \\ E[E_\phi(\theta_k,\phi_k,t)E_\phi^*(\theta_k,\phi_k,t)]=E[E_\phi(\theta_j,\phi_j,t)E_\phi^*(\theta_l,\phi_l,t)]=C & \text{for all } k,l\ . \end{cases} \tag{3.57}$$

Then, equation (3.55) can be simplified as

$$\begin{cases} E[u_iu_j^*]=C\chi\sum_{k=1}^N \vec{F}_i(\theta_k,\phi_k)\cdot\vec{F}_j^*(\theta_k,\phi_k) \\ E[u_iu_i^*]=C\chi\sum_{k=1}^N \vec{F}_i(\theta_k,\phi_k)\cdot\vec{F}_i^*(\theta_k,\phi_k) \\ E[u_iu_i^*]=C\chi\sum_{k=1}^N \vec{F}_j(\theta_k,\phi_k)\cdot\vec{F}_j^*(\theta_k,\phi_k). \end{cases} \tag{3.58}$$

In consequence, the received signal correlation coefficient can be represented by the radiation patterns, which is

$$\begin{aligned} \rho_{ij} =& \frac{\sum_{k=1}^N \vec{F}_i(\theta_k,\phi_k)\cdot\vec{F}_j^*(\theta_k,\phi_k)}{\sqrt{\sum_{k=1}^N|\vec{F}_i(\theta_k,\phi_k)|^2\sum_{k=1}^N|\vec{F}_j(\theta_k,\phi_k)|^2}} \\ \approx& \frac{\int \vec{F}_i(\theta,\phi)\cdot\vec{F}_j^*(\theta,\phi)d\Omega}{\sqrt{\int|\vec{F}_i(\theta,\phi)|^2d\Omega\int|\vec{F}_j(\theta,\phi)|^2d\Omega}}. \end{aligned} \tag{3.59}$$

This is also called the radiation pattern correlation coefficient between two antennas. Equation (3.59) is generally applied to assess the performance of MIMO antenna arrays.

To sum up, if there is no particular requirement for the radiation patterns, the design objectives of MIMO arrays are good power matching and low radiation pattern correlations between the array elements. It will be proved in Chapter 4 that for lossless antennas, if matching and decoupling are achieved, the radiation patterns are uncorrelated. In Chapter 6, a more rigorous derivation of the relationship between the pattern correlation and the channel correlation will be performed.

4 Matching and Decoupling Networks for Compact Antenna Arrays

In this chapter, matching and decoupling networks utilized for solving mutual coupling problems of compact antenna arrays are addressed. The two design theories exploited in this chapter are introduced, derived and compared. Two two-element and one four-element compact monopole antenna arrays are designed, fabricated and measured. The relationship between the radiation pattern correlation coefficient and S-parameters is derived, while the beamforming applications of compact monopole arrays are investigated as well. Parts of the achievements demonstrated in this chapter have been published in [Wang et al., 2013a,b,c, 2014e, 2015a].

4.1 Introduction to Matching and Decoupling Networks

The method of utilizing matching and decoupling networks is illustrated in Figure 4.1, where the matching and decoupling network is utilized between the compact antenna array and the input ports. The function of the network is to isolate the input ports and achieve power matching. This solution is universal because the design of the network only depends on the scattering parameters of the array and it is not related to the type of the radiation elements. For designing this network, there are two basic theories: the eigenmode excitation method and the multiport conjugate matching.

Eigenmode excitation means that each input port excites a certain mode in the antenna array through the additional network, which is an eigenvector of the scattering matrix of the antenna array. Based on the condition of multiport conjugate matching at the inputs of the antenna array, it is known that maximum power transmission is achieved for lossless feeding networks. Consequently, no reflection and coupling occur among the system input ports. The matching and decoupling networks can be realized by both lumped elements and transmission lines. However, the drawback of using lumped elements is that additional Ohmic losses are brought into the array, which reduces the efficiency. As a result, in this chapter the decoupling networks are designed according to approaches considering only transmission lines. In the following, monopole arrays at 2.45 GHz are utilized as examples for detailed investigations.

4.2 Eigenmode Excitation Method

4.2.1 Mathematical Description of the Eigenmode Excitation Method

The signal flow chart of the considered compact array with feeding network is shown in Figure 4.2, where $\vec{a}$ and $\vec{b}$ are the input and reflected wave vectors of the system. The matching and decoupling network is modeled as a $2N$-port network. The input wave amplitudes at the left-hand side of the network are given as a vector where $\vec{a}_l = [a_1, a_2 \cdots, a_N]^T$, the output wave vector at the left-hand side of the network is $\vec{b}_l = [b_1, b_2 \cdots, b_N]^T$. The input wave vector at the right-hand side of the network is $\vec{a}_r = [a_{N+1}, a_{N+2} \cdots, a_{2N}]^T$ and the output wave vector at the right-hand side is $\vec{b}_r = [b_{N+1}, b_{N+2} \cdots, b_{2N}]^T$. Then, the

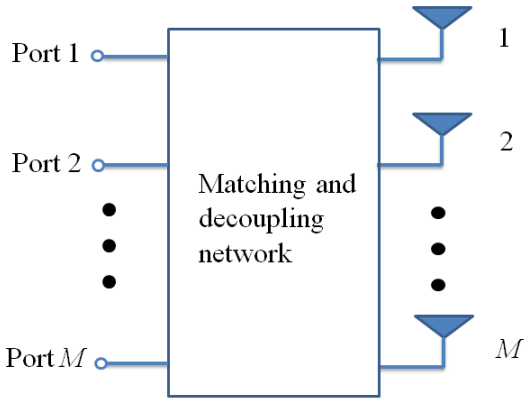

Figure 4.1: Configuration of an M-element compact antenna array with matching and decoupling network.

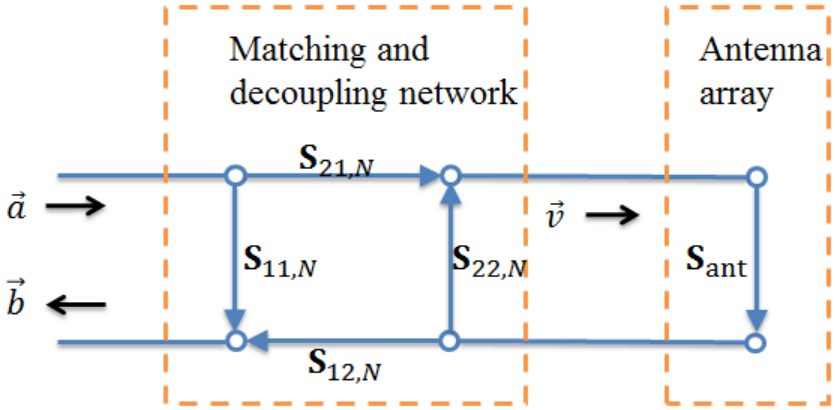

Figure 4.2: Signal flow chart of the antenna array with matching and decoupling network.

scattering matrix of the $2N$-port network can be decomposed into four sub-matrices, where $\vec{b}_l = \mathbf{S}_{11,N}\vec{a}_l$, $\vec{b}_l = \mathbf{S}_{12,N}\vec{a}_r$, $\vec{b}_r = \mathbf{S}_{21,N}\vec{a}_l$ and $\vec{b}_r = \mathbf{S}_{22,N}\vec{a}_r$. The network is cascaded with the compact antenna array with the scattering matrix $\mathbf{S}_{\text{ant}}$. For this configuration, the design target is to have the output vector $\vec{b}$ in Figure 4.2 equal to zero, which means there is no coupling between the ports and all the inputs ports are matched. The reflected wave vector $\vec{b}$ is

$$\vec{b} = \mathbf{S}_{11,N}\vec{a} + \mathbf{S}_{12,N}\mathbf{S}_{\text{ant}}\vec{v}, \tag{4.1}$$

where $\vec{v}$ is the input wave vector of the antenna array. The following equation can be applied to solve for $\vec{v}$:

$$\mathbf{S}_{21,N}\vec{a} + \mathbf{S}_{22,N}\mathbf{S}_{\text{ant}}\vec{v} = \vec{v}. \tag{4.2}$$

Then, $\vec{v}$ can be written in the form of

$$\vec{v} = (\mathbf{I} - \mathbf{S}_{22,N}\mathbf{S}_{\text{ant}})^{-1}\mathbf{S}_{21,N}\vec{a}. \tag{4.3}$$

For the derivation, it was assumed that the matrix $(\mathbf{I} - \mathbf{S}_{22,N}\mathbf{S}_{\text{ant}})$ is invertible. This assumption is physically based on the fact that there should be always a stable and unique solution of $\vec{v}$ for all passive networks with a certain input vector $\mathbf{S}_{21,N}\vec{a}$. Equation (4.1) becomes

$$\vec{b} = \mathbf{S}_{11,N}\vec{a} + \mathbf{S}_{12,N}\mathbf{S}_{\text{ant}}(\mathbf{I} - \mathbf{S}_{22,N}\mathbf{S}_{\text{ant}})^{-1}\mathbf{S}_{21,N}\vec{a}. \tag{4.4}$$

The scattering matrix of the system with the antenna array and the feeding network is

$$\mathbf{S}_{\text{sys}} = \mathbf{S}_{11,N} + \mathbf{S}_{12,N}\mathbf{S}_{\text{ant}}(\mathbf{I} - \mathbf{S}_{22,N}\mathbf{S}_{\text{ant}})^{-1}\mathbf{S}_{21,N}. \tag{4.5}$$

The design objective of the matching and decoupling network is to generate the corresponding eigenvectors by exciting a single input port, where the other input ports are decoupled. For an $N \times N$ matrix $\mathbf{S}_{\text{ant}}$, there exist N eigenvalues λ_i, which can be calculated through

$$|\mathbf{S}_{\text{ant}} - \lambda\mathbf{I}| = 0. \tag{4.6}$$

By solving for the eigenvalues of the scattering matrix of the antenna array, the eigenvectors are obtained. Their relationship is

$$\mathbf{S}_{\text{ant}}\vec{r}_i = \lambda_i\vec{r}_i, \tag{4.7}$$

where $\vec{r}_i$ is the ith eigenvector. This equation can be explained physically in a way that the reflected wave vector and the corresponding incident wave vector, which is the eigenvector of the array scattering matrix, are identical except for the multiplication with the eigenvalue λ_i. In order to let each port at the input side generate one eigenvector through the matching and decoupling network, the matrix $\mathbf{S}_{21,N}$ is created column by column through $\vec{g}_i = c_i\vec{r}_i$, where $\vec{g}_i$ is the ith column of $\mathbf{S}_{21,N}$ and c_i is a constant. Generally, the matching and decoupling network contains only passive elements. As a result, reciprocity can be expected, which means

$$\mathbf{S}_{21,N} = \mathbf{S}_{12,N}^{T}. \tag{4.8}$$

It is known that for a symmetric matrix the eigenvectors corresponding to different eigenvalues are orthogonal, which is

$$\vec{g}_i \cdot \vec{g}_j = 0 \quad | \quad \text{for } i \neq j\,. \tag{4.9}$$

Assume the ith port is excited, $\vec{a}_i = [0, 0, \cdots, a_i, \cdots, 0]^T$. According to the above relationship, it can be derived that

$$\mathbf{S}_{21,N}\vec{a}_i = a_i c_i \vec{g}_i \tag{4.10}$$

and based on equation (4.3),

$$\vec{v}_i = a_i c_i (\mathbf{I} - \mathbf{S}_{22,N}\mathbf{S}_{\text{ant}})^{-1}\vec{g}_i. \tag{4.11}$$

To maintain the vector $\vec{v}_i$ to be the eigenvector of the scattering matrix of the antenna array, the matrix $\mathbf{S}_{22,N}$ should be either a null matrix or a matrix owning the same eigenvectors as $\mathbf{S}_{\text{ant}}$. Assume $\mathbf{S}_{22,N}\mathbf{S}_{\text{ant}}\vec{g}_i = x_i\vec{g}_i$, then

$$(\mathbf{I} - \mathbf{S}_{22,N}\mathbf{S}_{\text{ant}})\vec{g}_i = (1 - x_i)\vec{g}_i, \tag{4.12}$$

and

$$(\mathbf{I} - \mathbf{S}_{22,N}\mathbf{S}_{\text{ant}})^{-1}\vec{g}_i = \frac{1}{1 - x_i}\vec{g}_i. \tag{4.13}$$

According to equation (4.4), the reflected wave vector can be written in the form of

$$\vec{b}_i = \mathbf{S}_{11,N}\vec{a}_i + \frac{a_i c_i \lambda_i}{1 - x_i}\mathbf{S}_{12,N}\vec{g}_i. \tag{4.14}$$

Together with the relationship shown in equation (4.8) and the orthogonality property shown in equation (4.9), it can be derived that

$$\mathbf{S}_{12,N}\vec{g}_i = \begin{bmatrix} 0 \\ 0 \\ \vdots \\ c_i\vec{g}_i \cdot \vec{g}_i \\ \vdots \\ 0 \end{bmatrix}, \tag{4.15}$$

which means, if the input wave vector of the antenna array is an eigenvector of its scattering matrix, the reflected wave vector from the antenna array only couples to the port which excites it. This property can be understood as the reciprocity of the matching and decoupling network. In order to ensure the decoupling between the input ports, the matrix $\mathbf{S}_{11,N}$ should be diagonal and there should be no direct coupling within the network on the left-hand side. To achieve the matching, the matching network at each input port should be properly designed and the following relationship should be achieved:

$$S_{ii} + \frac{c_i^2 \lambda_i}{1 - x_i}\vec{g}_i \cdot \vec{g}_i = 0, \tag{4.16}$$

where S_{ii} is the ith element on the diagonal of $\mathbf{S}_{11,N}$. Based on the above discussions, in order to solve the mutual coupling problem based on the eigenmode generation method, the following requirements should be fulfilled: a) the matching and decoupling network should be passive and reciprocal; b) each column of $\mathbf{S}_{21,N}$ should be an eigenvector of $\mathbf{S}_{\text{ant}}$; c) $\mathbf{S}_{22,N}$ should either be a null matrix or should have eigenvectors in common with $\mathbf{S}_{\text{ant}}$(eigenvalues can be different); d) $\mathbf{S}_{11,N}$ should be diagonal and the entries on the diagonal should be solved from equation (4.16).

4.2.2 Design of a Matching and Decoupling Network with Eigenmode Excitation for a Two-Element Monopole Antenna Array

In this section, the matching and decoupling network based on the eigenmode excitation method for a two-element monopole array operating around 2.45 GHz with element spacing of 10% of the free space wavelength is designed.

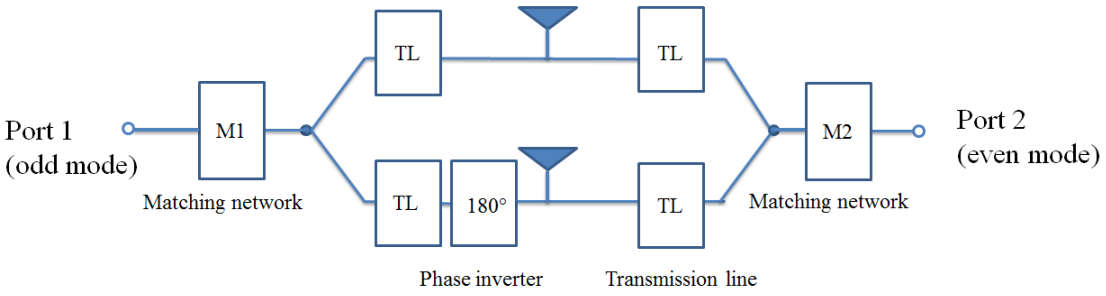

Figure 4.3: Schematic for the eigenmode excitation of a two-element compact antenna array. TL: transmission line.

For a two-element monopole antenna array, which is aligned symmetrically, the scattering matrix can be described mathematically as

$$\mathbf{S}_{\text{ant}} = \begin{bmatrix} r & c \\ c & r \end{bmatrix}, \tag{4.17}$$

where r denotes the reflection coefficient at each port and c is the coupling coefficient between the ports. To generate the eigenmodes at the antenna array, a four-port network is required. It is simply solved for the eigenvectors $\vec{v}_1 = [1, 1]^T$ and $\vec{v}_2 = [1, -1]^T$, together with the corresponding eigenvalues $\lambda_1 = r + c$ and $\lambda_2 = r - c$, respectively. The two modes can also be called the even mode and the odd mode, since for one of the modes the elements are excited in phase while for the other one the elements are excited out of phase.

Based on the above discussions, a simple matching and decoupling network is configured as shown in Figure 4.3. Port 1 is planned to generate the odd mode and port 2 is used to excite the even mode. The power from each port is divided into two branches by a microstrip divider and each branch is connected with one radiation element. In order to generate the odd mode, a 180° phase shifter is inserted in one of the branches near port 1. Instead of the antenna array, if two 50 Ω terminals are placed, the scattering matrix of the network can be obtained. It is obvious that this network contains only passive elements and the two rows of $\mathbf{S}_{21,N}$ are the eigenvectors of $\mathbf{S}_{\text{ant}}$. For such a network, $\mathbf{S}_{22,N}$ is not a null matrix, but it should have the same eigenvectors as $\mathbf{S}_{\text{ant}}$. The decoupling network can be modeled as shown in Figure 4.4. Since the circuit is passive, it is obvious that $S_{43} = S_{34}$ due to reciprocity. If $S_{33} = S_{44}$, it can be concluded that $\mathbf{S}_{22,N}$ has the same eigenvectors as $\mathbf{S}_{\text{ant}}$. To prove this, in the following the even-odd mode excitation analysis is utilized. Port 1 and port 2 can be equivalent to two loads of 50 Ω and after the impedance transformation by the matching network, the impedances are demonstrated as Z_1 and Z_2, respectively. Consequently, each of them can be divided into two loads in shunt with impedances of $2Z_1$ and $2Z_2$, respectively. The four transmission lines have equal length and the same characteristic impedance. Then, if port 3 and port 4 are excited simultaneously with the same amplitude and out of phase, which means $a_3 = -a_4 = a$, a virtual ground is formed in the middle on the upper branch and a virtual open is formed in the middle of the lower

branch as shown in Figure 4.4. In this case, the circuit can be decomposed into two one-port circuits and the equivalent reflection coefficients of the circuit at port 3 and port 4 can be derived as

$$\begin{cases} r_3 = \frac{b_3}{a_3} = \frac{S_{34}a_4 + S_{33}a_3}{a_3} = -S_{34} + S_{33} \\ r_4 = \frac{b_4}{a_4} = \frac{S_{43}a_3 + S_{44}a_4}{a_4} = -S_{43} + S_{44}. \end{cases} \tag{4.18}$$

It is already known that $S_{34} = S_{43}$, so if $r_3 = r_4$, $S_{33} = S_{44}$ is true. Comparing the two one-port equivalent circuits, the only difference is that there is a phase inverter in one of the branches for port 3. The effect of the phase inverter is investigated based on the circuit model shown in Figure 4.5. Without the phase inverter, the reflection coefficient is

$$\Gamma = \frac{b}{a}. \tag{4.19}$$

When a phase shifter is applied at the input, the new input wave amplitude is $a' = ae^{j\phi_0}$ and the output wave amplitude becomes $b' = be^{-j\phi_0}$, where ϕ_0 is the phase shift. Then, the reflection coefficient becomes

$$\Gamma' = \frac{b'}{a'} = \frac{be^{-j\phi_0}}{ae^{j\phi_0}} = \Gamma e^{-2j\phi_0}. \tag{4.20}$$

The phase shift of a phase inverter is 180°, in this case, $\Gamma' = \Gamma$. The input impedance of a one-port network is

$$Z_L = Z_0 \frac{1+\Gamma}{1-\Gamma}. \tag{4.21}$$

With the same reflection coefficient, the corresponding input impedances are identical. Consequently, it is concluded that the two one-port networks in Figure 4.4 are equivalent, so $r_3 = r_4$ and then $S_{33} = S_{44}$. As a result, $\mathbf{S}_{22,N}$ has the same eigenvectors as $\mathbf{S}_{\text{ant}}$. When the odd mode port is excited, destructive interference occurs at the node in front of the even port (port 2), as a result, $S_{21} = S_{12} = 0$ and $\mathbf{S}_{11,N}$ is diagonal. By properly designing the matching circuit, matching and decoupling of the array can be achieved.

The implementation of the matching and decoupling network for a compact monopole antenna array is shown in Figure 4.6. The rod monopole antennas are made of copper and they are mounted on an aluminum plate with the size of 150 mm × 150 mm. The thickness of the plate is 5 mm. The diameter of the copper rod is 2.5 mm. The matching and decoupling network is implemented on the other side of the aluminum plate for its convenience in installation and for avoiding radiation influences from the network. The substrate is FR 4 with a dielectric constant $\varepsilon_r = 4.518$, $\tan\delta = 0.016$, the thickness of the substrate is 1.5 mm and the metalization is 0.018 mm. In the plate, two holes are drilled to connect the rod antenna with the microstrip lines on the substrate. Inside of the hole, Teflon is filled into the space to hold the monopoles and the diameter of the hole is 5 mm. The length of the monopoles above the ground plate is 29.65 mm. Two monopoles are aligned in the middle of the plate and the center to center distance between the monopoles is 16 mm.

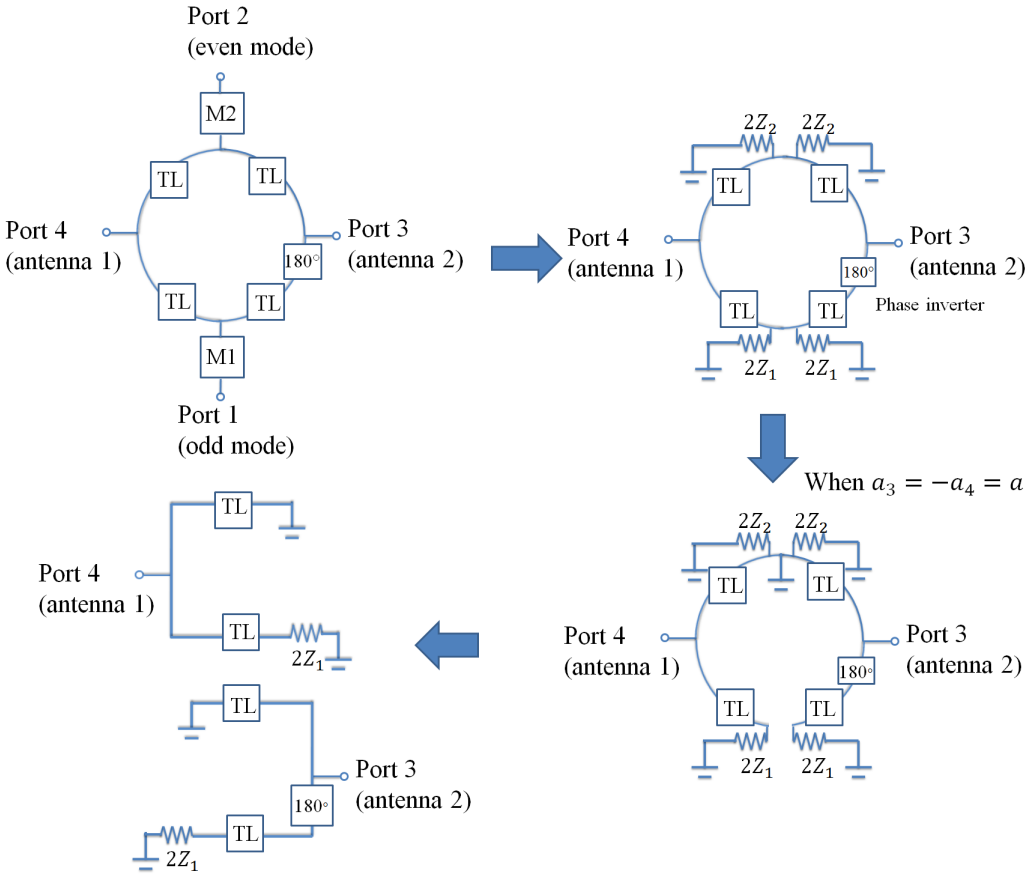

Figure 4.4: Simplification and decomposition of the schematic shown in Figure 4.3.

The proposed matching and decoupling network is shown in Figure 4.7(a). The feeds of the two monopole antennas are located at the center of the PCB board. In the network, a folded microstrip line structure with electric length of half the effective wavelength at around 2.45 GHz is applied to generate the odd mode from the excitation (the structure is named as microstrip balun). The miter at the corners compensates the parasitic effects caused by the 90° bending [Pozar, 2011]. Two narrow strip lines with particular length and characteristic impedance are implemented for the purpose of matching by the method of impedance transformation. Virtual ground points are formed due to the destructive interference at point A and B. When the odd mode is excited, point A is equal to a ground, which means the circuit after point A does not affect the operation of the odd mode and this is also true for point B when the even mode is excited. The transmission line lengths from the two points to the monopole feeding points are chosen approximately one quarter of the effective wavelength to transform the virtual ground into an open at the antenna feedings.

It is noticed that the transmission line used for matching the odd port is much narrower. This is due to the fact that the input impedance due to the odd mode radiation is very

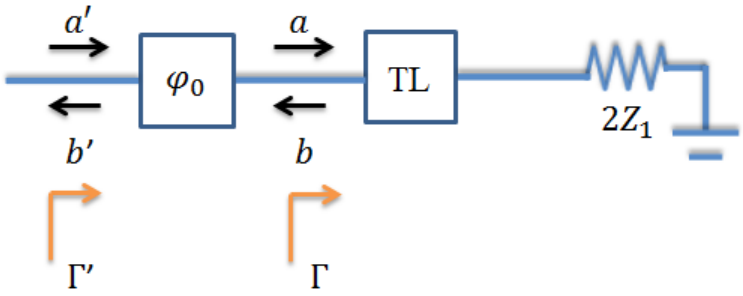

Figure 4.5: Transformation of the reflection coefficient by a phase shifter.

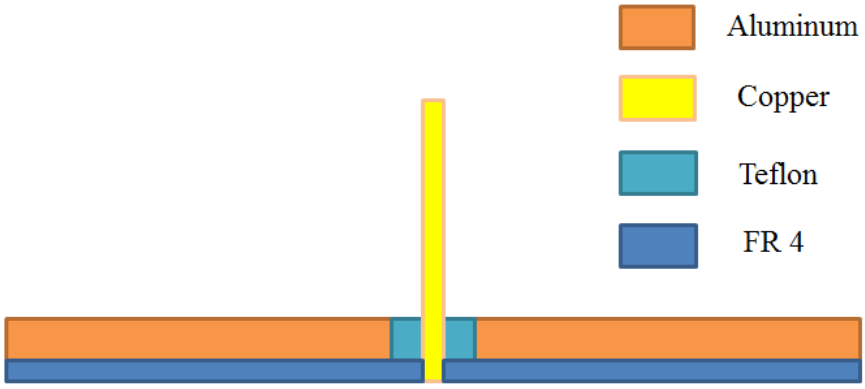

Figure 4.6: Feeding and implementation of the radiation elements.

small, which is transformed to a high impedance at point B. As a result, the matching transmission line is required to have a higher characteristic impedance. The simulated electric field distribution from CST MWS at 2.45 GHz is plotted in Figure 4.8. It is obvious that the field is almost zero at one port when the other port is excited. The simulated S-parameters are shown in Figure 4.9. The coupling between the two ports is reduced to as less as -30 dB at the operation frequency. The matching bandwidth for the measurement of the return loss of less than -10 dB is around 350 MHz for the even mode and 65 MHz for the odd mode. It was mentioned in Chapter 2 that the matching bandwidth is inversely proportional to the quality factor. For the odd mode, the two antenna elements are out of phase. Therefore, a virtual PEC plane can be assumed in the middle between the two monopoles and the electric fields are partially confined by it. As a result, the quality factor is very large and the matching bandwidth is limited. The pattern correlation is checked with the simulated far field radiation patterns. The calculated result of equation (3.59) is around 0.04 at 2.45 GHz.

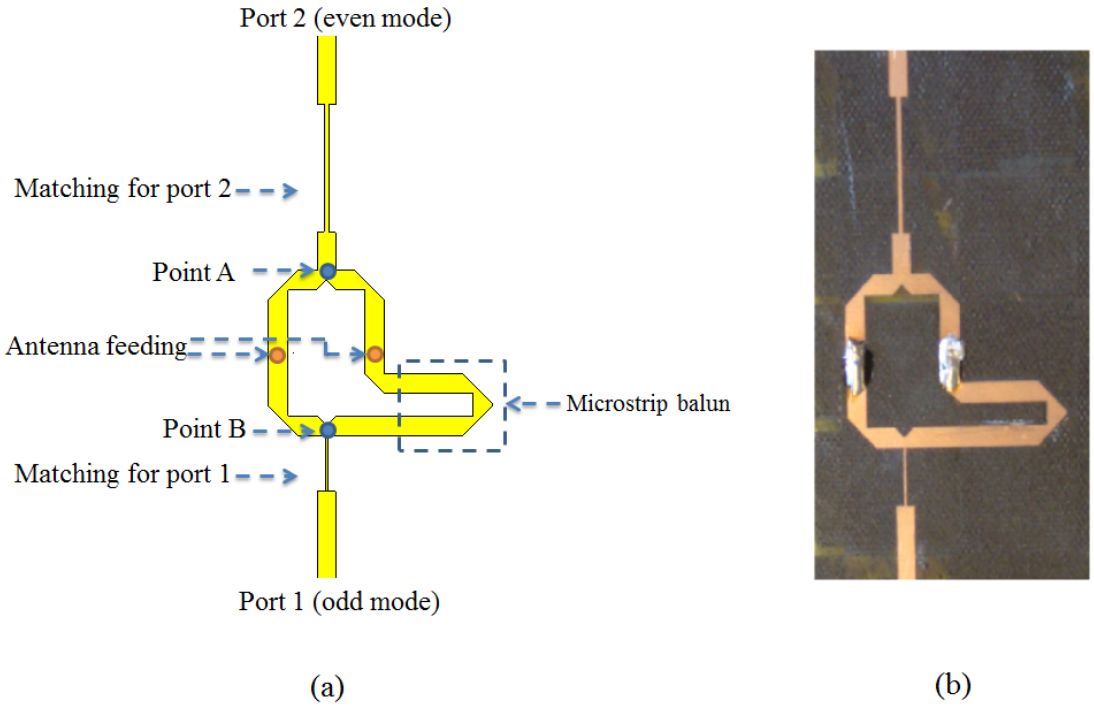

Figure 4.7: (a)The layout of the matching and decoupling network; (b) photograph of the fabricated circuit.

4.2.3 Measurement Results for the Compact Monopole Array

The fabricated antenna array is shown in Figure 4.10. The measurements of the S-parameters were carried out with a vector network analyzer (VNA) (Rohde & Schwarz ZVA 24) in the frequency range from 2 GHz to 3 GHz. The measured S-parameters are shown in Figure 4.11. Compared to the simulation results, the operation frequency is slightly shifted. This could be due to fabrication errors, e.g., the monopole length is a little bit shorter than the desired value. The antenna far field radiation patterns were also measured for the two ports by a full spherical scan with a step size of 1° vertically and 15° horizontally. The measurements were carried out by ASTRIUM GmbH, Munich. The measurement results in a vertical cut plane are shown in Figure 4.12. A gain measurement was also carried out, where the result is plotted in Figure 4.13. The directivity can be calculated through the measured 3D radiation patterns. Then, the measured radiation efficiencies at 2.45 GHz are 45% and 73% for the odd mode and the even mode, respectively.

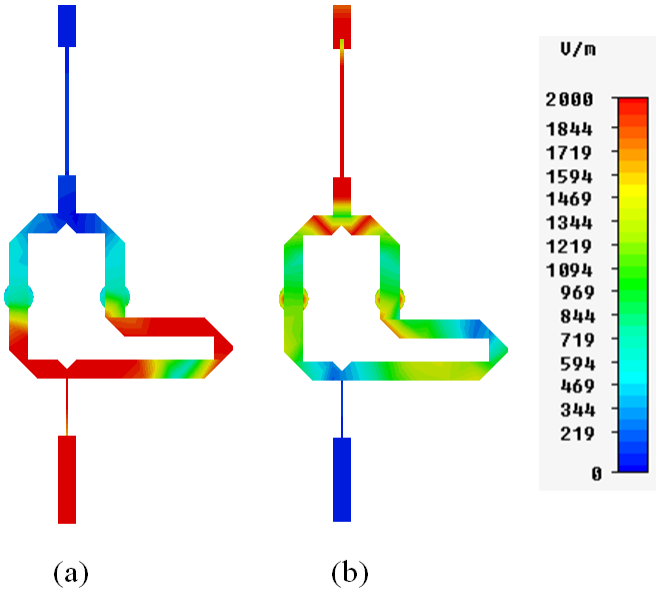

Figure 4.8: Electric field distribution from CST MWS at 2.45 GHz: (a) odd mode; (b) even mode.

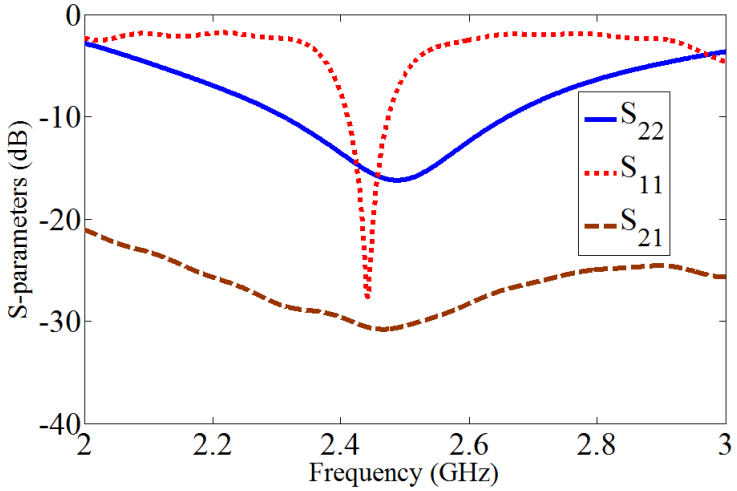

Figure 4.9: Simulated S-parameters for the array based on the eigenmode excitation method.

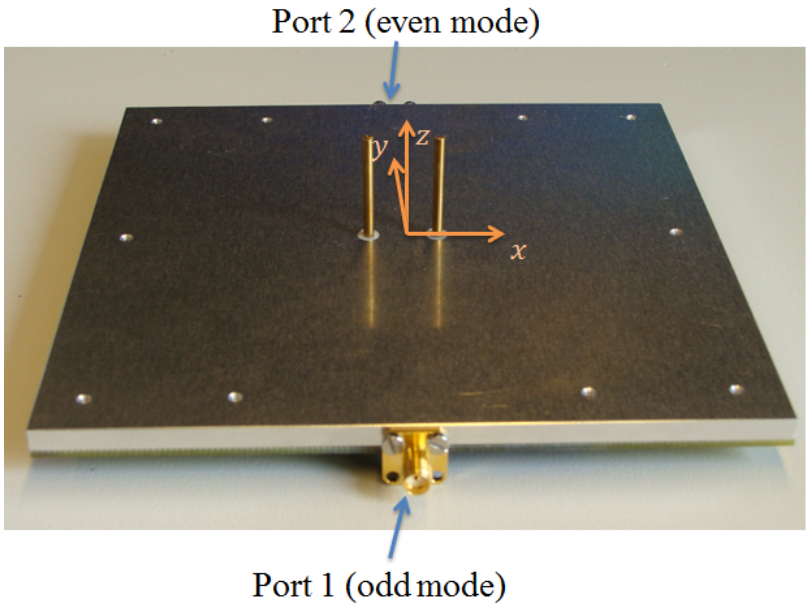

Figure 4.10: Photograph of the fabricated two-element compact monopole array.

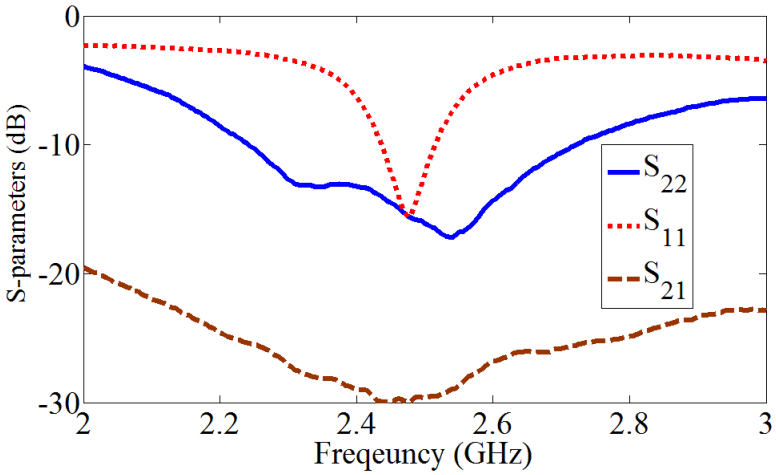

Figure 4.11: Measured S-parameters for the array based on the eigenmode excitation method.

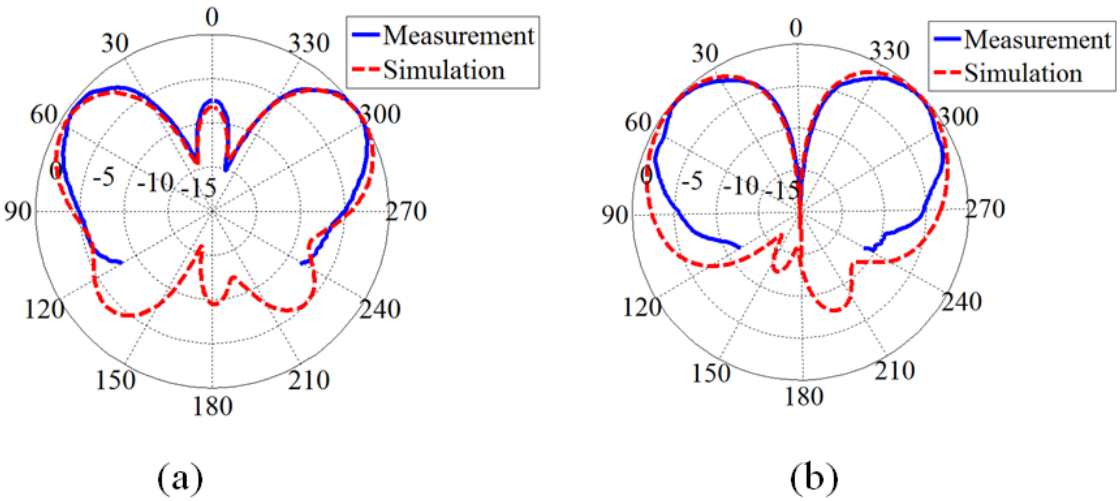

Figure 4.12: Normalized measured and simulated far field patterns of the array based on the eigenmode excitation method for $\phi = 0°$ at 2.45 GHz: (a) even mode; (b) odd mode.

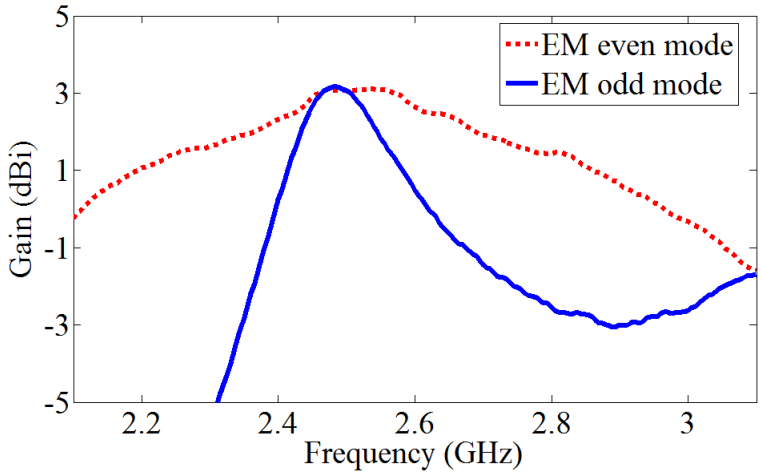

Figure 4.13: Measured antenna gain for the array based on the eigenmode excitation method.

4.3 Multiport Conjugate Matching Method

In this section, the second matching and decoupling approach named multiport conjugate matching is investigated. A decoupling network for the same compact monopole array as presented in the last section is designed.

4.3.1 Introduction of the Multiport Conjugate Matching Method

For an M-port matching and decoupling network, the total input power equals the scattered power plus the power loss in the network, which means

$$\begin{aligned} P_{\text{loss}} =& P_{\text{in}} - P_{\text{out}} \\ =& \frac{1}{2}\vec{a}^H\vec{a} - \frac{1}{2}\vec{b}^H\vec{b} \\ =& \frac{1}{2}\vec{a}^H\vec{a} - \frac{1}{2}\vec{a}^H\mathbf{S}_M^H\mathbf{S}_M\vec{a} \\ =& \frac{1}{2}\vec{a}^H(\mathbf{I} - \mathbf{S}_M^H\mathbf{S}_M)\vec{a}. \end{aligned} \tag{4.22}$$

If the network is lossless, $P_{\text{loss}} = 0$ and it is derived that $\mathbf{S}_M^H\mathbf{S}_M = \mathbf{I}$. For a $2N$-port network, this result is equivalent to the conditions [Wallace and Jensen, 2004]

$$\begin{cases} \mathbf{S}_{11,N}^H\mathbf{S}_{11,N} + \mathbf{S}_{21,N}^H\mathbf{S}_{21,N} = \mathbf{I}, \\ \mathbf{S}_{11,N}^H\mathbf{S}_{12,N} + \mathbf{S}_{21,N}^H\mathbf{S}_{22,N} = 0, \\ \mathbf{S}_{12,N}^H\mathbf{S}_{12,N} + \mathbf{S}_{22,N}^H\mathbf{S}_{22,N} = \mathbf{I}. \end{cases} \tag{4.23}$$

If the multiport conjugate matching condition $\mathbf{S}_{22,N} = \mathbf{S}_{\text{ant}}^H$ is achieved, the power is maximally transferred. The proof of this statement is provided in Appendix B.

Alternatively, the operation principle of the multiport conjugate matching can be explained physically as follows. Assume a two-port system as shown in Figure 4.14. After implementing the decoupling network, there are two parallel paths between the input ports of the system. One is the direct path due to the network (path 1 shown in Figure 4.14) and the other one is the mutual coupling contribution (path 2 in Figure 4.14) between the radiation elements. The essence of implementing the decoupling network is to avoid any signal flowing from port 1 into port 2. This means signals due to the two paths must be destructively interfered. This can also be recognized as a neutralization technique.

In the following, low loss networks are assumed lossless for the first step estimation based on the condition $\mathbf{S}_{22,N} = \mathbf{S}_{\text{ant}}^H$ of the design and optimization procedures are applied afterwards.

4.3.2 Design of a Matching and Decoupling Network with Multiport Conjugate Matching for a Two-Element Monopole Antenna Array

With the assistance of computer simulation software such as CST MWS or based on real array measurements, the scattering matrix of the compact antenna array can be obtained. As a result, the corresponding conjugate transpose matrix of it can be calculated.

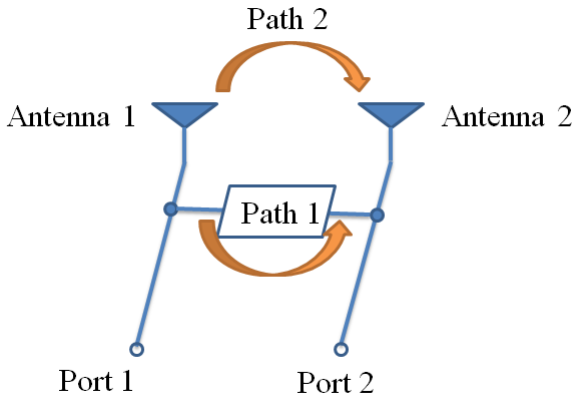

Figure 4.14: The two possible paths between the two ports of coupled antennas with decoupling network.

Consequently, the matching and decoupling network can be designed according to this matrix. In the last section, it was shown that the scattering matrix of the monopole array is symmetric, so the decoupling network should be symmetric as well. Here, a fast approximation design method based on even-odd excitation analysis is proposed. Considering the coupling and radiation properties of the array, an H-shaped schematic is utilized for designing the decoupling network as shown in Figure 4.15, where the input ports are considered as 50 Ω loads. The network consists of three two-port networks A, B and C. Initially, these networks are assumed to be lossless. In order to avoid the losses and reduce manufacturing complexity, the matching and decoupling network is realized with transmission lines.

When the network is excited in the odd mode on the right side of the decoupling network, a virtual ground is expected in the middle of the network, of which the equivalent one-port circuit is shown in Figure 4.15(b). On the other hand, if the even mode is excited, a virtual open is found. The corresponding reflection coefficients of the odd mode r_o and of the even mode r_e can be expressed as

$$\begin{cases} r_o = S_{11}^* - S_{12}^* \\ r_e = S_{11}^* + S_{12}^*, \end{cases} \tag{4.24}$$

where S_{11} and S_{12} are the elements of the array scattering matrix. For convenience, the network is synthesized by equivalent admittances, which are calculated through

$$Y_{o,e} = Y_0 \frac{1 - r_{o,e}}{1 + r_{o,e}} = Y_0 y_{o,e}, \tag{4.25}$$

where Y_0 is the reference admittance and $y_{o,e}$ are the admittances normalized by Y_0. It is noticed that the only difference of the equivalent one-port networks for the odd and even modes is that the symmetry point is modeled differently, e.g. a virtual ground or a virtual open. Because the network is lossless, the input admittance $Y_{o,M}$ and $Y_{e,M}$ at point M should have the same real part. The difference in the imaginary part is controlled by the network A and the virtual ground or open. The function of the two-port C realized by a

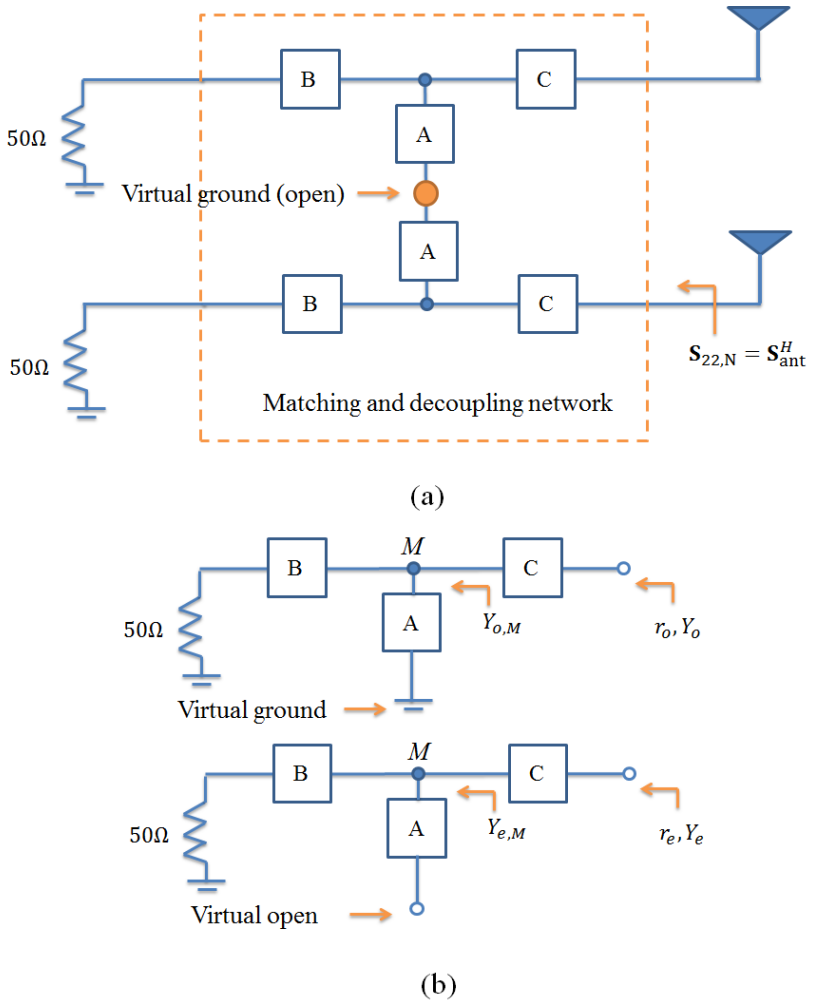

Figure 4.15: (a) H-shaped matching and decoupling network; (b) equivalent one-port circuit models of the even and odd mode excitation.

transmission line with a certain length and characteristic impedance is to transform the admittances $Y_{o,M}$ and $Y_{e,M}$ into the admittances Y_o and Y_e, respectively, which may have different real parts due to different array configurations. The function of the two-port C is mathematically described as

$$\mathrm{Re}\left[\frac{1 - r_o e^{2j\phi_c}}{1 + r_o e^{2j\phi_c}}\right] = \mathrm{Re}\left[\frac{1 - r_e e^{2j\phi_c}}{1 + r_e e^{2j\phi_c}}\right], \tag{4.26}$$

where ϕ_c is the electric length of the transmission line, Re[] is the real part of a complex value. Figure 4.16 plots the calculated result of $|\mathrm{Re}[y_o] - \mathrm{Re}[y_e]|$ based on the simulated scattering parameters of the compact monopole array. It shows that the value is 0 around 2.5 GHz, which means that the network C is not required at this frequency. For convenience, the design is proposed around 2.5 GHz.

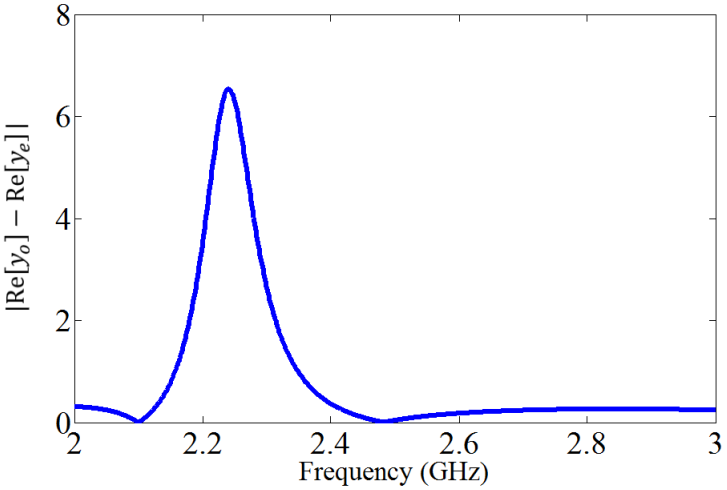

Figure 4.16: Calculated result of $|\mathrm{Re}[y_e] - \mathrm{Re}[y_o]|$.

Network B, which is realized as a quarter wavelength transformer, is used to transform the 50 Ω port impedance into the desired real part of the admittance at point M as shown in Figure 4.15(b). Network A is utilized to generate the required imaginary part of the admittance. The configuration shown in Figure 4.17 with two pieces of transmission lines is adopted to realize network A. The essence of the method is to transform the virtual ground and the virtual open into the required imaginary parts. Based on the impedance transformation formulas, the design parameters of network A can be determined from

$$\begin{cases} \mathrm{Im}\left[\dfrac{Z_0(Z_2+Z_1\frac{\tan\beta_2 l_2}{\tan\beta_1 l_1})}{Z_2(\frac{Z_1}{j\tan\beta_1 l_1}+jZ_2\tan\beta_2 l_2)}\right] = \mathrm{Im}\left[\dfrac{1-r_e e^{2j\phi_c}}{1+r_e e^{2j\phi_c}}\right] \\ \mathrm{Im}\left[\dfrac{Z_0(Z_2-Z_1\tan\beta_2 l_2\tan\beta_1 l_1)}{Z_2(jZ_1\tan\beta_1 l_1+jZ_2\tan\beta_2 l_2)}\right] = \mathrm{Im}\left[\dfrac{1-r_o e^{2j\phi_c}}{1+r_o e^{2j\phi_c}}\right], \end{cases} \tag{4.27}$$

where $Z_{1,2}$ and $l_{1,2}$ are the characteristic impedance and the length of the transmission lines as shown in Figure 4.17, respectively, Im[] is the imaginary part of a complex value. The propagation constants $\beta_{1,2}$ can be calculated from the microstrip line structures. Solving equation (4.27), the required values of the characteristic impedance and the line length are obtained.

The substrate used in this design is the same as the one utilized in the design of the array based on the eigenmode excitation method. The proposed matching and decoupling network is shown in Figure 4.18(a), the fabricated circuit is shown in Figure 4.18(b). The antenna array with the matching and decoupling network has been simulated in CST MWS. The simulated electric field distribution is shown in Figure 4.19. When the upper port is excited, it is found that the electric field is quite weak on the feeding line of the other port. The simulated S-parameters are plotted in Figure 4.20, the achieved matching and decoupling bandwidth is around 80 MHz (measurement of $|S_{11}| \leq$-10 dB and $|S_{21}| \leq$-15 dB). The calculated pattern correlation is around 0.09 at 2.45 GHz.

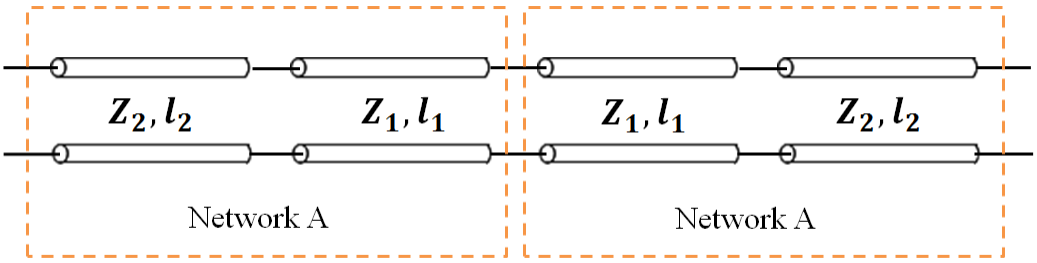

Figure 4.17: The approach for realizing network A.

4.3.3 Measurement Results for the Compact Monopole Array

The installation and measurements of the antenna array follow the same process as for the array with eigenmode excitation in the last section. The measured S-parameters are shown in Figure 4.21. Compared to the simulation results, the operation frequency is about 80 MHz higher, which is due to the possible fabrication errors and the uncertainties of FR 4. The measured far field radiation pattern is shown in Figure 4.22. The measured gain is plotted in Figure 4.23 and the radiation efficiency is about 76% for both ports.

4.4 Design of a Four-Element Compact Antenna Array Based on Multiport Conjugate Matching

In this section, a four-element compact monopole array is presented based on the multiport conjugate matching method. In [Coetzee and Yu, 2008], a four-element array is designed based on the eigenmode excitation method and a multilayer feeding network is adopted in order to excite the four radiation elements with corresponding modes, which is quite complex for fabrication. Here, a much simpler solution which decouples the ports by a single layer feeding network is introduced. The proposed four-element antenna array is shown in Figure 4.24, the separations of the antenna element are $l_1 = 13$ mm and $l_2 = 16$ mm.

4.4.1 Design of the Matching and Decoupling Network

Similar to the previous designs, FR 4 is utilized as the substrate for the decoupling network. The design process follows the multiport conjugate matching method as discussed in the last section. In the previous analysis, the even-odd excitation method has been applied to synthesize the network. Since the four radiation elements are symmetrically placed, the same method can be utilized as well, where more symmetry cut planes should be considered. The realizing H-shaped network is again exploited for the design. However, in this case, the network parameters are firstly approximated based on a two-element array and then an optimization process is applied to finalize the design. The designed decoupling network is shown in Figure 4.25(a) and the manufactured network is shown in Figure 4.25(b). The simulated electric field distribution is plotted in Figure 4.26 in the case that port 2

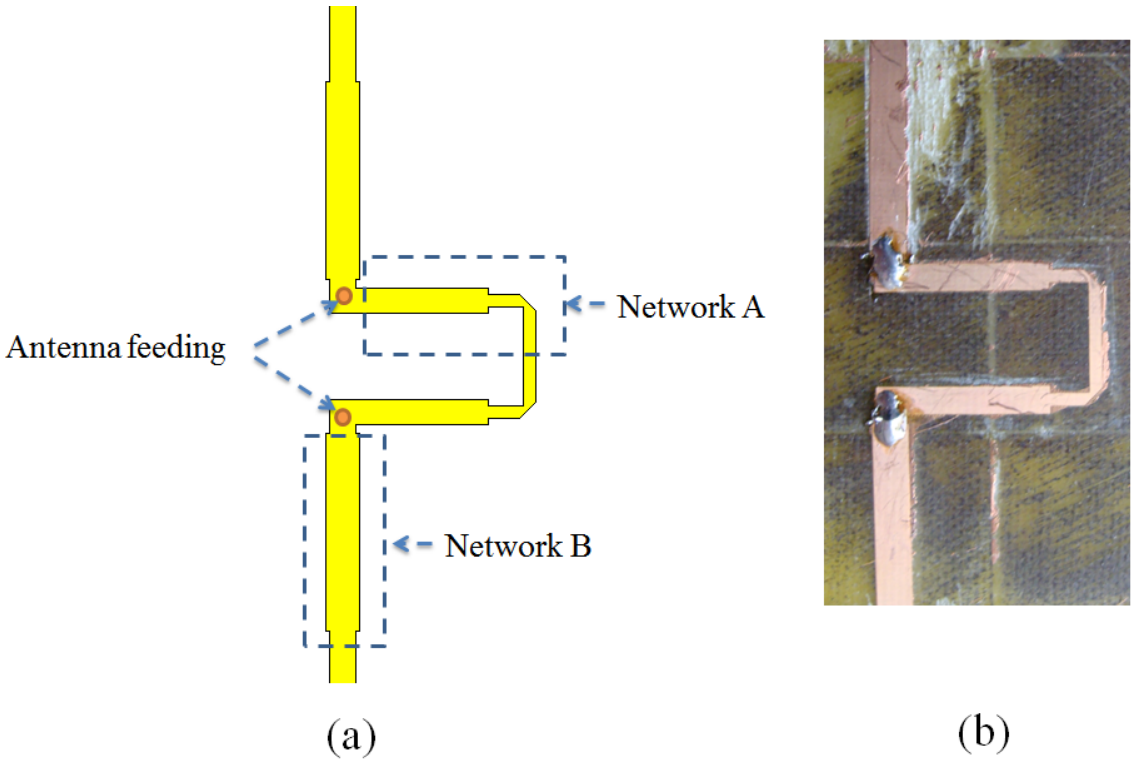

Figure 4.18: (a) The layout of the matching and decoupling network; (b) photograph of the fabricated circuits.

is excited. The simulated S-parameters are shown in Figure 4.27. Due to the symmetry properties, there are three independent parameters. S_{11} is the return loss of every input port. S_{21} indicates the coupling coefficient between the neighboring elements while S_{31} shows the coupling behavior between the elements which are center-symmetric. The achieved coupling coefficient is below -18 dB at the operating frequency and the matching bandwidth is around 80 MHz.

4.4.2 Measurement Results for the Compact Monopole Array

The fabricated antenna array is shown in Figure 4.28 and the measured S-parameters are plotted in Figure 4.29. Good agreement between the simulation and measurement is obtained. The measured far field radiation pattern is shown in Figure 4.30, since all the ports are centrosymmetric, only the radiation pattern of port 1 (indicated in Figure 4.28) is shown. The measured maximum gain in the operation frequency band is 3 dBi and the measured radiation efficiency is around 45%.

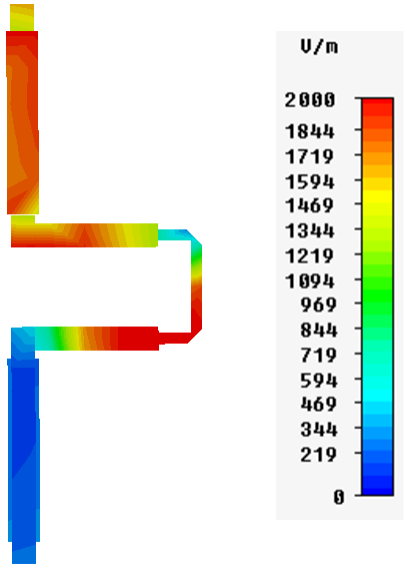

Figure 4.19: Electric field distribution from CST MWS due to the upper port excitation of the two-element array at 2.45 GHz.

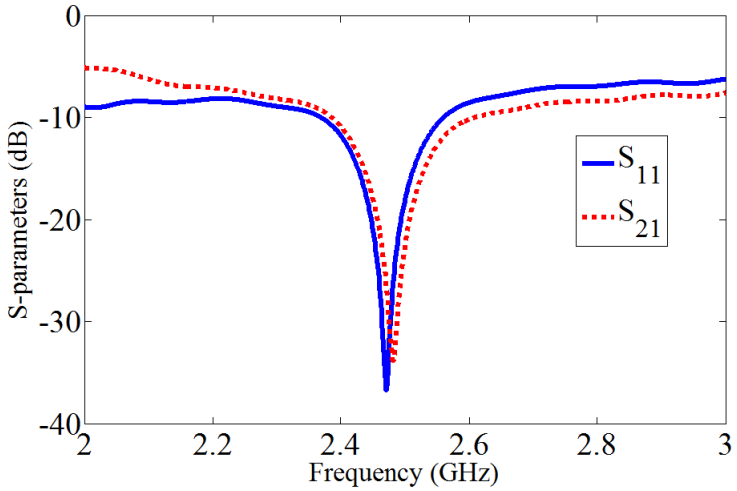

Figure 4.20: Simulated S-parameters for the two-element array based on multiport conjugate matching.

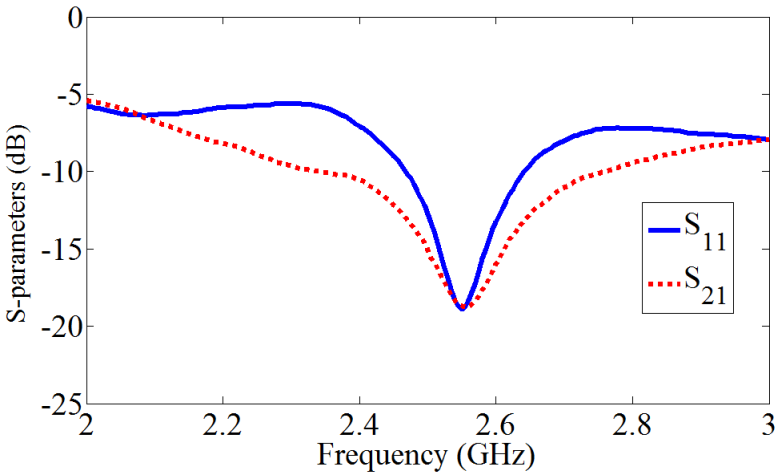

Figure 4.21: Measured S-parameters for the two-element array based on multiport conjugate matching.

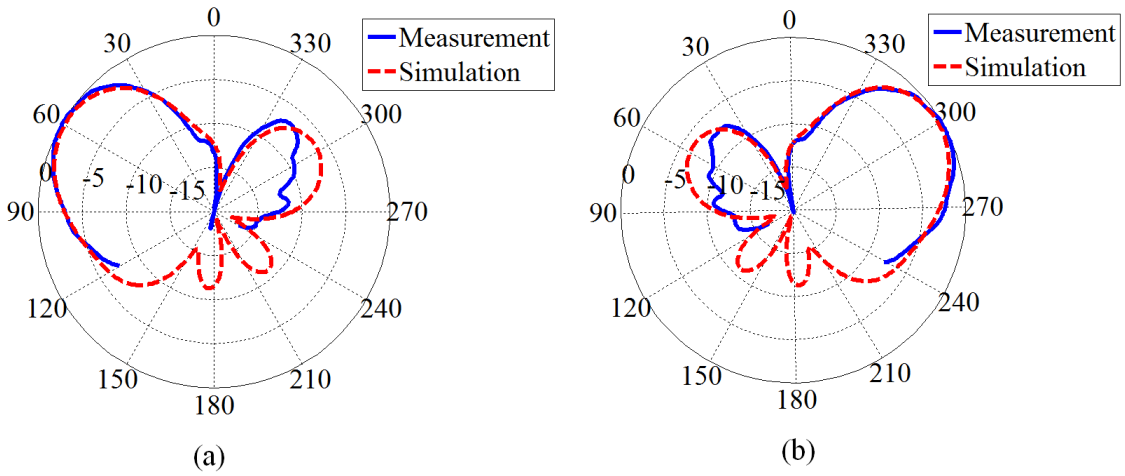

Figure 4.22: Normalized measured and simulated far field patterns of the two-element array based on multiport conjugate matching for $\phi = 0°$ at 2.55 GHz: (a) port 1; (b) port 2.

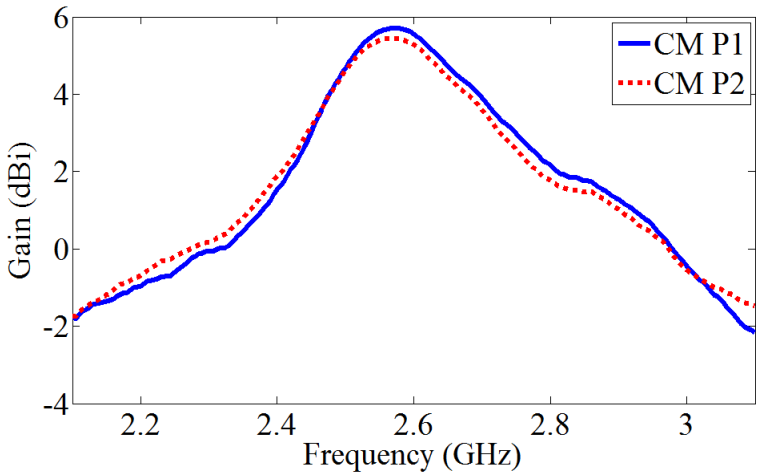

Figure 4.23: Measured antenna gain for the two-element array based on multiport conjugate matching.

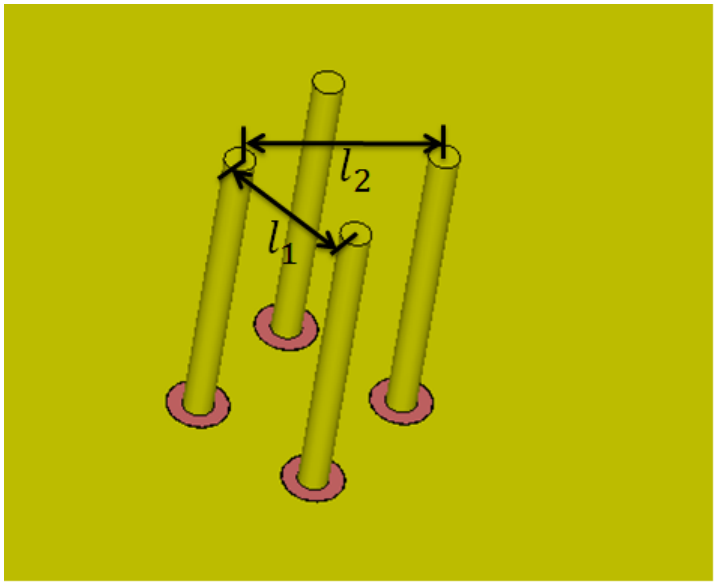

Figure 4.24: Symmetrically arranged four-element compact monopole array.

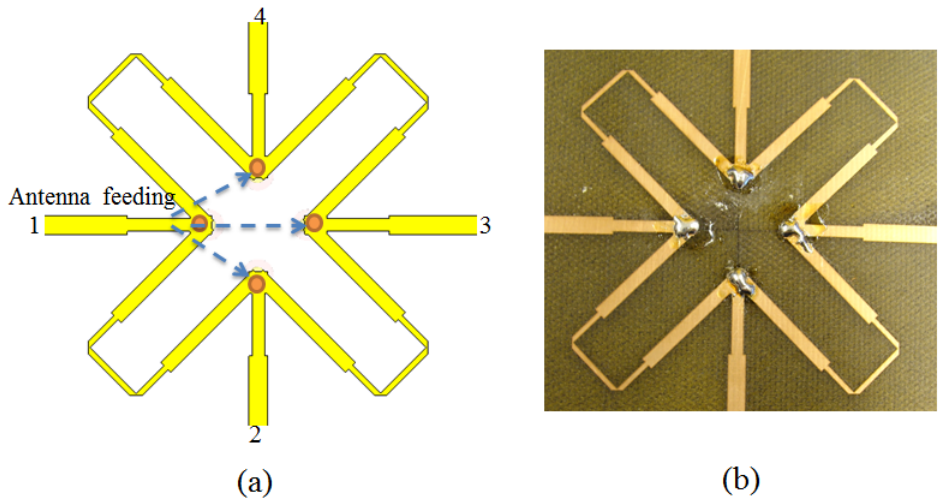

Figure 4.25: (a)The layout of the matching and decoupling network for the four-element array; (b) photograph of the fabricated circuits.

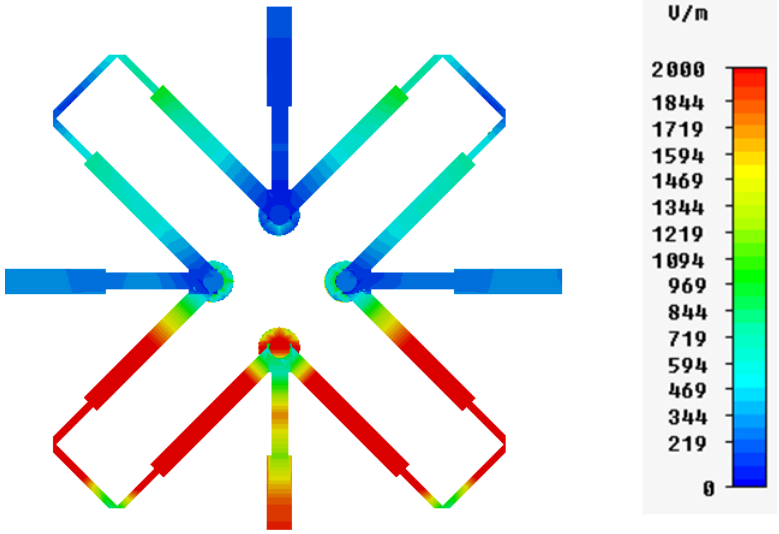

Figure 4.26: Electric field distribution from CST MWS for the four-element array due to the excitation of the port at the bottom at 2.45 GHz.

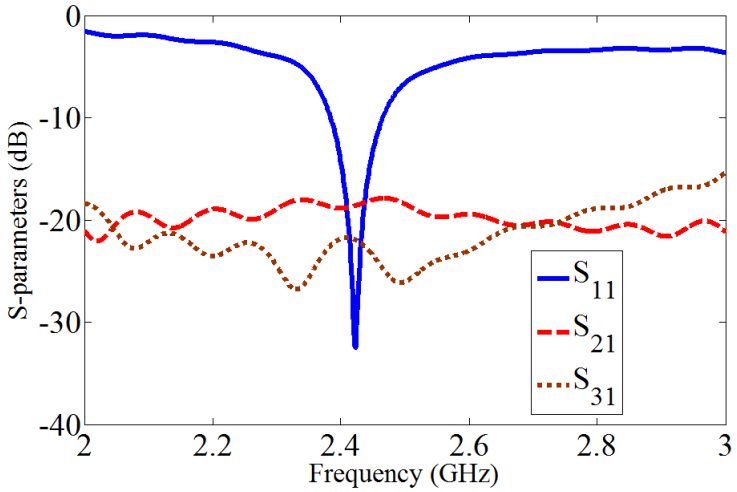

Figure 4.27: Simulated S-parameters for the four-element array based on multiport conjugate matching.

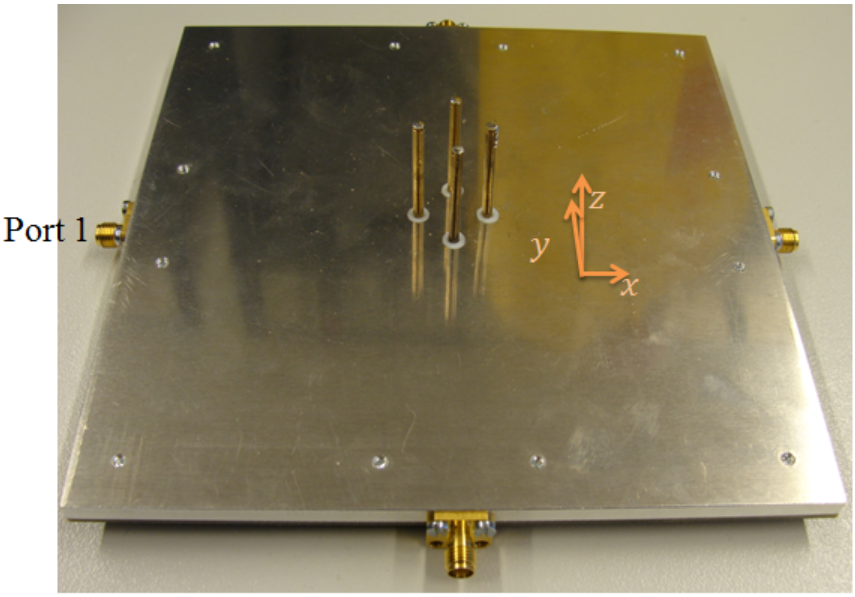

Figure 4.28: Photograph of the fabricated four-element compact monopole array.

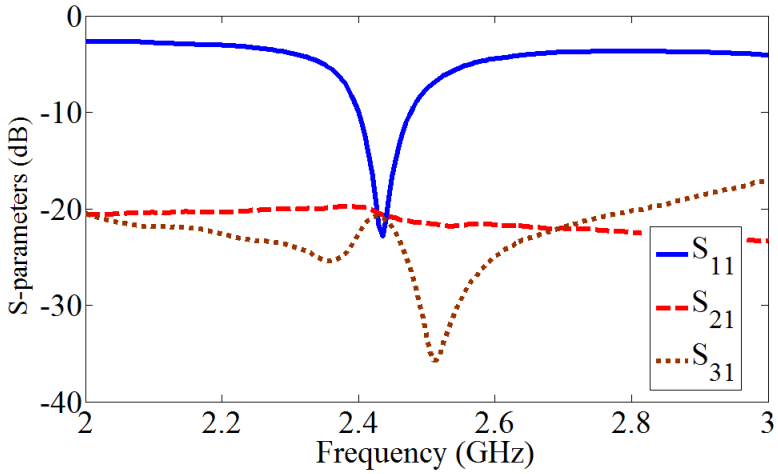

Figure 4.29: Measured S-parameters for the four-element array based on multiport conjugate matching.

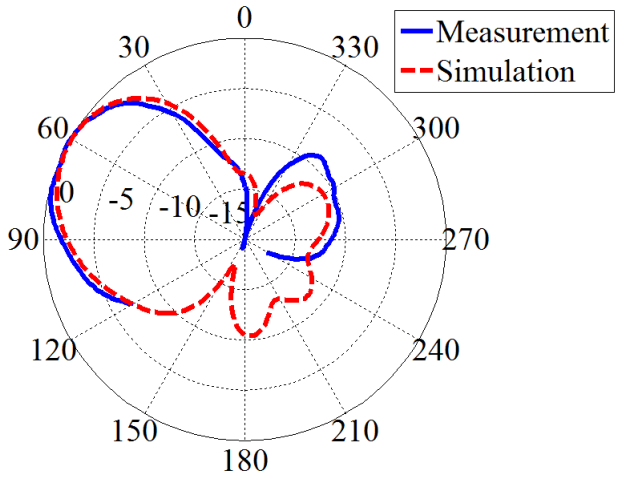

Figure 4.30: Normalized measured and simulated far field pattern of port 1 of the four-element array based on multiport conjugate matching for $\phi = 0°$ at 2.45 GHz.

4.5 Comparison of the Eigenmode Excitation Method and the Multiport Conjugate Matching Method

The performance of monopole arrays with different matching and decoupling networks has been demonstrated in the previous sections. In the following, comparisons between the two approaches are performed. Firstly, in terms of the configuration, the feeding network based on the eigenmode excitation method is more complicated as compared to the one based on multiport conjugate matching. Very narrow matching microstrip lines and a microstrip balun are required for the eigenmode excitation, whereas the multiport conjugate matching method is more favorable considering the fabrication. Secondly, for the operation bandwidth, the maximum available matching and decoupling bandwidths of both array types are less than 100 MHz for MIMO applications, but they are constrained due to different facts. The compact array based on eigenmode excitation owns very good decoupling properties in a broad band while the matching bandwidth is limited by the odd mode excitation. On the other hand, the bandwidth of the array based on multiport conjugate matching is limited by both the matching and the decoupling. Thirdly, with respect to the radiation efficiency, the odd mode of the array based on eigenmode excitation owns only 45% efficiency, which sometimes is not good enough especially for communication devices which are power sensitive and the array based on multiport conjugate matching is more advantageous with regard to efficiency. Lastly, with respect to the far field radiation patterns, the two modes of the eigenmode excitation array own patterns with irregular differences. The radiation patterns of the two ports of the array based on multiport conjugate matching are symmetric and the power patterns are almost orthogonal and this property is useful to detect from which directions the electromagnetic waves come. Both types of arrays are efficient in MIMO communications since the calculated pattern correlation coefficients of the arrays are low enough. According to the above comparisons, the decoupling approaches should be properly chosen for different practical applications. It should be also kept in mind that the multiport conjugate matching method is more advantageous for the design of compact arrays with more than two radiation elements due to the simplicity of the feeding network.

In the following, the relationship between the two methods is investigated, where it is proved that the modes generated by the network based on conjugate matching can be decomposed into the eigenmodes.

From the previous discussions, the eigenvectors of the array scattering matrix are orthogonal. Therefore, the normalized eigenvectors can be chosen as basis vectors, which are given as $\vec{v}_e = [\frac{\sqrt{2}}{2}, \frac{\sqrt{2}}{2}]^T$ and $\vec{v}_o = [\frac{\sqrt{2}}{2}, -\frac{\sqrt{2}}{2}]^T$. For the array based on multiport conjugate matching, when the ith port is excited, the input vector of the antenna array shown in Figure 4.2 is marked as $\vec{v}_i$. Due to the symmetric arrangement of the decoupling network, the vectors can be written in form of

$$\begin{cases} \vec{v}_1 = x\vec{v}_e + y\vec{v}_o \\ \vec{v}_2 = x\vec{v}_e - y\vec{v}_o, \end{cases} \tag{4.28}$$

where x and y are complex constants. The ratio between them indicates which eigenmode is dominant. As discussed before, if the input ports are matched and decoupled by a lossless

network and assuming the antennas are also lossless, the radiated power by the antenna array can be written in the form of

$$\begin{aligned} P_{\text{rad}} =& \frac{1}{2}\vec{v}^H\vec{v} - \frac{1}{2}\vec{v}^H\mathbf{S}_{\text{ant}}^H\mathbf{S}_{\text{ant}}\vec{v} \\ =& \frac{1}{2Z_s}\int |\vec{E}(\theta,\phi)|^2 d\Omega, \end{aligned} \tag{4.29}$$

where Z_s is the free space impedance. Based on this, the following group of equations can be found:

$$\begin{cases} \frac{1}{2}\vec{v}_1^H\vec{v}_1 - \frac{1}{2}\vec{v}_1^H\mathbf{S}_{\text{ant}}^H\mathbf{S}_{\text{ant}}\vec{v}_1 = \frac{1}{2Z_s}\int |\vec{E}_1(\theta,\phi)|^2 d\Omega, \\ \frac{1}{2}\vec{v}_2^H\vec{v}_2 - \frac{1}{2}\vec{v}_2^H\mathbf{S}_{\text{ant}}^H\mathbf{S}_{\text{ant}}\vec{v}_2 = \frac{1}{2Z_s}\int |\vec{E}_2(\theta,\phi)|^2 d\Omega, \\ \frac{1}{2}(\vec{v}_1+\vec{v}_2)^H(\vec{v}_1+\vec{v}_2) - \frac{1}{2}(\vec{v}_1+\vec{v}_2)^H\mathbf{S}_{\text{ant}}^H\mathbf{S}_{\text{ant}}(\vec{v}_1+\vec{v}_2) \\ = \frac{1}{2Z_s}\int |\vec{E}_1(\theta,\phi)+\vec{E}_2(\theta,\phi)|^2 d\Omega. \end{cases} \tag{4.30}$$

Calculated from the simulated patterns, the radiation pattern correlation is zero, which means

$$\int \vec{E}_1^*(\theta,\phi)\cdot\vec{E}_2(\theta,\phi)d\Omega = 0. \tag{4.31}$$

Together with equation (4.30), it is derived that

$$\vec{v}_1^H\vec{v}_2 - \vec{v}_1^H\mathbf{S}_{\text{ant}}^H\mathbf{S}_{\text{ant}}\vec{v}_2 = 0. \tag{4.32}$$

Then, putting equation (4.28) into equation (4.32) and applying the conditions that $\vec{v}_e^H\vec{v}_o = 0$, $\vec{v}_e^H\vec{v}_e = 1$, $\vec{v}_o^H\vec{v}_o = 1$, $\mathbf{S}_{\text{ant}}\vec{v}_e = \lambda_e\vec{v}_e$ and $\mathbf{S}_{\text{ant}}\vec{v}_o = \lambda_o\vec{v}_o$, where λ_e and λ_o are the corresponding eigenvalues, equation (4.32) is simplified as

$$(1-|\lambda_e|^2)|x|^2 = (1-|\lambda_o|^2)|y|^2. \tag{4.33}$$

Then, the ratio of $|y|$ and $|x|$ is

$$\frac{|y|}{|x|} = \sqrt{\frac{1-|\lambda_e|^2}{1-|\lambda_o|^2}}. \tag{4.34}$$

Since $\lambda_e = S_{11}+S_{21}$ and $\lambda_o = S_{11}-S_{21}$, equation (4.34) can be represented through

$$\frac{|y|}{|x|} = \sqrt{\frac{1-|S_{11}+S_{21}|^2}{1-|S_{11}-S_{21}|^2}}. \tag{4.35}$$

For example, for the two-element compact array utilized in the previous sections, is was found that $S_{11} = 0.17+0.20j$ and $S_{21} = 0.02-0.47j$ at 2.45 GHz. From this, it was calculated that $\frac{|y|}{|x|} = 1.3$, which means the decoupling network generates a stronger odd mode component. The above analysis based on the assumption of ideally uncorrelated patterns gives a general understanding of how the two methods are related.

4.6 Estimation of the Signal Correlation of Compact Arrays Through Scattering Parameters

It was discussed in Chapter 3 that the received signal correlation among the receiving ports of an antenna array, which is an important parameter for evaluating the MIMO system performance, can be estimated from the far field radiation pattern correlation. Through the power conservation law, it is reported in [Blanch et al., 2003] that it is possible to approximate the radiation pattern correlation coefficient from the scattering parameters for lossless antenna arrays. However, for lossy antenna arrays with decoupling networks, the scattering parameters are not sufficient to make the approximation, which in this case should be a matter of the power loss as well. For lossy arrays, results presented in [Hallbjörner, 2005] and [Stjernman, 2005] indicate why S-parameters are not sufficient for calculating the pattern correlation coefficient, but exact expressions for the pattern correlation were not provided. In [Li et al., 2013], the equivalent circuit model is applied to characterize the effects of the power loss, but this method is not applicable for arrays with matching and decoupling networks. In this section, the relationship between the scattering parameters, loss power and pattern correlation is analyzed and a set of equations are derived. Then, a more accurate and relatively simple estimation procedure for predicting the pattern correlation of arrays is presented, which is also applicable for arrays with lossy feeding networks. The previous two two-element compact monopole arrays with different decoupling networks, which are considered lossy, are investigated as examples. Good agreement between the proposed method and simulation results is achieved.

Before the theoretical study is carried out, a simple example is shown to demonstrate that the scattering parameters are not sufficient for calculating the pattern correlation. The example is shown in Figure 4.31, where the decoupling network for an array with two closely placed antennas is a lossy Wilkinson divider [Pozar, 2011]. Assuming the input impedance of the antenna array at point F is 50 Ω, the two input ports of the array are conjugate matched and the maximum power is transmitted into the system including both the radiation elements and the decoupling network. In this example, the input ports are well decoupled and matched, but the patterns are fully correlated (identical radiation patterns for the two ports). However, not all decoupling networks perform like such a Wilkinson divider. From this example it shows that S-parameters are not sufficient for calculating the patter correlation of lossy antenna arrays, the exact expression of pattern correlation is derived and complex decoupling networks are also considered in the analysis.

4.6.1 Mathematical Analysis

The derivation of the formula indicating the relationship between the S-parameters and the pattern correlation is based on the power conservation law [Hallbjörner, 2005, Stjernman, 2005]. Take a two-port antenna array as an example, the total input power can be written in the form of

$$P_{\text{in}} = P_{\text{rad}} + P_{\text{loss}} + P_1 + P_2, \tag{4.36}$$

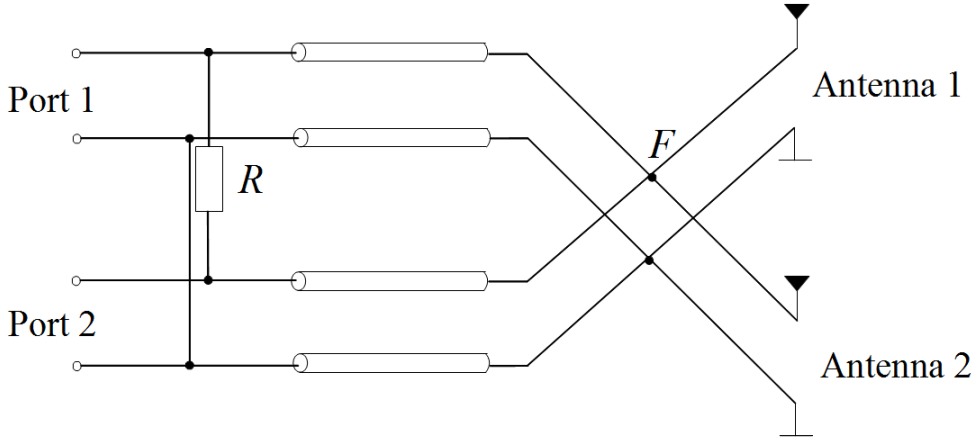

Figure 4.31: Two-element antenna array with a Wilkinson divider.

with

$$P_{\text{in}} = \frac{1}{2}|a_1|^2 + \frac{1}{2}|a_2|^2, \tag{4.37}$$

$$P_1 = \frac{1}{2}|S_{11}a_1 + S_{12}a_2|^2, \tag{4.38}$$

$$P_2 = \frac{1}{2}|S_{21}a_1 + S_{22}a_2|^2, \tag{4.39}$$

$$P_{\text{rad}} = \frac{1}{8}\int |\sqrt{G_1(1-|S_{11}|^2-|S_{21}|^2)}\vec{F}_1(\theta,\phi) + \sqrt{G_2(1-|S_{22}|^2-|S_{12}|^2)}\vec{F}_2(\theta,\phi)|^2 d\Omega, \tag{4.40}$$

$$P_{\text{loss}} = P_{\text{loss}}(|a_1|^2) + P_{\text{loss}}(|a_2|^2) + P_{\text{loss}}(a_1a_2^*) + P_{\text{loss}}(a_2a_1^*). \tag{4.41}$$

In the above equations, a_1 and a_2 are the input wave amplitudes of the two input ports, which are defined according to equation (2.29). G_1 and G_2 are the corresponding antenna gains for the two input ports. $\vec{F}_1(\theta,\phi)$ and $\vec{F}_2(\theta,\phi)$ are the normalized far field radiation patterns of the ports. It should be noticed that the radiation patterns can be different for different applications and scenarios, e.g., if the received signal is a measurement of the open circuit voltage, the pattern of one port should be measured while the other port is open circuit; if the received signal is a measurement of the received wave or if the transmitted signal correlation is considered, the far field pattern of one port should be measured with the other port loaded with 50 Ω. In this section, the use of the S-parameters to determine

the pattern correlation follows the second situation. Equation (4.36) means that the total input power P_{in} delivered to the ports should be the sum of the radiated power P_{rad}, the dissipated power losses P_{loss} in the decoupling network and radiation elements and the reflected powers at port 1, P_1, as well as port 2, P_2. The following analysis requires to write the loss power in the form of equation (4.41). $P_{\text{loss}}(|a_1|^2)$ and $P_{\text{loss}}(|a_2|^2)$ are the loss power contributions including only the contribution of $|a_1|^2$ and $|a_2|^2$, respectively. The term $P_{\text{loss}}(a_1 a_2^*)$ is named the coupling loss including only the loss power from the product $a_1 a_2^*$ and a similar definition is used for $P_{\text{loss}}(a_2 a_1^*)$.

Based on the above equations, the connections of radiation patterns, S-parameters and power loss can be found and expressed in the form of

$$\frac{1}{4\pi} G_1 \left(1 - |S_{11}|^2 - |S_{21}|^2\right) \int |\vec{F}_1(\theta,\phi)|^2 d\Omega = 1 - |S_{11}|^2 - |S_{21}|^2 - \frac{P_{\text{loss}}(|a_1|^2)}{\frac{1}{2}|a_1|^2}, \tag{4.42}$$

$$\frac{1}{4\pi} G_2 \left(1 - |S_{22}|^2 - |S_{12}|^2\right) \int |\vec{F}_2(\theta,\phi)|^2 d\Omega = 1 - |S_{22}|^2 - |S_{12}|^2 - \frac{P_{\text{loss}}(|a_2|^2)}{\frac{1}{2}|a_2|^2}, \tag{4.43}$$

$$\begin{aligned} &\frac{1}{4\pi} \sqrt{G_1(1 - |S_{11}|^2 - |S_{21}|^2)} \sqrt{G_2(1 - |S_{22}|^2 - |S_{12}|^2)} \int \vec{F}_1(\theta,\phi) \cdot \vec{F}_2^*(\theta,\phi) d\Omega \\ &= S_{12}^* S_{11} + S_{22}^* S_{21} + \frac{P_{\text{loss}}(a_1 a_2^*)}{\frac{1}{2} a_1 a_2^*}. \end{aligned} \tag{4.44}$$

Then, the pattern correlation calculated from equation (3.59) can be expressed in the way

$$\begin{aligned} \rho =& \frac{\int \vec{F}_i(\theta,\phi) \cdot \vec{F}_j^*(\theta,\phi) d\Omega}{\sqrt{\int |\vec{F}_i(\theta,\phi)|^2 d\Omega \int |\vec{F}_j(\theta,\phi)|^2 d\Omega}} \\ =& \frac{S_{12}^* S_{11} + S_{22}^* S_{21} + \frac{P_{\text{loss}}(a_1 a_2^*)}{\frac{1}{2} a_1 a_2^*}}{\sqrt{\left(1 - |S_{11}|^2 - |S_{21}|^2 - \frac{P_{\text{loss}}(|a_1|^2)}{\frac{1}{2}|a_1|^2}\right)\left(1 - |S_{22}|^2 - |S_{12}|^2 - \frac{P_{\text{loss}}(|a_2|^2)}{\frac{1}{2}|a_2|^2}\right)}}, \end{aligned} \tag{4.45}$$

so that the radiation pattern correlation can be calculated through the S-parameters and the power loss. In the lossless case, the relation shows that S-parameters are sufficient for the calculation. As discussed before, one of the design targets is to have maximum power transfer which means that the input ports are matched and decoupled. When the reflection coefficient and the coupling coefficient are relatively small, the magnitude of the pattern correlation can be approximated by

$$|\rho| = \left| \frac{P_{\text{loss}}(a_1 a_2^*)}{\frac{1}{2} a_1 a_2^*} \right| \frac{1}{\sqrt{\eta_1 \eta_2}} \tag{4.46}$$

where η_1 and η_2 are the radiation efficiencies of the two ports, respectively. If $P_{\text{loss}}(a_1 a_2^*)$ is 0, the patterns are uncorrelated, but if not, η should also be considered during the calculation of the correlation coefficient.

The example shown in Figure 4.31 can be explained with the previous discussions. According to the Kirchhoff laws, the power dissipated in the resistor can be written in the form of

$$P_{\text{loss}} = \frac{1}{2R}\left|a_1\sqrt{Z_0} - a_2\sqrt{Z_0}\right|^2, \tag{4.47}$$

where $R = 2Z_0$. By solving the above equation, it is found that $P_{\text{loss}}(a_1 a_2^*) = 0.25 a_1 a_2^*$, assuming the radiation elements are lossless. The radiation efficiency of such a system with a Wilkinson divider is, however, 50%, and the result of equation (4.46) becomes 1, which matches well with the conclusion of 'full correlation'.

In order to achieve an accurate value for $|\rho|$, in the following subsections, an analysis of the losses of the radiation elements and of the decoupling networks of the compact monopole antenna arrays from the previous sections is performed. It should be noticed that in order to emphasize the significance of the loss effect, the value of $\tan\delta$ is chosen as 0.025 for the substrate in the simulations carried out in CST MWS. Finally, an analytical estimation method for the coupling loss based on S-parameters is proposed. With this method, it is possible to perform the pattern correlation approximation based on S-parameters only for lossy arrays with lossy matching and decoupling networks.

4.6.2 Loss Mechanism Analysis

The loss mechanisms of compact antenna arrays with matching and decoupling networks should contain the Ohmic losses of lumped elements such as capacitors and inductors, losses from transmission lines and radiation element losses. As a result, the coupling loss contribution in all involved components should be analyzed.

Firstly, the power loss in the radiation elements is investigated. It is known that the power loss of the monopoles is influenced by the skin effect. The following steps are utilized to derive the mathematical expression of the power loss. The skin depth is

$$t = \sqrt{\frac{2}{\mu\omega\kappa}}, \tag{4.48}$$

where μ is the permeability, κ is the conductivity of the material and $\omega = 2\pi f$ is the angular frequency. Then, the average resistance per unit length of the monopole is

$$R' = \frac{1}{\kappa\pi(D-t)t}, \tag{4.49}$$

where D is the diameter of the rod.

The loss of the ground plane is relatively small compared with the loss of the rod because the current density on the rod is much higher. In order to relate the power loss to the S-parameters, the following assumptions and approximations are made. On the monopole,

the current is a standing wave of which the amplitude distribution can be approximated by a sinusoidal function as shown in Figure 4.32 and the current is assumed evenly distributed on the rod. The two monopoles should own similar current distributions with differences in amplitude which can be characterized through the S-parameters. For example, assume that port 1 is excited and port 2 is loaded. Through the relationship discussed in equation (2.29), the current amplitude on monopole 1 is

$$I_1(z) = (1 - S_{11})\frac{a_1}{\sqrt{Z_0}}\cos\left(\frac{2\pi}{\lambda}z\right), \tag{4.50}$$

where z is the the distance from the feeding point to the antenna, $z \in [0, l]$. The current on the other monopole, of which the port is not excited, can be approximated by

$$I_2(z) = S_{21}\frac{a_1}{\sqrt{Z_0}}\cos\left(\frac{2\pi}{\lambda}z\right). \tag{4.51}$$

The ratio between the current distributions of the excited monopole and the parasitic monopole is

$$\tau_{1,2} = \frac{I_{1,2}}{I_{2,1}} = \frac{S_{21,12}}{1 - S_{11,22}}. \tag{4.52}$$

Based on the above equations, when both ports are excited, the dissipated power on the rods is

$$\begin{aligned} P_{\text{loss}} =& \int_0^l \frac{1}{2} I_1^{sum}(z) R' I_1^{sum*}(z) dz + \int_0^l \frac{1}{2} I_2^{sum}(z) R' I_2^{sum*}(z) dz \\ =& \frac{1}{8Z_0}\pi R' |(1 - S_{11})a_1 + S_{12}a_2|^2 + \frac{1}{8Z_0}\pi R' |(1 - S_{22})a_2 + S_{21}a_1|^2, \end{aligned} \tag{4.53}$$

where $I_i^{sum}(z)$ is the overall current on the ith rod due to the excitation of both ports, l is the length of the monopoles. The loss power P_{loss} is now expressed by the S-parameters and the input wave amplitudes. Consequently, the pattern correlation components consisting of the coupling loss contribution $P_{\text{loss}}(a_1 a_2^*)$ can be calculated by further evaluation of the above equations.

In the above considerations, the power loss of the radiation elements has been investigated. In the following, the losses in the matching and decoupling network are analyzed. Generally, the matching and decoupling network contains both lumped elements and transmission lines, the loss in lumped elements can be simply analyzed by following the Kirchhoff laws as discussed in the example with the Wilkinson divider. The loss in a transmission line can be shown in the following form. It is well known that the loss in transmission lines is due to the loss on the conducting layers such as the strips and ground of microstrip lines and the loss in the substrate. The transmission loss is characterized by the attenuation constant α. Now consider the situation shown in Figure 4.33, where a_1 and a_3 are the wave amplitudes at the left end for waves with the propagation direction from left to right, while a_2 is a wave amplitude at the right end of a wave which propagates towards the opposite direction. Then, the loss of this piece of transmission line is

$$P_{\text{loss}} = \frac{1}{2}(1 - e^{-2\alpha l})|a_1 + a_3|^2 + \frac{1}{2}(1 - e^{-2\alpha l})|a_2|^2. \tag{4.54}$$

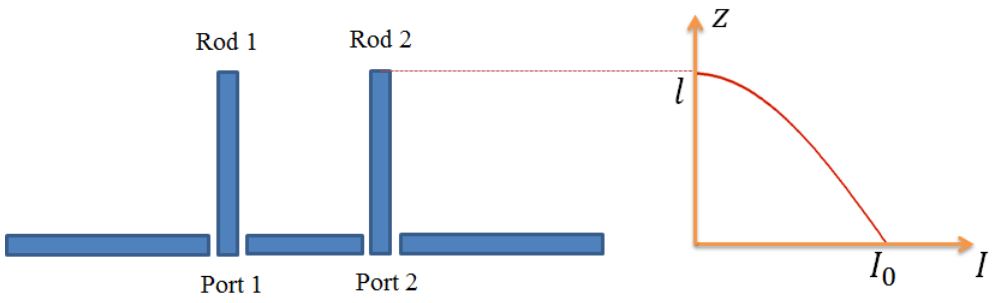

Figure 4.32: The current distribution of two compactly placed monopole antennas.

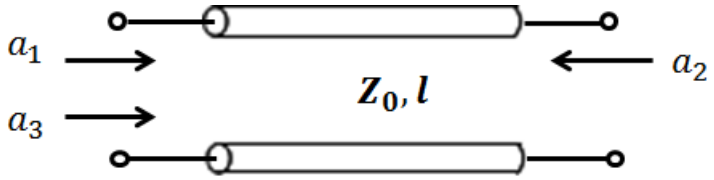

Figure 4.33: Three wave amplitudes on a lossy transmission line.

It can be noticed that the loss which is caused by signals propagating towards different directions on the transmission line does not contribute to the coupling loss. On the other hand, only the wave amplitudes propagating towards the same direction should be taken into account for the coupling loss calculation. In the following analysis of the coupling loss, a_1 might be due to the excitation of one port in the feeding network while a_3 might be the wave amplitude due to the excitation of the other port in the same transmission line.

The loss mechanisms from the radiation elements and the feeding networks have been analyzed above. For the purpose of calculating the coupling loss, it is required to find the wave amplitudes on each transmission line in the matching and decoupling network and the current distributions on the rods corresponding to the input wave amplitudes. In the following subsections, the two-element compact monopole arrays are investigated.

4.6.3 Analysis of Coupling Loss for the Compact Array Based on Eigenmode Excitation

The operating principle of the eigenmode excitation method has been demonstrated in Section 4.2. The two input ports generate two orthogonal modes of the array, which are the eigenvectors of the array scattering matrix. If the two radiation elements are symmetrically placed, the modes are even and odd. The feeding network only contains transmission lines and a microstrip balun is utilized for creating the odd mode. The matching is achieved by individual matching circuits at each port. In this subsection, the input wave amplitudes at the feed are expressed in the form of a_{even} and a_{odd}, which stand for the even and odd mode, respectively. Due to the symmetry property, the currents on the two antennas I_1

and I_2 can be written in the form

$$\begin{cases} I_1(z) = (c_1 a_{even} + c_2 a_{odd}) \cos(\frac{\lambda}{2\pi} z), \\ I_2(z) = (c_1 a_{even} - c_2 a_{odd}) \cos(\frac{\lambda}{2\pi} z), \end{cases} \tag{4.55}$$

where c_1 and c_2 are complex constants indicating the relationship between the current at the antenna feeding points and the excitation wave amplitudes. Based on equation (4.53), the power loss on the monopoles is

$$\begin{aligned} P_{\text{loss}} = &\int_0^l \frac{1}{2}(c_1 a_{even} + c_2 a_{odd}) R' (c_1 a_{even} + c_2 a_{odd})^* \cos^2\left(\frac{\lambda}{2\pi} z\right) dz + \\ &\int_0^l \frac{1}{2}(c_1 a_{even} - c_2 a_{odd}) R' (c_1 a_{even} - c_2 a_{odd})^* \cos^2\left(\frac{\lambda}{2\pi} z\right) dz. \end{aligned} \tag{4.56}$$

By evaluating this equation, it is simply found that the coefficient of the component containing the product $a_{even} a_{odd}^*$ is 0. This means, the losses in the monopoles do not contribute to the coupling loss.

Next, the losses in the transmission lines are analyzed. Firstly, the matching and decoupling network should be modeled and simplified. As mentioned before, the joint points A and B in Figure 4.7 are modeled as virtual ground with respect to different excitations, which is an important property during the simplification procedure of the network. As a result, the matching circuits behind the points A and B do not contribute to the coupling loss. Then, the feeding network consisting of several transmission lines are modeled and numbered as shown in Figure 4.34. The parameters of the feeding network are given in Table 1.

Table 1: Parameters of the decoupling network shown in Figure 4.34

Transmission line	Characteristic impedance	Loss constant	Length
TL 1	45 Ω	1.09 m^{-1}	16.5 mm
TL 2	45 Ω	1.09 m^{-1}	16.5 mm
TL 3	45 Ω	1.09 m^{-1}	16.5 mm
TL 4	45 Ω	1.09 m^{-1}	49.5 mm
TL 5	128 Ω	1.04 m^{-1}	9.4 mm
TL 6	95 Ω	1.05 m^{-1}	21.3 mm
TL 7	50 Ω	1.09 m^{-1}	6.3 mm

In order to simplify the analysis, the following approximation is made. It is assumed that the power is evenly distributed at the antenna feeding points. On each transmission line, the waves, which are mostly standing waves, can be expressed by the summation of two waves propagating towards different directions. These wave amplitudes on the transmission lines are marked as $a_{je,o}$ and $b_{je,o}$, where a is the wave which propagates from the left to the right while b indicates the wave propagating from right towards left. Here, j is the number of the transmission line and Z_j is the characteristic impedance of TL j, which is approximated by its real value according to the lossless case [Pozar, 2011]. e and o demonstrate the corresponding excitations for the even and odd ports, respectively. It

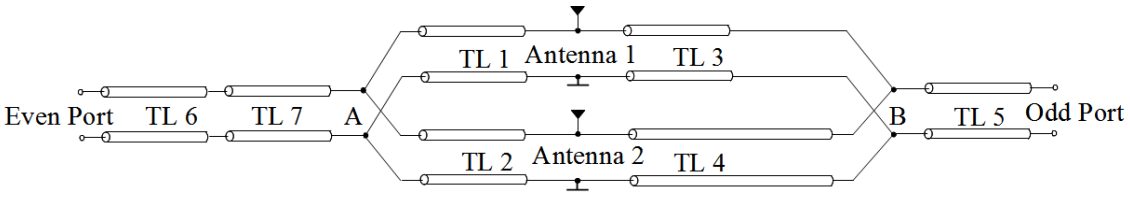

Figure 4.34: Simplified model of the transmission lines for the network based the eigenmode excitation method.

should be also mentioned that $a_{je,o}$ are the wave amplitudes defined at the starting point of a transmission line, which is assumed at the end close to the exciting port. For example, a_{1e} is the wave amplitude defined at the left end of TL 1 which is due to the excitation of the even port and b_{2o} is the wave amplitude at the right end of TL 2 which is due to the excitation of the odd port. In order to characterize the coupling loss, the relationship between wave amplitudes on transmission lines and the input wave amplitudes a_{even} and a_{odd} should be calculated. Their relationships are given by the coefficients in

$$\begin{cases} ya_{1e} = ya_{2e} = xa_{3e} = ga_{4e} = a_{even}, \\ y'b_{1e} = y'b_{2e} = x'b_{3e} = g'b_{4e} = a_{even}, \\ nb_{1o} = -nb_{2o} = mb_{3o} = hb_{4o} = a_{odd}, \\ n'a_{1o} = -n'a_{2o} = m'a_{3o} = h'a_{4o} = a_{odd}, \end{cases} \tag{4.57}$$

where $y, x, y', x, m, n, m', n', g, h, g', h'$ are complex coefficients. The power loss in the transmission lines can be calculated according to equation (4.54). Similar to the calculation of the loss in the monopoles, the sum of the coupling losses in TL 1 and TL 2 equals zero, which means only the loss powers in TL 3 and TL 4 need to be calculated in order to approximate the coupling loss. Then, the coupling loss contributions are

$$\frac{P_{\text{loss}}(a_{even}a_{odd}^*)}{\frac{1}{2}a_{even}a_{odd}^*} = e^{j\psi}\left((1-e^{-2\alpha_4 l_4})(\frac{1}{gh'^*}+\frac{1}{g'h^*})+(1-e^{-2\alpha_3 l_3})(\frac{1}{xm'^*}+\frac{1}{x'm^*})\right), \tag{4.58}$$

where ψ is an arbitrary value related to the phase shifts of the transmission lines.

To calculate these coefficients, the wave amplitudes on each transmission line are estimated by the following approach. The proposed method is based on a step-wise analysis of the voltage and current continuity relationships such as $V_{m,n}$ and $I_{m,n}$ in Figure 4.35 at the nodes between different transmission lines, where $V_{m,n}$ and $I_{m,n}$ are the voltage and current between the mth and the nth transmission line. The voltage corresponds to the sum of the forward and backward propagating waves and the current corresponds to the subtraction of them. At all the nodes, the voltages and currents satisfy Kirchhoff laws. For example,

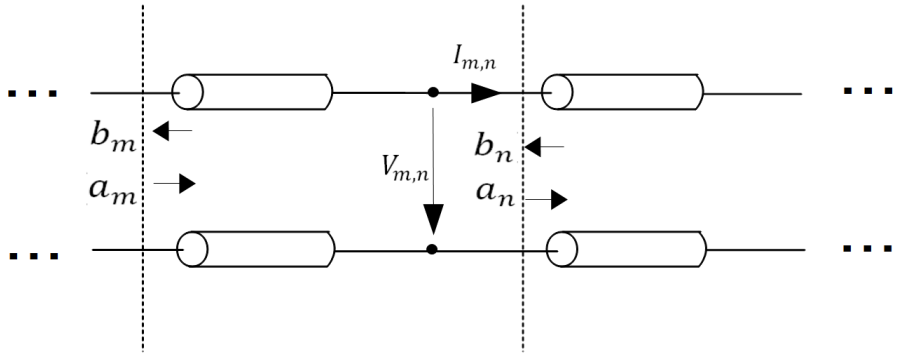

Figure 4.35: Schematic for analyzing wave amplitudes on transmission lines.

the relationships can be written in the form

$$\begin{cases} V_{m,n} = (a_m e^{-\gamma_m l_m} + b_m e^{\gamma_m l_m})\sqrt{Z_m} = (a_n + b_n)\sqrt{Z_n}, \\ I_{m,n} = (a_m e^{-\gamma_m l_m} - b_m e^{\gamma_m l_m})\frac{1}{\sqrt{Z_m}} = (a_n - b_n)\frac{1}{\sqrt{Z_n}}, \\ V_{0,1} = (a_0 + r a_0)\sqrt{Z_0}, \\ I_{0,1} = (a_0 - r a_0)\frac{1}{\sqrt{Z_0}}, \end{cases} \tag{4.59}$$

where $\gamma_m = \alpha_m + j\beta_m$, $V_{0,1}$ and $I_{0,1}$ are the voltage and the current at the input ports of the system, Z_m is the characteristic impedance of TL m. $V_{0,1}$ and $I_{0,1}$ can be determined by the reflection coefficient r, which can be obtained by either simulations or measurements. Consequently, the wave amplitudes on the following transmission lines can be calculated step by step through the above equations. The nodes between neighboring transmission lines with shunt connections should be analytically solved by Kirchhoff laws, such as the node between TL 2 and TL 4 in Figure 4.34. The other important consideration is the use of the virtual grounds. In consequent continuation of the above considerations, for example, the circuit model of the even mode excitation is simplified in the configuration shown in Figure 4.36, where Z_e is the equivalent even mode impedance of the array. This equivalent impedance can be solved from

$$Z_{e,o} = Z_0 \frac{1 + r_{e,o}}{1 - r_{e,o}}, \tag{4.60}$$

where $r_{e,o}$ is the corresponding equivalent even or odd mode reflection coefficient, which can be calculated through

$$\begin{cases} r_o = S_{11} - S_{12} \\ r_e = S_{11} + S_{12}, \end{cases} \tag{4.61}$$

where S_{11} and S_{12} are the elements of the array S-parameters. Since $Z_{e,o}$ is obtained from the antenna array S-parameters, the current distribution between TL 2 and TL 4 is calculated and the calculation can be continued. Similarly, the wave amplitudes of the odd

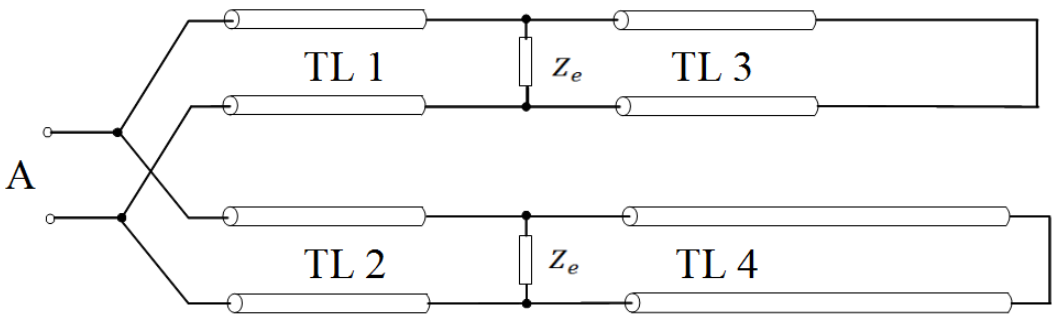

Figure 4.36: Simplified analysis model for the even mode excitation.

port excitation can be found through creating a similar simplified model and by performing the step-wise calculations.

The wave amplitudes on TL3 and TL 4 are solved through the discussed approach. Based on these amplitudes according to equation (4.57), the radiation pattern correlation coefficient is calculated through equation (4.45) together with the simulated S-parameters from CST MWS. The estimation results within the frequency range 2.42 GHz to 2.52 GHz are shown in Figure 4.37. For comparison, the results directly obtained from the simulated far field patterns through equation (3.59) and calculated results using only S-parameters are also plotted. It can be noticed that good agreement between the calculation based on the far field patterns, which is used as a reference, and the proposed approach is found. The conventional method based on S-parameters only owns low accuracy when the antenna array and the matching and decoupling network are lossy.

4.6.4 Analysis of Coupling Loss for the Compact Array Based on Multiport Conjugate Matching

In Section 4.3, the theoretical basics and the operation principle of the matching and decoupling network based on multiport conjugate matching have been introduced. There is also an equivalent virtual ground point formed when one of the ports is excited. The two virtual ground points are located at the antenna feeding points as shown in Figure 4.18. The matching networks are located between the input ports and the antenna feeding points and they do not contribute to the coupling loss, similar to the case of the network based on the eigenmode excitation method.

Firstly, the loss contribution consisting of the losses of the radiation elements is analyzed. The current distribution is estimated by equation (4.53), where the power loss is expressed by the input wave amplitudes and the S-parameters. To relate the loss with the input wave amplitudes, the relationship

$$\vec{v} = \begin{bmatrix} v_1 \\ v_2 \end{bmatrix} = (\mathbf{I} - \mathbf{S}_{22,N}\mathbf{S}_{\text{ant}})^{-1}\mathbf{S}_{21,N} \begin{bmatrix} a_1 \\ a_2 \end{bmatrix} \tag{4.62}$$

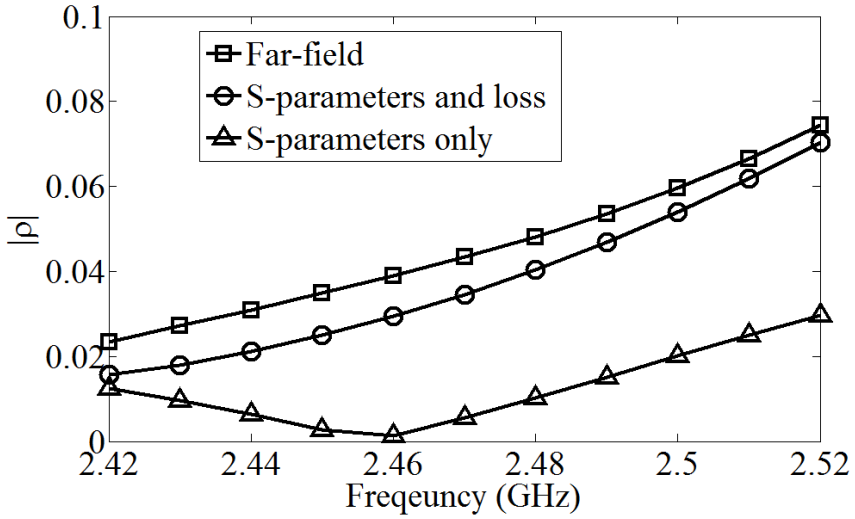

Figure 4.37: Pattern correlation coefficient of the array based on the eigenmode excitation method calculated with different approaches.

is utilized, where a_1 and a_2 are wave amplitudes at the input ports, v_1 and v_2 are the input wave amplitudes of the antenna array. Since the rods consist of copper of which the conductivity is 5.8e7 S/m, the calculated coupling loss contribution from the radiation elements $\frac{P_{\text{loss}}(a_1 a_2^*)}{\frac{1}{2}a_1 a_2^*}$ is found to be 0.038%, which is negligible.

The other contribution to the coupling loss is from the matching and decoupling network, which is simplified to the configuration shown in Figure 4.38, where the virtual ground point is used for simplification. The step-wise analysis approach discussed in the previous subsection is again utilized in the analysis of the wave amplitudes on the transmission lines. Then, the coupling loss power $P_{\text{loss}}(a_1 a_2^*)$ is calculated. The calculated radiation pattern correlation coefficients between 2.42 GHz and 2.52 GHz from equation (4.45), from the direct calculation with the simulated far field patterns and from the approximation results with S-parameters only are plotted in Figure 4.39. Very good agreement is achieved between the proposed estimation method and the reference (direct calculation through the simulated far field patterns). Without consideration of the coupling loss, the calculated result is quite inaccurate. For example, at 2.48 GHz the calculated correlation coefficient is almost 0 based on S-parameters only, while the actual value is around 14%. Additionally, at this frequency, the results based on the proposed method and the reference show the best agreement, which is due to the fact that good approximation accuracy of the virtual ground is achieved at this frequency (lowest coupling coefficient S_{21} at this frequency). This also explains why the estimation results for the array with the eigenmode excitation method own better accuracy in a broad bandwidth.

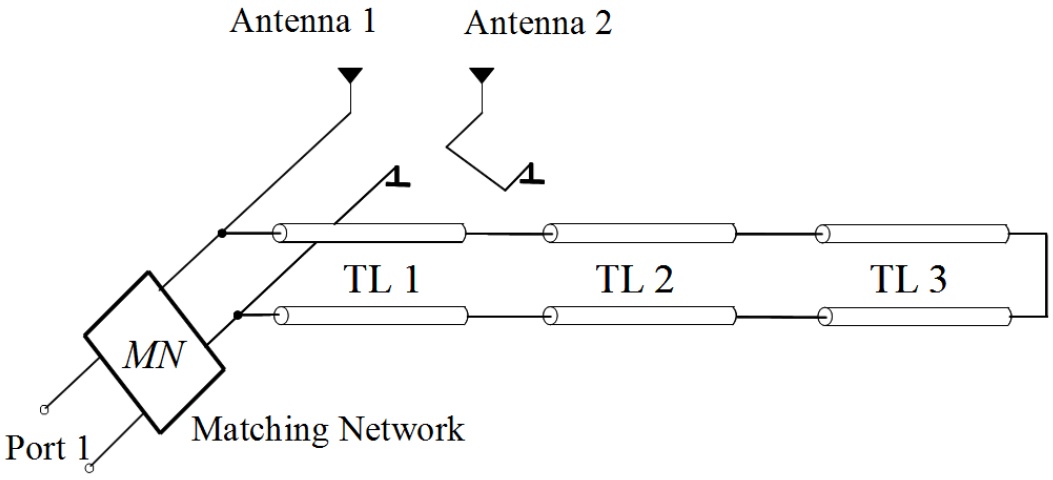

Figure 4.38: Simplified model of the transmission lines for the network based on the multiport conjugate matching.

4.6.5 Discussion

The proposed analysis approach based on simplified network modeling with the usage of virtual ground points and a step-wise analysis of transmission lines shows good efficiency and accuracy. Even though, it might be more convenient to perform the array simulation and use the simulated far field pattern to make the corresponding correlation computation directly, the presented method is still important due to the following facts. The method can be used to perform first step estimations, e.g., to decide which type of decoupling network should be implemented and in order to estimate the loss tolerance during choosing the substrate for the decoupling network. This analysis procedure is also helpful to gain insight into the physics of the problem. For the two monopole arrays, the analysis method makes it directly clear, why the array with eigenmode excitation, of which the coupling loss is quite low, has considerably lower pattern correlation than the array with multiport conjugate matching network.

To sum up, for compact lossy antenna arrays with lossy matching and decoupling networks, the pattern correlation cannot be simply approximated through the S-parameters. It was proved that the previous conclusions are not applicable for compact arrays with decoupling network. For the array based on the eigenmode excitation method, for instance the patterns of two ports can be uncorrelated even with very low radiation efficiencies, if the microstrip balun is replaced by a lossless balun. It was proved that it is of significance to analyze the coupling losses in the feeding network of compact antenna arrays. If low loss materials are used in the design, the influence from the coupling loss would be further reduced. The proposed analysis concept can also simply be implemented for decoupling networks including lumped elements or other techniques.

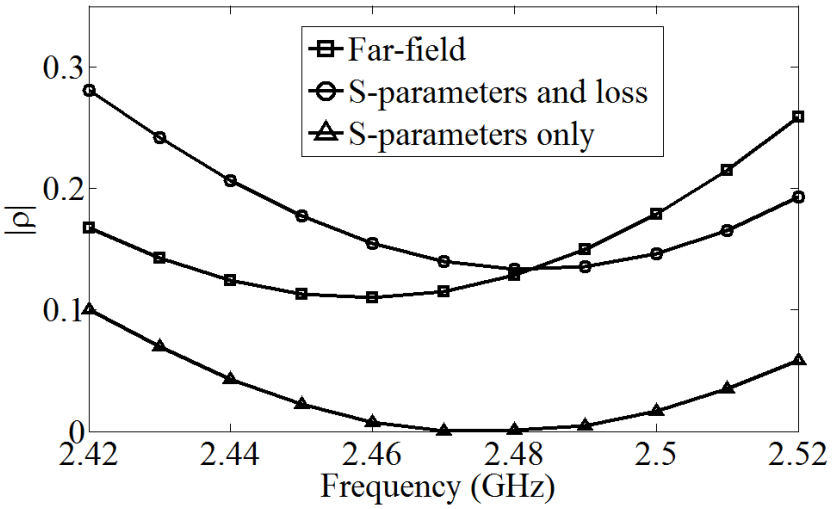

Figure 4.39: Pattern correlation coefficient of the array based on the multiport conjugate matching calculated with different approaches.

4.7 Beamforming Applications of Compact Monopole Arrays

MIMO systems would benefit considerably if compact antenna arrays would provide the function of beamforming, too [Li et al., 2010a, Zhang et al., 2012]. The previous sections proved that compact antenna arrays with certain decoupling techniques can achieve good power matching. In this section, studies with respect to beamforming applications of compact monopole arrays with decoupling networks are performed.

4.7.1 Decoupling Network for a Linearly Arranged Monopole Array

In Section 4.3, it was shown that the condition for multiport conjugate matching is $\mathbf{S}_{22,N} = \mathbf{S}_{\text{ant}}^{H}$. However, for linearly arranged compact monopole arrays with more than two radiation elements, the admittance matrix appears to be more convenient in the design as compared to the scattering matrix. According to the transformations in equation (2.33), the multiport conjugate matching condition is equivalent to $\mathbf{Y}_{22,N} = \mathbf{Y}_{\text{ant}}^{H}$. In order to design the decoupling network, the antenna array should be firstly modeled correspondingly. For a three-element monopole array, which is linearly aligned, the model shown in Figure 4.40 is utilized, where C1 and C2 are two-port networks, which indicate the coupling properties between the radiation elements. S1 and S2 are one-port networks. Actually, for such a three-element monopole array, C2 can be neglected. This property can be explained as the fact that the direct coupling from monopole 1 to monopole 3 is quite weak.

Based on this model, the proposed configuration of the decoupling network is shown in Figure 4.41. Network D1 is a two-port network which is used to neutralize the coupling effect from C1. To achieve this objective, the following conditions must be fulfilled by C1 and D1:

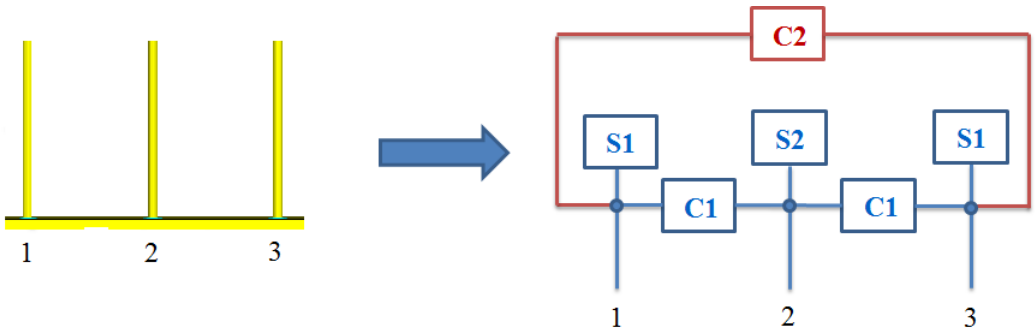

Figure 4.40: Model of a three-element compact monopole array.

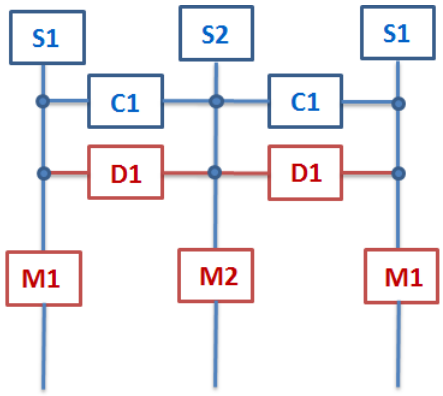

Figure 4.41: Matching and Decoupling approach for the network model shown in Figure 4.40.

- Network D1 must be lossless to satisfy the preliminary requirement of the multiport conjugate matching method.
- The real part of C1 should be 0 ($\mathrm{Re}[Y_{21,\mathrm{C1}}] = 0$), because D1 is lossless. This can be achieved by adding transmission lines at the antenna feed (similar to network C in Figure 4.15). Another choice is to modify the monopole length.
- The summation of the imaginary part of the admittance of C1 and D1 should be 0,

$$\mathrm{Im}[Y_{21,\mathrm{C1}}] + \mathrm{Im}[Y_{21,\mathrm{D1}}] = 0,$$

  which can be achieved by properly designing the decoupling network.

The function of the networks M1 and M2 is to match the three individual input ports. In the following, the realization of network D1 is discussed.

Once the coupling due to C1 has been neutralized by network D1, the joint point at the one side is equivalent to a virtual ground when the network is excited at the other

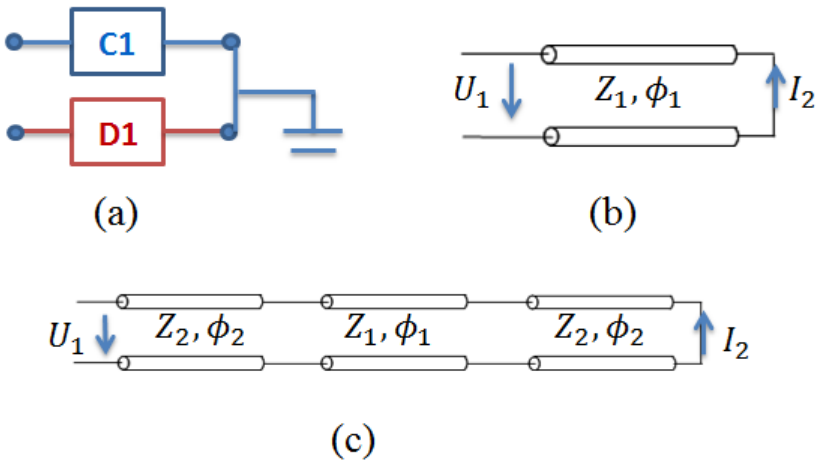

Figure 4.42: Realization of network D1: (a) schematic of the network; (b) realized with 1 piece of transmission line; (c) realized with 3 pieces of transmission lines.

side as shown in Figure 4.42(a). In this design, network D1 is realized with transmission lines. By definition, the mutual admittance is the ratio between the short circuit current on one port and the voltage on the other port. For a piece of transmission line as shown in Figure 4.42(b), the mutual admittance is expressed as

$$Y_{21,\mathrm{D1}} = \frac{I_2}{U_1} = -\frac{1}{Z_1 \sin\phi_1} j, \tag{4.63}$$

where Z_1 is the characteristic impedance of this transmission line and ϕ_1 is the electric length. As a result, by properly choosing the width and length of the microstrip lines, the decoupling can be achieved. It should be noticed that the value of ϕ_1 should avoid integer multiples of π. Otherwise, the transmission line would transform the virtual ground directly to the input and cause difficulties for the matching. The value of ϕ_1 should be close to $(2n+1)\frac{\pi}{4}$ and in this case, $Y_{21,\mathrm{D1}} \approx \frac{1}{Z_1} j$. Now, the mutual admittance depends only on the characteristic impedance, but extremely large or small values are possibly required, which cannot be fabricated due to a very large or very narrow line width. As a result, multi-section transmission lines are implemented such as the one shown in Figure 4.42(c). For this configuration, the mutual impedance can be expressed in the form of

$$\begin{aligned} Y_{21,\mathrm{D1}} =& \frac{I_2}{U_1} \\ =& \frac{1}{-Z_1 \cos^2\phi_2 \sin\phi_1 + \frac{Z_2^2}{Z_1} \sin^2\phi_2 \sin\phi_1 - 2Z_2 \cos\phi_2 \sin\phi_2 \cos\phi_1} j. \end{aligned} \tag{4.64}$$

By choosing $\phi_1 = \phi_2 \approx \frac{\pi}{4}$, the mutual admittance becomes $Y_{21,\mathrm{D1}} \approx \frac{Z_1}{Z_2^2} j$. Now, the admittance value is determined by both Z_1 and Z_2. By properly adjusting the ratio between them, the required mutual admittance can be generated and extremely wide or narrow microstrip lines are avoided.

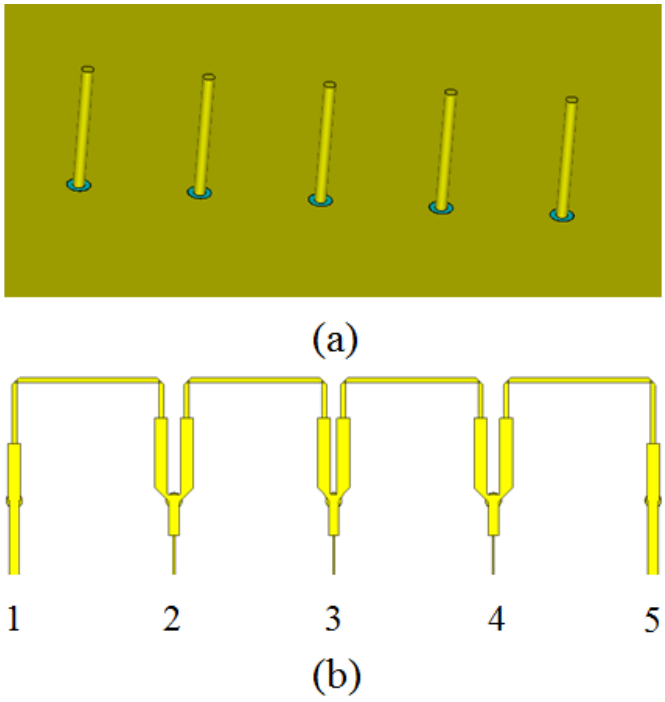

Figure 4.43: (a) Five-element compact monopole array; (b) decoupling network for this array.

Based on the above equations and the optimization process, a decoupling network for a five-element compact monopole array has been designed as shown in Figure 4.43. The center to center distance between the neighboring elements in the array is 25 mm. The transmission lines close to the antenna feeding points at the ports 2, 3 and 4 are coupled lines. During the design process, the network C2 shown in Figure 4.40 is neglected. However, there are still some direct couplings. To obtain better decoupling, the coupled lines are optimized to neutralize the effect as for C2. This decoupling network is built on a low loss substrate Rogers 4350. The simulated S-parameters in CST MWS are plotted in Figure 4.44. The matching bandwidth is quite limited for the ports connected with the radiation elements in the middle. The minimum bandwidth is around 16 MHz for -10 dB return loss measurement and 29 MHz for -6 dB return loss measurement. The coupling is below -12 dB between the input ports. In the following, the beamforming property of this array is investigated.

4.7.2 Beamforming Applications of Linearly Arranged Monopole Array

Based on the Huygens' Principle, the far field radiation pattern can be calculated through the equivalent electric and magnetic currents corresponding to the tangential magnetic and electric fields on a closed surface enclosing the antenna elements [Rumsey, 1959]. For antennas made from PEC, on the Huygens' surface the tangential component of the electric fields is 0 and only the electric current density $\vec{J}$ is taken into account for calculating

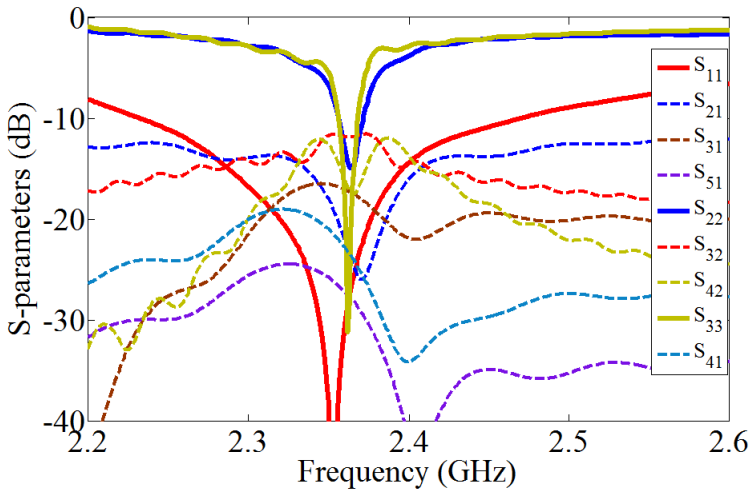

Figure 4.44: Simulated S-parameters of the five-element compact monopole array with matching and decoupling networks as shown in Figure 4.43.

the far fields (the feeding gap is neglected). The vector potential $\vec{A}$ is applied to find the far fields, and it is defined via

$$\vec{H} = \frac{1}{\mu} \nabla \times \vec{A}, \tag{4.65}$$

where $\vec{H}$ is the magnetic field due to the corresponding electric current source and μ is the permeability of the environment. By solving the Maxwell equations, the electric field is written in the form of [Balanis, 2005]

$$\vec{E} = -j\omega\vec{A} - j\frac{1}{\omega\mu\varepsilon}\nabla(\nabla \cdot \vec{A}), \tag{4.66}$$

where ε is the environment permittivity and ω is the angular frequency. Once the vector potential $\vec{A}$ has been found, the electromagnetic fields due to certain electric current sources can be derived. $\vec{A}$ is calculated through

$$\vec{A} = \frac{\mu}{4\pi} \iiint_V \frac{e^{-jkR}}{R} \vec{J} dV', \tag{4.67}$$

where $k = \omega\sqrt{\mu\varepsilon}$ and R is the distance between the corresponding current source point and the observation point.

The currents on the monopoles are assumed to be standing waves and distributed in a sinusoidal form as shown in Figure 4.31. It is also assumed that the currents are evenly distributed on the rods. In order to generate the beamforming patterns for such a linearly aligned monopole array, certain current distributions at the antenna feeds should be generated.

The currents at the feeding points can be expressed in the form of $\vec{I} = [I_1, I_2, I_3, I_4, I_5]^T$. Based on the previous knowledge, the current vector can be calculated through

$$\vec{I} = \frac{1}{\sqrt{Z_0}}(\mathbf{I} - \mathbf{S}_{\text{ant}})\vec{v}, \tag{4.68}$$

where $\vec{v}$ is the input wave vector at the array feeding, which is expressed as

$$\vec{v} = (\mathbf{I} - \mathbf{S}_{22,N}\mathbf{S}_{\text{ant}})^{-1}\mathbf{S}_{21,N}\vec{a}, \tag{4.69}$$

where $\vec{a}$ is the input vector of the system with decoupling network. According to the above equations, the relationship between the current vector at the monopole feeds and the input vector can be found as

$$\vec{a} = \sqrt{Z_0}\mathbf{S}_{21,N}^{-1}(\mathbf{I} - \mathbf{S}_{22,N}\mathbf{S}_{\text{ant}})(\mathbf{I} - \mathbf{S}_{\text{ant}})^{-1}\vec{I}. \tag{4.70}$$

The current vector is calculated through the required beamforming directions, e.g., if the beamforming at broadside is desired, the currents should be equal in both amplitude and phase. In consequence, the required input wave amplitudes can be calculated. In the receiving mode, it is also applicable to estimate the directions of the incoming signals. By summing up the received signals with certain weights, the signal from a certain direction can be obtained. It is calculated through

$$y(t) = \sum_{i=1}^{N} w_i u_i(t), \tag{4.71}$$

where w_i is the ith element of the normalized required input vector for a certain beamforming direction obtained from equation (4.70).

The beamforming applications for compact antenna arrays need to be specially treated due to the following aspect. In equation (2.28), the array factor of linearly arranged antennas has been derived. Here, by setting $\psi = -\frac{2\pi}{\lambda}d\cos\alpha$, the array factor is written in the form of

$$F_A(\psi) = \sum_{i=1}^{N} e^{j(N-1)(\psi+\triangle\beta)}. \tag{4.72}$$

In the first example, the radiation elements are considered to be excited in phase ($\triangle\beta = 0$). It is noticed that $F_A(\psi)$ is periodic and one period is 2π. The range of ψ is called the visible region, which is $[-\frac{2\pi}{\lambda}d, \frac{2\pi}{\lambda}d]$. The visible region depends on the ratio between the antenna spacing d and the wavelength λ. When $\frac{d}{\lambda} = 0.5$ the visible region is exactly one period of $F_A(\psi)$. For compact antenna arrays, the value of $\frac{d}{\lambda}$ is very small, so that the visible region is quite limited, which means that the antenna array might not achieve the desired beamforming directivity for in-phase excitation. For example, $F_A(\psi)$ is plotted in Figure 4.45 for a five-element antenna array with 25 mm element separation and for a three-element antenna array with 50 mm element separation at 2.4 GHz. The area with dashed lines indicates the visible region. With reducing the distance between

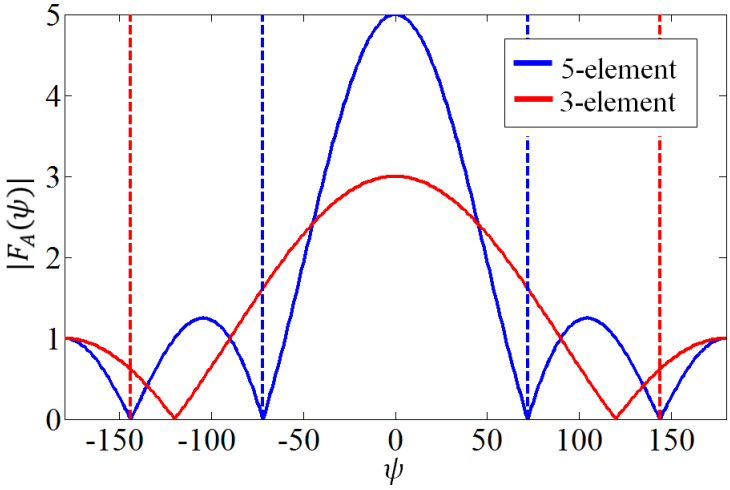

Figure 4.45: Amplitude of $F_A(\psi)$ for the arrays with three and five elements, the dashed lines indicate the corresponding visible region.

the antenna element, $F_A(\psi)$ in the visible region becomes more flat and the beamforming performance degrades. When the element spacing becomes 0, the directivity of the isotropic antenna array becomes 0 dB. To illustrate this mathematically, the directivity of the array can be expressed by $F_A(\psi)$. In equation (2.26), the radiated electric field is written as a function of α within the plane C in parallel with the array alignment. In the following, the directivity is referred to a 2D directivity D' in a certain plane C. The radiated power density in direction to the angle α is

$$S(\alpha, C) = \frac{1}{2Z_s}|\vec{E}_1(\alpha, C)|^2|F_A(\alpha)|^2, \tag{4.73}$$

where $\vec{E}_1(\alpha, P)$ is the radiated electric field of the first element. Then, D' is calculated through

$$D'(C) = \frac{2\pi \max\left(S(\alpha, C)\right)}{\int_\alpha S(\alpha, C)d\alpha}. \tag{4.74}$$

If the radiation pattern of the elements is assumed isotropic, based on the above equations, the direcitvity can be written in the form of

$$D'(C) = \frac{\triangle\psi \max(|F_A(\psi)|^2)}{\int_\psi |F_A(\psi)|^2 d\psi}, \tag{4.75}$$

where $\triangle\psi$ is the range of ψ. The calculated result of the above equation for the five-element compact array with 25 mm spacing is 2.2 for the broadside direction. The result of a three-element array with 50 mm spacing between the elements is around 2.5, which is higher than the case with five elements. As a result, for a linearly aligned antenna array, more excited radiation elements in the array might lead to a lower directivity when the

elements are compactly placed. For validation, simulations have been performed by utilizing the post processing calculation function named 'far field array' in CST MWS, which is a purely mathematical tool for array far field calculations based on a single element, where the mutual coupling between elements is not considered. Figure 4.46 shows the simulated results of two different scenarios, for the same length of 100 mm of the array. With three radiation elements the achieved directivity is found 0.76 dB higher than in the case of five elements. To sum up, in equation (4.68), the required current vector for broadside beamforming should be $\vec{I} = [1, 0, 1, 0, 1]^T$. Similarly, when beam steering is utilized, the same procedure should be applied and the corresponding current vector for beamforming at a particular direction should be achieved. In Figure 4.47, some beamforming results from simulations are plotted based on the designed five-element monopole array and the above discussed method. Very good beamforming performance is demonstrated. Recently, compact antenna arrays are widely utilized for the design of the 'super directive' antennas, of which the beamforming at end-fire direction is realized [Ivrlac and Nossek, 2010].

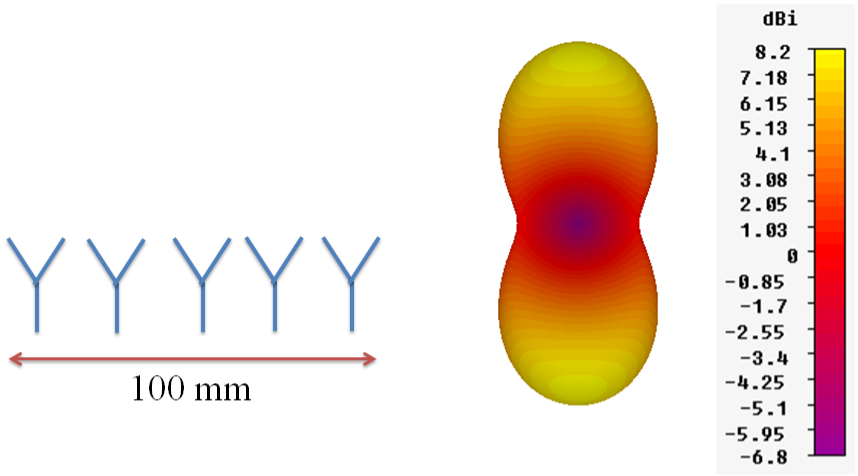

(a)

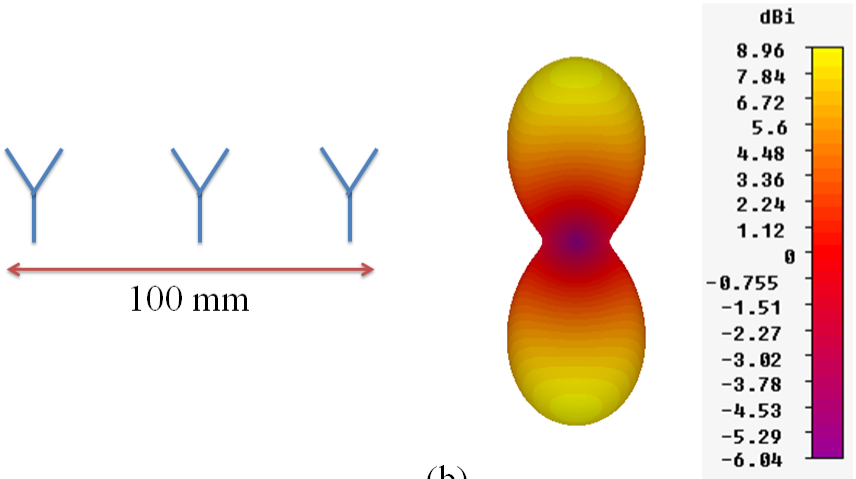

(b)

Figure 4.46: Beamforming directivity at broadside: (a) five radiation elements; (b) three radiation elements.

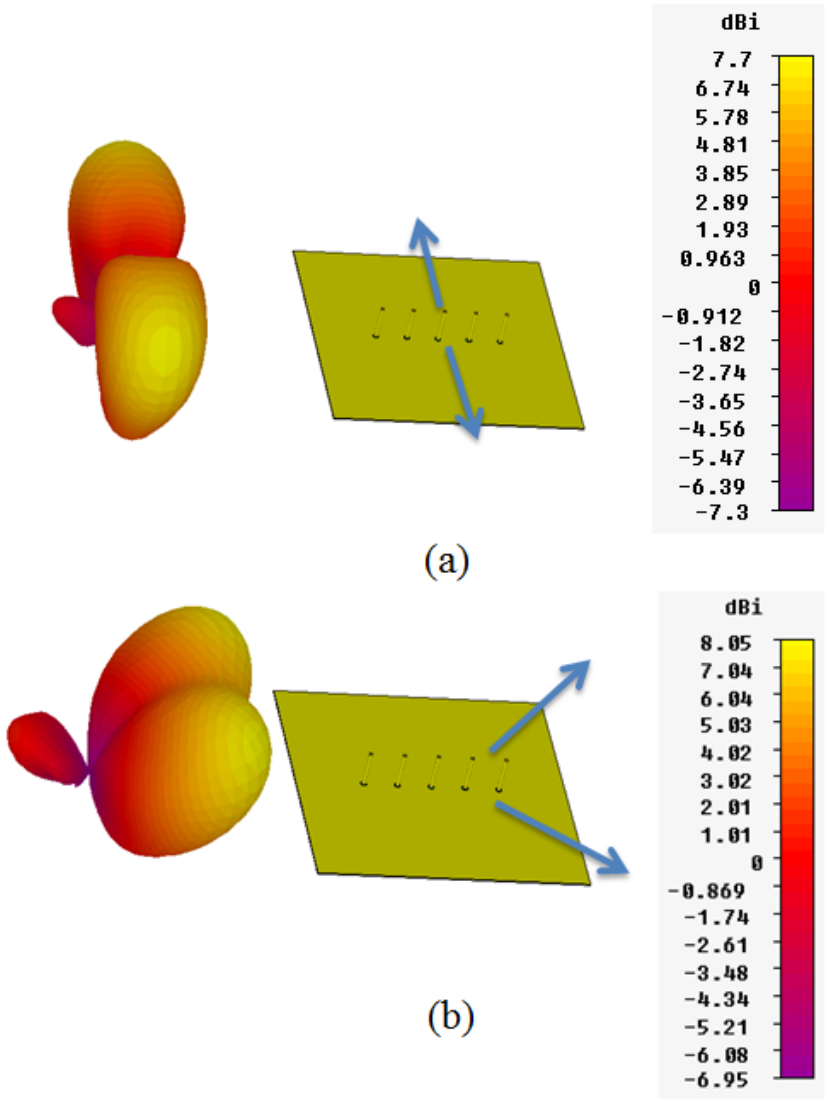

Figure 4.47: Simulated 3D far field radiation patterns of the beamforming results for different directions.

5 Design of Compact Printed Antenna Arrays

In the previous chapter, matching and decoupling networks for designing compact antenna arrays have been introduced. The advantage of this decoupling approach is that in theory it is applicable for all types of antenna arrays, of which analytical solutions are obtained based on the scattering matrix of the antenna array. However, the implementation of the additional network requires more space, which is often not available in modern communication devices such as smart phones. For low profile antenna designs, planar technologies are often deployed. Therefore, in this chapter, several novel approaches for designing compact printed antenna arrays are investigated. Through these methods, compact printed antenna arrays are designed and excellent performance such as broad matching and decoupling bandwidth is achieved. Some of the results obtained in this chapter have been published in [Wang et al., 2014a,c,d, 2015b,c].

5.1 Compact Two-Element Printed Monopole Array with Partially Extended Ground Plane

In this section, according to the particular features of printed monopoles, novel decoupling and matching strategies for two-element compact printed monopole arrays are investigated, of which the obtained operation bandwidth is much broader as compared to other decoupling methods and the antenna elements as well as the decoupling structure are quite simple for fabrication. The proposed antenna array operates around 6 GHz.

5.1.1 Basic Design Concept

The substrate Rogers 4350 is utilized for all the printed antenna designs. As mentioned before, the dielectric constant of such a material is 3.66, $\tan\delta = 0.004$, the thickness is 0.762 mm, and the metallization thickness is 0.018 mm.

The proposed decoupling structure for the printed monopole array is realized as a partially extended ground (PEG) plane as shown in Figure 5.1, which is extended from the middle of the ground layer. In order to illustrate its function, simulations with and without the PEG structure have been carried out in CST MWS. The simulation results are plotted in Figure 5.2. It shows that in the operation band, the coupling coefficient between the monopoles is reduced from -9 dB to -20 dB by implementing the PEG structure. In the following, the PEG operation principle is analyzed.

Since the monopoles are symmetrically placed, the even and odd mode excitation analysis is utilized. The equivalent one-port model for the analysis is shown in Figure 5.3. The equivalent reflection coefficients for the two modes are given in equation (4.61). When the two ports are excited with the same amplitude in phase, in the symmetry plane a PMC wall is formed as shown in Figure 5.3(b). On the other hand, if the two ports are excited with the same amplitude out of phase, a PEC wall is formed. If the two ports are decoupled, $S_{21} = 0$, the one-port equivalent reflection coefficients of the even and odd modes should be equal, i.e., $r_e = r_o$. The only difference of the even and odd equivalent circuits is the

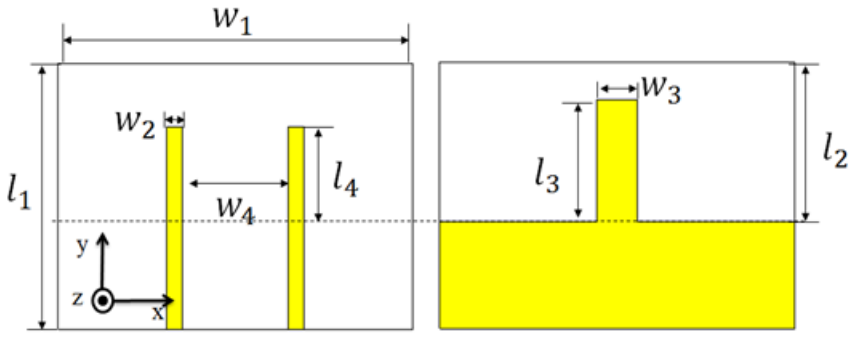

Figure 5.1: Printed two-port monopole array with decoupling structure: $l_1 = 25, l_2 = 15, l_3 = 11.5, l_4 = 9, w_1 = 35, w_2 = 1.6, w_3 = 4, w_4 = 10.4$, unit: mm.

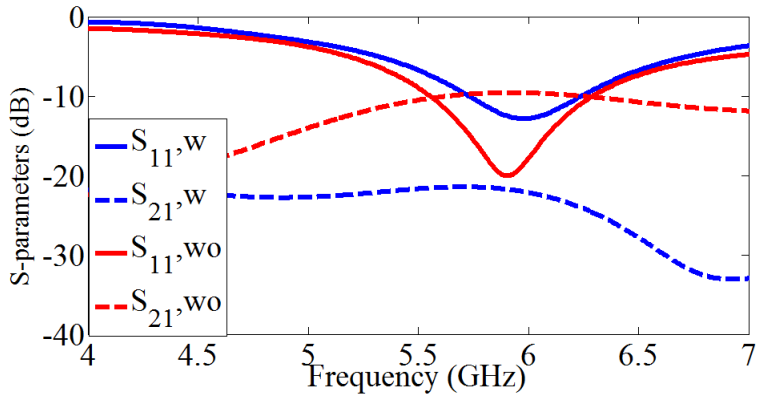

Figure 5.2: Simulated S-parameters of the model shown in Figure 5.1 with (w) and without (wo) the PEG structure.

PMC and PEC wall in the symmetry plane. The monopoles with the ground plane and the PEC or PMC wall can be treated as lossy transmission lines, where the losses are due to the radiation. If the substrate height, which is marked as h in Figure 5.3, is much smaller than the distance from the inner edge of the monopole to the symmetry plane, which is marked as d in Figure 5.3, the electric fields are mostly confined around the edge of the PEG and the PEC or PMC plane should have less effect on the field distributions. Then, the even and odd mode equivalent circuits are equivalent and $r_e \approx r_o$ is obtained, so that the ports are decoupled by the PEG structure. The distance from the edge of the PEG to the monopole inner edge is marked as c as shown in Figure 5.3(b). Simulations are carried out with different values of d when the values of h and c are fixed. The simulated coupling coefficient is plotted in Figure 5.4. With increasing d, the coupling between the ports is reduced. Similar simulations have been performed by changing c with fixing h and d. The simulation results are plotted in Figure 5.5. With increasing c, the coupling coefficient increases. As a result, for a certain substrate thickness h and antenna spacing $2d$, c should be as small as possible in order to obtain better decoupling between the ports. However, if

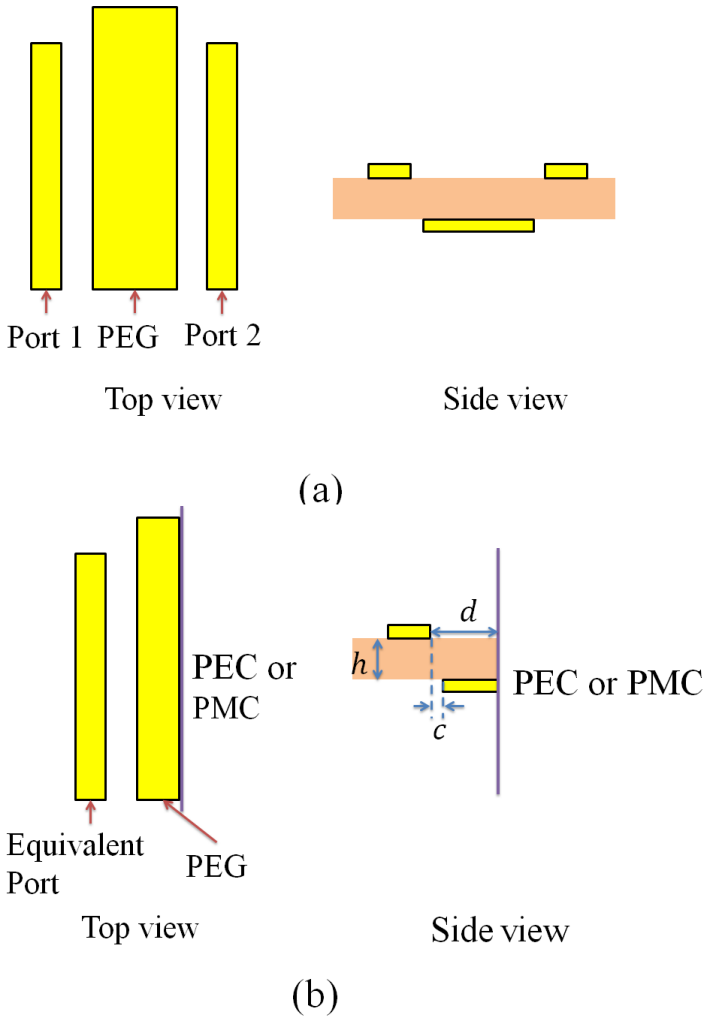

Figure 5.3: (a) Top view and side view of the printed monopole array with PEG; (b) equivalent structure with PMC and PEC wall for even and odd mode excitation.

c is too small, most of the electric field is bound around the PEG and the radiated power is reduced, which leads to a relatively high quality factor and in consequence a low operation bandwidth. Therefore, a certain distance should be maintained between the monopoles and the PEG. In addition, the input matching is achieved without extra networks. The monopole and the PEG together with the gap between them form a piece of transmission line. It transforms the open circuit to an inductive reactance at the antenna input, which compensates the parasitic capacitance at the radiation aperture located on the side of the monopole without the PEG.

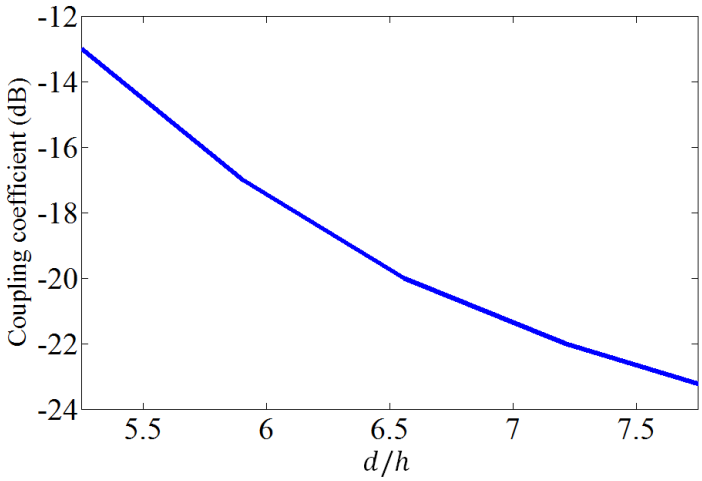

Figure 5.4: Coupling coefficient between the two monopoles with different values of d/h.

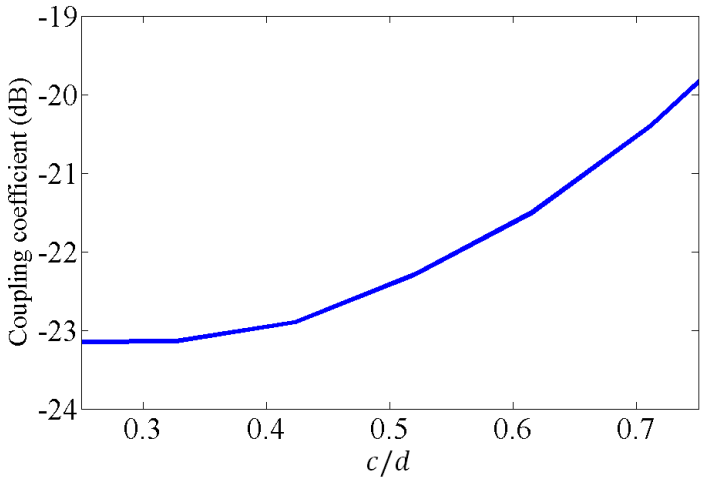

Figure 5.5: Coupling coefficient between the two monopoles with different values of c/d.

5.1.2 Design and Measurement of a Compact Printed Monopole Array with PEG Structure

In Figure 5.2, the matching bandwidth is reduced after implementing the PEG structure, resulting in around 300 MHz centered at 6 GHz. It is found that increasing the length of the substrate is an efficient approach for improving the matching bandwidth. For example, if l_1 is increased up to 60 mm, much broader matching bandwidth is achieved. The reason is that the monopole excites surface wave propagation along the edge of the ground, which becomes part of the radiation aperture. Therefore, the more power is radiated, the larger bandwidth is obtained. Based on the above discussions, the manufactured antenna array with long substrate is shown in Figure 5.6 and the measured S-parameters are shown in Figure 5.7. The matching bandwidth is enhanced by a factor of 5 (up to 1.5 GHz).

However, the antenna array now is dependent on the substrate dimensions and the far field radiation pattern becomes irregular due to the long substrate. For example, the simulated 3D far field radiation patterns at 6 GHz are shown in Figure 5.8(a) and 5.8(b) for the arrays with short and long substrate, respectively. In Figure 5.8(a), the direction of the main lobe of the far field pattern is almost perpendicular to the monopole axis, which is similar to the patterns of general printed monopoles. On the other hand, in Figure 5.8(b), the main lobe is shifted towards the rear side of the board, which might not be desirable. As a result, in order to maintain the large matching bandwidth and to obtain a desired far field radiation pattern together with a compact size, the structure shown in Figure 5.9 is exploited. Two cutting slots are implemented at the two edges of the ground plane. The function of these slots is to increase the effective electric length of the ground plane and in consequence increases the matching and decoupling bandwidth. Meanwhile, a U-shaped slot is implemented close to the edge of the PEG in order to enhance the decoupling between the two monopoles [Lin et al., 2013]. The manufactured prototype is shown in Figure 5.10 and the measured S-parameters are shown in Figure 5.11. The measured matching bandwidth remains broad which is from 5.1 GHz to 6.6 GHz and the coupling is further reduced, which is below -30 dB at 6 GHz. The simulated 3D far field radiation pattern is plotted in Figure 5.8(c). Compared to Figure 5.8(b), the pattern main lobe is no longer too much shifted to the rear part. The calculated result of the radiation pattern correlation coefficient between the two ports is 0.079 and 0.059 for 5.35 GHz and 6 GHz, respectively. So, it can be concluded that very promising MIMO performance is obtained. The simulated radiation efficiency in the operation band is above 92%, since low loss material is utilized as the substrate in this design. The simulated antenna gain is 4.55 dBi and 4.26 dBi at 5.35 GHz and 6 GHz, respectively.

In order to check the degree of agreements between the simulation and the measurement results, the antenna far field radiation pattern has been measured in the antenna measurement chamber at the chair of High-Frequency Engineering at Technische Universität München. In Figure 5.10, two SMA connectors have been implemented in order to connect the measurement devices to the proposed monopole array. Because the dimension of the antenna array is small compared to the mounting facilities in the measurement, the radiation patterns are distorted by all these components. As a result, for the comparisons between simulation and measurement results, a particular simulation model in which the SMA connectors and coaxial cables are considered as shown in Figure 5.12, has been created and simulated as a reference instead of the previous model. The far field patterns in certain cuts from the measurements and the simulation results at 5.35 GHz are shown in Figure 5.13(a) and 5.13(b), the coordinates are defined in Figure 5.9. Figure 5.13(c) and 5.13(d) depict the far field patterns at 6 GHz. Good agreement between the measurement and simulation results is found. The differences in the patterns can be due to the reflections from the feeding cable and mounting components as well as the shadowing area due to the carrier platform. According to the symmetric alignment of the radiation elements in the array, the other port shows a similar far field radiation pattern which is the image of the pattern shown in Figure 5.12 corresponding to the *yoz* plane. In real application environments, the array would operate much more similar to the simulation model shown in Figure 5.9, since there would be no additional components such as the ones used for the measurements.

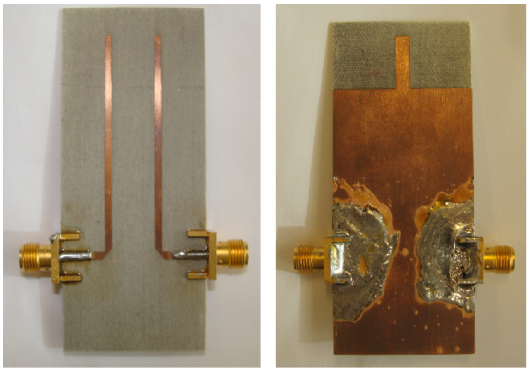

Figure 5.6: Photograph of the fabricated printed monopole antenna array with long substrate.

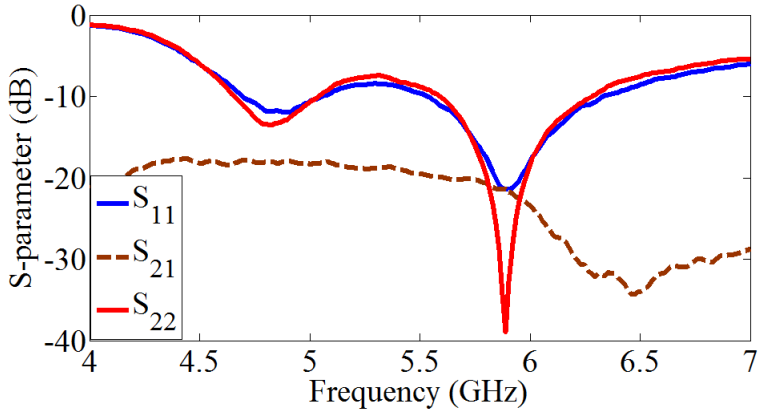

Figure 5.7: Measured S-parameters of the printed monopole antenna array with long substrate.

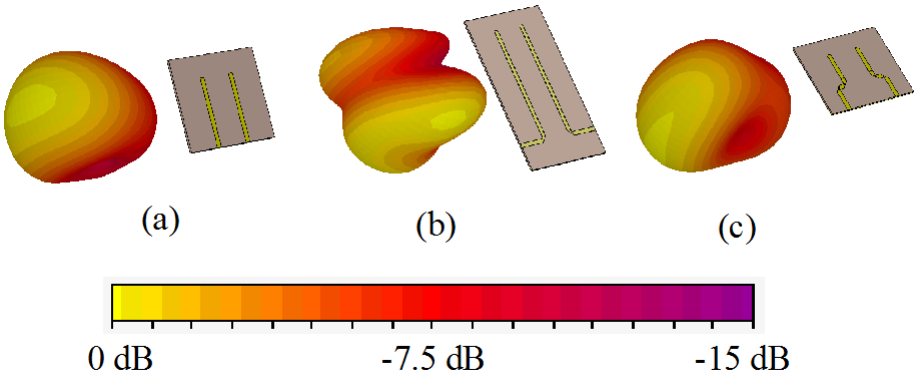

Figure 5.8: Simulated 3D far field radiation patterns at 6 GHz with left port excited.

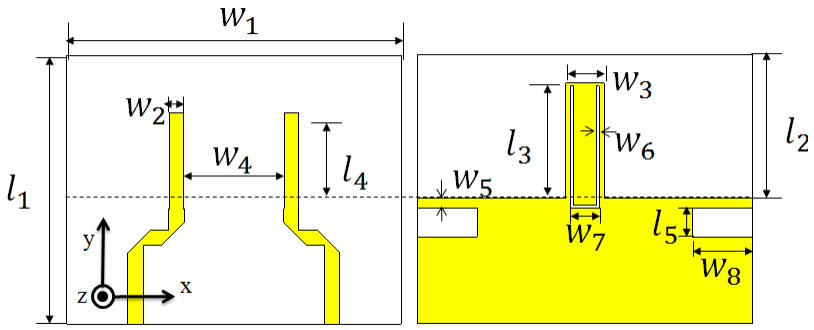

Figure 5.9: Compact two-element printed monopole array with the PEG structure and short substrate: $l_1 = 25, l_2 = 15, l_3 = 11.5, l_4 = 9, w_1 = 35, w_2 = 1.6, w_3 = 4, w_4 = 10.4$, unit: mm.

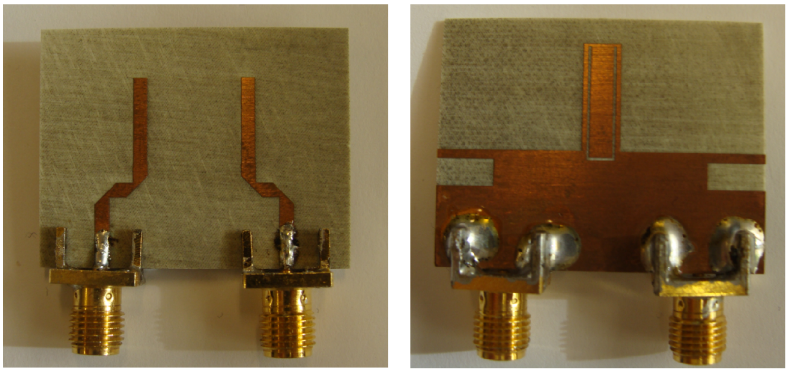

Figure 5.10: Photograph of the fabricated monopole antenna array with short substrate.

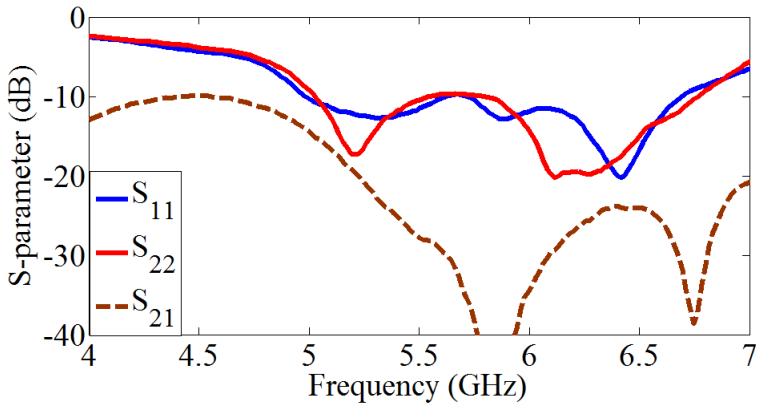

Figure 5.11: Measured S-parameters of the printed monopole antenna array with short substrate.

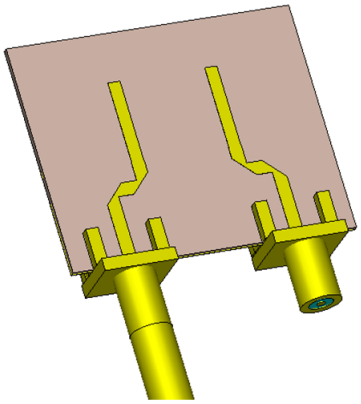

Figure 5.12: Simulation model with the SMA connectors and coaxial cables.

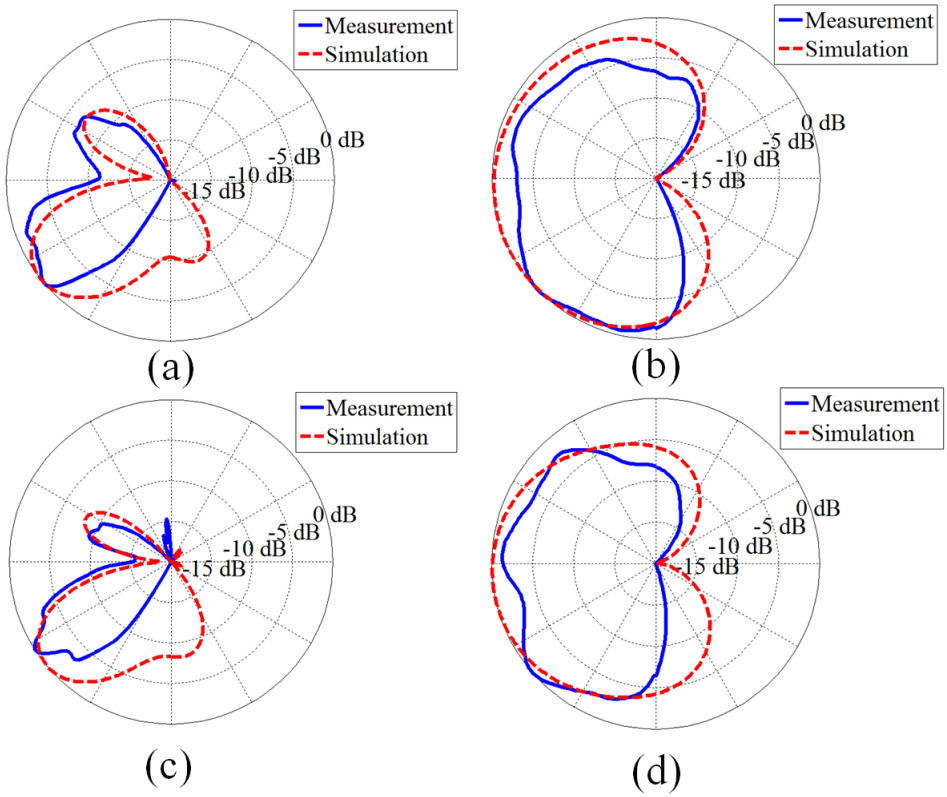

Figure 5.13: Measured and simulated far field patterns. (a) and (b): 5.35 GHz; (c) and (d): 6 GHz. (a) and (c): $\theta = 90°$ cut; (b) and (d): $\phi = 30°$ cut.

5.2 Compact Three-Element Printed Antenna Array

In this section, a compact three-element printed antenna array size is designed, manufactured and measured. By combining two different types of the radiation elements, broad matching and decoupling bandwidth is achieved and good MIMO performance is obtained.

5.2.1 Design of the Radiation Elements

In the previous section, a two-element compact printed monopole array was introduced and the PEG structure shows promising performance for the purpose of decoupling. However, it is difficult to realize a three-element compact printed antenna array with a similar method by inserting a third antenna in the middle and using two PEG structures as shown in Figure 5.14. For the monopole in the middle quite little power can be radiated to the space, due to the existence of the two PEG structures which constrain most of the fields. Consequently, the input impedance of this monopole is located almost at the outer bound in the Smith Chart and its matching is difficult. Although it is possible to match it at a certain frequency, the operation bandwidth is limited. Considering the main radiation directions of the monopoles which are perpendicular to the monopole axis, there is still one direction left for the third radiation element, which is the direction of the monopole axis. The planar quasi-Yagi antenna is a suitable candidate for the third radiation element in this configuration [Deal et al., 2000]. Generally, the planar quasi-Yagi antenna contains a radiation driven dipole, planar directors, a microstrip balun and the matching transmission line. However, these components occupy considerable space, which is not suitable for compact array designs. Therefore, the structure in the middle of the array shown in Figure 5.15 is exploited to reduce the space occupation. The radiation driven dipole is formed by two pieces of strip lines on the top and bottom layers which are fed by the feeding strip line on the top and a strip line extended from the ground plane, respectively. Then, the bulky microstrip balun is avoided. The two ends of the driven dipole are bent up in order to further reduce the lateral dimension. Above the dipole, two pieces of strip directors are implemented on the top and bottom layers of the substrate, respectively. However, the drawback of utilizing this configuration is that the achieved matching bandwidth is less than in conventional designs of the planar quasi-Yagi antenna. Since the quasi-Yagi antenna occupies much space in lateral direction, the overall size of the monopole element should be reduced as well. For this purpose, the monopoles are placed much closer to the PEG. However, this brings problems for the antenna input matching. As discussed before, the monopole and the PEG form a guiding structure which is longer than a quarter of the effective wavelength. It transforms the open circuit to an equivalent inductor, which is in parallel with the equivalent input admittance due to the radiation slot at the antenna input. The characteristic impedance of a transmission line is calculated through [Pozar, 2011]

$$Z_c = \sqrt{\frac{R' + j\omega L'}{G' + j\omega C'}}, \tag{5.1}$$

where R' is the series resistance due to the finite conductivity, G' is the shunt conductance due to the dielectric loss, L' is the self inductance of the conductors and C' is the shunt

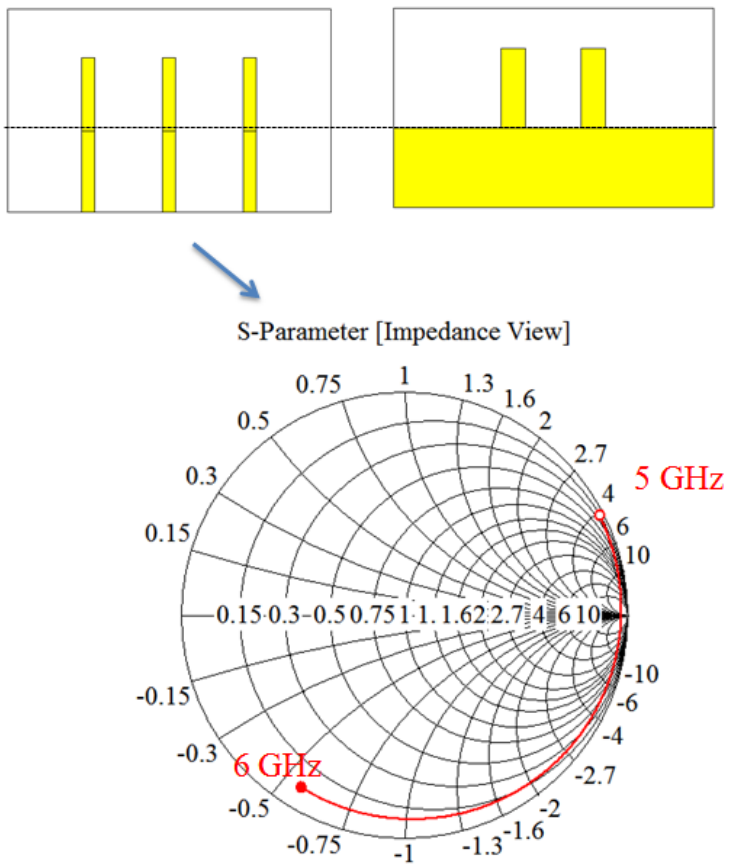

Figure 5.14: Three-element compact printed monopole array with two PEG structures and the simulated input impedance of the middle port shown in a Smith Chart.

capacitance between the conductors. Normally, the loss in transmission lines is quite low, so that the characteristic impedance can be approximated by $\sqrt{\frac{L'}{C'}}$. L' and C' depend on the dimension of the guided structure, e.g., if the distance between the conductors is becoming shorter, C' increases. Then, the characteristic impedance is smaller. In consequence, the equivalent inductance transformed from the open circuit is also decreased according to the impedance transformation technique. Generally, the small inductance in shunt leads to poor matching. As a result, the modified monopoles, of which the length is reduced while the width is increased, are utilized at the two sides of the array as shown in Figure 5.15. Increasing the width of the monopole enlarges the parasitic capacitance around the feed of the monopoles, which compensates the equivalent inductance and improves the matching. Another observation is that a shorter monopole length is beneficial for reducing the mutual coupling between the radiation elements.

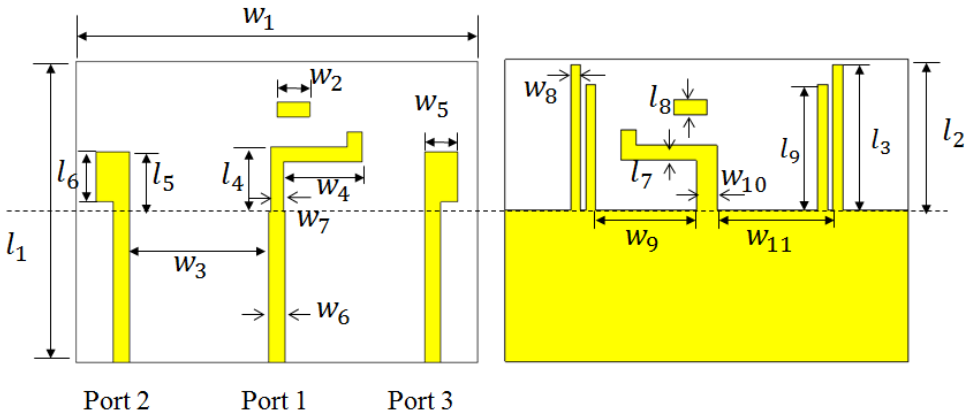

Figure 5.15: Printed three-port compact antenna array with decoupling structures: $l_1 = 30, l_2 = 15, l_3 = 14.5, l_4 = 6.5, l_5 = 6, l_6 = 5, l_7 = 1.5, w_1 = 40, w_2 = 3.25, w_3 = 13.9, w_4 = 7.875, w_5 = 3.3, w_6 = 1.6, w_7 = 1.25, w_8 = 1, w_9 = 10, w_10 = 2w_11 = 11.5$, unit: mm.

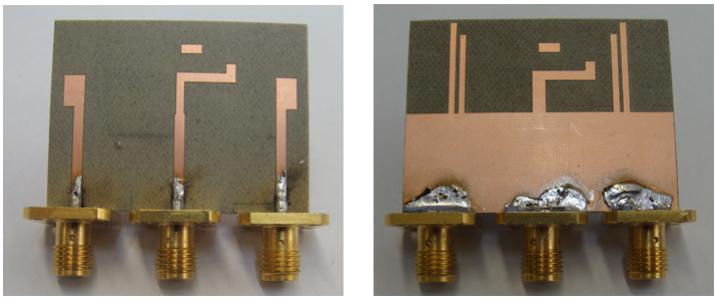

Figure 5.16: Photograph of the fabricated printed three-port compact antenna array.

5.2.2 Simulations and Measurements

The input matching of the three ports has been enhanced by optimizing the dimensions of all the radiation elements and no additional matching circuit has been implemented. As a result, the effective radiation area only occupies 40 mm × 15 mm. The photograph of the manufactured antenna array is shown in Figure 5.16. The measured S-parameters are plotted in Figure 5.17. The obtained operation bandwidth is around 1 GHz (from 5.4 GHz to 6.4 GHz). The coupling coefficients between the input ports are less than -15 dB. The simulated 3D far field radiation pattern at 6 GHz in CST MWS is shown in Figure 5.18. The radiation pattern of port 1 is plotted in Figure 5.18(a), while Figure 5.18(b) and 5.18(c) indicate the patterns for port 2 and 3, respectively. Good pattern diversity is obtained, since the antennas radiate towards different directions. The simulated radiation efficiencies for all the ports are more than 95% and the simulated antenna gains are 4.34 dBi, 5.41 dBi and 5.37 dBi for port 1, 2 and 3, respectively. The calculated pattern correlation coefficients are 0.15 between ports 1 and 2 (ports 1 and 3) and 0.07 between ports 2 and 3.

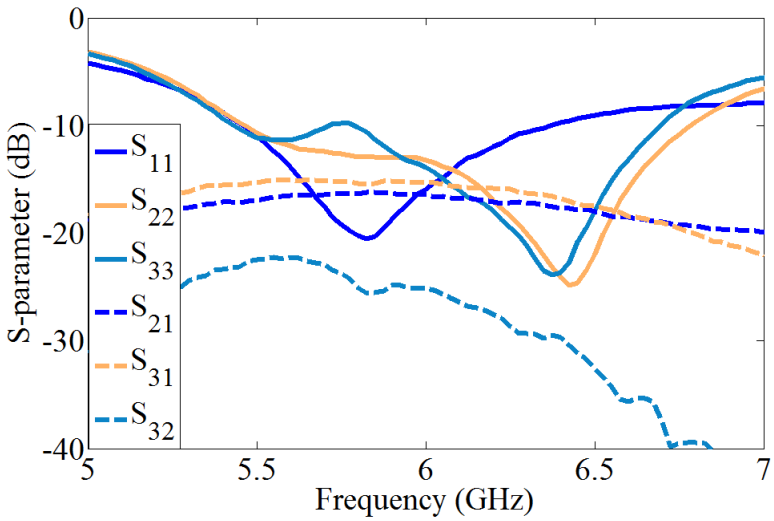

Figure 5.17: Measured S-parameters of the fabricated printed three-port compact antenna array.

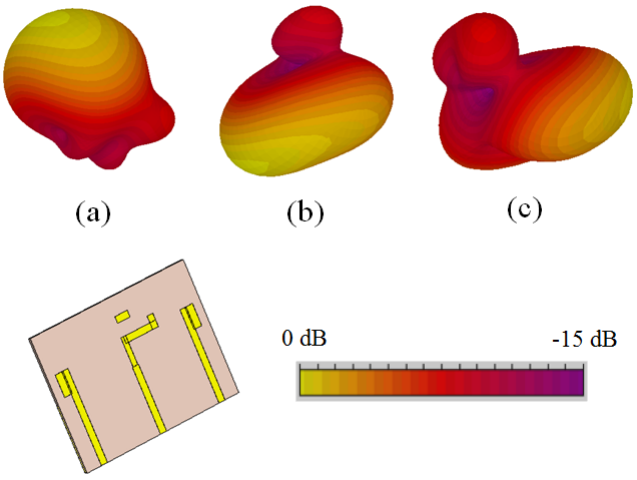

Figure 5.18: Simulated 3D far field radiation patterns at 6 GHz of the printed three-port compact antenna array.

5.3 Contour Integrated Dual Band Compact Antenna Elements and Arrays for Low Profile Mobile Terminals

Compact antenna arrays with printed radiation elements have been designed in the previous sections. In this section, radiation elements for modern wireless communication devices such as mobile phones are studied. The antennas in smart devices should not only be small in size but also able to support multiple frequency bands with respect to different applications. As a result, the antenna arrays designed in the last sections are not applicable for mobile terminals, because the printed monopoles are of large space occupation. In order to achieve a size reduction of antennas, several successful techniques have been investigated and published. For example, the planar inverted F antenna (PIFA) has become one of the most popular candidates for mobile phone antenna designs [Lee and Wong, 2009, Nepa et al., 2005, Rowell and Murch, 1997, 1998, Wang et al., 2007]. However, in general, there is still a certain area which is required for mounting the PIFAs in mobile terminals, e.g., 9 mm extended length from the ground plane is required for a PIFA for WLAN applications as presented in [Wang et al., 2007]. Commonly, this extended area brings additional difficulties when realizing antennas in mobile devices due to the limited available space. This issue would even be more problematic in future, since the thickness of up-coming smart phone generations is becoming smaller and smaller and this leads to further reduced available space inside the phones, e.g., the thickness of a smart phone can be as small as 1 mm in the future. As a result, it is quite challenging to utilize the common antenna types such as PIFA in future phone designs. Following the theme of this dissertation, multiple antenna systems have become very attractive. However, only a few of the previously published designs of MIMO arrays support multiband applications [Karimian et al., 2013, Lin et al., 2012, Sharawi et al., 2013, 2012, Wong et al., 2013, Zhou et al., 2012]. In [Sharawi, 2013], a number of successful approaches for designing multiband compact printed antenna arrays are summarized. However, it seems that all of these solutions cannot satisfy the size requirements for low profile mobile devices. Recently, some promising solutions have been published in literature for decreasing the overall dimension of radiation elements. For example, in [Martens et al., 2011], according to the characteristic mode theory, certain chassis modes can be created through inductive and capacitive couplings by current loops and capacitive elements, which occupy a little space. However, it is quite difficult to design an excitation source, which can generate the characteristic modes in multiple frequency bands through this method. Additionally, the design is dependent on the chassis structure. In [Anguera et al., 2013], low profile monopole pads have been utilized for different frequency bands. For this approach, the size of the pads itself is minimized, but it is still required that the remaining extended area containing the pads must not be metallic. Furthermore, it is also difficult to implement decoupling strategies with less space occupation for compact MIMO arrays of which the radiation elements are the low profile monopole pads.

In this section, a novel approach for designing low profile radiation elements occupying little space is investigated. The proposed antennas can be integrated at the contour of mobile devices and only very little space along the contour of the device is required. Also, the designed antennas operate independently from the particular shape of the chassis. Promising antenna performance is obtained by combining several novel and previously published techniques. In order to make such antennas applicable, bandwidth enhancement strategies

are carried out. Appropriate operation bandwidth is achieved through realizing novel multiple resonances structures. Following the same concepts, a two-element compact MIMO array is also designed and a novel decoupling concept especially for arrays with radiation elements with two radiation apertures, named self-neutralization, is introduced as well. The proposed antenna elements and the compact array operate at two frequency bands around 2.4 GHz and 5.5 GHz and support WLAN and LTE 2300 applications. Three prototypes have been manufactured and measured to prove the design concepts.

5.3.1 Operation Principle of the Contour Integrated Antenna

A 3D model of the first proposed design concept is shown in Figure 5.19, where a radiation element occupying only $W_s \times 2.5 \times 0.762$ mm^3 extended area is integrated at the contour of the chassis and W_s is the width of the chassis. Strips are mounted on the top and bottom layers of the substrate, which are close to the ground plane (the chassis of the mobile device). In order to realize resonant antennas, the lengths of these strips should be integer multiples of half the effective wavelength λ_{eff} at the desired frequencies.

A. Antenna Design Around 2.45 GHz

The investigation of all prototypes in this section is still based on the substrate Rogers 4350 with a thickness of 0.762 mm. For the first prototype, W_s is chosen as 58 mm and the length of the chassis L_s=50 mm (the real chassis for mobile devices is normally longer). For designing the lower frequency band resonator antenna, the strip on the bottom layer is implemented as a half wavelength resonator together with the ground plane as shown in Figure 5.20(a). The effective wavelength in such a resonator structure is approximately 86 mm at 2.45 GHz. The quality factor Q for such a resonator is high because of the limited size of the radiation apertures at the two open ends and the usage of low loss material. According to the previous knowledge, this high Q leads to small operation bandwidth. To increase the bandwidth, multiple resonance structures are promising solutions and are commonly exploited such as for the E-shaped and U-shaped patch antennas [Huynh and Lee, 1995, Wong and Hsu, 1997, 2001, Yang et al., 2001]. It is obvious that the E-shaped structure cannot be applied to the proposed resonator antenna, since one of the conductor layers is just a piece of strip. Therefore, a novel structure as shown in Figure 5.20(b) to obtain multiple resonances is utilized. As illustrated in the figure, the floating strip and the ground are connected in the middle through another short strip. Without this short strip, the resonance occurs when $\lambda_{\text{eff},1} = 2L_{st}$ (the fringe fields effects are neglected in this analysis), where L_{st} is the strip length. The short strip has no effect on this resonance mode, because for such a half wavelength resonator with open ends at the two sides, as shown in Figure 5.20(a), there is a virtual short (null electric field) in the middle and any PEC structure at this virtual short does not influence the field distribution of the resonance mode. When the strip in the middle is considered, currents can flow through it and the second resonance occurs when $\lambda_{\text{eff},2} = 2(L_{st} + \triangle L)$, where $\triangle L$ is the length of the inserted short strip. Consequently, two resonance modes are created by the proposed structure. The

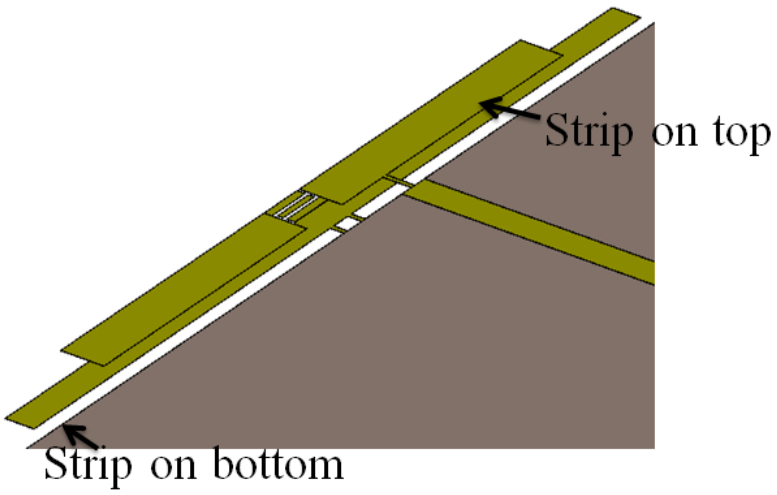

Figure 5.19: 3D view of the proposed antenna structure.

frequency of the second resonance is lower than the first one by the amount of

$$\triangle f = f_1 - f_2 = \frac{c}{2\sqrt{\varepsilon_{\text{eff}}}}(\frac{1}{L_{st}}\frac{1}{L_{st}+\triangle L}), \tag{5.2}$$

where c is the speed of light, ε_{eff} is the effective permittivity of the structure. The operation of the two modes are demonstrated through the current flows in Figure 5.21. Meanwhile, the simulated surface currents in x-direction (coordinates are defined in Figure 5.20) from CST MWS at 2.35 GHz and 2.5 GHz are shown in Figure 5.22 and the results agree well with the estimations. In order to enlarge the matching bandwidth, both two resonance modes should be excited through the same feeding point. Since proximity coupled feeds are promising solutions for input matching and bandwidth enhancement [Kim et al., 2011], a feeding strip on the top layer of the substrate is utilized as shown in Figure 5.20(c) according to the feed position shown in Figure 5.21(b). Figure 5.23 shows the simulation results for the return loss with different structures. It can be seen that the matching bandwidth is improved from 50 MHz to 260 MHz through implementing the proposed bandwidth enhancement strategies, where it is beneficial for the bandwidth to shape the short strip in the middle of the resonator as an 'H', which is illustrated in the inset of Figure 5.20(b). The electric field distribution of the two modes at the radiation apertures is different. For instance, for the first mode resonating at the higher frequency, the electric field components in x direction E_x at the two radiation slots are in phase while the components in y direction E_y are out of phase. Oppositely, for the second mode resonating at the lower frequency, at the radiation slots, E_x are out of phase and the components E_y are in phase. As a result, the far field radiation pattern is different for the two modes. The simulated radiation patterns in the plane xoy at the two resonance frequencies are shown in Figure 5.24 and the differences in the patterns can be clearly noticed.

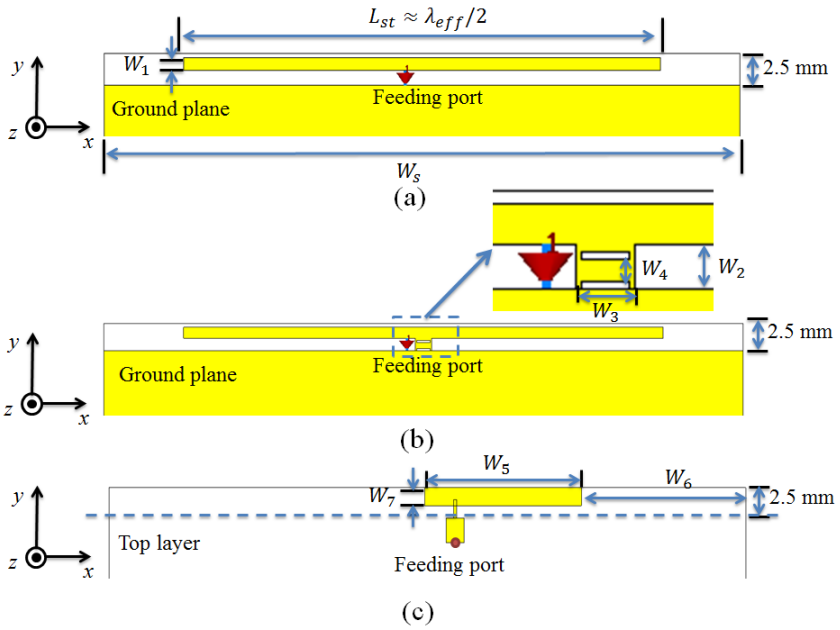

Figure 5.20: Contour integrated resonator antenna: (a) Basic structure; (b) with H-shape shorting strip in middle; (c) with coupling feed on the top layer. $W_s = 58, L_st = 43, W_1 = 1, W_2 = 1.15, W_3 = 1.5, W_4 = 0.75, W_5 = 14.5, W_6 = 13.75, W_7 = 1.5$, unit: mm.

B. Antenna Design Around 5.5 GHz

Figure 5.25 presents the proposed antenna structure for the higher frequency band which is around 5.5 GHz. The strip for this frequency band is located on the top layer while the radiation structure for 2.45 GHz is located on the bottom layer. A one effective wavelength long resonator is created by the strip on the top layer together with the strip on the bottom layer. It can be noticed in the figure that an interdigital printed capacitor is inserted. There are two reasons for implementing this capacitor. The first reason is to minimize the influence from the top strip to the lower frequency band resonator antenna and to maintain the functionality of the proximity coupled feeding. For this purpose, the capacitor performs as a high-pass filter, where the 2.4 GHz should be located in the stop band while the 5.5 GHz is in the pass band. Otherwise, the proximity coupled feeding would not be functional with a too long strip on the top layer. The second reason for utilizing this capacitor is to create an additional resonance mode. Without the capacitor, a regular one wavelength resonator is formed. In this case, a virtual open (null magnetic field) exists in the center of the strip. Therefore, the inserted capacitor is not functional at this resonant frequency. For the second resonance mode, an equivalent circuit model with the capacitor is illustrated in Figure 5.26. According to the theory of transmission lines, when the line length is longer than a quarter effective wavelength but shorter than half a wavelength, the open circuit would be transformed into an equivalent inductor. Therefore, in order to create

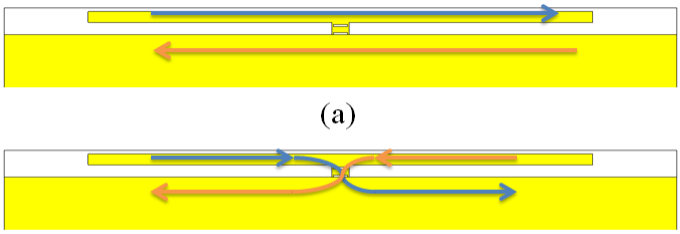

Figure 5.21: Surface current propagation of two modes: (a) higher frequency mode; (b) lower frequency mode.

the second resonance, the condition

$$\frac{1}{j\omega C} + 2j\omega L = 0. \tag{5.3}$$

should be fulfilled. In consequence, the second resonance mode is formed at a little lower frequency. Similarly, if an inductor is inserted instead of the capacitor in the middle, an additional resonance mode at a higher frequency can be realized. Figure 5.27 illustrates the two modes by plotting the electric field distributions at a time instance where the maximum exists at the two ends. For the second resonance mode, the electric field is inverted at the two sides of the capacitor. After the optimization process of the positions of all the strips, both resonance modes can be excited through one feeding point. The simulated E_y distribution in CST MWS is plotted in Figure 5.28(a) and 5.28(b) for the two resonance modes, respectively, which matches well with the analysis. The simulated return loss is shown in Figure 5.29 and the matching bandwidth is enlarged from 90 MHz to 370 MHz through inserting the capacitor. Similar to the two resonance modes around 2.45 GHz, the two modes around 5.5 GHz possess different electric field distributions as well. As a result, the far field radiation patterns of the two modes are different, e.g., the simulated radiation patterns in the plane *xoy* at the two resonance frequencies are shown in Figure 5.30.

5.3.2 Antenna Design and Measurements

The first antenna prototype is manufactured according to the discussions in the last subsection. The photograph of the fabricated antenna is shown in Figure 5.31. The measured S-parameters together with the simulation results are plotted in Figure 5.32, where the obtained matching bandwidths are around 250 MHz (2.27 GHz to 2.52 GHz) and 300 MHz (5.45 GHz to 5.75 GHz). Some discrepancies between the simulation and measurement results in the high frequency band are observed. This could be due to the errors during the manufacturing process. As shown in equation (5.3), the second resonance frequency is quite sensitive to the capacitance value. Very small modifications of the capacitance can lead to a frequency shift. The measured and simulated far field radiation patterns in certain cut planes are indicated in Figure 5.33 at 2.45 GHz and 5.5 GHz. Good agreement among

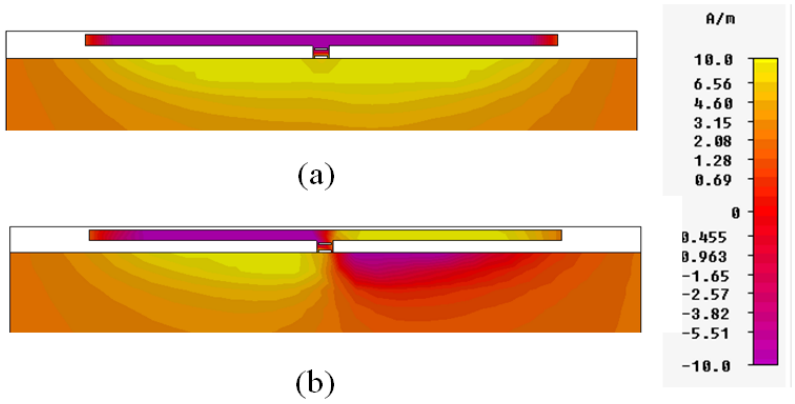

Figure 5.22: Simulated surface current distribution in x direction for two modes: (a) higher frequency mode; (b) lower frequency mode.

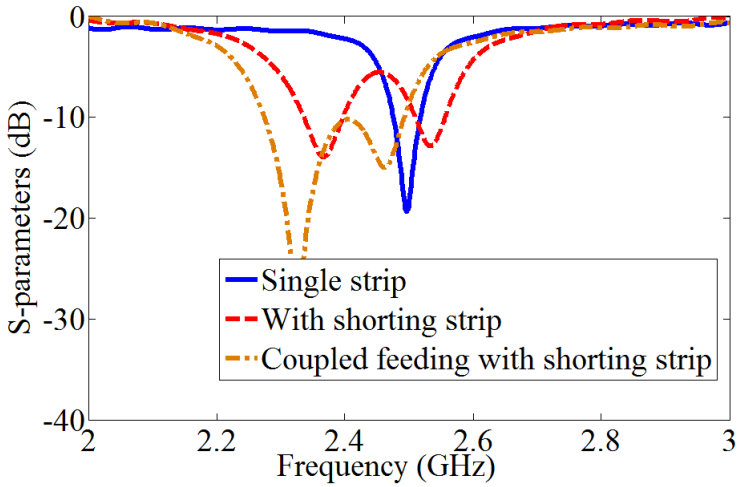

Figure 5.23: Simulated return loss of three different structures.

the measured and simulated results is obtained. The simulated antenna gains are 1.65 dBi and 4.43 dBi and the simulated efficiencies are 92% and 89% at 2.45 GHz and 5.5 GHz, respectively. At 2.45 GHz, the radiation pattern contains the features from both of the two resonance modes in this band. For example, the pattern main lobes of the lower frequency mode are found in directions of $+z$ and $-z$. The main polarization of the electric field in the far field is the ϕ component. For the other resonance mode around 2.45 GHz, the pattern main lobe is located in the direction of $+y$ and the major polarization of the electric field in the far field is still the ϕ component. In the higher frequency band, the pattern at 5.5 GHz contains the features of the two resonance modes as well. The radiation of the lower frequency mode directs towards the $+y$ direction, where it should be noticed that after optimizing the strip positions, the main lobe is tilted a little towards the direction of $-x$. The major polarization in the far field is the ϕ component. On the other hand, for the

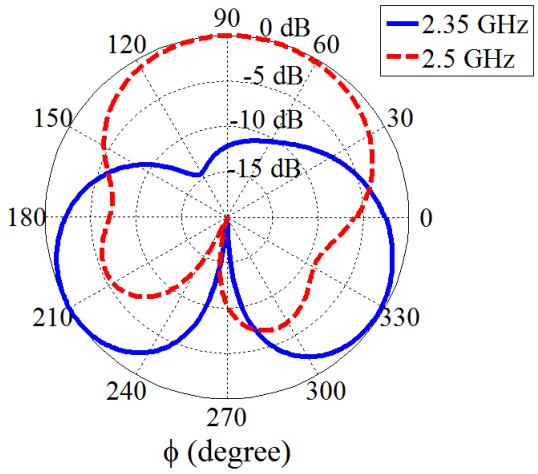

Figure 5.24: Normalized simulated radiation pattern in the plane *xoy* at the two resonance frequencies around 2.45 GHz.

higher frequency resonance mode, the main radiation direction is towards $+z$ and the main polarization in the far field is the θ component.

The proposed antenna can be integrated at one of the edges of a mobile terminal. However, not all devices can offer an edge with a width of more than 50 mm and this antenna prototype is also not convenient to be utilized for designing compact MIMO antenna arrays in mobile devices. As a result, some modifications should be carried out to make the antenna more universal for a wide variety of applications. The modified antenna prototype is shown in Figure 5.34, where the strips are shifted and bent. Then, the antenna is convenient to be integrated at the corner of the mobile device (width W_s=50 mm, length L_s=50 mm) due to its L-shape. Compared with the previous prototype, some parameters such as the length of the strip and the width of the slot for the coupled lines need to be changed slightly through the optimization to compensate parasitic effects caused by the bending of the strips. For example, W_4 in Figure 5.26 is modified from 0.275 mm to 0.25 mm. The photograph of the fabricated antenna is shown in Figure 5.35. The measured and simulated S-parameters are plotted in Figure 5.36. The obtained matching bandwidths are 250 MHz (2.27 GHz to 2.52 GHz) and 240 MHz (5.29 GHz to 5.53 GHz). The normalized measured and simulated far field radiation patterns are shown in Figure 5.37 for different cut planes at 2.45 GHz and 5.5 GHz. It is noticed that in Figure 5.37(b), it is different between the simulated and measured results at around $\phi = 270°$. This is because the feeding and mounting facilities for the far field measurements are implemented around this angle, which is also called the shadow area of the measurement. According to the simulation, the gains are 2.5 dBi and 4.1 dBi and the efficiencies are 93% and 85% at 2.45 GHz and 5.5 GHz, respectively. With respect to the far field radiation pattern, compared to the previous antenna, the L-shaped antenna owns the following features. The radiation patterns of the two resonance modes around 2.45 GHz are similar. The main lobe of both modes is towards the directions of $+z$ and $-z$ and the major polarization of the electric field in the far field is the ϕ component.

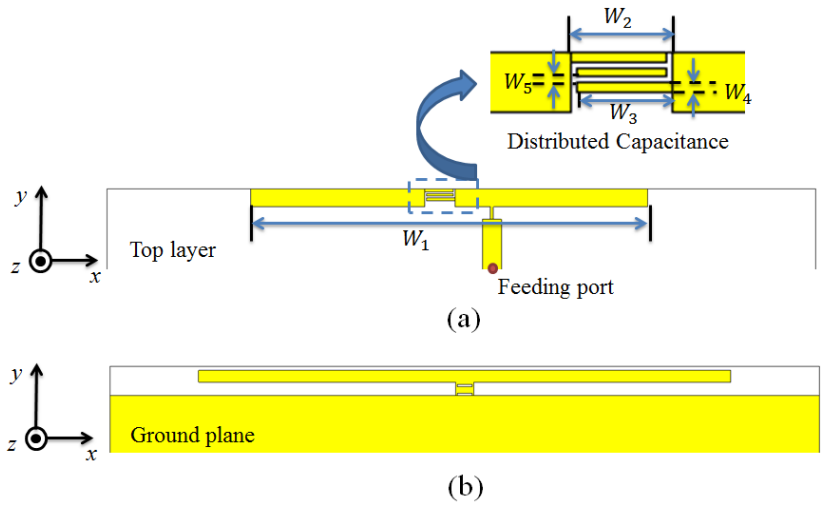

Figure 5.25: Contour integrated resonator antenna with dual operation band: (a) top layer; (b) ground plane. $W_1 = 32.5, W_2 = 2.5, W_3 = 2.35, W_4 = 0.275, W_5 = 0.125$, unit: mm.

In the 5.5 GHz band, the two resonant modes radiate towards different directions. For example, the main lobe of the lower frequency mode is located in the direction between $+x$ and $+y$, and the ϕ component is the dominant polarization in the far field. The main lobe of the higher frequency mode is in the direction of $+z$ with some tilts towards $-x$ and $-y$. The θ component is the main polarization in the far field. The pattern at 5.5 GHz is a combination of the patterns of the two resonance frequencies.

5.3.3 Two-Element Compact Antenna Array

In this subsection, a two-element compact antenna array is designed according to the L-shaped corner integrated dual band antenna. In this design, the shortest edge to edge distance between the radiation elements is around $0.22\lambda_{\text{eff}}$ and λ_{eff} is the effective wavelength at 2.45 GHz. The proposed compact antenna array is shown in Figure 5.38, where the two radiation elements are integrated at the two corners on an edge of the chassis (width W_s=50 mm, length L_s=110 mm). For this configuration, the two radiation elements are close to each other and strong mutual coupling exists. As a result, for decoupling the input ports, several decoupling strategies are utilized. A novel decoupling concept which is named self-neutralization is exploited. The proposed approach is quite effective for antenna arrays with radiation elements owning two radiation apertures. It is shown in Figure 5.38 that there are two possible coupling paths from antenna 1 to antenna 2: the first one is the direct coupling through path 1; the second coupling is due to the excited surface wave propagating along the edges of the chassis, which is marked as path 2. The simulated distributions of surface currents from CST MWS at 2.45 GHz are shown in Figure 5.39. The currents are mainly distributed along the edges of the substrate and the currents on the center of

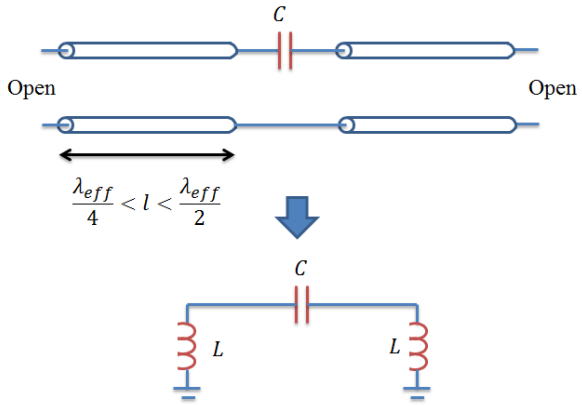

Figure 5.26: Principle of generating the additional resonance mode by the capacitor.

the chassis are very small and thus negligible. In order to realize the port decoupling, the equation

$$c_1 a_1 + c_2 a_1 = 0 \tag{5.4}$$

should be fulfilled, where c_i is the propagation coefficient due to the ith path and a_1 is the input wave amplitude at antenna 1. For this configuration, the magnitude of c_1 should be larger than the magnitude of c_2. In Figure 5.40, the ratio between the simulated magnitudes of c_2 and c_1 in CST MWS is illustrated with different substrate length L_s at 2.36 GHz and 5.4 GHz, respectively. In the higher frequency band, since $|c_2| << |c_1|$, the concept of self-neutralization is not functional. At the lower frequency band, for minimizing the magnitude of c_1+c_2, destructive interference of coupled waves due to the two paths is expected. Assume coefficient c_1 is fixed, the magnitude and phase of coefficient c_2 depend on the length of the chassis. As a result, an investigation is carried out for the relationship between the maximum coupling coefficient at the lower frequency band and the length of the chassis. Figure 5.41 depicts the results from simulations. The maximum coupling coefficient in the lower frequency band varies from -8 dB to -15 dB with different substrate length. Based on the simulation results, for minimizing the coupling, the substrate length in the design is chosen as 110 mm. For further reducing the coupling, two U-shaped strips are implemented at the radiation slots on the bottom layer as shown in Figure 5.42. These U-shaped strips reduce the radiated power at these radiation apertures and then decrease the magnitude of c_1. However, the drawback is that they lead to a reduction of the matching bandwidth. In real application environments, the sizes of the chassis are always fixed in general. The self-neutralization can then be achieved by properly positioning the arms of the L-shaped radiation elements. Path 1 is dominant for the mutual coupling at the higher frequency band. Cutting slots is a quite efficient solution for reducing the mutual coupling, e.g., a T-shaped slot in [Wang and Du, 2014a] leads to very good results. For isolating the presented radiation elements around 5.5 GHz, in Figure 5.42, a T-shaped slot is exploited. By inserting this T-shaped slot, discontinuities of the electric field in the propagation path along the edge are created and then the maximum coupling coefficient is reduced from -14 dB to -22 dB

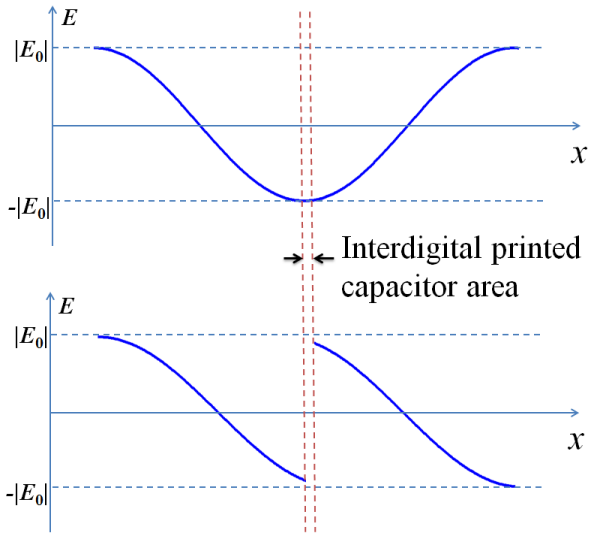

Figure 5.27: The electric field distribution of the two modes in the 5.5 GHz band: the upper one is for the higher frequency mode and the one below it is for the lower frequency mode.

in the higher frequency band as shown in Figure 5.43. However, after implementing the T-shaped slot, the value of c_1 at 2.36 GHz changes from $0.27e^{-66°j}$ to $0.26e^{-75°j}$. c_1 changes in phase by 9° and this 9° phase shift should be compensated by re-selecting the length of the substrate. However, the required change of the substrate length is only 1.1 mm and it is negligible.

The proposed antenna is manufactured as shown in Figure 5.44. The simulated and measured S-parameters are shown in Figure 5.45, where the simulated coupling coefficient is as low as -17 dB at the lower frequency band. However, the measured coupling coefficient at the lower frequency band is higher than the value in the simulation. This is due to the fact that the connecting coaxial cables for the measurement devices block path 2 and this effect degrades the performance of the self-neutralization. The obtained matching bandwidths from the measurement of the proposed compact array are 160 MHz (from 2.34 GHz to 2.5 GHz) and 320 MHz (from 5.18 GHz to 5.5 GHz). The measured far field radiation patterns are shown in Figure 5.46 and 5.47 at 2.45 GHz and at 5.5 GHz. Good agreement is found between the simulation and the measurement results except for some mismatches in the measurement shadow area. The radiated power at 2.45 GHz of antenna 1 is distributed on the half sphere around $+x$ and the main polarization in the far field is the ϕ component. The radiated power at 5.5 GHz of antenna 1 is mainly directed towards the direction of $+z$ and the electric field is polarized in ϕ direction. Due to the symmetry alignment, the far field radiation patterns of antenna 2 are the images of the patterns of antenna 1 with respect to the *yoz* plane. In the simulation, the gains are 1.5 dBi and 3.0 dBi, the radiation efficiencies are 92% and 76% at 2.45 GHz and 5.5 GHz, respectively. The pattern correlation coefficients between the two antennas are below 0.2 and 0.15 in the low and high frequency band, respectively.

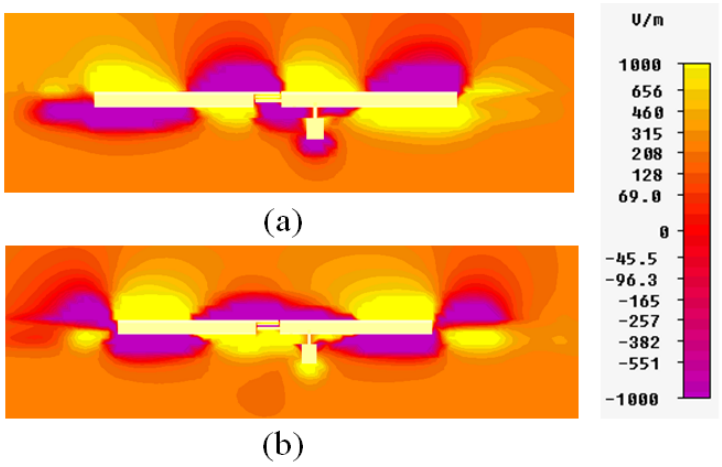

Figure 5.28: Simulated E_y in CST MWS: (a) lower frequency mode; (b) higher frequency mode.

5.3.4 Discussion

The designed contour integrated antennas and the two-element array show advantageous performance in space occupation and broad operation bandwidth. To better illustrate the advantage, a common PIFA array occupying similar space has been simulated in CST MWS for comparison. The two PIFAs realized with virtual inductors have been implemented around the edges at the two sides of the chassis with 2.5 mm extended area. The simulation results of the S-parameters for such a PIFA array are shown in Figure 5.48. The PIFA array achieves good matching and decoupling results at 2.4 GHz. The radiation efficiency at 2.4 GHz is about 88% for both ports. However, this two-element conventional PIFA array operates only in one frequency band and the bandwidth is around 120 MHz. Thus, it can be concluded that the performance of the new array is considerably better. The second advantage of the proposed array is that the operation is chassis independent. For example, in Figure 5.49, the simulated S-parameters of an antenna array with defected chassis are shown. Compared to the S-parameters shown in Figure 5.45, there are only small variations caused by the defect chassis. This feature makes the introduced design concept suitable for a wide variety of applications where only metallic contours are needed. As a result, compared to the small antenna designs based on the characteristic mode excitation method, the proposed design gives much more freedom in selecting the shape of the chassis. If materials with higher permittivity are utilized as a substrate, the operation frequency of the antenna can be reduced slightly. According to simulations, the proposed method works properly with materials with relative permittivity smaller than 10 and the lower band operation frequency can be as low as 1.6 GHz. However, for even lower frequencies, the proposed approach encounters the problem that the obtained matching bandwidth becomes small.

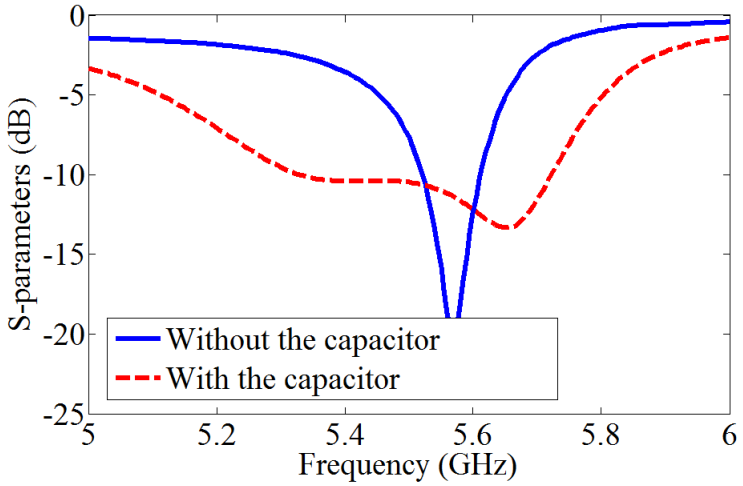

Figure 5.29: Simulated return loss for the cases with and without the capacitor.

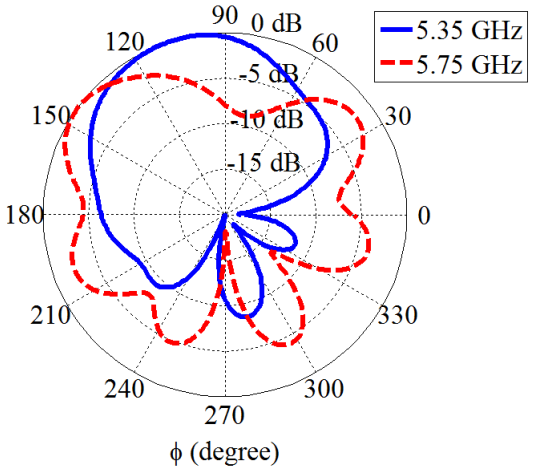

Figure 5.30: Normalized simulated radiation patterns in the plane *xoy* for the two resonance frequencies around 5.5 GHz.

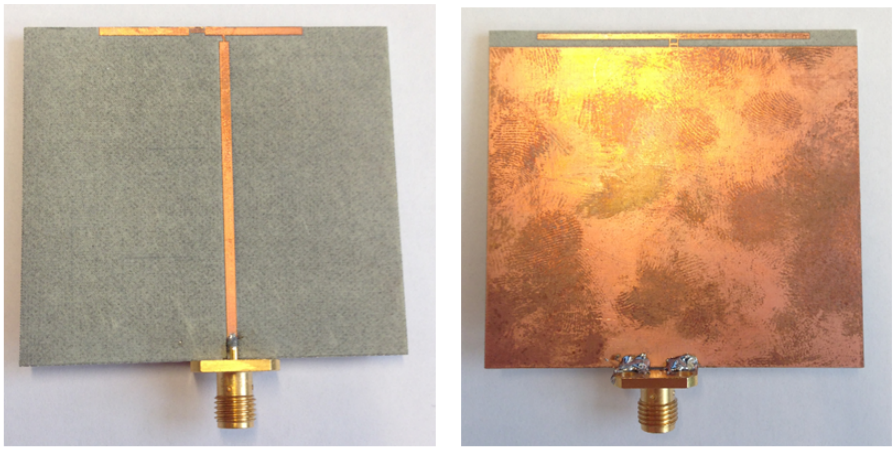

Figure 5.31: Photograph of the manufactured antenna.

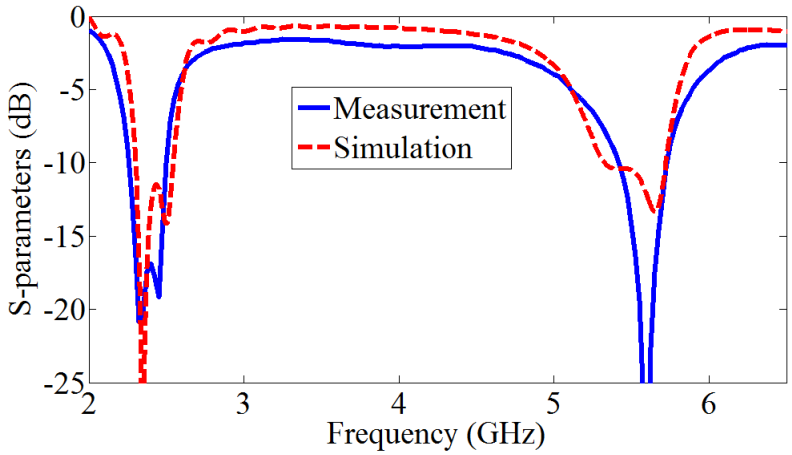

Figure 5.32: Measured and simulated S-parameters of the proposed antenna which is shown in Figure 5.31.

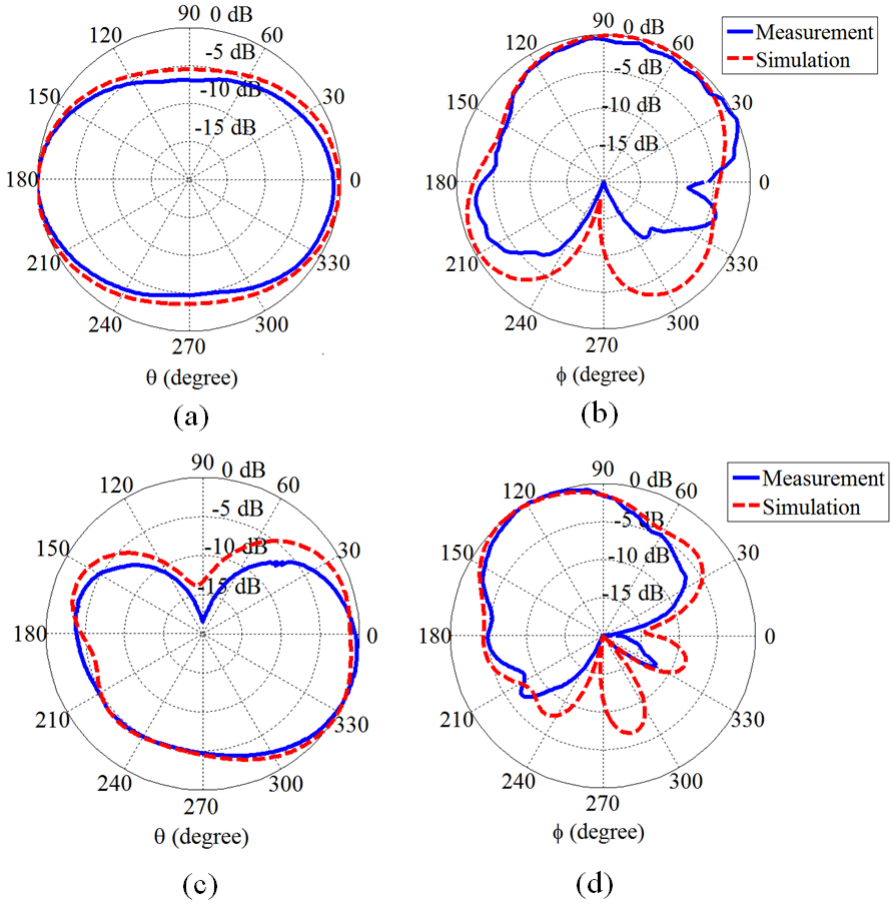

Figure 5.33: Normalized measured and simulated radiation patterns in cut planes: (a) *xoz* at 2.45 GHz; (b) *xoy* at 2.45 GHz; (c) *xoz* at 5.5 GHz; (d) *xoy* at 5.5 GHz.

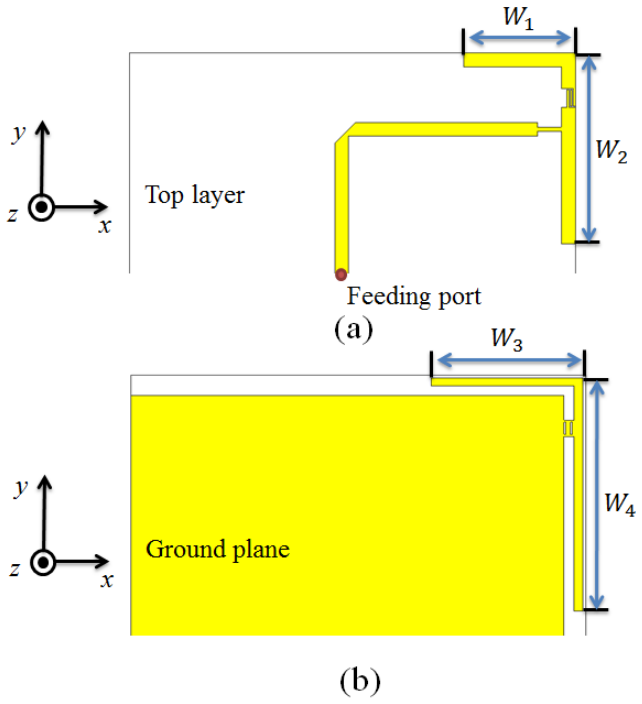

Figure 5.34: Corner integrated L-shape dual band antenna: $W_1 = 13.15, W_2 = 22.7, W_3 = 17.5, W_4 = 28.5$, unit: mm.

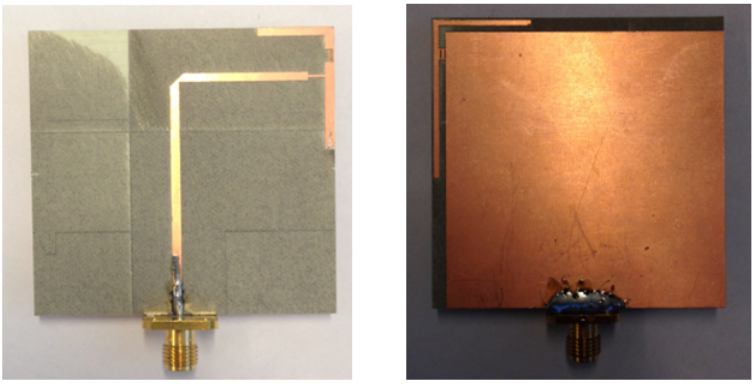

Figure 5.35: Photograph of the manufactured antenna based on the model which is shown in Figure 5.34.

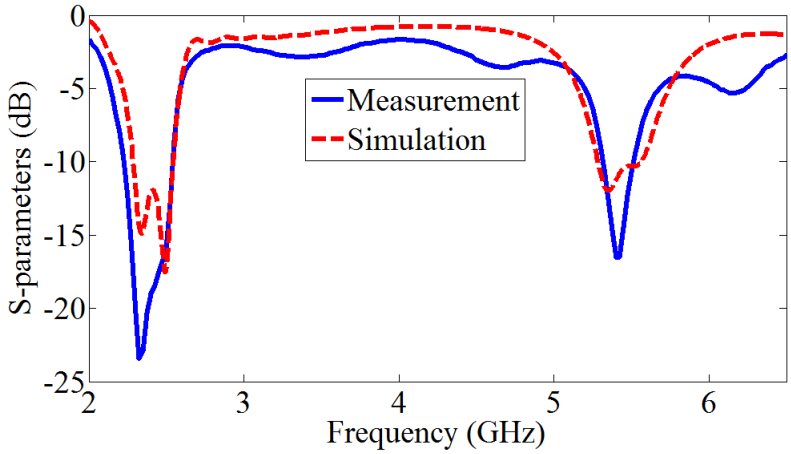

Figure 5.36: Measured and simulated S-parameters of the proposed antenna which is shown in Figure 5.35.

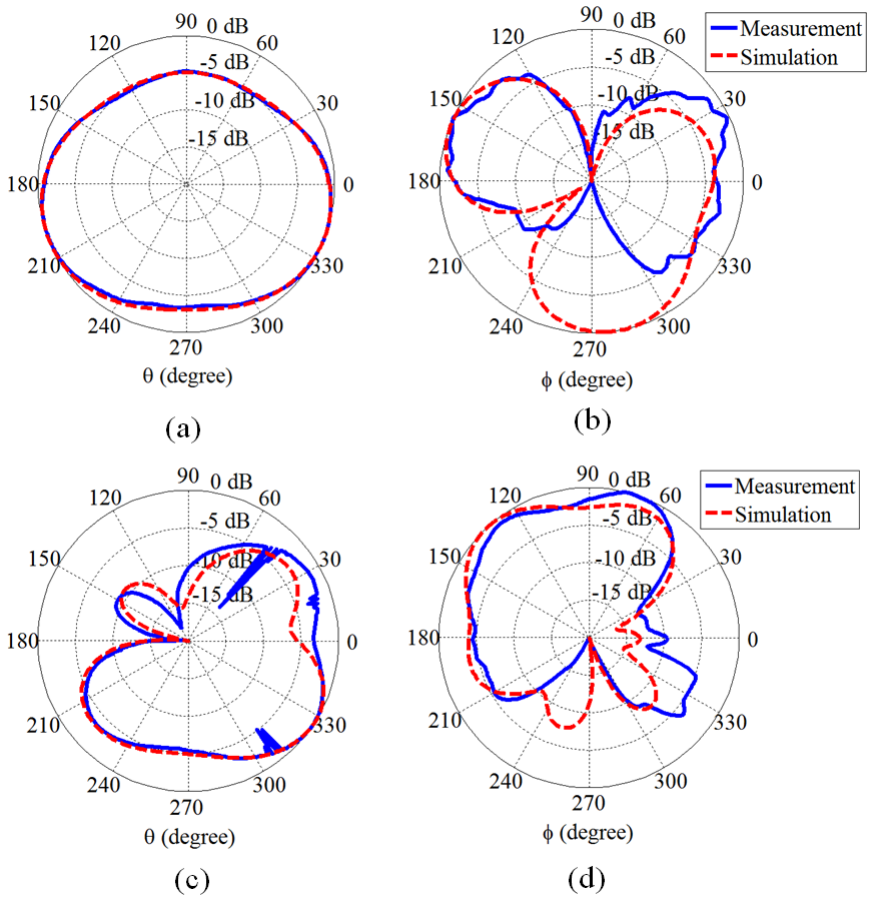

Figure 5.37: Normalized measured and simulated radiation patterns in cut planes: (a) *xoz* at 2.45 GHz; (b) *xoy* at 2.45 GHz; (c) *xoz* at 5.5 GHz; (d) *xoy* at 5.5 GHz.

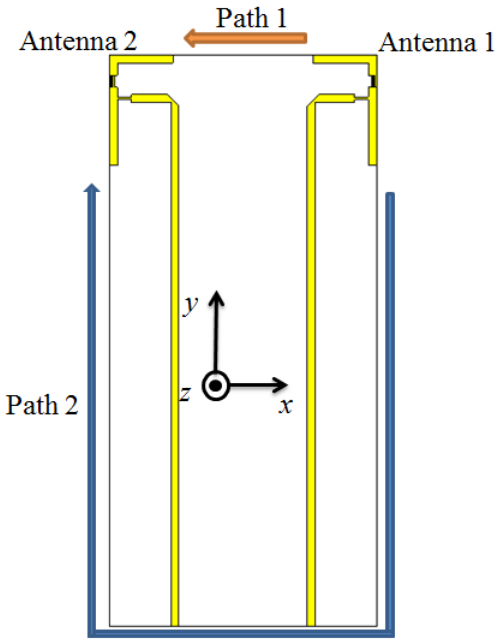

Figure 5.38: Schematic of the two-element compact antenna array.

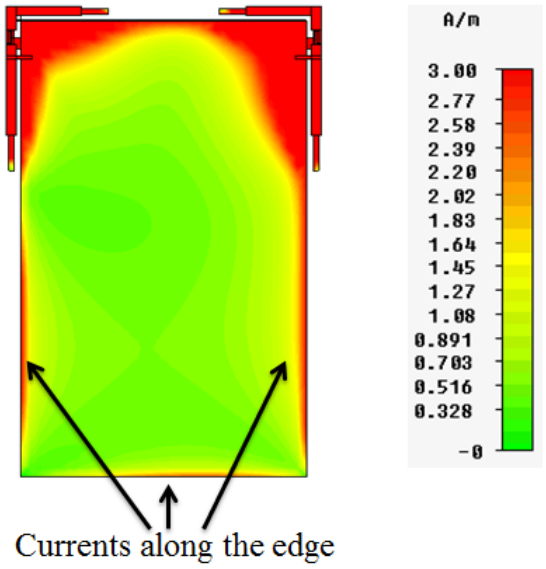

Figure 5.39: Simulated surface current distribution at 2.45 GHz in CST MWS.

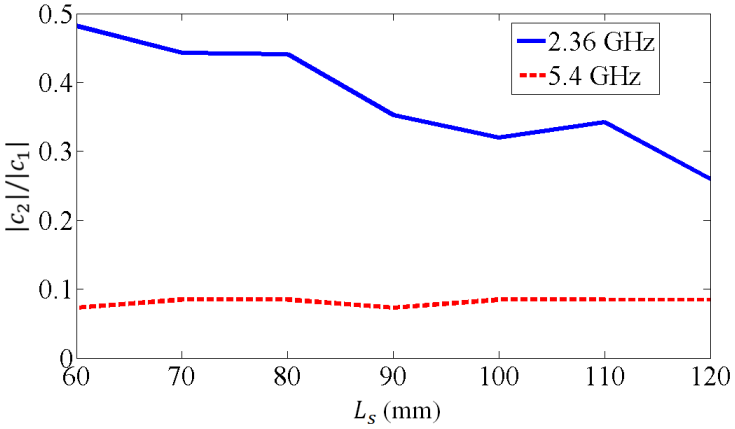

Figure 5.40: The ratio of $|c_2|$ and $|c_1|$ with different substrate lengths at different frequencies.

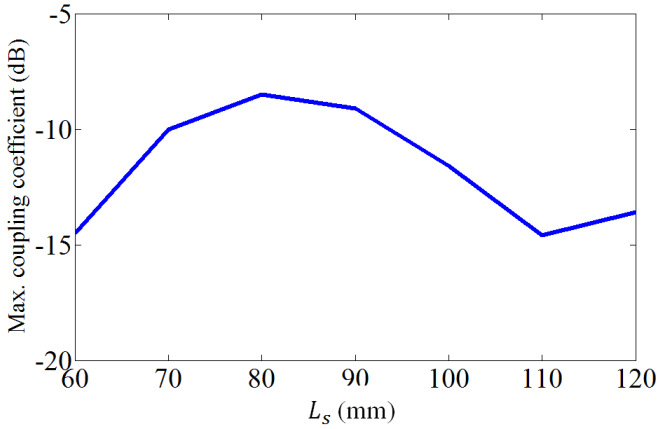

Figure 5.41: Simulated maximum coupling coefficient in the lower frequency band between the two antennas with different substrate lengths.

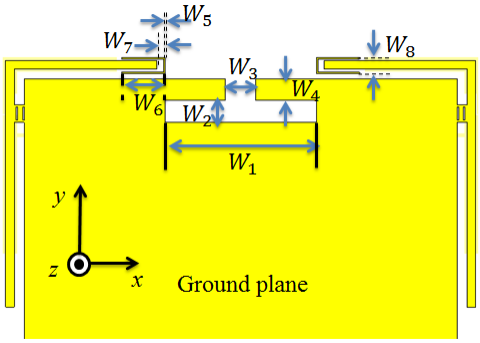

Figure 5.42: Modified ground plane for decoupling the two antennas: $W_1 = 17.5, W_2 = 2.5, W_3 = 3.5, W_4 = 2.5, W_5 = 14.5, W_6 = 0.175, W_7 = 0.9, W_8 = 1.75$, unit: mm.

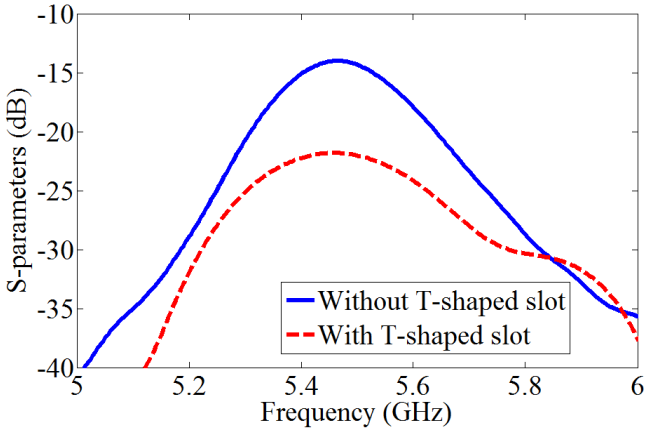

Figure 5.43: Simulated coupling coefficients in the higher frequency band between the two antennas with and without the T-shape slot.

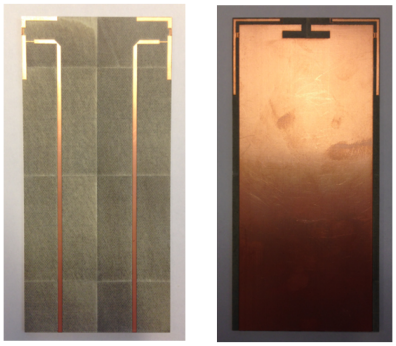

Figure 5.44: Photograph of the manufactured two-element MIMO antenna array.

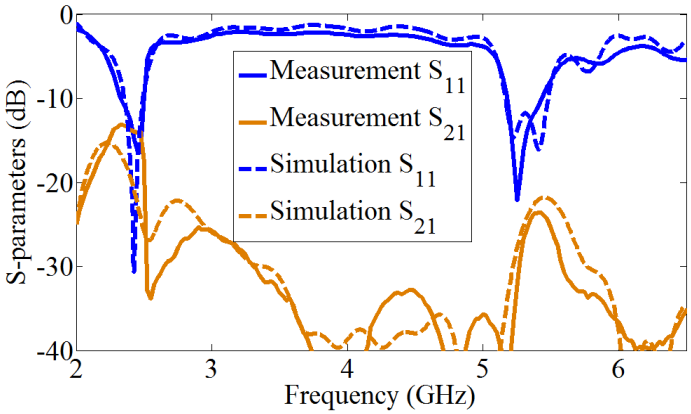

Figure 5.45: Measured and simulated S-parameters of the proposed antenna which is shown in Figure 5.44.

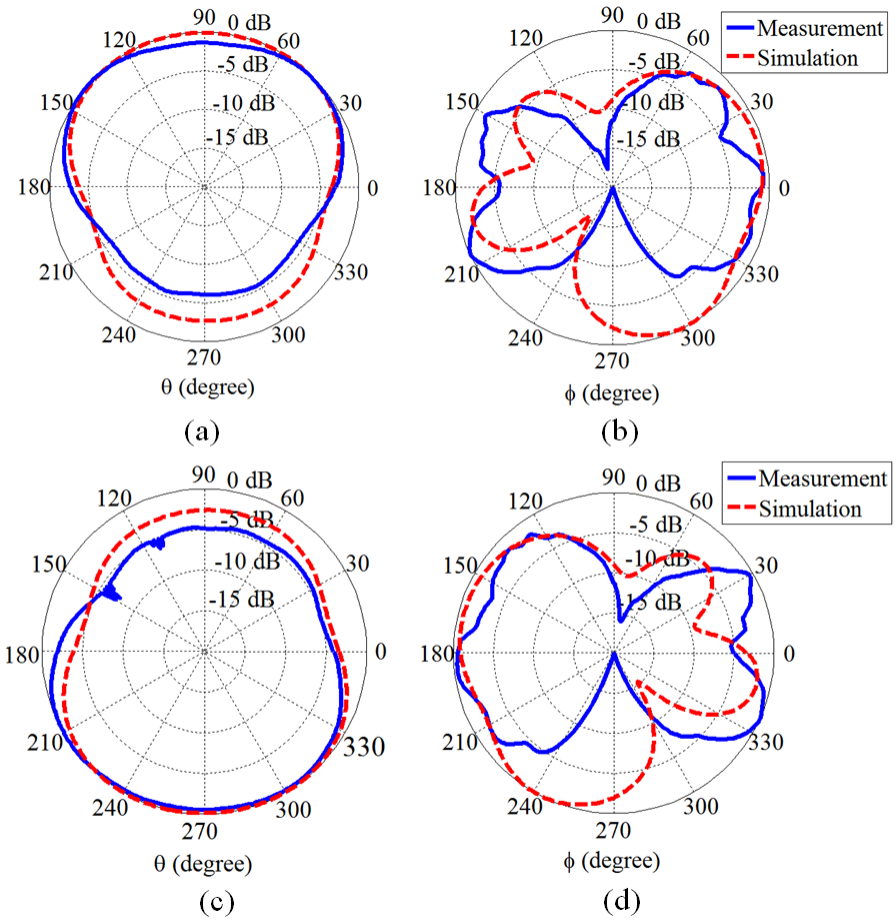

Figure 5.46: Normalized measured and simulated radiation patterns in cut planes: (a) *xoz* at 2.45 GHz of antenna 1; (b) *xoy* at 2.45 GHz of antenna 1; (c) *xoz* at 2.45 GHz of antenna 2; (d) *xoy* at 2.45 GHz of antenna 2.

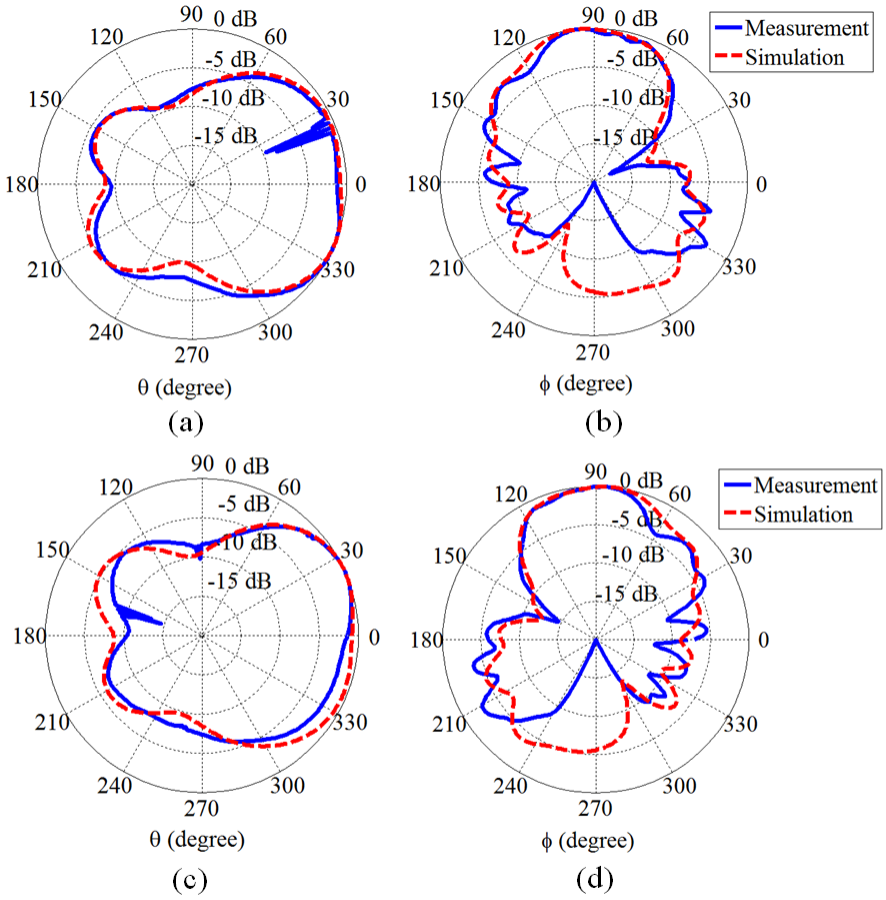

Figure 5.47: Normalized measured and simulated radiation patterns in cut planes: (a) *xoz* at 5.5 GHz of antenna 1; (b) *xoy* at 5.5 GHz of antenna 1; (c) *xoz* at 5.5 GHz of antenna 2; (d) *xoy* at 5.5 GHz of antenna 2.

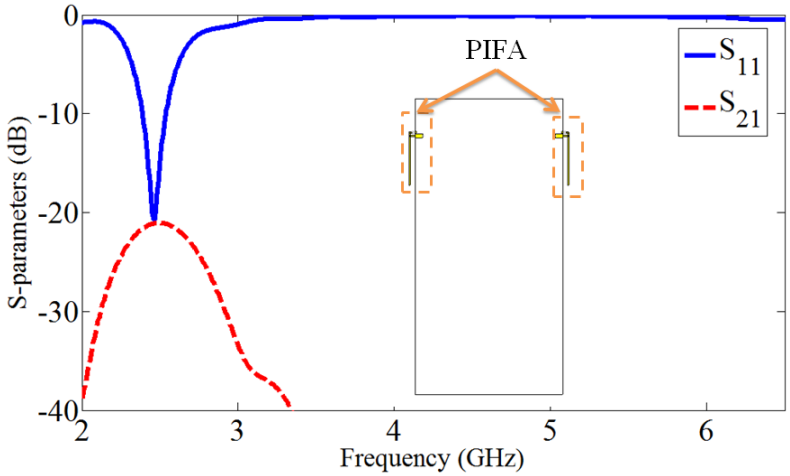

Figure 5.48: Simulated S-parameters of a PIFA antenna array.

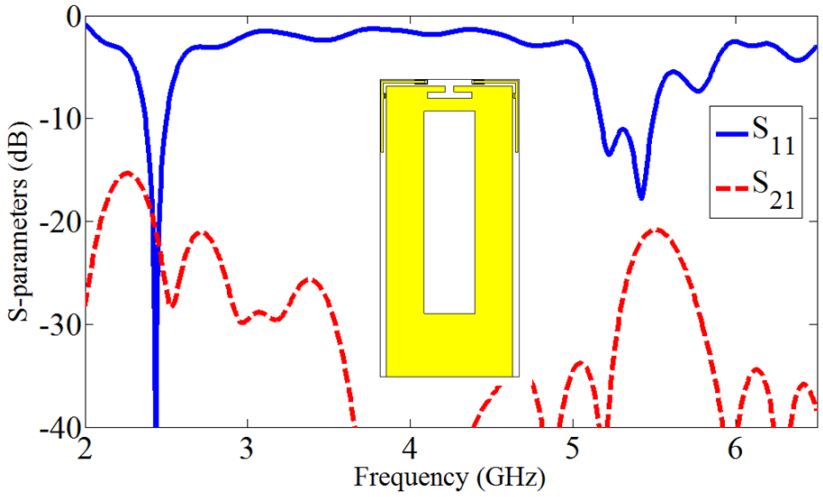

Figure 5.49: Simulated S-parameters of the proposed antenna array with defect chassis.

6 Evaluation of the Channel Capacity for Compact Multiple Antenna Systems

It has been proved in Chapter 3 that MIMO systems are beneficial for pursuing large channel capacities. With certain SNR and bandwidth at the receiver, the channel capacity only depends on the channel matrix. In this chapter, the channel characteristics of MIMO wireless communication systems are investigated. Both statistical and deterministic channel models for different circumstances are utilized for the study. The channel capacities of MIMO systems realized with the two-element compact monopole antenna arrays designed in Chapter 4 are evaluated. For different decoupling strategies, the obtained results are different as well. For the deterministic model of indoor communication systems, a ray tracing method is exploited to track the channel matrix. Following the same procedures, the antenna arrays designed in Chapter 5 can be evaluated as well.

6.1 Channel Capacity Analysis for Outdoor Wireless Communication Systems with Rich Scattering Environment

An outdoor communication environment contains commonly rich and random scattering objects, where line of sight (LOS) transmission between the transmitter and receiver does not exist. Generally, Rayleigh fading channels are exploited for investigations [Biglieri et al., 1998, Chizhik et al., 2003]. Statistically, if the channels are all uncorrelated, the channel matrix $\mathbf{H}$ is a random matrix with complex, zero-mean, independent, identically Gaussian distributed entries. According to [Telatar, 1999], the real and imaginary parts of each entry in the matrix should also be Gaussian, zero-mean and independent from each other, where the variance of them should be identical and equal to half of the variance of the magnitude of each entry in $\mathbf{H}$. Once the channel matrix has been found, the channel capacity can be evaluated. In the following analysis, it is assumed that a large number of scattering objects exist around both the transmitter and the receiver. Signals transmitted to all directions from the TX array can be received by the RX antennas from random incoming directions. Based on these assumptions, a modeling method including the far field radiation patterns of the antennas is developed for characterizing the channel capacity.

6.1.1 Description of the Modeling Approach

Within the proposed method, the channels need to be represented by sub-channels between sub-transmitters and sub-receivers, which are related to the far fields of the TX and RX array elements. One sub-transmitter is assumed to transimit its signal to a single fixed direction in the far field and the sum of the transmitted powers by all the sub-transmitters is equal to the radiated power of the corresponding antenna. A similar definition is applied to the sub-receivers. This assumption physically is not possible for individual measurements, but it can be utilized for the statistical analysis. Without considering noise, the sub-channel

matrix can be represented in the form of

$$\vec{r} = \frac{1}{\sqrt{XY}} \sqrt{g} \mathbf{H}_s \vec{t}, \tag{6.1}$$

where $\vec{r}$ is the vector containing the sub-receivers, $\vec{t}$ is the vector containing the sub-transmitters, $\mathbf{H}_s$ is the corresponding random channel matrix, g is the average channel gain, X and Y are the numbers of the sub-transmitters or sub-receivers in the ϕ and θ cut planes, and XY is the total number of the sub-transmitters or sub-receivers. In this case, the average channel gain depicts the relationship between the transmitted power in each sub-transmitter and the power density of the incident plane wave at the RX antennas. The expectation of the magnitude of the entries of $\mathbf{H}_s$ should be unity. The entries of $\mathbf{H}_s$ are identically distributed and independent from each other, which means the sub-channels are uncorrelated. The sub-transmitter vector is directly derived from the far field pattern, e.g., the one for the ith element in the TX array is calculated through

$$\vec{t_i} = a_i \sqrt{\frac{G_i(1 - \sum_k |S_{ki,T}|^2)}{8\pi}} \begin{bmatrix} F_i(\theta_1, \phi_1)\sqrt{\triangle\Omega(\theta_1, \phi_1)} \\ F_i(\theta_1, \phi_2)\sqrt{\triangle\Omega(\theta_1, \phi_2)} \\ \vdots \\ F_i(\theta_X, \phi_Y)\sqrt{\triangle\Omega(\theta_X, \phi_Y)} \end{bmatrix}, \tag{6.2}$$

with

$$\triangle\Omega(\theta_x, \phi_y) = \frac{\pi}{X}\frac{2\pi}{Y}\sin(\theta_x), \tag{6.3}$$

where a_i is the ith input wave amplitude of the TX array, $F_i(\theta, \phi)$ is the normalized radiation pattern of the ith port, $S_{ki,T}$ are the S-parameters of the TX elements, G_i is the gain of the ith port and $\triangle\Omega$ is the sampling interval in the far field. It should be noticed that the polarization is not considered and it will be discussed later. On the receiver side, the received wave amplitude of the jth port for the sub-receiver can be written in the form of

$$b_j = \sqrt{\frac{G_j\lambda^2(1 - \sum_k |S_{kj,R}|^2)}{2\pi}} \begin{bmatrix} F_j(\theta_1, \phi_1)\sqrt{\frac{XY}{4\pi}\triangle\Omega(\theta_1, \phi_1)} \\ F_j(\theta_1, \phi_2)\sqrt{\frac{XY}{4\pi}\triangle\Omega(\theta_2, \phi_2)} \\ \vdots \\ F_j(\theta_N, \phi_M)\sqrt{\frac{XY}{4\pi}\triangle\Omega(\theta_X, \phi_Y)} \end{bmatrix}^T \vec{r}_j, \tag{6.4}$$

where λ is the wavelength of the desired frequency in free space and $S_{kj,R}$ are the S-parameters of the RX elements. Then, the channel coefficient between the ith TX port and the jth RX port, which is the element of the channel matrix $\mathbf{H}$ is calculated through

$$h_{ji} = \frac{b_j}{a_i}. \tag{6.5}$$

In consequence, the channel matrix is generated. The channel capacity is calculated through equation (3.25). After adequate individual simulations with different realizations of $\mathbf{H}$, the

average channel capacity is expressed as

$$C' = E\left[\log_2\left|\mathbf{I}_N + \frac{P_{\mathrm{TX}}}{MP_n}\mathbf{H}\mathbf{H}^H\right|\right], \tag{6.6}$$

where it is assumed that the power is evenly distributed at the TX ports.

However, the polarization properties have not been considered so far, which also plays an important role during the channel characterization. For this modeling approach, two orthogonal polarizations are treated separately. For example, the sub-transmitters are divided into two parts, $\vec{t}_\theta$ and $\vec{t}_\phi$ according to the far field components of θ and ϕ, together with four channel matrices $\mathbf{H}_{s,\theta\theta}$, $\mathbf{H}_{s,\theta\phi}$, $\mathbf{H}_{s,\phi\theta}$ and $\mathbf{H}_{s,\phi\phi}$, which are independent from each other. The same decomposition is also applied to the sub-receivers. With polarization characteristics, the sub-receiver vector becomes

$$\begin{cases} \vec{r}_\theta = \frac{1}{\sqrt{XY}}\sqrt{\frac{g}{2}}(\mathbf{H}_{s,\theta\theta}\vec{t}_\theta + \mathbf{H}_{s,\theta\phi}\vec{t}_\phi) \\ \vec{r}_\phi = \frac{1}{\sqrt{XY}}\sqrt{\frac{g}{2}}(\mathbf{H}_{s,\phi\theta}\vec{t}_\theta + \mathbf{H}_{s,\phi\phi}\vec{t}_\phi). \end{cases} \tag{6.7}$$

The corresponding received wave amplitudes can be calculated through equation (6.4). To sum up, the generation process of the channel matrix can be concluded as: a) calculate the sub-transmitter for every TX port according to the far field pattern and gain for different polarizations; b) generate Gaussian complex random matrices with zero-mean independent entries; c) calculate the channel matrix between the transmitter and receiver through the relevant equations and calculate the channel capacity; d) repeat step a) to c) often enough and calculate the mean value of the channel capacity. Afterwards, the channel capacity can be obtained.

6.1.2 Channel Capacity Evaluation for 2×2 MIMO Systems with Compact Monopole Arrays

In this subsection, the channel capacities for MIMO systems with the antenna arrays discussed in Chapter 4 are investigated. Here, four 2×2 communication systems are evaluated for comparison. For each of them, the same type of array is utilized for the TX and RX arrays. The four types of arrays are the compact array with eigenmode excitation method (CEM) of 0.1λ separation, the compact array with multiport conjugate matching method (CCM), the compact monopole array with no decoupling network (CNDN), and an additional sparse array without decoupling network (SNDN) of around 0.3λ separation. All of the antenna arrays operate at the same frequency around 2.45 GHz.

Firstly, the influence on the channel capacity from the radiation patterns is studied. To make fair comparisons, the effects from power matching and radiation efficiency should be eliminated. This is achieved through a mathematical power regulation, e.g., in the TX mode, if one antenna is mismatched, more power should be delivered to this port to ensure that all the antennas transmit the same amount of power. For the RX mode, the directivity pattern should be applied instead of the gain pattern and all the RX ports are assumed to be matched. Based on the above discussions, simulations have been performed with

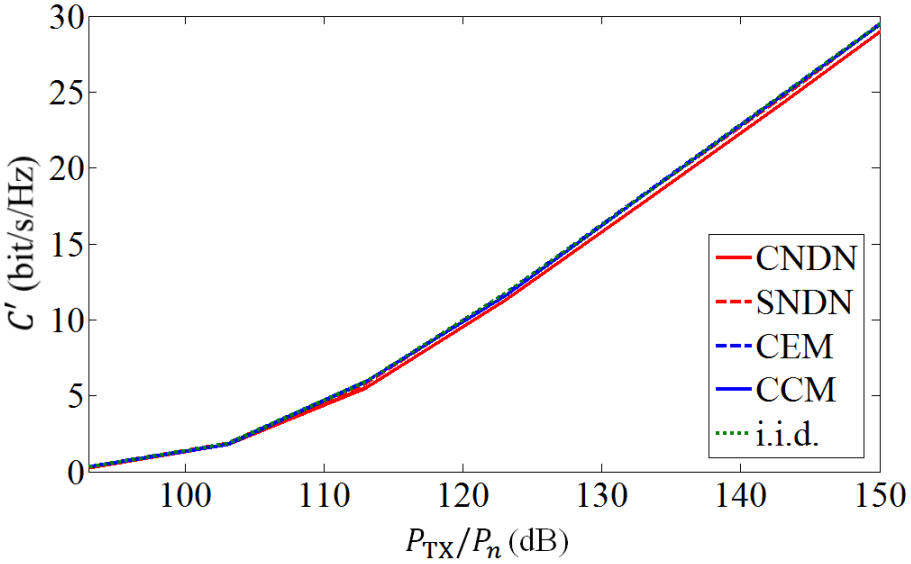

Figure 6.1: The average channel capacity of different MIMO systems for the outdoor statistical model, where only the influence from the radiation patterns is considered.

the MATLAB software [MathWorks, 2011]. Each simulation was carried out dependent on the ratio of the total transmitted power and the noise power at the receiving port. In the following investigations, the channel gain g is assumed to be -70 dB and the sampling step in the far field is 5° for both θ and ϕ. For one round, 1000 simulations were performed and the mean value of the average channel capacity was calculated.

The simulated average channel capacity is plotted in Figure 6.1. For comparison, the simulation results of a 2×2 MIMO system with independent identically distributed (i.i.d.) channels are also plotted as a reference, of which $\mathbf{H}$ is a 2×2 matrix with i.i.d. entries [Cover et al., 1980]. Particularly for the proposed modeling approach, the channel coefficient of the i.i.d. channel satisfies

$$E[|h_{i.i.d.}|^2] = \frac{1}{2}\frac{\lambda^2 g P_{\mathrm{TX}}}{4\pi M}. \tag{6.8}$$

The reason for multiplying $\frac{1}{2}$ is that the monopole antenna is linearly polarized and statistically the average probability of polarization matching between the TX and RX antennas is 50%. It is noticed that the i.i.d. channel shows the best performance of the channel capacity. The MIMO systems based on compact antenna arrays with decoupling networks show similar performance as compared to the system with the array with larger element spacing, which are quite close to the performance of the system with i.i.d. channel. The system with CNDN arrays shows the worst results.

It is reported in [Chiani et al., 2003, Louie et al., 2008, Shiu et al., 2000] that the channel correlation is influential on the statistical channel capacity and in most cases without additional signal processing techniques, the channel correlation degrades the channel

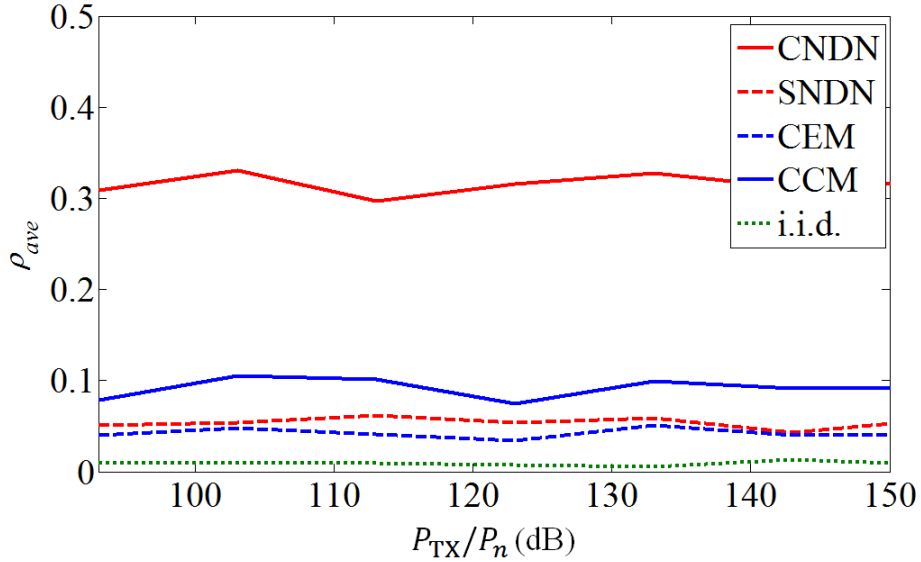

Figure 6.2: The average channel correlation coefficient of different MIMO systems, where only the influence from radiation patterns is considered.

capacity. The channel correlation coefficient is calculated through

$$\rho_{ji,nm} = \frac{E[h_{ji}h_{nm}^*]}{\sqrt{E[h_{ji}h_{ji}^*]E[h_{nm}h_{nm}^*]}}. \tag{6.9}$$

Then, the average channel correlation coefficient is calculated through

$$\rho_{ave} = \frac{2\sum_{i,j,m,n}|\rho_{ji,nm}|}{(M+N)(M+N-1)} \quad \Big| \quad \text{for } j \neq n \text{ and } i \neq m, \tag{6.10}$$

which is the mean value of the magnitude of the channel correlation coefficient between all different channels. The results of the average channel correlation coefficient for different arrays are plotted in Figure 6.2 versus the ratio between the transmitted power and the noise power. The channel correlation for the compact arrays with decoupling networks is much lower than the compact array without decoupling networks. Therefore, it is proved that channel correlations reduce the channel capacity in Rayleigh like channels.

What should also be checked in the simulation is the SNR at the receiving ports. The SNR at each RX port is calculated through

$$\text{SNRr}_j = \frac{\sum_i E[|h_{ji}|^2]P_{TX}}{MP_n}, \tag{6.11}$$

where SNRr_j is the average SNR at the jth receiver port. Figure 6.3 plots the simulation results. Since the mismatch and loss are not considered, the RX ports of all the arrays should own the same SNR. The simulation results show good agreement with this expectation.

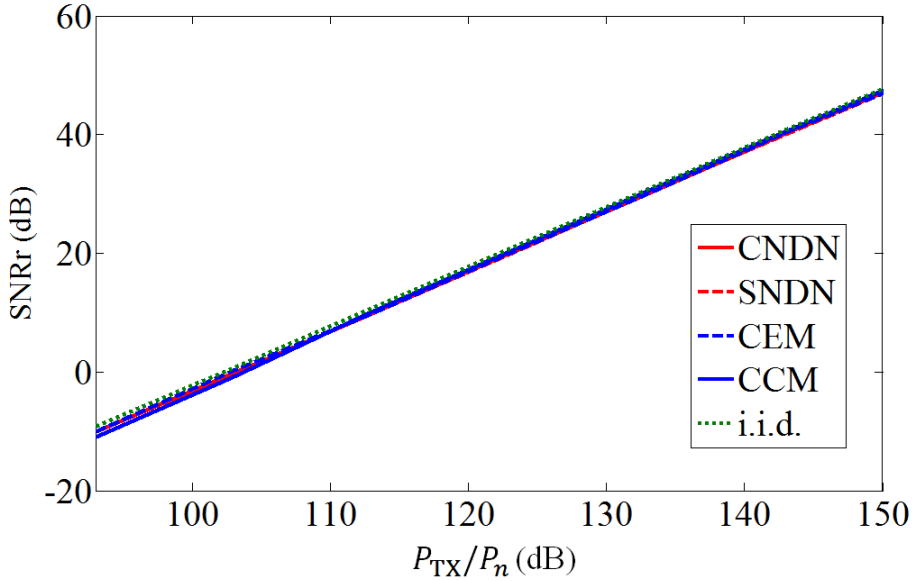

Figure 6.3: The SNR at each RX port of different MIMO systems, where only the influence from radiation patterns is considered.

In the above, the effects of antenna radiation patterns on channel capacity for Rayleigh like channel models have been investigated. In the following, the power matching and losses are considered as well. The power is still assumed to be evenly allocated over the TX ports. After the same simulation process, the simulation results are plotted in Figure 6.4. It is noticed that the channel capacity of the MIMO system with the CEM array is just a little bit higher than for the system with the CNDN array. This is due to the fact that the radiation efficiency of the odd mode port of the CEM array is as low as 53% in the simulation, while it is almost 100% for the CNDN array. So, the benefits from the uncorrelated channels are lost due to the low radiation efficiency. In order to describe this in a clearer manner, the MIMO average transmission efficiency is utilized, which is defined as

$$\eta_{\text{MIMO}} = \frac{\sum_i \eta_{t,Ti} \sum_j \eta_{t,Rj}}{MN}, \tag{6.12}$$

where $\eta_{t,Ti}$ is the total efficiency for the jth TX antenna and it can be calculated through

$$\eta_{t,Tj} = (1 - \sum_k |S_{kj,T}|^2)\eta_{r,Tj}, \tag{6.13}$$

where $S_{kj,T}$ is the S-parameter between the kth and the jth TX port, $\eta_{r,Tj}$ is the radiation efficiency of the jth TX port. The same definition is applied for the RX ports. For comparison, the average MIMO efficiency together with the S-parameters and the radiation efficiency for different MIMO systems are shown in Table 2. Here, the system with i.i.d. channel is assumed to be matched and decoupled and the radiation elements own 100% radiation efficiency, of which the result can be understood as the upper bound of the channel capacity of a 2×2 MIMO system. The simulated SNR at the receiver side is plotted in

Table 2: The average MIMO efficiency together with the S-parameters and radiation efficiency

Array type	$\|S_{11}\|$	$\|S_{21}\|$	$\|S_{22}\|$	$\eta_{r,1}$	$\eta_{r,2}$	η_{MIMO}
CNDN	0.27	0.54	0.27	100%	100%	40.5%
SNDN	0.11	0.29	0.11	100%	100%	81.6%
CEM	0.09	0.03	0.17	53%	75%	40.3%
CCM	0.09	0.12	0.09	80%	80%	61.15%
i.i.d.	0	0	0	100%	100%	100%

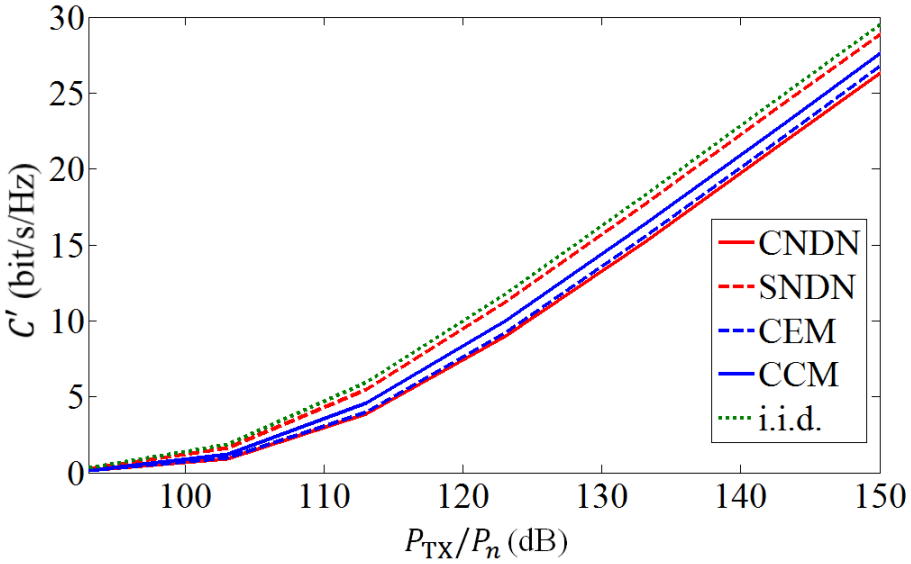

Figure 6.4: The average channel capacity of different MIMO systems for outdoor statistical model.

Figure 6.5. For the system with CEM arrays, the results of both ports are indicated due to its asymmetric configuration. As expected, the SNR at the odd mode port of the CEM array in the RX array is the lowest among all the systems. In this case, it is concluded that the multiport conjugate matching method shows the best performance for the MIMO systems with compact arrays. However, if low loss materials are utilized instead of FR 4, the channel capacity performance of the CEM array can be further improved. It can also be concluded that it is significant to implement matching and decoupling strategies to increase the average MIMO efficiency.

6.1.3 Simulation Simplification Based on Channel Correlation

It is reported in [Hui and Wang, 2010, Oestges, 2006] that it is possible to simplify the system simulation if the channel correlation is known. It is known that a random matrix with correlated entries can be generated by another random matrix with uncorrelated entries

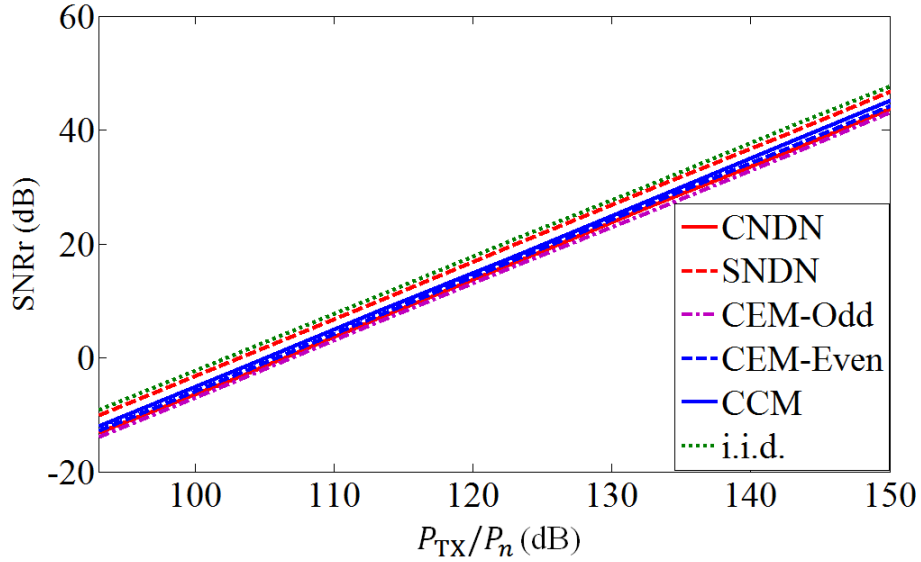

Figure 6.5: The SNR at each RX port of different MIMO systems.

through

$$\text{vec}(\mathbf{H}) = \mathbf{R}^{\frac{1}{2}}\text{vec}(\mathbf{H}_u), \tag{6.14}$$

$$\mathbf{R} = E[\text{vec}(\mathbf{H})\text{vec}(\mathbf{H}^H)], \tag{6.15}$$

where vec() is an operator which stacks the matrix into a vector column by column, $\mathbf{H}_u$ is a random matrix with uncorrelated entries, $\mathbf{R}$ is a $(M \times N) \times (M \times N)$ matrix of which the entries are the correlation coefficients between the entries of $\mathbf{H}$, e.g., $\mathbf{R}(1,2)$ is the correlation coefficient of h_{11} and h_{21}. As a result, once the channel correlation has been calculated, the normalized channel matrix can be derived in a simpler way. Then, by multiplying the relevant coefficients such as the channel gain, the channel matrix representing a certain communication system is generated and the channel capacity can be evaluated afterwards. This simplified modeling process is named as the Kronecker model.

Next, the channel correlation should be derived from the channel environment and the antenna radiation property. It is shown in Appendix C that the channel correlations can be approximated by the pattern correlations. The channel correlation coefficient is the multiplication of the far field radiation pattern correlation coefficient of the TX antennas and RX antennas, of which the amplitude is

$$|\rho_{ji,nm}| = |\rho'_{jn}||\rho'_{im}|, \tag{6.16}$$

where ρ'_{jn} is the pattern correlation coefficient between the jth and nth RX port and ρ'_{im} is the pattern correlation coefficient between the ith and mth TX port. The channel correlation between the channels with no TX and RX ports in common is the minimum

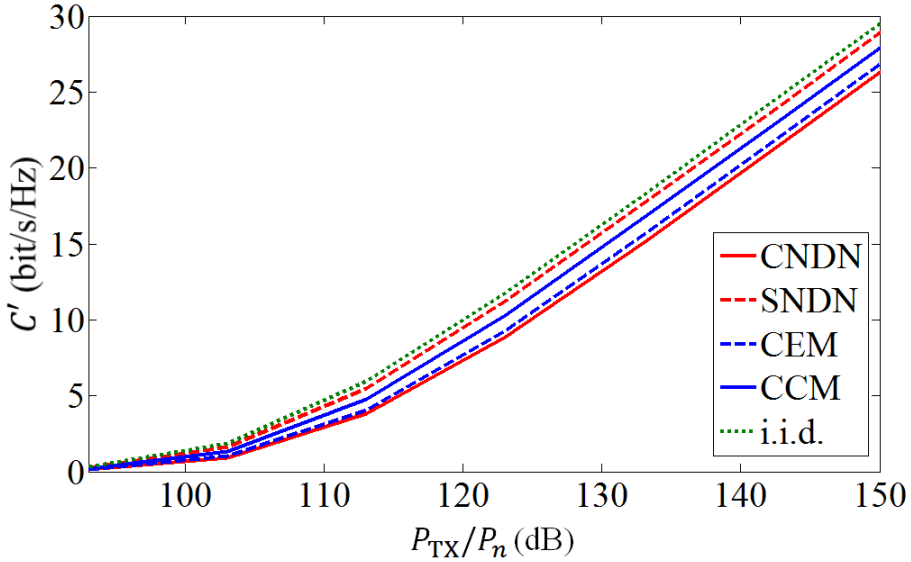

Figure 6.6: The average channel capacity of different MIMO systems based on the Kronecker model.

such as $\rho_{11,22}$ and $\rho_{12,21}$. However, the expectations of the obtained magnitude of all the channels according to equation (6.14) are unique, in order to show the influence from the MIMO transmission efficiency, the coefficients with respect to the port total efficiency and the channel gain should be multiplied with the channel coefficient according to equation (6.8),

$$h'_{ji} = \frac{1}{2}\sqrt{\frac{g\lambda^2}{4\pi}}\sqrt{\eta_{t,Ti}\eta_{t,Rj}}h_{ji}. \tag{6.17}$$

Afterwards, the channel capacity can be estimated by equation (6.6). In order to show the accuracy of this method, the channel capacity of different MIMO systems of which the results are shown in Figure 6.4 is analyzed again with the Kronecker model and the results are shown in Figure 6.6. Good agreement is found between the results of the two methods.

6.1.4 Embedded Keyhole Effect of Antenna Radiation Patterns

When the channel capacity is evaluated based on statistical models, it is not always true that low channel correlation leads to high channel capacity. For example, the keyhole effect was investigated in [Almers et al., 2006, Loyka and Kouki, 2002]. The keyhole effect means that the channel capacity is less than the expected result based on the Kronecker model, when the channels are of low correlation but with low degrees of freedom. In order to demonstrate the keyhole effect, the following situation is analyzed. For a particular communication environment of a MIMO system, it is assumed that the channel coefficients are always equal in magnitude and satisfy the Rayleigh distribution, while the phases of them

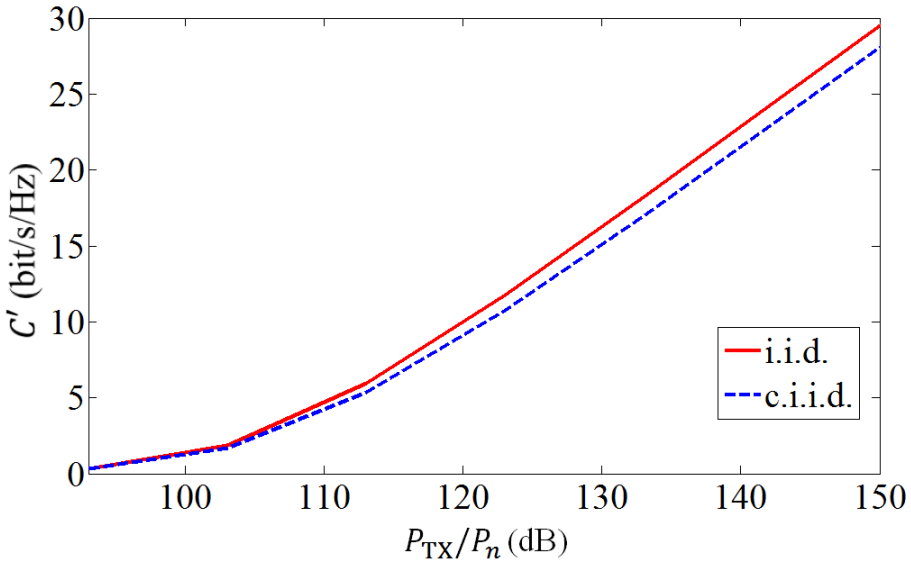

Figure 6.7: The average channel capacity of an i.i.d. model and a c.i.i.d model.

are random and independent from each other. So, mathematically, the channel coefficient can be expressed as

$$h_{ji} = |h_m| e^{j\psi_{ji}}, \tag{6.18}$$

where ψ_{ji} is a random phase constant from 0 to 2π and $|h_m|$ is the magnitude of all channel coefficients. Then, the condition

$$E[h_{ji} h_{nm}^*] = E[|h_m|^2] E[e^{j\psi_{ji}} e^{-j\psi_{nm}}] = 0 \tag{6.19}$$

exists. This channel property is named as conditional i.i.d. (c.i.i.d.). The simulated results of the corresponding 2×2 MIMO systems in MATLAB are plotted in Figure 6.7, where it is obvious that the channel capacity of the c.i.i.d. channel is lower than the i.i.d. channel. As a result, the conclusion is drawn that the previous Kronecker model might be inaccurate, because it is not able to extract the magnitude correlation from the channel correlation coefficient. This keyhole effect can be embedded in the radiation patterns, i.e., the power patterns of tow ports can be identical while the phase patterns of them are orthogonal.

6.2 Channel Capacity Analysis for Indoor Wireless Communications Based on a Statistical Model

In this section, the statistical MIMO channel capacity of indoor communication environments is evaluated. The approach exploited for the evaluation is based on the Saleh-Valenzuela (SV) model [Saleh and Valenzuela, 1987]. The capacity of 2×2 MIMO systems with different arrays is compared and a general method for performance prediction according to radiation patterns is addressed.

6.2.1 Introduction of the Saleh-Valenzuela Channel Model

The SV model was firstly proposed in [Saleh and Valenzuela, 1987], where a statistical model for an indoor multipath environment was introduced based on clustering assumptions. In [Saleh and Valenzuela, 1987], it is assumed that the received signals arrive in different time periods, which are recognized as different clusters. Each cluster can be understood as an arrival due to one of the multipaths. In one cluster, there are a certain number of rays due to scattering effects. It was observed in the experiments in [Saleh and Valenzuela, 1987] that the average received power decays exponentially with the time between the clusters and within one cluster. The impulse response of such a channel with L clusters and K rays in each cluster can be written in the form of

$$h(t) = \sum_{l=1}^{L} \sum_{k=1}^{K} g_{kl} \delta(t - T_l - \tau_{kl}), \tag{6.20}$$

with

$$\delta(x) = \begin{cases} 1, & x = 0 \\ 0, & x \neq 0, \end{cases} \tag{6.21}$$

where g_{kl} is the complex amplitude of the channel coefficient of the kth ray in the lth cluster, T_l is the time delay of the lth cluster and τ_{kl} is the time delay of the kth ray in the lth cluster with the assumption of $T_0 = 0$ and $\tau_{0l} = 0$. The magnitude of g_{kl} is assumed to be Rayleigh distributed and the average received signal power is expressed in the form of

$$P_{ave,kl} = E[|g_{kl}|^2] = E[|g_{00}|^2] e^{-T_l/\Gamma} e^{-\tau_{kl}/\gamma}, \tag{6.22}$$

where Γ and γ are defined as the cluster arrival decay time constant and the ray arrival decay time constant. Both of these two constants are closely related to the surrounding environment of the communication systems. The number of clusters depends on the number of multipaths, e.g., in a complex indoor environment with lots of scatterers, the average number of clusters should be more than the one in a simpler environment such as an empty office. The arrival of the rays and clusters can be treated as two independent Poisson processes with cluster arrival rate R and ray arrival rate r.

However, from the aspect of antenna designs, the models containing the spatial information are more attractive. In [Spencer et al., 2000], the spatial properties of indoor communication environments were investigated and a model expanded from [Saleh and Valenzuela, 1987] including both time and spatial information was shown. In the new model, the angle of arrival (AOA) and angle of departure (AOD) are considered and it was named as the SVA model in [Wallace and Jensen, 2002]. Then, the channel response can be rewritten as

$$h(t) = \sum_{l=1}^{L} \sum_{k=1}^{K} g_{kl} \delta(t - T_l - \tau_{kl}) \delta\left((\theta, \phi) - (\theta_l, \phi_l) - (\theta'_{kl}, \phi'_{kl})\right), \tag{6.23}$$

where (θ_l, ϕ_l) is the mean angle of the lth cluster and $(\theta'_{kl}, \phi'_{kl})$ is the angle referred to (θ_l, ϕ_l) of the kth ray in the lth cluster, of which the relationship is plotted in Figure 6.8.

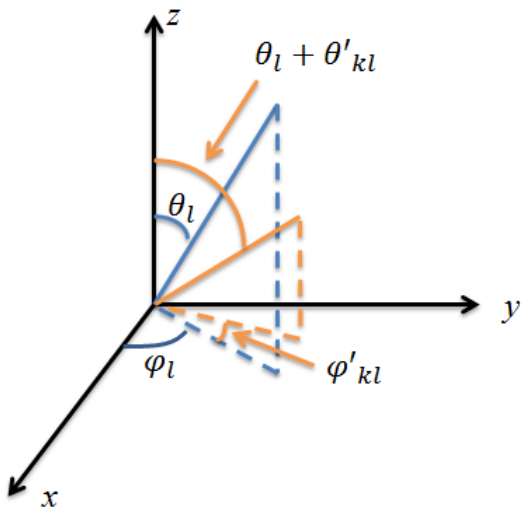

Figure 6.8: Indication of the clustering theory for the SVA model.

In [Spencer et al., 2000], it was proved through measurements that the received power from the transmitter is mostly confined in the paths in the horizontal plane if the RX and TX antennas are aligned with similar height, which reduces the complexity during the modeling. Assuming the xoy plane represents the horizontal plane, the AOA can be recognized as $(\pi/2, \phi_l)$ and $(\pi/2, \phi'_{kl})$. From the experimental observations in [Spencer et al., 2000], ϕ'_{kl} is a random value statistically satisfying the Laplacian distribution with zero mean and standard deviation σ. The value of σ depends on the particular communication environments as well.

6.2.2 Implementation of the Saleh-Valenzuela Channel Model with Angle Information

Based on the above introduction, narrow band evaluations of the channel performance are carried out. Since flat fading is assumed, the time domain expansion of the signal is neglected. Then, the channel response is

$$h(\theta, \phi) = \sum_{l=1}^{L} \sum_{k=1}^{K} g_{kl} \delta \left((\theta, \phi) - (\theta_l, \phi_l) - (\theta'_{kl}, \phi'_{kl}) \right). \tag{6.24}$$

Because the AOA is independent from the time of arrival, the power of the rays from different angles is also different. It is suggested in [Wallace and Jensen, 2002] that the ray power in every cluster should satisfy the Rayleigh distributed. The rule for the exponential decay still holds between clusters. However, equation (6.24) only contains the information of the RX array. In order to form the transmission matrix, it is assumed that the AOD

owns an identical distribution as the AOA and the transmission coefficient becomes

$$h = \sum_{l=1}^{L} \sum_{k=1}^{K} g_{kl} \delta\left((\theta^T, \phi^T) - (\theta_l^T, \phi_l^T) - (\theta_{kl}'^T, \phi_{kl}'^T)\right) \delta\left((\theta^R, \phi^R) - (\theta_l^R, \phi_l^R) - (\theta_{kl}'^R, \phi_{kl}'^R)\right), \tag{6.25}$$

where T and R denote the transmitting and receiving cases, respectively. The mean angle of each cluster is assumed to be independent and uniformly distributed in space. In order to obtain the channel matrix, equation (6.25) should be further calculated together with the antenna radiation properties.

Similar to equation (6.2), the transmitted signal of a ray from the ith TX antenna in the horizontal plane with a beamwidth $\triangle\Omega(\pi/2, \phi_i)$ is defined as

$$t_{i,p}(\pi/2, \phi_i) = a_i \sqrt{\frac{(1 - \sum_k |S_{ki,T}|^2)}{8\pi}} \sqrt{\triangle\Omega(\pi/2, \phi_i)} (\sqrt{G_{i,p}} F_{i,p}(\pi/2, \phi_i)), \tag{6.26}$$

where p denotes two orthogonal polarization components, 1 and 2, and $F_{i,p}$ is again the normalized radiation pattern. The received signal of a ray for the jth RX element is

$$b_{j,p1} = \sqrt{\frac{\lambda^2(1 - \sum_k |S_{kj,R}|^2)}{2\pi}} \left(\sqrt{G_{j,p1}} F_{j,p}(\pi/2, \phi_j)\right) (\cos(\psi_1) h_{ij,p1}(\phi_i, \phi_j) t_{i,p1} + \sin(\psi_2) h_{ij,p2}(\phi_i, \phi_j) t_{i,p2}), \tag{6.27}$$

$$b_{j,p2} = \sqrt{\frac{\lambda^2(1 - \sum_k |S_{kj,R}|^2)}{2\pi}} \left(\sqrt{G_{j,p2}} F_{j,p}(\pi/2, \phi_j)\right) (\sin(\psi_1) h_{ij,p1}(\phi_i, \phi_j) t_{i,p1} + \cos(\psi_2) h_{ij,p2}(\phi_i, \phi_j) t_{i,p2}), \tag{6.28}$$

where $h_{ij,p}(\phi_i, \phi_j)$ is the transmission coefficient between the ray of departure and the ray of arrival, which is assumed to be Rayleigh distributed in magnitude. $\psi 1$ and $\psi 2$ are two independent random values uniformly distributed from 0 to 2π, which are used to represent the polarization mismatch. Considering the indoor environment, two physical effects are dominant during the wave propagation, reflection and diffraction, as shown in Figure 6.9. For most of the materials, the power reflection coefficient and the diffraction loss are not polarization dependent, but the phase change after reflection or diffraction is quite sensitive to polarization [Balanis, 1989]. Under these circumstances, it is defined in the simulation that $|h_{ij,p1}| = |h_{ij,p2}|$. However, the phase difference between the two coefficients is random and uniformly distributed from 0 to 2π. Considering the power conservation, two arrival rays from the same cluster or different clusters might be from the same departure ray. If so, the ray power should be normalized by a factor X, which is the number of the occurrences of a transmitted ray at the receiver.

As discussed before, multipath transmissions are mainly distributed in the horizontal plane, so in equation (6.25) the calculation is based on the global coordinates, in which

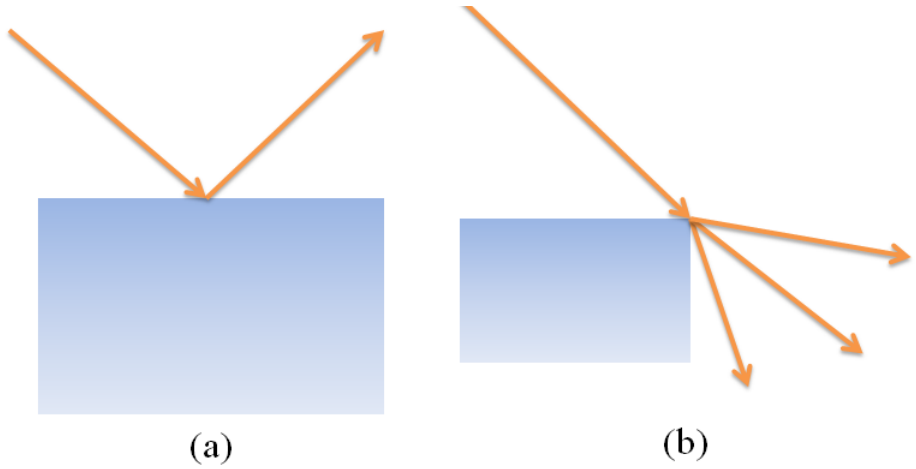

Figure 6.9: Two possible physical effects on the wave propagation channel:(a) reflection; (b) diffraction.

the *xoy* plane is the horizontal plane. However, in reality, the antenna arrays can be randomly rotated. Therefore, certain transformations from the antenna radiation pattern local coordinates to the global coordinates should be carried out.

According to the above discussions, the simulation process of an SVA indoor channel model can be summarized as follows: a) choose the basic parameters such as frequency, mean cluster number, mean ray number, exponential decay constant, the standard deviation of the AOA and AOD and so on; b) randomly select a cut plane of the radiation pattern of the antennas for the TX and RX array, respectively; c) set up the cluster and ray distributions according to the Poisson process; d) generate the channel matrix according to equations (6.24) to (6.28); e) repeat step b) to d) with adequate runs to obtain the statistical result of the channel capacity.

6.2.3 Simulation Results of the Saleh-Valenzuela Channel Model with Angle Information

In this subsection, the channel performances of the MIMO systems with the two-element compact antenna arrays operating at 2.45 GHz are evaluated and compared based on the SVA model. The significance of the power matching has already been addressed in the previous section. Therefore, in this part, the effects on the channel capacity from antenna radiation patterns are investigated, where the influences from the power mismatch and losses are extracted.

For the first simulation, the mean cluster number is chosen as 3 and the mean ray number in each cluster is chosen as 10. The standard deviation of the ray angular distribution is 26°, the beamwidth of a ray direction is chosen as 5° in elevation and 1° in azimuth. The average path gain of the first cluster is assumed to be -30 dB and the decay rate is 2 (fast decay) which is the ratio between the cluster arrival period and the cluster decay constant.

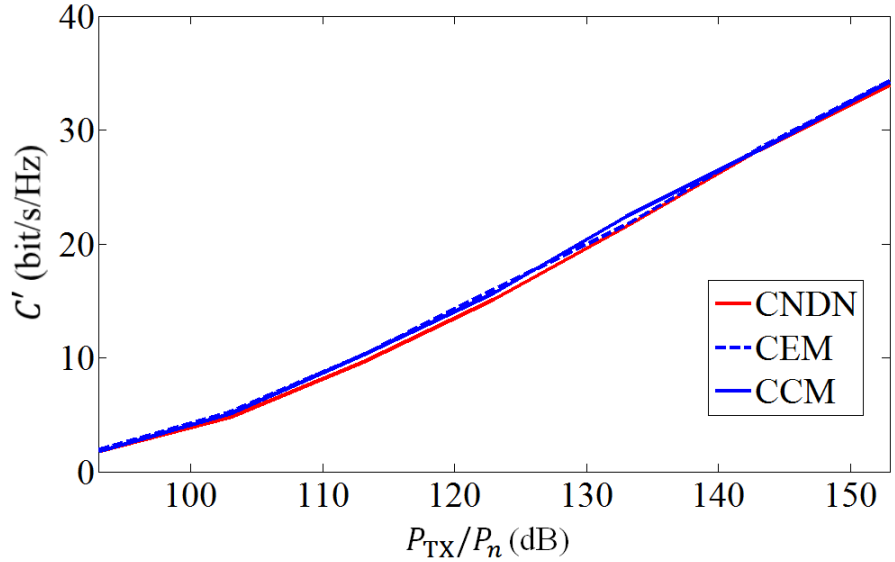

Figure 6.10: The average channel capacity for the indoor statistical model, of which the decay rate is 2 and the mean cluster number is 3.

The power is set to be evenly allocated among the ports in the TX array. The simulated channel capacity is shown in Figure 6.10 with the ratio between the total transmitted power and the noise power at one RX port. It is noticed that the results are quite close between the systems based on different arrays. The slight differences are discussed later in the following subsection.

The second simulation was performed by changing the mean cluster number to 10 and the mean ray number in one cluster to 20, and the decay rate to 1 (slow decay). The simulation results are shown in Figure 6.11 and the performances of the three systems are still similar. However, compared to the first simulation, it is found that the channel capacity is increased. One reason is that the decay rate is reduced and more power can be received by the RX array. The second reason could be due to the increase of the cluster and ray numbers. For proving this, a third simulation was performed, of which both the mean cluster number and the mean ray number were increased to 30, while the rest parameters are the same as in the second simulation. For instance, the change of the channel capacity for the system based on the CEM array is plotted in Figure 6.12, where a 1 bit/s/Hz increase is seen.

6.2.4 Evaluation of the Channel Capacity Performance Based on Radiation Patterns

The channel correlation is related to the statistical capacity performance according to the discussion in the previous section. For a fixed cluster distribution, the channel correlation can be obtained through calculating the sum of the weighted ray correlations [Wallace and Jensen, 2002]. In this subsection, the average channel correlation due to a

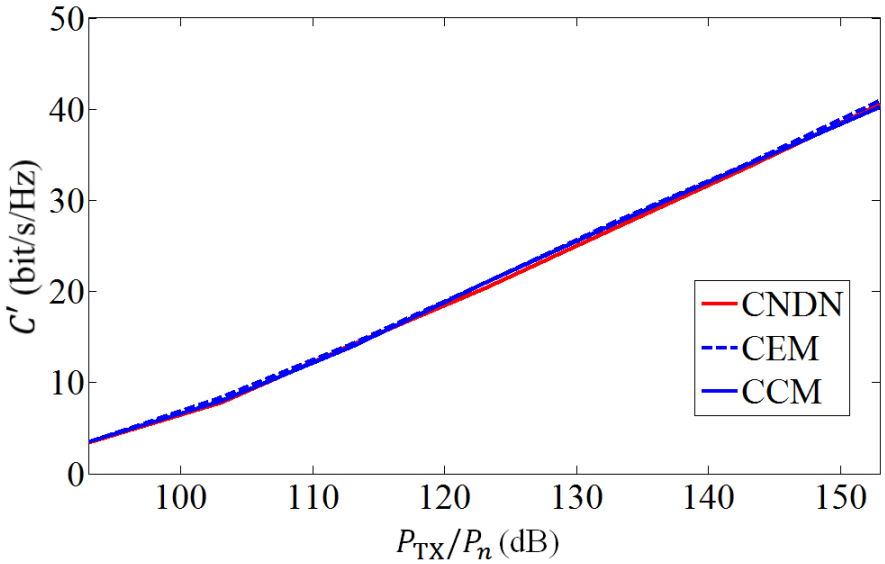

Figure 6.11: The average channel capacity for indoor statistical model, of which the decay rate is 1 and the mean cluster number is 10.

larger number of experiments is evaluated.

Since the mean angles of different clusters are uniformly distributed, the channel correlation between the channels with different TX ports (port i and k) but the same RX element (port j) $\rho_{ji,jk}$ can be expressed as

$$\rho_{ji,jk} = \frac{\sum_{n=1}^{L} e^{-\frac{(L-1)}{\Gamma\Lambda}} E[(\vec{F}_i(\theta_n,\phi_n)\cdot\vec{h}(\theta_n,\phi_n))(\vec{F}_k(\theta_n,\phi_n)\cdot\vec{h}(\theta_n,\phi_n))^*]}{\sqrt{\sum_{n=1}^{L} e^{-\frac{(L-1)}{\Gamma\Lambda}} E[|\vec{F}_i(\theta_n,\phi_n)\cdot\vec{h}(\theta_n,\phi_n)|^2]}\sqrt{\sum_{n=1}^{L} e^{-\frac{(L-1)}{\Gamma\Lambda}} E[|\vec{F}_k(\theta_n,\phi_n)\cdot\vec{h}(\theta_n,\phi_n)|^2]}}, \tag{6.29}$$

where (θ_n,ϕ_n) is the mean angle of the nth cluster, $\vec{h}(\theta_n,\phi_n)$ is the channel coefficient to the direction of (θ_n,ϕ_n). $\vec{h}(\theta_n,\phi_n)$ contains two orthogonal polarization elements and it is expressed in the form of

$$\vec{h}(\theta_n,\phi_n) = h_\theta(\theta_n,\phi_n)\vec{e}_\theta + h_\phi(\theta_n,\phi_n)\vec{e}_\phi. \tag{6.30}$$

As discussed before, the channel is Rayleigh like and independent from the choice of the mean angle of a cluster, so that the condition

$$\begin{aligned} &E[(\vec{F}_i(\theta_n,\phi_n)\cdot\vec{h}(\theta_n,\phi_n))(\vec{F}_k(\theta_n,\phi_n)\cdot\vec{h}(\theta_n,\phi_n))^*] \\ =&E[\vec{F}_i(\theta_n,\phi_n)\cdot\vec{F}_k{}^*(\theta_n,\phi_n)]E[|\vec{h}(\theta_n,\phi_n)|^2] \end{aligned} \tag{6.31}$$

exists. It is obvious that $E[|\vec{h}(\theta_n,\phi_n)|^2]$ is constant for all directions. For all the clusters, it is found that

$$E[\vec{F}_i(\theta_n,\phi_n)\cdot\vec{F}_k{}^*(\theta_n,\phi_n)] = E[\frac{\sum_{m=1}^{M}\vec{F}_i(\theta_{n,m}\phi_{n,m})\cdot\vec{F}_k{}^*(\theta_{n,m},\phi_{n,m})}{M}] \approx \int \frac{1}{4\pi}\vec{F}_i\cdot\vec{F}_k{}^* d\Omega, \tag{6.32}$$

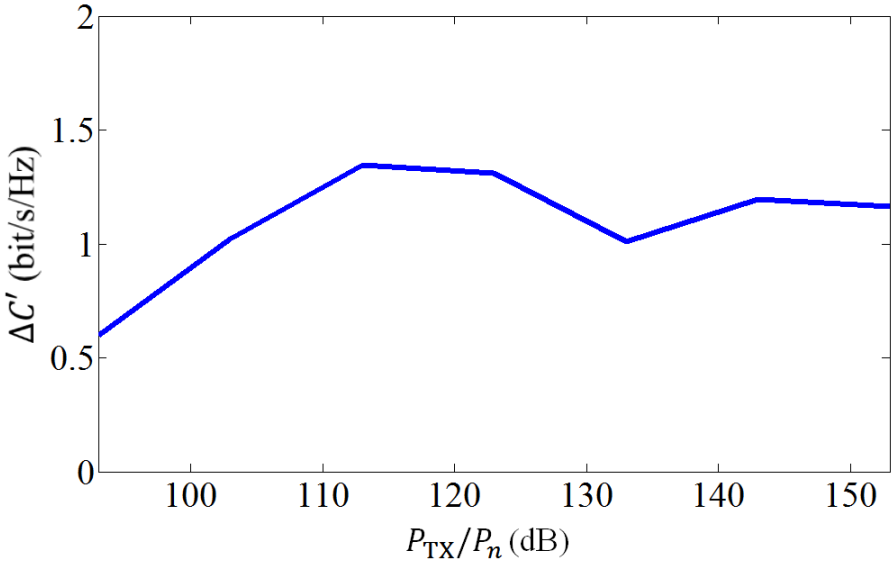

Figure 6.12: The increase of the average channel capacity of the MIMO system based on CEM array for different cluster numbers.

where $(\theta_{n,m}, \phi_{n,m})$ is the direction of the mth ray in the nth cluster. By utilizing the above equations and relationships, equation (6.29) is further simplified as

$$\rho_{ij,kj} = \frac{\int \vec{F}_i \cdot \vec{F}_k^{\,*} d\Omega}{\sqrt{\int |\vec{F}_i|^2 d\Omega}\sqrt{\int |\vec{F}_k|^2 d\Omega}}, \tag{6.33}$$

which is actually the pattern correlation coefficient of the TX antennas. Therefore, for statistical indoor channel models, the channel correlation can be estimated through the radiation pattern correlation as well. However, different from the outdoor case, the channel correlation is not adequate for evaluating the channel performance due to a limited number of clusters. For example, if there is only 1 cluster at a particular direction, the radiated power from one element in the TX array might be very low. In such a case, the multiple output becomes a single output for a 2×2 MIMO communication system, which degrades the channel capacity. To describe this mathematically, in this thesis, a parameter named average 'on-off' ratio of the pattern is utilized. The 'on-off' ratio is defined as

$$r_{ik} = \int \frac{1}{4\pi} \frac{||\vec{F}_i| - |\vec{F}_k||}{|\vec{F}_i| + |\vec{F}_k|} d\Omega. \tag{6.34}$$

The maximum value of r is 1, which means, for all directions when one antenna is 'on' (radiating), the other one is 'off' (no radiation). If the cluster number is larger than 1, the probability of complete 'on-off' is reduced by $\frac{1}{2^{(L-1)}}$. Therefore, the 'on-off' ratio is redefined by considering the effect of the number of clusters,

$$r_{ik} = \frac{1}{2^{(L-1)}} \int \frac{1}{4\pi} \frac{||\vec{F}_i| - |\vec{F}_k||}{|\vec{F}_i| + |\vec{F}_k|} d\Omega. \tag{6.35}$$

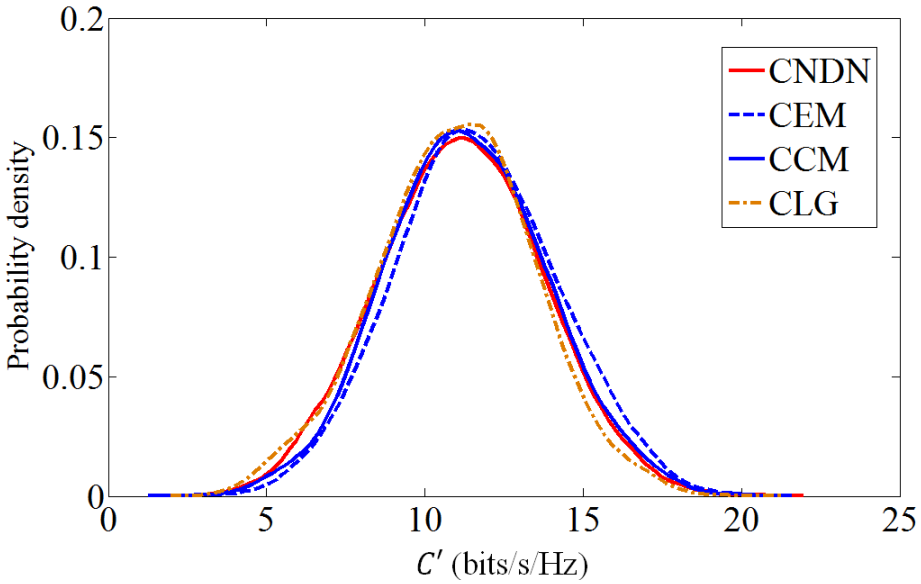

Figure 6.13: The probability density distribution of the average channel capacity for MIMO systems with different arrays.

According to the above discussions, a more general parameter for evaluating the indoor statistical channels based on the radiation patterns is defined as

$$\xi = \rho_T \rho_R + r_T r_R, \tag{6.36}$$

where T and R stand for the TX and RX array, respectively.

In order to verify the derivations, an investigation is carried out based on the first simulation in the last subsection and the following parameters are modified, i.e., the number of clusters is set to 1 and the decay rate is chosen as 1. Other than the systems with the above mentioned three antenna arrays, a system based on compact arrays with a large ground plate in the middle between the two elements (CLG), is also simulated. The dimension of the inserted ground plane is 150 mm $\times$ 150 mm as shown in Figure 6.14. The CLG array represents the case with high on-off ratio but low pattern correlation. The simulated probability density is shown in Figure 6.13 at $P_{\mathrm{TX}}/P_n = 113$ dB. The system with the CEM array shows the best performance and the one with the CLG array is the worst. For details, the related parameters are described in Table 3. In consequence, the results of the simulation with 3 clusters are shown in Table 4. The results show good agreement with the evaluation parameters derived in equation (6.36).

6.3 Channel Capacity Analysis for Indoor Wireless Communications Based on Ray Tracing

In this section, the channel capacities of the MIMO systems with different arrays are analyzed based on the ray tracing method.

Table 3: Parameters for evaluating the channel capacity performance with 1 cluster

Array Type	Channel Capacity	Correlation Coefficient	On-Off Ratio	ξ
CNDN	11.2 bit/s/Hz	0.39	0.09	0.16
CEM	11.6 bit/s/Hz	0.04	0.2	0.04
CCM	11.2 bit/s/Hz	0.12	0.32	0.12
CLG	10.9 bit/s/Hz	0.03	0.58	0.33

Table 4: Parameters for evaluating the channel capacity performance with 3 clusters

Array Type	Channel Capacity	Correlation Coefficient	On-Off Ratio	ξ
CNDN	13.6 bit/s/Hz	0.39	0.05	0.15
CEM	14.1 bit/s/Hz	0.04	0.1	0.01
CCM	13.9 bit/s/Hz	0.12	0.16	0.04
CLG	14.0 bit/s/Hz	0.03	0.27	0.08

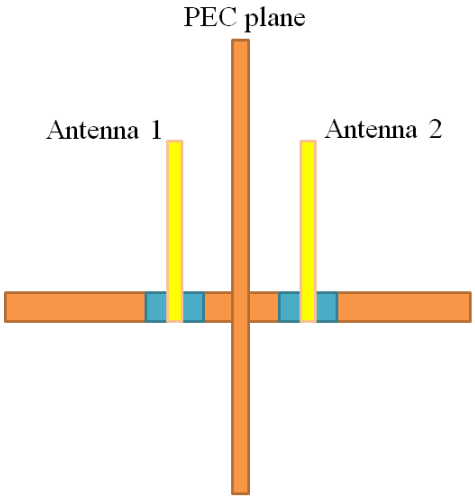

Figure 6.14: Two-element compact monopole array with a large ground plane in the middle.

6.3.1 Introduction to the Ray Tracing Method

Ray tracing is a convenient simulation and modeling tool to approximate electromagnetic wave propagation [McKown and Hamilton, 1991]. The ray tracing method is able to solve forward propagation problems in a more efficient manner as compared to conventional computational electromagnetics methods and the achieved accuracy is promising as well. The basic theories for realizing electromagnetic ray tracing are Geometrical Optics (GO), Geometrical Theory of Diffraction (GTD) and Uniform Geometrical Theory of Diffraction (UTD) which is an improved version of GTD. GO is deployed to model the propagation of locally plane electromagnetic waves in the form of optical rays. In homogeneous medium, the ray should be straight forward with a certain direction. When the ray travels from one medium to another, effects such as reflection, transmission and refraction take place. Physical theories such as the Fresnel equations are applied in the simulation tools. How-

ever, GO is not able to treat diffraction problems, which are caused by the discontinuity of scattering structures such as edges. One ray can be diffracted into several rays and this can be solved through GTD and UTD. Besides, UTD is able to calculate the fields at the shadow boundaries, which cannot be obtained through GTD [Fuertes Pals, 2014].

The ray tracing software exploited in this section has been developed by the Chair of High-Frequency Engineering, Chair of Robotics and Embedded Systems at Technische Universität München together with AUDI AG Ingolstadt [Mocker et al., 2015]. The computation process of this ray tracing software is carried out on Graphics Processing Units (GPUs). Compared to previous programs based on Central Processing Units (CPUs), the new technique is much more efficient since the GPU is quite advantageous in parallel computations. In this software, a certain number of rays is launched from the transmitter with random directions according to the Shooting and Bouncing Rays (SBR) method. The rays from the TX antenna are utilized by the radiation pattern of the antenna, e.g., the power density of the ray is referred to the radiated electric field from an antenna at a certain distance from the phase center. The rays hit the scattering objects and they are reflected, refracted and diffracted. Most of the rays meet a power attenuation constraint and terminate then. Some of the rays are received by the RX antennas. Considering the receiving process, a sphere with a certain radius is utilized as the effective receiving area. The rays hitting this sphere are considered as rays to be received. The size of the sphere should be neither too large nor too small due to the matter of accuracy. The choice of the radius of the sphere is based on certain rules described in [Fuertes Pals, 2014], which depend on the angular sampling rate of the rays and the distance between the TX and RX antennas. However, only one ray among the rays from the same wave front should be considered in the RX sphere. Generally, the one closest to the RX phase center is taken into account.

In the following simulations, the far field radiation patterns from CST MWS are exported as the one of the source files. The simulation configuration is constructed in Blender software [Blender, 2015]. 100000 rays are set to be launched from the TX antenna. In the configuration, concrete is selected as the material for the reflectors (walls), of which the complex relative permittivity is $5 - 0.1j$. The reflection and diffraction orders are chosen according to different scenarios, which means that after certain numbers of reflections or diffractions, the rays are no longer considered in the simulation.

6.3.2 Simulation Results Based on the Ray Tracing Method

The MIMO systems with different monopole antenna arrays such as the compact array without decoupling network (CNDN), the compact array based on eigenmode excitation (CEM), and the compact array based on conjugate matching (CCM), are investigated for the indoor environments based on the ray tracing software.

A. Room Scenario

In this part, a scenario for an empty room is utilized for investigation. The room is modeled as a cuboid, which is 6 m wide, 8 m long and 4 m high. The center of the cuboid is selected as the origin point of the coordinate system. The range of the cuboid on the

x, y, z axis is [-3, 3], [-4, 4], [-2, 2], respectively, of which the units are meter. Figure 6.15 indicates the simulation model. The TX antenna array is fixed at the position (0, -3, 0). The RX array is positioned in the xoy plane and moves along two trails. One of the trails is defined along the y axis from (0, 0, 0) to (0, 2.4, 0). The other one is along the x axis from (-2.3, 1.5, 0) to (2.3, 1.5, 0).

Similar to the last sections, only the effect from the radiation patterns is considered in the simulation, while the influences from power mismatch and losses are extracted in the post processing. The radiation elements of the arrays are aligned in parallel with the x axis in Figure 6.15. This is reasonable for obtaining the optimal total transferred power. The movement step along the trails is chosen as 0.1 m. In this model, the limitation of the reflection numbers are chosen as 2. For calculating the channel capacity, it is assumed that the ratio between the total transmitted power and the noise power at each port is 100 dB.

Figure 6.16 shows the ray tracing result for a certain RX position. All the rays received by the RX sphere are indicated in this figure. The yellow lines denote the launched rays and the green lines around the RX sphere are the received rays due to the direct path and due to reflections. According to the Friis equation and the phase of the propagation, the complex transmission coefficient of each ray is calculated and then by summing up all the transmission coefficients, the channel coefficient is obtained. The channel capacity is evaluated consequently.

The calculated channel capacity for the RX array in the trail along the y axis is plotted in Figure 6.17. It is noticed that when the RX array is located at (0, 0, 0), the systems with the CEM array and the CCM array show similar performance. However, with increasing the distance between the TX and RX arrays, the channel capacity of the system with the CEM array decays much faster than the one with the CCM array. The system with the CNDN array shows the lowest capacity. On the other hand, for the case that the RX array moves on the trail along the x axis, the channel capacity is plotted in Figure 6.18. Along the trail, the system with the CCM array shows the highest channel capacity and the curve in the figure is quite flat. The system with the CEM array also owns good performance, but it varies a lot for different positions. The obtained channel capacity of the system with the CNDN array is again much lower. It is concluded that in such a room scenario the CCM array is the best candidate for realizing MIMO systems with high channel capacity. The possible explanation for this is that the radiation patterns of the elements of the CCM array own good angular diversity, e.g., the monopole on the left radiates mostly towards the left. As a result, the channel matrix due to the first order reflection, which is the strongest signal path other than the direct path in the room scenario, is always diagonal and it ensures good MIMO performance according to the knowledge in Chapter 3.

B. Corridor Scenario

In this part, a corridor scenario is investigated, which is more complicated compared to the room scenario due to multiple reflections and diffraction. The corridor model exploited for the simulation is shown in Figure 6.19. The corridor is formed by two cuboids centered at the same point. The dimension of the inner cuboid is 8 m in length and width and 4 m in height, while the dimension of the outer one is 12 m in length and width and 4 m in

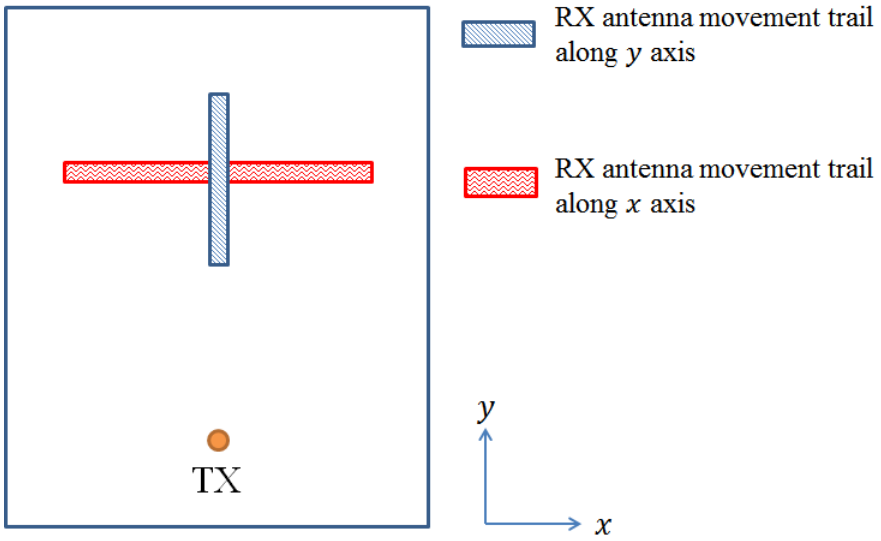

Figure 6.15: The model of the room scenario utilized for the ray tracing software.

height. Then, the 2 m wide and 4 m high corridor is formed. The TX array is located at (0, -5, 0) and the RX array is set to move along the trail as shown in Figure 6.19. The trail starts from the point (-5, -3.5, 0) and ends at the point (-5, 3.5, 0). For the TX array, the monopoles are aligned in parallel with the y axis and for the RX array, they are aligned along the x axis.

In the corridor model, the transmitted signal experiences more reflections until it reaches the receiver, so that the maximum number of reflections is set to 8 in the ray tracing software. The four edges along the z axis of the inner cuboid can diffract the rays, so diffraction effects are considered as well and the maximum number of the diffractions is set to 1. The ray tracing result is plotted in Figure 6.20, where the pink lines denote the diffracted rays and the edges in the orange color are the diffraction edges. In consequence, the channel coefficients are obtained through simulations. Figure 6.21 depicts the calculated channel capacity for the systems with different arrays. The ratio between the total transmitted power and the noise power at each port is 100 dB. All the systems show very fast decay when the RX array moves further away from the TX array, e.g., after point (-5, 0, 0) the channel capacity becomes almost 0. However, the MIMO system based on the CCM array still shows better performance, while the systems based on the CEM array and the CNDN array obtain comparable results. Therefore, the radiation patterns of the CCM array are more advantageous in terms of channel capacity for both room and corridor scenarios according to the results from the ray tracing method. This is because the patterns of the two ports of the CCM array are symmetric and with good angular diversity, while the pattern of the odd mode of the CEM array is quite directive. As a result, the CCM array performs better than the CEM array for indoor MIMO systems.

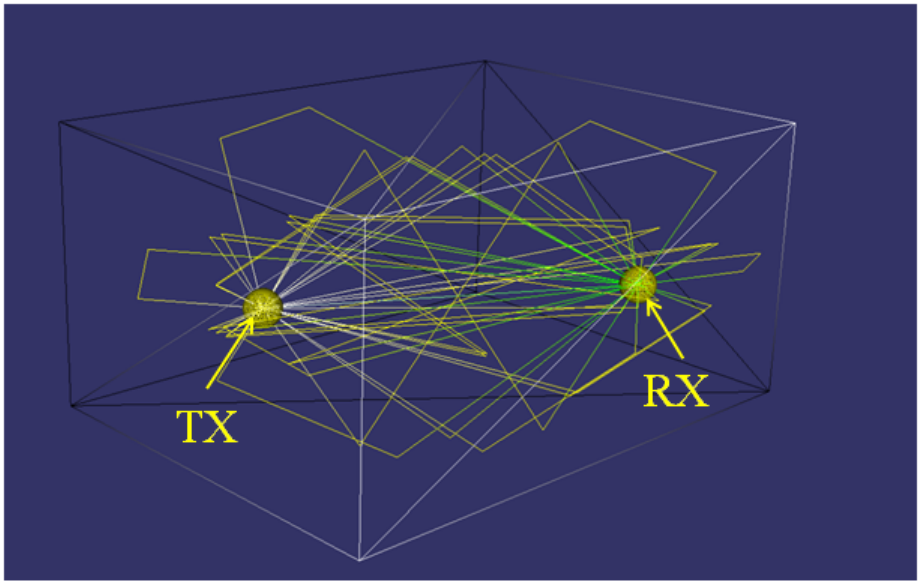

Figure 6.16: Ray tracing result for the room scenario.

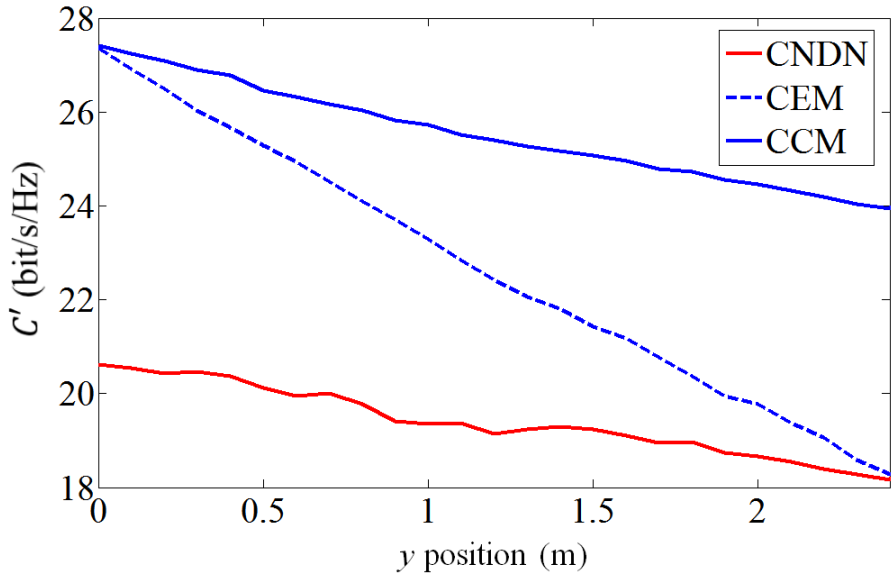

Figure 6.17: The calculated average channel capacity for the room scenario with the RX trail along the y axis.

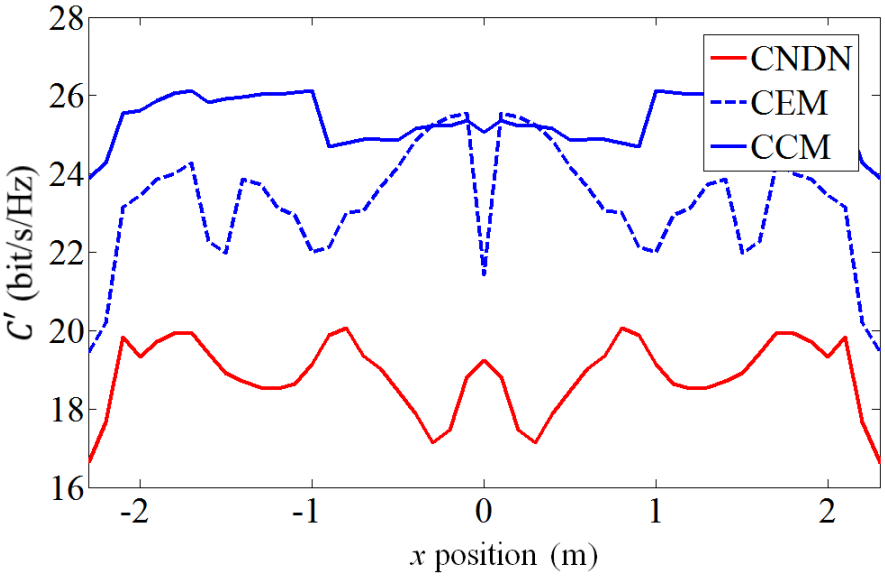

Figure 6.18: The calculated average channel capacity for the room scenario with the RX trail along the x axis.

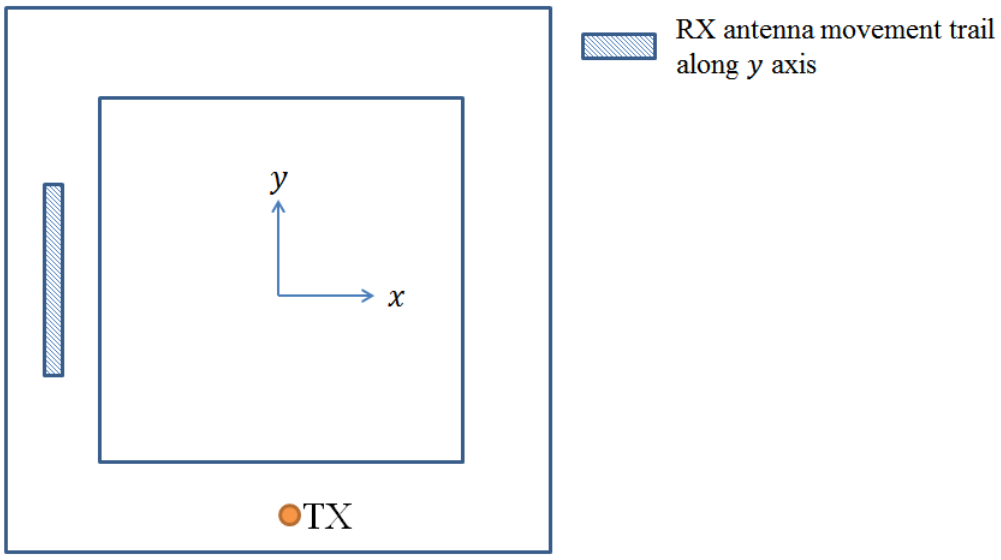

Figure 6.19: The model of the corridor scenario utilized within the ray tracing software.

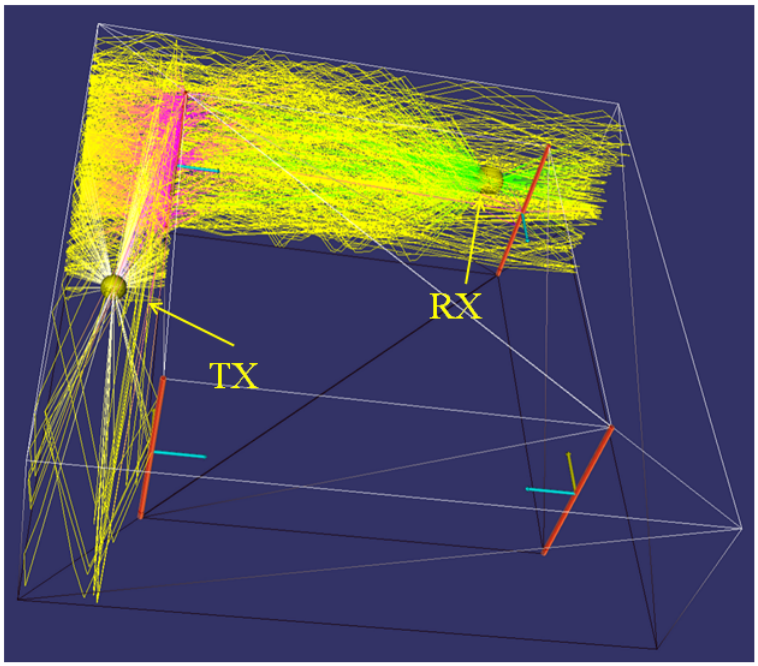

Figure 6.20: Ray tracing result for the corridor scenario.

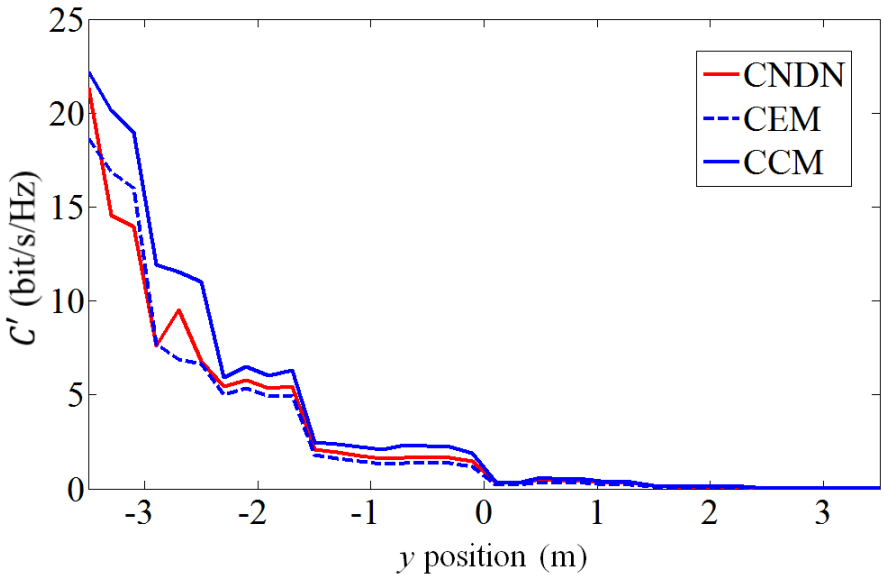

Figure 6.21: The calculated average channel capacity for the room scenario with the RX trail along the y axis.

7 Summary and Outlook

In this thesis, detailed investigations and performance improvements of multiple input multiple output antenna arrays were carried out. Several types of novel compact antenna arrays were analyzed, designed, manufactured, measured and evaluated. Through the properly designed matching and decoupling approaches, very good MIMO performance has been obtained. In the following, all the chapters are briefly summarized. Afterwards, a short outlook of the relative work in this field is presented.

The background of this thesis was discussed in Chapter 1 and the overview of the thesis was also described.

In Chapter 2, the relevant antenna basics were introduced. The antenna development history was shortly summarized. Later on, basic and important parameters for antennas such as gain and radiation efficiency, which are required for this thesis, were illustrated and some of them were derived as well.

The discussions with respect to the purposes and advantages of utilizing multiple radiation elements in wireless communication systems were carried out in Chapter 3. The channel capacity was counted as an evaluation standard for wireless communication systems. It was proved mathematically that multiple antennas are beneficial in obtaining large capacity within a limited frequency band. Based on the mathematical descriptions of channel capacity, matching and decoupling were found important for compact array designs. Meanwhile, it was also proved that the pattern correlation should be kept as low as possible to ensure the diversity performance of the antenna array.

Chapter 4 was dedicated to the study of compact monopole antenna arrays with matching and decoupling networks. Two two-element compact monopole arrays and a four-element array were designed based on two theories, the eigenmode excitation and the multiport conjugate matching, which were mathematically derived as well. These two methods were compared and discussed and interesting conclusions were drawn. The relationship between them was investigated and it was found that the antenna excitation through the multiport conjugate matching can be decomposed by even and odd modes. The connection between the radiation pattern correlation coefficient and the scattering matrix were proved and a new approach with good accuracy for estimating the pattern correlation was developed, which is in particular suitable for the arrays with lossy matching and decoupling networks. Beamforming applications of compact arrays were also studied. It was shown that beamforming for compact arrays can be different compared to conventional arrays, e.g., for a certain array size, exciting three elements shows better directivity than the case of five elements in the broadside direction of the array.

In Chapter 5, decoupling approaches for printed antennas were investigated. Firstly, printed monopole arrays were studied. The partially extended ground plane was found an simple and efficient solution for reducing the coupling. Some additional ground plane modifications were also carried out to regularize the radiation pattern of the monopoles. Based on this, a three-element compact printed antenna array with combined antenna types was designed as well. Later on, a novel approach for designing compact antennas occupying little space was developed. The designed antennas can be integrated at the contour of

mobile devices. Several novel approaches for matching and decoupling were addressed. All the antenna elements and arrays show promising performance.

The evaluation of the compact array performance based on channel capacity was performed in Chapter 6. The statistical models for outdoor and indoor communications were exploited firstly. It was shown that the power matching is of great significance for achieving high channel capacity. Afterwards, the power was normalized for all the arrays and the effects of the radiation patterns were investigated. For statistical models, it was found that the pattern correlation is directly related to the average capacity. For the indoor communications it was derived that a parameter named pattern on-off ratio is also influential. Finally, ray tracing method was deployed for analyzing the deterministic channel capacity for room and corridor scenarios.

With the development of wireless communications, more and more studies and investigations in this field are required. Here, a short outlook is presented. Firstly, implementing more antenna elements in small mobile terminals for lower frequency bands such as the LTE 700 MHz is still quite challenging. Secondly, the antenna array designs for Massive MIMO applications are also difficult, since it requires more effort to achieve matching and decoupling for a great number of radiation elements within a limited available area [Hoydis et al., 2013, Larsson et al., 2014]. Last but not least, for the coming generation of wireless communications, millimeter wave antennas are highly demanded, so that consequent researches for millimeter wave antenna arrays should be carried out. For example, proper antenna arrays for enhancing the receiving power with a wide receiving angular range are currently designed at the Chair of High-Frequency Engineering at Technische Universität München [Wang et al., 2015d].

Appendix A

Gain and Efficiency for Compact Antenna Arrays

For an N-port MIMO antenna array, the accepted power by the array from the ith port is defined as

$$P_{\mathrm{ac},i} = P_{\mathrm{in},i} - \sum_{j=1}^{N} |S_{ji}|^2 P_{\mathrm{in},i}, \tag{A.1}$$

where $P_{\mathrm{in},i}$ is the input power of the ith port. Due to the mutual coupling, a multiport matching efficiency is defined as the ratio between the accepted power and the input power,

$$\eta_{M,i} = \frac{P_{\mathrm{ac},i}}{P_{\mathrm{in},i}} = 1 - \sum_{j=1}^{N} |S_{ji}|^2. \tag{A.2}$$

The radiation efficiency is still defined as the ratio of the radiated power and the accepted power, which is

$$\eta_{r,i} = \frac{P_{\mathrm{rad},i}}{P_{\mathrm{ac},i}}, \tag{A.3}$$

with

$$P_{\mathrm{ac},i} = P_{\mathrm{rad},i} + P_{\mathrm{loss},i}. \tag{A.4}$$

$P_{\mathrm{loss},i}$ is the power loss in the antenna array when the ith port is excited and the remaining ports are loaded with the port impedance. It should be noted that if other ports are terminated with other impedances, the power losses can be different. As a result, in this definition, it is required that the remaining ports are loaded with 50 Ω. Based on the above equations, the total efficiency is defined as the ratio between the radiated power and the input power as

$$\eta_{t,i} = \frac{P_{\mathrm{rad},i}}{P_{\mathrm{in},i}} = \eta_{M,i}\eta_{r,i}. \tag{A.5}$$

The radiation pattern of one port of the MIMO array is obtained with all the other ports loaded. Under such conditions, the gain of the ith port is defined as

$$G_i(\theta, \phi) = D_i(\theta, \phi)\eta_{r,i}, \tag{A.6}$$

where $D_i(\theta, \phi)$ is the directivity of the ith port. However, during the antenna measurement of the gain of MIMO arrays, when the other ports are terminated, the directly measured value is not the desired result. The actual value for the so called IEEE gain can be calculated through

$$G_i(\theta, \phi) = G_{m,i}(\theta, \phi)\frac{1 - |S_{ii}|^2}{1 - \sum_{j=1}^{N} |S_{ji}|^2}, \tag{A.7}$$

where $G_{m,i}(\theta, \phi)$ is the directly measured result.

Appendix B

Provement of Multiport Conjugate Matching

Based on SVD, the scattering matrix of a $2N$-port can be decomposed as

$$\mathbf{S}_{ij,N} = \mathbf{U}_{ij,N}\mathbf{D}_{ij,N}\mathbf{V}_{ij,N}^{H}. \tag{B.1}$$

As described in Chapter 3, $\mathbf{U}$ and $\mathbf{V}$ are unitary matrices of which the columns are the eigenvectors of $\mathbf{S}\mathbf{S}^{H}$ and $\mathbf{S}^{H}\mathbf{S}$, respectively. $\mathbf{D}$ is a diagonal matrix of which the entries are the square root of the eigenvalues of $\mathbf{S}\mathbf{S}^{H}$ in descent order. Then, the first condition in equation (4.23) can be written in the form of

$$\mathbf{V}_{11,N}\mathbf{D}_{11,N}^{H}\mathbf{U}_{11,N}^{H}\mathbf{U}_{11,N}\mathbf{D}_{11,N}\mathbf{V}_{11,N}^{H} + \mathbf{V}_{21,N}\mathbf{D}_{21,N}^{H}\mathbf{U}_{21,N}^{H}\mathbf{U}_{21,N}\mathbf{D}_{21,N}\mathbf{V}_{21,N}^{H} = \mathbf{I}. \tag{B.2}$$

Since $\mathbf{U}_{ij,N}^{H}\mathbf{U}_{ij,N} = \mathbf{I}$ and it is assumed that $\mathbf{D}_{ij,N}^{H}\mathbf{D}_{ij,N} = \Lambda_{ij,N}$, where $\Lambda_{ij,N}$ is diagonal and real, the above equation can be expressed as

$$\mathbf{V}_{11,N}\Lambda_{11,N}\mathbf{V}_{11,N}^{H} + \mathbf{V}_{21,N}\Lambda_{22,N}\mathbf{V}_{21,N}^{H} = \mathbf{I}. \tag{B.3}$$

If $\mathbf{V}_{11,N}^{H}$ and $\mathbf{V}_{11,N}$ are multiplied from the left and right, respectively, the above equation becomes

$$\mathbf{V}_{11,N}^{H}\mathbf{V}_{11,N}\Lambda_{11,N}\mathbf{V}_{11,N}^{H}\mathbf{V}_{11,N} + \mathbf{V}_{11,N}^{H}\mathbf{V}_{21,N}\Lambda_{21,N}\mathbf{V}_{21,N}^{H}\mathbf{V}_{11,N} = \mathbf{V}_{11,N}^{H}\mathbf{V}_{11,N}. \tag{B.4}$$

This leads to

$$\Lambda_{11,N} + \mathbf{T}\Lambda_{21,N}\mathbf{T}^{H} = \mathbf{I}, \tag{B.5}$$

where $\mathbf{T} = \mathbf{V}_{11,N}^{H}\mathbf{V}_{21,N}$ and $\mathbf{T}\mathbf{T}^{H} = \mathbf{I}$. This equation is equivalent to

$$\mathbf{T} = (\mathbf{I} - \Lambda_{11,N})\mathbf{T}\Lambda_{21,N}^{-1}. \tag{B.6}$$

A certain mode should be generated at the antenna array through the decoupling network by a certain excitation, so it can be assumed that $\mathbf{S}_{21,N} = \mathbf{S}_{12,N}^{T}$ is full rank. It is noticed that $(\mathbf{I} - \Lambda_{11,N})$ and $\Lambda_{21,N}^{-1}$ are diagonal and equation (B.6) holds for arbitrary $\Lambda_{11,N}$ and $\Lambda_{21,N}$. Then, the matrix $\mathbf{T}$ must be diagonal. Since $\mathbf{T}\mathbf{T}^{H} = \mathbf{I}$, it can be concluded that $\mathbf{T}$ is diagonal and the entries are complex values with unit magnitude. As a result, equation (B.5) is equivalent to $\Lambda_{11,N} + \Lambda_{21,N} = \mathbf{I}$. Based on the same method, the third condition in equation (4.23) leads to $\Lambda_{22,N} + \Lambda_{12,N} = \mathbf{I}$ and $\mathbf{G} = \mathbf{V}_{22,N}^{H}\mathbf{V}_{12,N}$, where $\mathbf{G}$ is diagonal and the entries are complex values with unit magnitude. The second condition in equation (4.23) leads to

$$\mathbf{D}_{11,N}^{H}\mathbf{U}_{11,N}^{H}\mathbf{U}_{12,N}\mathbf{D}_{12,N} = -\mathbf{T}\mathbf{D}_{21,N}^{H}\mathbf{U}_{21,N}^{H}\mathbf{U}_{22,N}\mathbf{D}_{22,N}\mathbf{G}. \tag{B.7}$$

If $\mathbf{S}_{22,N} = \mathbf{S}_{\text{ant}}^{H}$, the the scattering matrix of the system becomes

$$\mathbf{S}_{\text{sys}} = \mathbf{S}_{11,N} + \mathbf{S}_{12,N}\mathbf{S}_{22,N}^{H}(\mathbf{I} - \mathbf{S}_{22,N}\mathbf{S}_{22,N}^{H})^{-1}\mathbf{S}_{21,N}. \tag{B.8}$$

In this case, it is assumed that $(\mathbf{I} - \mathbf{S}_{22,N}\mathbf{S}_{22,N}^H)$ is invertible. Based on the SVD, it is calculated that

$$\begin{aligned}(\mathbf{I} - \mathbf{S}_{22,N}\mathbf{S}_{22,N}^H)^{-1} =&(\mathbf{I} - \mathbf{U}_{22,N}\Lambda_{22,N}\mathbf{U}_{22,N}^H)^{-1}\\ =&(\mathbf{U}_{22,N}(\mathbf{I} - \Lambda_{22,N})\mathbf{U}_{22,N}^H)^{-1}\\ =&(\mathbf{U}_{22,N}\Lambda_{12,N}\mathbf{U}_{22,N}^H)^{-1}\\ =&\mathbf{U}_{22,N}\Lambda_{12,N}^{-1}\mathbf{U}_{22,N}^H. \end{aligned} \tag{B.9}$$

The system matrix can then be expressed in the form of

$$\begin{aligned}\mathbf{S}_{\text{sys}} =&\mathbf{U}_{11,N}\mathbf{D}_{11,N}\mathbf{V}_{11,N}^H+\\ &\mathbf{U}_{12,N}\mathbf{D}_{12,N}\mathbf{V}_{12,N}^H\mathbf{V}_{22,N}\mathbf{D}_{22,N}^H\mathbf{U}_{22,N}^H\mathbf{U}_{22,N}\Lambda_{12,N}^{-1}\mathbf{U}_{22,N}^H\mathbf{U}_{21,N}\mathbf{D}_{21,N}\mathbf{V}_{21,N}^H\\ =&\mathbf{U}_{11,N}\mathbf{D}_{11,N}\mathbf{V}_{11,N}^H + \mathbf{U}_{12,N}\mathbf{D}_{12,N}\mathbf{G}^H\mathbf{D}_{22,N}^H\Lambda_{12,N}^{-1}\mathbf{U}_{22,N}^H\mathbf{U}_{21,N}\mathbf{D}_{21,N}\mathbf{V}_{21,N}^H\\ =&(\mathbf{U}_{11,N}\mathbf{D}_{11,N} + \mathbf{U}_{12,N}\mathbf{D}_{12,N}\mathbf{G}^H\mathbf{D}_{22,N}^H\Lambda_{12,N}^{-1}\mathbf{U}_{22,N}^H\mathbf{U}_{21,N}\mathbf{D}_{21,N}\mathbf{T}^H)\mathbf{V}_{11,N}^H. \end{aligned} \tag{B.10}$$

Based on equation (B.7), the product of $\mathbf{U}_{11,N}\mathbf{D}_{11,N}$ can be expressed in the way of

$$\mathbf{U}_{11,N}\mathbf{D}_{11,N} = -\mathbf{U}_{12,N}\mathbf{D}_{12,N}^{H\ -1}\mathbf{G}^H\mathbf{D}_{22,N}^H\mathbf{U}_{22,N}^H\mathbf{U}_{21,N}\mathbf{D}_{21,N}\mathbf{T}^H. \tag{B.11}$$

Plugging the above results in equation (B.10), results in

$$\mathbf{S}_{\text{sys}} = \left(\mathbf{U}_{12,N}(-\mathbf{D}_{12,N}^{H\ -1}\mathbf{G}^H\mathbf{D}_{22,N}^H + \mathbf{D}_{12,N}\mathbf{G}^H\mathbf{D}_{22,N}^H\Lambda_{12,N}^{-1})\mathbf{U}_{22,N}^H\mathbf{U}_{21,N}\mathbf{D}_{21,N}\mathbf{T}^H\right)\mathbf{V}_{11,N}^H. \tag{B.12}$$

It is known that for diagonal matrix multiplications, changing the multiplication order of the diagonal matrices will not change the result. So the following term in equation (B.12) can be reordered and calculated as

$$\begin{aligned}&-\mathbf{D}_{12,N}^{H\ -1}\mathbf{G}^H\mathbf{D}_{22,N}^H + \mathbf{D}_{12,N}\mathbf{G}^H\mathbf{D}_{22,N}^H\Lambda_{12,N}^{-1}\\ =&-\mathbf{D}_{12,N}^{H\ -1}\mathbf{G}^H\mathbf{D}_{22,N}^H + \Lambda_{12,N}^{-1}\mathbf{D}_{12,N}\mathbf{G}^H\mathbf{D}_{22,N}^H\\ =&-\mathbf{D}_{12,N}^{H\ -1}\mathbf{G}^H\mathbf{D}_{22,N}^H + \mathbf{D}_{12,N}^{H\ -1}\mathbf{G}^H\mathbf{D}_{22,N}^H\\ =&0, \end{aligned} \tag{B.13}$$

which means $\mathbf{S}_{\text{sys}} = 0$ and the input ports are matched and decoupled with $\mathbf{S}_{22,N} = \mathbf{S}_{\text{ant}}^H$.

Appendix C

Channel Correlation and Radiation Pattern Correlation

In this appendix, the channel correlation is derived for the Rayleigh like channel model. According to equations (6.2) to (6.4) and considering the polarizations in equation (6.8), the channel coefficient can be summarized in the form of

$$
\begin{aligned}
h_{ji} =& \sqrt{\frac{G_{i,\theta}(1-\sum_k |S_{ki,T}|^2)}{8\pi}} \sqrt{\frac{G_{j,\theta}\lambda^2(1-\sum_k |S_{kj,R}|^2)}{2\pi}} \sqrt{\frac{g}{8\pi}} \\
& \begin{bmatrix} F_{j,\theta}(\theta_1,\phi_1)\sqrt{\triangle\Omega(\theta_1,\phi_1)} \\ F_{j,\theta}(\theta_1,\phi_2)\sqrt{\triangle\Omega(\theta_2,\phi_2)} \\ \vdots \\ F_{j,\theta}(\theta_N,\phi_M)\sqrt{\triangle\Omega(\theta_X,\phi_Y)} \end{bmatrix}^T \mathbf{H}_{s,\theta\theta} \begin{bmatrix} F_{i,\theta}(\theta_1,\phi_1)\sqrt{\triangle\Omega(\theta_1,\phi_1)} \\ F_{i,\theta}(\theta_1,\phi_2)\sqrt{\triangle\Omega(\theta_1,\phi_2)} \\ \vdots \\ F_{i,\theta}(\theta_X,\phi_Y)\sqrt{\triangle\Omega(\theta_X,\phi_Y)} \end{bmatrix} \\
& + \\
& \sqrt{\frac{G_{i,\phi}(1-\sum_k |S_{ki,T}|^2)}{8\pi}} \sqrt{\frac{G_{j,\theta}\lambda^2(1-\sum_k |S_{kj,R}|^2)}{2\pi}} \sqrt{\frac{g}{8\pi}} \\
& \begin{bmatrix} F_{j,\theta}(\theta_1,\phi_1)\sqrt{\triangle\Omega(\theta_1,\phi_1)} \\ F_{j,\theta}(\theta_1,\phi_2)\sqrt{\triangle\Omega(\theta_2,\phi_2)} \\ \vdots \\ F_{j,\theta}(\theta_N,\phi_M)\sqrt{\triangle\Omega(\theta_X,\phi_Y)} \end{bmatrix}^T \mathbf{H}_{s,\theta\phi} \begin{bmatrix} F_{i,\phi}(\theta_1,\phi_1)\sqrt{\triangle\Omega(\theta_1,\phi_1)} \\ F_{i,\phi}(\theta_1,\phi_2)\sqrt{\triangle\Omega(\theta_1,\phi_2)} \\ \vdots \\ F_{i,\phi}(\theta_X,\phi_Y)\sqrt{\triangle\Omega(\theta_X,\phi_Y)} \end{bmatrix} \\
& + \\
& \sqrt{\frac{G_{i,\theta}(1-\sum_k |S_{ki,T}|^2)}{8\pi}} \sqrt{\frac{G_{j,\phi}\lambda^2(1-\sum_k |S_{kj,R}|^2)}{2\pi}} \sqrt{\frac{g}{8\pi}} \\
& \begin{bmatrix} F_{j,\phi}(\theta_1,\phi_1)\sqrt{\triangle\Omega(\theta_1,\phi_1)} \\ F_{j,\phi}(\theta_1,\phi_2)\sqrt{\triangle\Omega(\theta_2,\phi_2)} \\ \vdots \\ F_{j,\phi}(\theta_N,\phi_M)\sqrt{\triangle\Omega(\theta_X,\phi_Y)} \end{bmatrix}^T \mathbf{H}_{s,\phi\theta} \begin{bmatrix} F_{i,\theta}(\theta_1,\phi_1)\sqrt{\triangle\Omega(\theta_1,\phi_1)} \\ F_{i,\theta}(\theta_1,\phi_2)\sqrt{\triangle\Omega(\theta_1,\phi_2)} \\ \vdots \\ F_{i,\theta}(\theta_X,\phi_Y)\sqrt{\triangle\Omega(\theta_X,\phi_Y)} \end{bmatrix} \\
& + \\
& \cos(\psi)\sqrt{\frac{G_{i,\phi}(1-\sum_k |S_{ki,T}|^2)}{8\pi}} \sqrt{\frac{G_{j,\phi}\lambda^2(1-\sum_k |S_{kj,R}|^2)}{2\pi}} \sqrt{\frac{g}{8\pi}} \\
& \begin{bmatrix} F_{j,\phi}(\theta_1,\phi_1)\sqrt{\triangle\Omega(\theta_1,\phi_1)} \\ F_{j,\phi}(\theta_1,\phi_2)\sqrt{\triangle\Omega(\theta_2,\phi_2)} \\ \vdots \\ F_{j,\phi}(\theta_N,\phi_M)\sqrt{\triangle\Omega(\theta_X,\phi_Y)} \end{bmatrix}^T \mathbf{H}_{s,\phi\phi}) \begin{bmatrix} F_{i,\phi}(\theta_1,\phi_1)\sqrt{\triangle\Omega(\theta_1,\phi_1)} \\ F_{i,\phi}(\theta_1,\phi_2)\sqrt{\triangle\Omega(\theta_1,\phi_2)} \\ \vdots \\ F_{i,\phi}(\theta_X,\phi_Y)\sqrt{\triangle\Omega(\theta_X,\phi_Y)} \end{bmatrix}. \qquad \text{(C.1)}
\end{aligned}
$$

where G_θ and G_ϕ are the maximum gain of the θ and ϕ component, respectively. Then, the channel correlation is calculated by further derivation of the above equation. During the calculation, the following conditions are applied for the simplification, $E[h_{ij,s,\theta} h^*_{kl,s,\phi}] = 0$

for any i, j, k and l, $E[h_{ij,s,\theta}h^*_{ij,s,\theta}] = E[h_{ij,s,\phi}h^*_{ij,s,\phi}] = 1$ for any i and j, $E[h_{ij,s,\theta}h^*_{kl,s,\theta}] = E[h_{ij,s,\phi}h^*_{kl,s,\phi}] = 0$ for any $ij \neq kl$. It is also realistic to assume that the polarization mismatch is independent from the Rayleigh like channel distributions. As a result, such results can be implemented in the following calculations. Consequently, by further evaluating the above equation of different channel coefficients, the following expression is obtained,

$$
\begin{aligned}
E[h_{ji}h^*_{nm}] =& \frac{g^2}{128\pi^3}\sqrt{(1-\sum_k |S_{ki,T}|^2)(1-\sum_k |S_{kj,R}|^2)(1-\sum_k |S_{km,T}|^2)(1-\sum_k |S_{kn,R}|^2)} \\
&\Bigg(A\sum_{x,y} F_{j,\theta}(\theta_x,\phi_y)F^*_{n,\theta}(\theta_x,\phi_y)\triangle\Omega(\theta_x,\phi_y)\sum_{u,v} F_{i,\theta}(\theta_u,\phi_v)F^*_{m,\theta}(\theta_u,\phi_v)\triangle\Omega(\theta_u,\phi_v) \\
&\qquad + \\
&B\sum_{x,y} F_{j,\theta}(\theta_x,\phi_y)F^*_{n,\theta}(\theta_x,\phi_y)\triangle\Omega(\theta_x,\phi_y)\sum_{u,v} F_{i,\phi}(\theta_u,\phi_v)F^*_{m,\phi}(\theta_u,\phi_v)\triangle\Omega(\theta_u,\phi_v) \\
&\qquad + \\
&C\sum_{x,y} F_{j,\phi}(\theta_x,\phi_y)F^*_{n,\phi}(\theta_x,\phi_y)\triangle\Omega(\theta_x,\phi_y)\sum_{u,v} F_{i,\theta}(\theta_u,\phi_v)F^*_{m,\theta}(\theta_u,\phi_v)\triangle\Omega(\theta_u,\phi_v) \\
&\qquad + \\
&D\sum_{x,y} F_{j,\phi}(\theta_x,\phi_y)F^*_{n,\phi}(\theta_x,\phi_y)\triangle\Omega(\theta_x,\phi_y)\sum_{u,v} F_{i,\phi}(\theta_u,\phi_v)F^*_{m,\phi}(\theta_u,\phi_v)\triangle\Omega(\theta_u,\phi_v)\Bigg),
\end{aligned}
$$

where

$$
\begin{aligned}
A &= \sqrt{G_{i,\theta}G_{j,\theta}G_{m,\theta}G_{n,\theta}}, \\
B &= \sqrt{G_{i,\phi}G_{j,\theta}G_{m,\phi}G_{n,\theta}}, \\
C &= \sqrt{G_{i,\theta}G_{j,\phi}G_{m,\theta}G_{n,\phi}}, \\
D &= \sqrt{G_{i,\phi}G_{j,\phi}G_{m,\phi}G_{n,\phi}}.
\end{aligned} \tag{C.2}
$$

When $\triangle\Omega$ is smaller enough, the discrete summation is equivalent as

$$
\sum_{x,y} F_{j,\phi}(\theta_x,\phi_y)F^*_{n,\phi}(\theta_x,\phi_y)\triangle\Omega(\theta_x,\phi_y) = \int F_{j,\phi}(\theta,\phi)F^*_{n,\phi}(\theta,\phi)d\Omega. \tag{C.3}
$$

According to the knowledge from Chapter 2, the far field gain pattern can be written in the form

$$
\sqrt{G}\vec{F}(\theta,\phi) = \sqrt{G_\theta}F_\theta(\theta,\phi)\vec{e}_\theta + \sqrt{G_\phi}F_\phi(\theta,\phi)\vec{e}_\phi. \tag{C.4}
$$

Then, the following expression can be used for shortening equation (C.2),

$$
\begin{aligned}
\int \sqrt{G_{i,\theta}G_{m,\theta}}F_{i,\theta}(\theta,\phi)F^*_{m,\theta}(\theta,\phi)d\Omega + \int \sqrt{G_{i,\phi}G_{m,\phi}}F_{i,\phi}(\theta,\phi)F^*_{m,\phi}(\theta,\phi)d\Omega \\
= \int \sqrt{G_iG_m}\vec{F}_i(\theta,\phi)\cdot\vec{F^*}_m(\theta,\phi)d\Omega.
\end{aligned} \tag{C.5}
$$

Finally, the channel correlation coefficient in equation (6.9) can be summarized as

$$
\rho_{ji,nm} = \frac{\int \vec{F}_i(\theta,\phi)\cdot\vec{F^*}_m(\theta,\phi)d\Omega}{\sqrt{\int|\vec{F}_i(\theta,\phi)|^2\int|d\Omega\vec{F}_m(\theta,\phi)|^2d\Omega}} \times \frac{\int \vec{F}_j(\theta,\phi)\cdot\vec{F^*}_n(\theta,\phi)d\Omega}{\sqrt{\int|\vec{F}_j(\theta,\phi)|^2\int|d\Omega\vec{F}_n(\theta,\phi)|^2d\Omega}}. \tag{C.6}
$$

References

Almers, P., Tufvesson, F., and Molisch, A. F. (2006). Keyhole effect in MIMO wireless channels: measurements and theory. *IEEE Transactions on Wireless Communications*, 5(12):3596–3604.

Anguera, J., Andujar, A., and Garcia, C. (2013). Multiband and small coplanar antenna system for wireless handheld devices. *IEEE Transactions on Antennas and Propagation*, 61(7):3782–3789.

AntennaWeb (2015). The Antenna Theory Website. *www.antenna-theory.com*.

Balanis, C. A. (1989). *Advanced Engineering Electromagnetics*, John Wiley & Sons.

Balanis, C. A. (1992). Antenna theory: a review. *Proceedings of the IEEE*, 80(1):7–23.

Balanis, C. A. (2005). *Antenna Theory: Analysis and Design*, John Wiley & Sons.

Biglieri, E., Proakis, J., and Shamai, S. (1998). Fading channels: Information theoretic and communications aspects. *IEEE Transactions on Information Theory*, 44(10):2619–2692.

Blanch, S., Romeu, J., and Corbella, I. (2003). Exact representation of antenna system diversity performance from input parameter description. *Electronics Letter*, 39(9):705–707.

Blender (2015). Blender 2.74. *www.blender.org*.

Chaloupka, H. J. and Wang, X. (2004). Novel approach for diversity and MIMO antennas at small mobile platforms. *15th IEEE International Symposium on Personal, Indoor and Mobile Radio Communications*, Barcelona, Spain.

Chaloupka, H. J., Wang, X., and Coetzee, J. C. (2004). Performance enhancement of smart antenna with reduced element spacing. *IEEE Wireless Communication and Networking Conference*, New Orleans, LA.

Chiani, M., Win, M. Z., and Zanella, A. (2003). On the capacity of spatially correlated MIMO Rayleigh-fading channels. *IEEE Transactions on Information Theory*, 49(10):2363–2371.

Chizhik, D., Ling, J., Wolniansky, P. W., Valenzuela, R. A., Costa, N., and Huber, K. (2003). Multiple-input-multiple-output measurements and modeling in Manhattan. *IEEE Journal on Selected Areas in Communications*, 21(3):321–331.

Coetzee, J. C. and Yu, Y. (2008). New modal feed network for a compact monopole array with isolated ports. *IEEE Transactions on Antennas and Propagation*, 56(12):3872–3875.

Collin, R. E. and Zucker, F. J. (1969). *Antenna Theory, Part 1*, McGraw-Hill.

Cover, T., Gamal, A., and Salehi, M. (1980). Multiple access channels with arbitrarily correlated sources. *IEEE Transactions on Information Theory*, 26(6):648–657.

Cover, T. and Gamal, A. E. (1979). Capacity theorems for the relay channel. *IEEE Transactions on Information Theory*, 25(5):572–584.

CST MWS (2014). CST Microwave Studio. *www.cst.com*.

Deal, W. R., Kaneda, N., J. Sor, Y. Q., and Itoh, T. (2000). A new quasi-Yagi antenna for planar active antenna arrays. *IEEE Transactions on Microwave Theory and Techniques*, 48(6):910–918.

Dietrich, C. B., Dietze, K., Nealy, J. R., and Stutzman, W. L. (2001). Spatial, polarization, and pattern diversity for wireless handheld terminals. *IEEE Transactions on Antennas and Propagation*, 49(9):1271–1281.

Dikaiakos, M., Florides, A., Nadeem, T., and Iftode, L. (2007). Location-aware services over vehicular Ad-Hoc networks using car-to-car communication. *IEEE Journal on Selected Areas in Communications*, 25(8):1590–1602.

FEKO (2014). Altair FEKO. *www.feko.info*.

Fuertes Pals, V. A. (2014). Investigation and Evaluation of Electromagnetic Wave Propagation Simulations using Ray Tracing. Master Thesis, Technische Universität München.

Georgakopoulos, S. V., Birtcher, C. R., and Balanis, C. A. (2001). Coupling modeling and reduction techniques of cavity-backed slot antennas: FDTD versus measurements. *IEEE Transactions on Electromagnetic Compatibility*, 43(3):261–272.

Gesbert, D., Bölcskei, H., Gore, D. A., and Paulraj, A. J. (2002). Outdoor MIMO wireless channels: models and performance prediction. *IEEE Transactions on Communications*, 50(12):1926–1934.

Goldsmith, A., Jafar, S. A., Jindal, N., and Vishwanath, S. (2003). Capacity limits of MIMO channels. *IEEE Journal on Selected Areas in Communications*, 21(5):684–702.

Gray, R. M. (2011). *Entropy and Information Theory, 2nd Edition*, Springer.

Hallbjörner, P. (2005). The significance of radiation efficiencies when using S-parameters to calculate the received signal correlation from two antennas. *IEEE Antennas and Wireless Propagation Letters*, 4:97–99.

HFSS (2014). ANSYS HFSS. *www.ansys.com*.

Hoydis, J., Brink, S., and Debbah, M. (2013). Massive MIMO in the UL/DL of cellular networks: how many antennas do we need? *IEEE Journal on Selected Areas in Communications*, 31(2):160–171.

Hui, H. T. and Wang, X. (2010). Building antenna characteristics into multiple-input and multiple-output channel simulation. *International Journal of Electronics*, 97(6):703–714.

Huynh, T. and Lee, K.-F. (1995). Single-layer single-patch wideband microstrip antenna. *Electronics Letters*, 31(16):1310–1312.

IEEE (1983). IEEE Standard Definitions of Terms for Antennas. *IEEE Std 145-1983*.

Ivrlac, M. and Nossek, J. (2010). High-efficiency super-gain antenna arrays. *International ITG Workshop on Smart Antennas*, Bremen, Germany.

Jensen, M. A. and Wallace, J. W. (2004). A review of antennas and propagation for MIMO wireless communication. *IEEE Transactions on Antennas and Propagation*, 52(11):2810–2824.

Kaneda, N., Deal, W. R., Qian, Y., Waterhouse, R., and Itoh, T. (2002). A broadband planar quasi-Yagi antenna. *IEEE Transactions on Antennas and Propagation*, 50(8):1158–1160.

Karimian, R., Oraizi, H., Fakhte, S., and Farahani, M. (2013). Novel F-shaped quadband printed slot antenna for WLAN and WiMAX MIMO systems. *IEEE Antennas and Wireless Propagation Letters*, 12:405–408.

Kildal, P.-S. and Rosengren, K. (2004). Correlation and capacity of MIMO systems and mutual coupling, radiation efficiency, and diversity gain of their antennas: simulations and measurements in a reverberation chamber. *IEEE Communications Magazine*, 42(12):104–112.

Kim, K. J., Lee, S., Kim, B. N., Jung, J. H., and Yoon, Y. J. (2011). Small antenna with a coupling feed and parasitic elements for multiband mobile applications. *IEEE Antennas and Wireless Propagation Letters*, 10:290–293.

Kim, S.-H., Lee, J.-Y., Nguyen, T., and Jang, J.-H. (2013). High-performance MIMO antenna with 1-D EBG ground structures for handset application. *IEEE Antennas and Wireless Propagation Letters*, 12:1468–1471.

Larsson, E. G., Edfors, O., Tufvesson, F., and Marzetta, T. L. (2014). Massive MIMO for next generation wireless systems. *IEEE Communications Magazine*, 52(2):186–195.

Lau, B. K. and Andersen, J. B. (2012). Simple and efficient decoupling of compact arrays with parasitic scatters. *IEEE Transactions on Antennas and Propagation*, 60(2):464–472.

Lee, C. T. and Wong, K. L. (2009). Two PIFA-related miniaturized dual-band antennas. *IEEE Transactions on Antennas and Propagation*, 57(4):1252–1258.

Li, H., Lin, X., Lau, B. K., and He, S. (2010a). Performance evaluation of capacity-aware MIMO beamforming schemes in OFDM-SDMA systems. *IEEE Transactions on Communications*, 58(1):79–83.

Li, H., Lin, X., Lau, B. K., and He, S. (2013). Equivalent circuit based calculation of signal correlation in lossy MIMO antennas. *IEEE Transactions on Antennas and Propagation*, 61(10):5214–5222.

Li, H., Miers, Z. T., and Lau, B. K. (2014). Design of orthogonal MIMO handset antennas based on characteristic mode manipulation at frequency bands below 1 GHz. *IEEE Transactions on Antennas and Propagation*, 62(5):2756–2766.

Li, Q., Li, G., Lee, W., Lee, M., Mazzarese, D., Clerckx, B., and Li, Z. (2010b). MIMO techniques in WiMAX and LTE: a feature overview. *IEEE Communications Magazine*, 48(5):86–92.

Lin, C.-C., Tang, T.-C., and Lin, K.-H. (2013). Broadband MIMO antennas for MIMO radar systems. *IEEE International Symposium on Antennas and Propagation*, Orlando, USA.

Lin, K. C., Wu, C. H., Lai, C. H., , and Ma, T. G. (2012). Novel dual-band decoupling network for two-element closely spaced array using synthesized microstrip lines. *IEEE Transactions on Antennas and Propagation*, 60(11):5118–5128.

Louie, R. H. Y., McKay, M. R., and Collings, I. B. (2008). Impact of correlation on the capacity of multiple access and broadcast Channels with MIMO-MRC. *IEEE Transactions on Wireless Communications*, 7(6):2397–2403.

Loyka, S. and Kouki, A. (2002). On MIMO channel capacity, correlations, and keyholes: analysis of degenerate channels. *IEEE Transactions on Communications*, 50(12):1886–1888.

Lui, H.-S. and Hui, H. T. (2010). Improved mutual coupling compensation in compact antenna arrays. *IET Microwaves, Antennas and Propagation*, 4(10):1506–1516.

Maharaj, B. T., Linde, L. P., and Wallace, J. W. (2007). MIMO channel modelling: The Kronecker Model and Maximum Entropy. *IEEE Wireless Communications and Networking Conference*, Kowloon, Hong Kong.

Martens, R., Safin, E., and Manteuffel, D. (2011). Inductive and capacitive excitation of the characteristic modes of small terminals. *Loughborough Antennas and Propagation Conference*, Loughborough, UK.

MathWorks (2011). MATLAB R2011a. *www.mathework.com*.

McKown, J. W. and Hamilton, R. L. (1991). Ray tracing as a design tool for radio networks. *IEEE Network Magazine*, 5(6):27–30.

Mocker, M. S. L., Liu, S., Fuertes, V. A., Tazi, H., and Eibert, T. F. (2015). Influence of the vehicle environment on the radiation characteristics of vehicle roof antennas. *German Microwave Conference*.

Nepa, P., Manara, G., Serra, A. A., and Nenna, G. (2005). Multiband PIFA for WLAN applications. *IEEE Antennas and Wireless Propagation Letters*, 4:349–350.

Oestges, C. (2006). Validity of the Kronecker model for MIMO correlated channels. *IEEE Vehicular Technology Conference*, Melbourne, Australia.

Paulraj, A., GORE, D., Nabar, R., and Bolcskei, H. (2004). An overview of MIMO communications - a key to gigabit wireless. *Proceedings of the IEEE*, 92(2):198–218.

Pelosi, M., Knudsen, M. B., , and Pedersen, G. F. (2012). Multiple antenna systems with inherently decoupled radiators. *IEEE Transactions on Antennas and Propagation*, 60(2):503–515.

Pozar, D. M. (2011). *Microwave Engineering, 4th edition*, John Wiley & Sons.

Ramsay, J. (1981). Highlights of antenna history. *IEEE Antennas and Propagation Society Newsletter*, 23(6):7–20.

Rogers (2015). Rogers Corporation. *www.rogerscorp.com*.

Rowell, C. R. and Murch, R. D. (1997). A capacitively loaded PIFA for compact mobile telephone handsets. *IEEE Transactions on Antennas and Propagation*, 45(5):837–842.

Rowell, C. R. and Murch, R. D. (1998). A compact PIFA suitable for dual-frequency 900/1800-MHz operation. *IEEE Transactions on Antennas and Propagation*, 46(4):596–598.

Rumsey, V. H. (1959). Some new forms of Huygens' principle. *IRE Transactions on Antennas and Propagation*, 7(5):103–116.

Salama, S. and Solbach, K. (2014). Parasitic elements based decoupling technique for monopole four square array antenna. *44th European Microwave Conference*, Rome, Italy.

Saleem, R., Bilal, M., Bajwa, K., and Shafique, M. (2015). Eight-element UWB-MIMO array with three distinct isolation mechanisms. *Electronics Letters*, 51(4):311–313.

Saleh, A. A. M. and Valenzuela, R. A. (1987). A statistical model for indoor multipath propagation. *IEEE Journal on Selected Areas in Communications*, 5(2):128–137.

Shannon, C. E. (1948). A mathematical theory of communication. *The Bell System Technical Journal*, 27(3):379–423.

Sharawi, M. S. (2013). Printed multi-band MIMO antenna systems and their performance metrics. *IEEE Antennas and Propagation Magazine*, 55(5):218–232.

Sharawi, M. S., Numan, A. B., and Aloi, D. N. (2013). Isolation improvement in a dual-band dual-element MIMO antenna system using capacitively loaded loops. *Progress in Electromagnetics Research*, 134:247–266.

Sharawi, M. S., Numan, A. B., Khan, M. U., and Aloi, D. N. (2012). A dual-element dual-band MIMO antenna system with enhanced isolation for mobile terminals. *IEEE Antennas and Wireless Propagation Letters*, 11:1006–1009.

Shiu, D.-S., Foschini, G. J., Gans, M. J., and Kahn, J. M. (2000). Fading correlation and its effect on the capacity of multielement antenna systems. *IEEE Transactions on Communications*, 48(3):502–513.

Spencer, Q., Jeffs, B., Jensen, M., and Swindlehurst, A. (2000). Modeling the statistical time and angle of arrival characteristics of an indoor multipath channel. *IEEE Journal on Selected Areas in Communications*, 18(3):347–360.

Stjernman, A. (2005). Relationship between radiation pattern correlation and scattering matrix of lossless and lossy antennas. *Electronics Letter*, 41(12):678–680.

Su, S.-W., Lee, C.-T., and Chang, F.-S. (2012). Printed mimo-antenna system using neutralization-line technique for wireless USB-dongle applications. *IEEE Transactions on Antennas and Propagation*, 60(2):456–463.

Telatar, E. (1999). Capacity of multi-antenna Gaussian channels. *European Transactions on Telecommunications*, 10(6):585–595.

UIUC (2015). Lecture 21. The Multivariate Normal Distribution. *http://www.math.uiuc.edu*.

Vaughan, R. J. and Anderson, J. B. (1987). Antenna diversity in mobile communications. *IEEE Transactions on Vehicular Technology*, 36(4):149–172.

Volmer, C., Sengül, M., Weber, J., Stephan, R., and Hein, M. A. (2008a). Broadband decoupling and matching of a superdirective two-port antenna array. *IEEE Antennas and Wireless Propagation Letters*, 7:613–616.

Volmer, C., Weber, J., Stephan, R., Blau, K., and Hein, M. A. (2008b). An Eigen-analysis of compact antenna arrays and its application to port decoupling. *IEEE Transactions on Antennas and Propagation*, 56(2):360–370.

Wallace, J. W. and Jensen, M. A. (2002). Modeling the indoor MIMO wireless channel. *IEEE Transactions on Antennas and Propagation*, 50(5):591–599.

Wallace, J. W. and Jensen, M. A. (2004). Termination-dependent diversity performance of coupled antennas: Network theory. *IEEE Transactions on Antennas and Propagation*, 52(1):98–105.

Wang, B., Zhang, J., and Host-Madsen, A. (2005). On the capacity of MIMO relay channels. *IEEE Transactions on Information Theory*, 51(1):29–43.

Wang, K., Li, L., and Eibert, T. F. (2013a). A highly compact four-element monopole array with one-layer decoupling and matching network. *IEEE International Symposium on Antennas and Propagation*, Orlando, USA.

Wang, K., Li, L., and Eibert, T. F. (2013b). Comparison of compact monopole antenna arrays with Eigenmode excitation and multiport conjugate matching. *IEEE Transactions on Antennas and Propagation*, 61(8):4054–4062.

Wang, K., Li, L., and Eibert, T. F. (2014a). A decoupling technique based on partially extended ground plane for compact two-Port printed monopole antenna arrays. *German Microwave Conference*, Aachen, Germany.

Wang, K., Li, L., and Eibert, T. F. (2014b). Compact three-port printed diversity array with combined antenna types. *IEEE International Symposium on Antennas and Propagation*, Memphis, USA.

Wang, K., Li, L., and Eibert, T. F. (2015a). Estimation of signal correlation of lossy compact monopole arrays with decoupling networks. *IEEE Transactions on Antennas and Propagation*, 63(1):357–363.

Wang, K., Li, L., Eibert, T. F., and Tooni, S. (2013c). Equivalent circuits of compact monopole arrays based on scattering parameters. *European Conference on Antennas and Propagationn*, Gothenburg, Sweden.

Wang, K., Mauermayer, R. A. M., and Eibert, T. F. (2014c). Compact two-element printed monopole array with partially extended ground plane. *IEEE Antennas and Wireless Propagation Letters*, 13:138–140.

Wang, K., Mauermayer, R. A. M., and Eibert, T. F. (2015b). Contour integrated dual band compact antenna elements and arrays for low profile mobile terminals. *IEEE Transactions on Antennas and Propagation*, 63(7):3305–3311.

Wang, K., Mauermayer, R. A. M., Li, L., and Eibert, T. F. (2015c). A highly compact broadband near-edge antenna for low profile communication Devices. *European Conference on Antennas and Propagation*, Lisbon, Portugal.

Wang, K., Sun, S., and Eibert, T. F. (2014d). Investigations on beamforming applications of compact monopole arrays. *IEEE International Symposium on Antennas and Propagation*, Memphis, USA.

Wang, K., Wächter, T. J., Hartmuth, H., Fei, H., Hamberger, G. F., and Eibert, T. F. (2015d). Self-mixing antenna arrays with wide receiving angular range. *IEEE International Symposium on Antennas and Propagation*, Vancouver, Canada.

Wang, Y. and Du, Z. (2014a). A wideband quad-antenna system for mobile terminals. *IEEE Antennas and Wireless Propagation Letters*, 13:1521–1524.

Wang, Y. and Du, Z. (2014b). A wideband printed dual-antenna with three neutralization lines for mobile terminals. *IEEE Transactions on Antennas and Propagation*, 62(3):1495–1500.

Wang, Y.-S., Lee, M.-C., and Chung, S.-J. (2007). Two PIFA-related miniaturized dual-band antennas. *IEEE Transactions on Antennas and Propagation*, 55(3):805–811.

Wikipedia (2015a). Parabolic antenna. *www.wikipedia.org*.

Wikipedia (2015b). Planar inverted F antenna. *www.wikipedia.org*.

Wikipedia (2015c). Yagi-Uda antenna. *www.wikipedia.org*.

Wong, K. L. and Hsu, W. H. (1997). Broadband triangular microstrip antenna with U-shaped slot. *Electronics Letters*, 33(25):2085–2087.

Wong, K. L. and Hsu, W. H. (2001). A broad -band rectangular patch antenna with a pair of wide slits. *IEEE Transactions on Antennas and Propagation*, 49(9):1345–1347.

Wong, K. L., Jiang, H. J., and Kao, Y. C. (2013). High-isolation 2.4/5.2/5.8 GHz WLAN MIMO antenna array for laptop computer application. *Microwave and Optical Technology Letters*, 55(2):382–387.

Yaghjian, A. D. and Best, S. R. (2005). Impedance, bandwidth, and Q of antenna. *IEEE Transactions on Antennas and Propagation*, 53(4):1298–1324.

Yagi, H. (1928). Beam transmission of ultra short waves. *Radio Engineers, Proceedings of the Institute of*, 16(6):715–740.

Yang, F. and Rahmat-Samii, Y. (2003a). Microstrip antennas integrated with electromagnetic band-gap (EBG) structures: a low mutual coupling design for array applications. *IEEE Transactions on Antennas and Propagation*, 51(10):2936–2946.

Yang, F. and Rahmat-Samii, Y. (2003b). Reflection phase characterizations of the EBG ground plane for low profile wire antenna applications. *IEEE Transactions on Antennas and Propagation*, 51(10):2691–2703.

Yang, F., Zhang, X. Z., and Rahmat-Samii, Y. (2001). Wideband E-shaped patch antennas for wireless communications. *IEEE Transactions on Antennas and Propagation*, 49(7):1094–1100.

Younkyu, C., Seong-Sik, J., Ahn, D., Jae-Ick, C., and Itoh, T. (2004). High isolation dual-polarized patch antenna using integrated ground structure. *IEEE Microwave Wireless Componoents Letters*, 14(1):4–6.

Yu, K., Bengtsson, M., Ottersten, B., McNamara, D., Karlsson, P., and Beach, M. (2004). Modeling of wide-band MIMO radio channels based on NLoS indoor measurements. *IEEE Transactions on Vehicular Technology*, 53(3):655–665.

Yu, Y. and Hui, H. T. (2011). Design of a mutual coupling compensation network for a small receiving monopole array. *IEEE Transactions on Microwave Theory and Technology*, 59(9):2241–2245.

Yu, Y., Lui, H.-S., Niow, C. H., and Hui, H. T. (2011). Improved DOA estimations using the receiving mutual impedances for mutual coupling compensation an experimental study. *IEEE Transactions on Wireless Communications*, 10(7):2228–2233.

Zhang, L., Li, Y., and Cimini, L. (2012). Statistical performance analysis for MIMO beamforming and STBC when co-channel interferers use arbitrary MIMO modes. *IEEE Transactions on Communications*, 60(10):2926–2937.

Zhang, X. and Sarris, C. D. (2014). A high-accuracy ADI scheme for the vector parabolic equation applied to the modeling of wave propagation in Tunnels. *IEEE Antennas and Wireless Propagation Letters*, 13:650–653.

Zhou, X., Quan, X., and Li, R. L. (2012). A dual-broadband MIMO antenna system for GSM/UMTS/LTE and WLAN handsets. *IEEE Antennas and Wireless Propagation Letters*, 11:551–554.

Zhu, F.-G., Xu, J.-D., and Xu, W. (2009). Reduction of mutual coupling between closely-packed antenna elements using defected ground structure. *Electronics Letters*, 45(12):601–602.

List of Supervised Student Projects

Bachelor Thesis

- Alexander Paulus, Novel Decoupling Structure for Patch Antennas of a Compact Radar Transceiver, Technische Universität München, 2013.
- Hyazinth Hartmuth, Entwurf und Realisierung eines rauscharmen Verstärkers für den Frequenzbereich 8 GHz bis 12 GHz, Technische Universität München, 2014.

Master Thesis

- Hong Fei, Single Element Design for Sparse Antenna Array with Large Effective Receiving Area, Technische Universität München, 2013.

List of Publications of the Author

Wang, K., Li, L., Schmidt, C., Bonerz, S., Siart, U., and Eibert, T. F. (2012). A coaxial line based propagation channel for wireless communication between rotating machine components. *10th International Symposium on Antennas, Propagation, and EM Theory*, Xian, China.

Wang, K., Li, L., and Eibert, T. F. (2013a). A highly compact four-element monopole array with one-layer decoupling and matching network. *IEEE International Symposium on Antennas and Propagation*, Orlando, USA.

Wang, K., Li, L., and Eibert, T. F. (2013b). Comparison of compact monopole antenna arrays with Eigenmode excitation and multiport conjugate matching. *IEEE Transactions on Antennas and Propagation*, 61(8):4054–4062.

Wang, K., Li, L., Eibert, T. F., and Tooni, S. (2013c). Equivalent circuits of compact monopole arrays based on scattering parameters. *European Conference on Antennas and Propagationn*, Gothenburg, Sweden.

Li, L., Wang, K., and Eibert, T. F. (2014a). A new radial-angular-R2 transformation for singular integrals on triangular meshes. *European Conference on Antennas and Propagation*, The Hague,S Netherlands.

Li, L., Wang, K., and Eibert, T. F. (2014b). A projection height independent adaptive radial-angular-R2 transformation for singular integrals. *IEEE Transactions on Antennas and Propagation*, 62(10):5381–5386.

Li, L., Wang, K., Li, H., and Eibert, T. F. (2014c). Analytical finite element matrix elements and global matrix assembly for hierarchical 3D vector basis functions within the hybrid finite element boundary integral method. *Advances in Radio Science*, 12:1–11.

Wang, K., Li, L., and Eibert, T. F. (2014a). A decoupling technique based on partially extended ground plane for compact two-Port printed monopole antenna arrays. *German Microwave Conference*, Aachen, Germany.

Wang, K., Paulus, A., Wächter, T. J., Siart, U.,and Eibert, T. F. (2014b). Compact CW radar transceiver antennas with novel decoupling technique based on neutralization. *European Conference on Antennas and Propagation*, The Hague, Netherlands.

Wang, K., Li, L., and Eibert, T. F. (2014c). Compact three-port printed diversity array with combined antenna types. *IEEE International Symposium on Antennas and Propagation*, Memphis, USA.

Wang, K., Mauermayer, R. A. M., and Eibert, T. F. (2014d). Compact two-element printed monopole array with partially extended ground plane. *IEEE Antennas and Wireless Propagation Letter*, 13:138–140.

Wang, K., Sun, S., and Eibert, T. F. (2014e). Investigations on beamforming applications of compact monopole arrays. *IEEE International Symposium on Antennas and Propagation*, Memphis, USA.

Wang, K., Li, L., and Eibert, T. F. (2015a). Estimation of signal correlation of lossy compact monopole arrays with decoupling networks. *IEEE Transactions on Antennas and Propagation*, 63(1):357–363.

Wang, K., Mauermayer, R. A. M., Li, L., and Eibert, T. F. (2015b). A highly compact broadband near-edge antenna for low profile communication Devices. *European Conference on Antennas and Propagation*, Lisbon, Portugal.

Wang, K., Mauermayer, R. A. M., and Eibert, T. F. (2015c). Contour integrated dual band compact antenna elements and arrays for low profile mobile terminals. *IEEE Transactions on Antennas and Propagation*, 63(7):3305–3311.

Wang, K., Wächter, T., Hartmuth, H., Fei, H., Hamberger, G. F., and Eibert, T. F. (2015d). Low profile dual band wlan antenna array for mobile terminals. *IEEE International Symposium on Antennas and Propagation*, Vancouver, Canada.

Wang, K. and Eibert, T. F. (2015e). Low profile dual band wlan antenna array for mobile terminals. *IEEE International Symposium on Antennas and Propagation*, Vancouver, Canada.